Evolution of the Brightest Cluster Galaxies

Dongyao Zhao

The University of
Nottingham

Thesis submitted to the University of Nottingham
for the degree of Doctor of Philosophy

May 2016

Abstract

In this thesis, I explore the evolution of the brightest cluster galaxies (BCGs) over the last 10 billion years through detailed studies of both local BCGs from SDSS and their high-z progenitors from CANDELS UDS.

First, I study a large sample of local BCGs and link their morphologies to their structural properties. We derive visual morphologies for these BCGs and find that $\sim 57\%$ of local BCGs are cD galaxies, $\sim 13\%$ are ellipticals, and $\sim 21\%$ belong to intermediate classes, mostly between E and cD. There is a continuous distribution in the properties of the BCG's envelopes, ranging from undetected (elliptical BCGs) to clearly detected (cD galaxies), with intermediate classes showing increasing degrees of the envelope presence. A minority ($\sim 7\%$) of BCGs have disk morphologies, with spirals and S0s in similar proportions, and the rest ($\sim 2\%$) are mergers. After carefully fitting the galaxy light distributions using Sérsic models, I find a clear link between BCG morphology and structure, such that cD galaxies are typically larger than elliptical BCGs, and the visually extended envelope of cD galaxies is a distinct structure differing from the central bulge. Based on this BCG morphology–structure correlation, I develop a statistically robust way to separate cD from non-cD BCGs, by which cD galaxies can be selected with reasonably high completeness and low contamination.

Next, I investigate the effect of environment on the properties of local BCGs by studying the relationship between the BCG's internal properties (stellar mass, structure and morphology) and their environment (local density and cluster halo mass). I find that the size of BCGs is determined by the intrinsic BCG stellar mass, with a weak correlation with the cluster environment. Additionally, more massive BCGs tend to inhabit denser regions and more massive clusters than lower mass BCGs. The growth of the BCGs seems to be linked to the hierarchical growth of the structures they inhabit:

as the groups and clusters became denser and more massive, the BCGs at their centres also grew. Moreover, I demonstrate that cD galaxies are $\sim 40\%$ more massive than elliptical BCGs, and prefer denser regions and more massive haloes. My results, together with the findings of previous studies, suggest an evolutionary link between elliptical and cD BCGs. I propose that most present-day cDs started their life as ellipticals at $z \sim 1$, which subsequently grew in stellar mass and size due to mergers. In this process, the cD envelope developed. This process is nearing completion since the majority of the local BCGs have cD morphology. However, the presence of BCGs with intermediate morphological classes suggests that the growth and morphological transformation of BCGs is still ongoing.

Finally, I present a new method for tracing the evolution of BCGs from $z \sim 2$ to $z \sim 0$. I conclude, on the basis of semi-analytical models, that the best method to select BCG progenitors at $z \sim 2$ is a hybrid environmental density and stellar mass ranking approach. Ultimately I am able to retrieve 45% of BCG progenitors. Although the selected high-z progenitor sample is a mixture of BCG and non-BCG progenitors, I demonstrate that their properties can be used to trace BCG evolution. Applying this method to the CANDELS UDS data, I construct an observational BCG progenitor sample at $z \sim 2$. A local BCG comparison sample is constructed using the SDSS data, taking into account the likely contamination from non-BCGs to ensure a fair comparison between high-z and low-z samples. Using these samples I demonstrate that BCG sizes have grown by a factor of ~ 3.2 since $z \sim 2$, and BCG progenitors are mainly late-type galaxies, exhibiting less concentrated profiles than their early-type local counterparts. I also find that BCG progenitors have more disturbed morphologies, while local BCGs have much smoother profiles. Moreover, I find that the stellar masses of BCGs have grown by a factor of ~ 2.5 since $z \sim 2$, and the SFR of BCG progenitors has a median value of $\sim 14\ M_{\odot}\mathrm{yr}^{-1}$, much higher than their quiescent local descendants. I demonstrate that at $1 < z < 2$ star formation and merging contribute approximately equally to BCG mass growth. However, merging plays a dominant role in BCG assembly at $z \lesssim 1$. I also find that BCG progenitors at high-z are not significantly different from other galaxies of similar mass at the same epoch. This suggests that the processes which differentiate BCGs from normal massive elliptical galaxies must occur at $z \lesssim 2$.

Acknowledgements

Acknowledgements

Publications

All the work in this thesis has been presented in several papers. The results of Chapters 2 have been published in Paper I. Paper II contains the study in Chapter 3. The work presented in Chapter 4 will be published in a forthcoming Paper III.

I) **Zhao, Dongyao**; Aragón-Salamanca, Alfonso; Conselice, Christopher J., *"The Link Between Morphology and Structure of Brightest Cluster Galaxies: Automatic Identification of cDs"*, 2015, MNRAS, 448, 2530

II) **Zhao, Dongyao**; Aragón-Salamanca, Alfonso; Conselice, Christopher J., *"Evolution of the Brightest Cluster Galaxies: the Influence of Morphology, Stellar Mass and Environment"*, 2015, MNRAS, 453, 4444

III) **Zhao, Dongyao**; Conselice, Christopher J.; Aragón-Salamanca, Alfonso; Almaini, Omar; Hartley, William G.; Lani, Caterina; Mortlock, Alice; Old, Lyndsay, *"Exploring the Progenitors of Brightest Cluster Galaxies at $z \sim 2$"*, 2016, MNRAS, submitted

Contents

List of Figures

List of Tables

Evolution of the Brightest Cluster Galaxies

Chapter 1

Introduction

People began to explore our universe from thousands of years ago. Starting with naked eye observations, our knowledge on the formation and evolution of our universe has developed rapidly since the discovery of the telescope and the later development of modern telescopes. It is known today that galaxies, rather than stars, are the basic units to study the universe. Galaxies were once thought of as "nebulae" within our Milky Way. The thought that they might be outside our home galaxy can be traced back to the eighteenth century. This hypothesis was eventually proven around 1925 by Edwin Hubble who used Cepheid variable stars in the constellation of Sagittarius to determine the distance to the so-called "nebulae" and demonstrated that these nebulae are actually located outside our Milky Way (Hubble 1925a,b). He concluded that the "nebulae" are extragalactic in nature and are individual galaxies as our own system. This is the beginning of extragalactic astronomy. With the discovery that there are hundreds of billions of galaxies populating the universe, people are keen to answer fundamental questions such as how galaxies form and evolve.

1.1 Galaxy Evolution

The current paradigm for galaxy formation and evolution is the ΛCDM model which takes into account dark energy in the form of a cosmological constant Λ and cold dark matter (CDM). In this model, structures in the universe result from the growth of overdensities in the primordial density fluctuations observed in the cosmic microwave

background (CMB). In the early universe, the seeds of overdensity were amplified through gravitational collapse of dark matter haloes, and small haloes form first (Peebles 1980). Merging with other dark matter haloes, small haloes grow into more massive dark matter systems over cosmic time (White & Rees 1978). Computer simulations have shown that the hierarchical growth of structures based on this model can successfully reproduce the large-scale distribution of dark matter in our universe (e.g., Millennium simulation, Springel *et al.* 2005). Along with the build up of dark matter haloes, the baryonic matter also collapses at the centre of the haloes under the influence of gravity, and hence galaxies form.

Observationally, galaxies display a clear bimodality in many properties. This diversity was first discovered in the galaxy morphologies by Hubble (1926) through visual inspection of the appearance of 400 galaxies. He classified galaxies into four types: ellipticals, lenticulars, spirals and irregulars, which are presented in his famous tuning fork diagram (see Fig. 1.1). Elliptical and lenticular galaxies are referred as "*early-type*" galaxies which display smooth ellipsoidal morphologies without visible internal structures. Spiral galaxies are classified as "*late-type*" galaxies with spiral features embedded in a disc structure. Irregular galaxies, as the name implies, have no regular structures such as a spheroid or disk. This classification scheme, which is usually called "the Hubble Sequence", represents the degree of complexity in galaxy structure, and is still widely used today.

Subsequent studies show that diversity also exists in other galaxy properties, such as galaxy colours. By studying the optical colour distribution of galaxies in the Sloan Digital Sky Survey (SDSS), an intrinsic colour bimodality in the local galaxy population is confirmed (e.g., Kauffmann *et al.* 2003; Balogh *et al.* 2004). The upper-left panel of Fig. 1.2 shows the bimodal distribution for SDSS galaxies in $u - r$ colour. The galaxy population with bluer colours are now called as the "*blue cloud*" because of their scattered colour-mass distribution, while the red galaxy population are commonly known as the "*red sequence*" since they have a tight colour-mass correlation (see the lower-left panel of Fig. 1.2). These colours reveal the stellar populations that are within galaxies. Galaxies appear blue in the optical if they host many hot and massive OB stars which are extremely bright, thus being able to overwhelm the total light
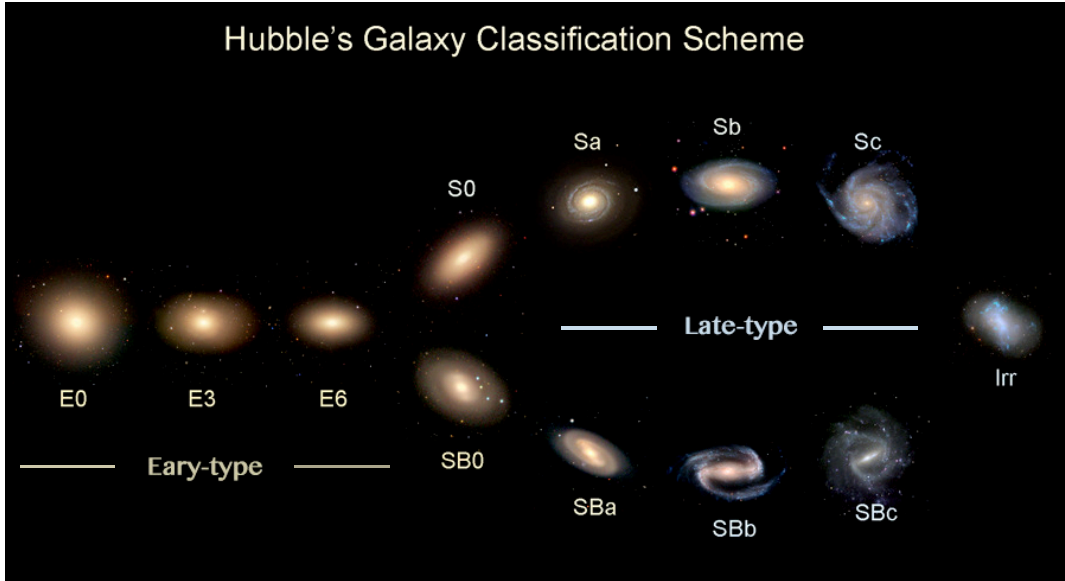
Figure 1.1: The Hubble tuning fork. This figure was created by using galaxies from the Sloan Digital Sky Survey (SDSS; York *et al.* 2000) which are classified by the GalaxyZoo project (Lintott *et al.* 2008; image credits http://www.galaxyzoo.org).
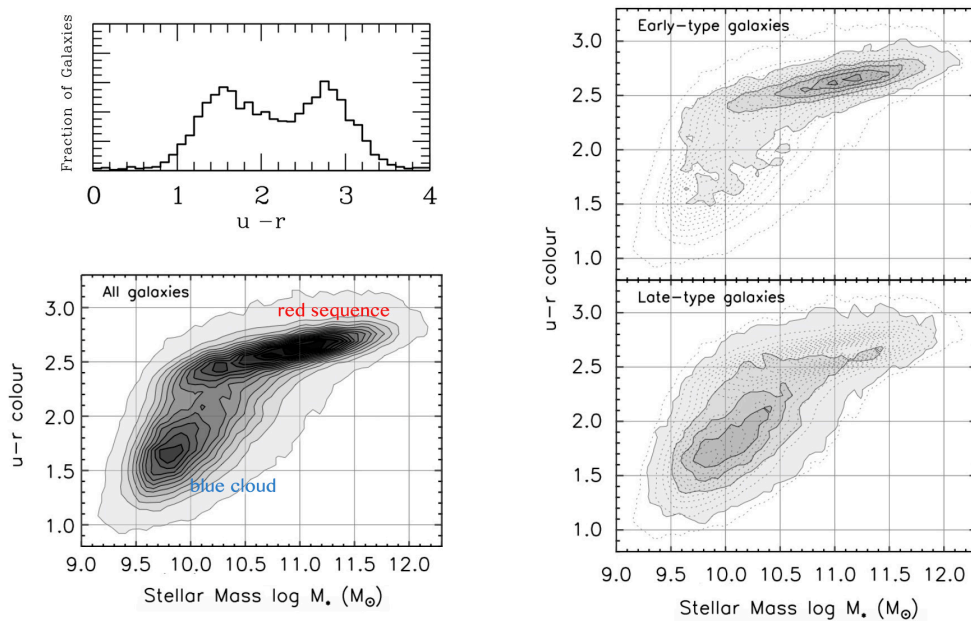
Figure 1.2: The *upper-left* panel illustrates the distribution of $u-r$ colour of SDSS galaxies (Strateva *et al.* 2001). It shows a clear bimodality in galaxy colours such that a red galaxy population separates from the blue galaxies. The *lower-left* panel is the diagram of $u-r$ colour vs. stellar mass for SDSS galaxies from Schawinski *et al.* (2010). Galaxies with blue $u-r$ colours distribute in a diffused region called the "blue cloud". Galaxies with red $u-r$ colours which are in a tight colour-mass correlation lie on the "red sequence". The two panels in right, which are also from Schawinski *et al.* (2010), show the correlation between colour bimodality and galaxy morphology. The *upper-right* panel shows that the early-type (elliptical and lenticular) galaxies are generally optically red, and their $u-r$ colour-mass diagram follows the "red sequence". The *lower-right* panel, on the other hand, illustrates that the late-type (spiral) galaxies have bluer colours and widely spread in the "blue cloud" region.

produced by the fainter stars (Ellis, Abraham & Dickinson 2001). Since OB stars are short-lived (only tens of Myrs in the stellar main sequence), their presence indicates star formation within the galaxies. Therefore, blue galaxies are characterized by on-going or recent star formation. In contrast, galaxies with optical red colours have few or no OB stars and are dominated by old passive star populations.

The bimodality in galaxy colour is broadly linked with galaxy morphology (see the two right panels in Fig. 1.2). Late-type (spiral) galaxies are generally bluer in colour and have strong nebular emission lines implying a high level of star formation. Early-type (elliptical and lenticular) galaxies, on the other hand, are typically red in the optical and lack emission lines, indicating negligible star formation within them. It becomes clear that there are two distinct main galaxy populations in the universe: blue star-forming galaxies with late-type morphologies, and old red passive galaxies with early-type morphologies. In this thesis we are interested in one special kind of early-type galaxies called the brightest cluster galaxies (BCGs).

1.2 Properties of the Brightest Cluster Galaxies

BCGs are the most luminous and massive galaxies in the local universe, usually locating at the centre of galaxy clusters or groups (see Fig. 1.3). To first order BCGs appear to be giant elliptical galaxies. However, their unique properties and special host environments make them differ from normal (giant) elliptical galaxies and are one of the most important kinds of galaxies to understand the evolutionary history of massive galaxies, galaxy clusters and large scale structures. In this section, I review the properties of BCGs in many aspects to present how special they are.

1.2.1 Luminosity

The first studies of BCGs focussed on their extremely high luminosities. With absolute magnitudes between -21.5 and -23.5 in the V-band, BCGs are typically 10 times more luminous than normal elliptical galaxies (e.g., Sandage & Hardy 1973; Schombert 1986). Earlier studies found that the luminosities of BCGs are too high to
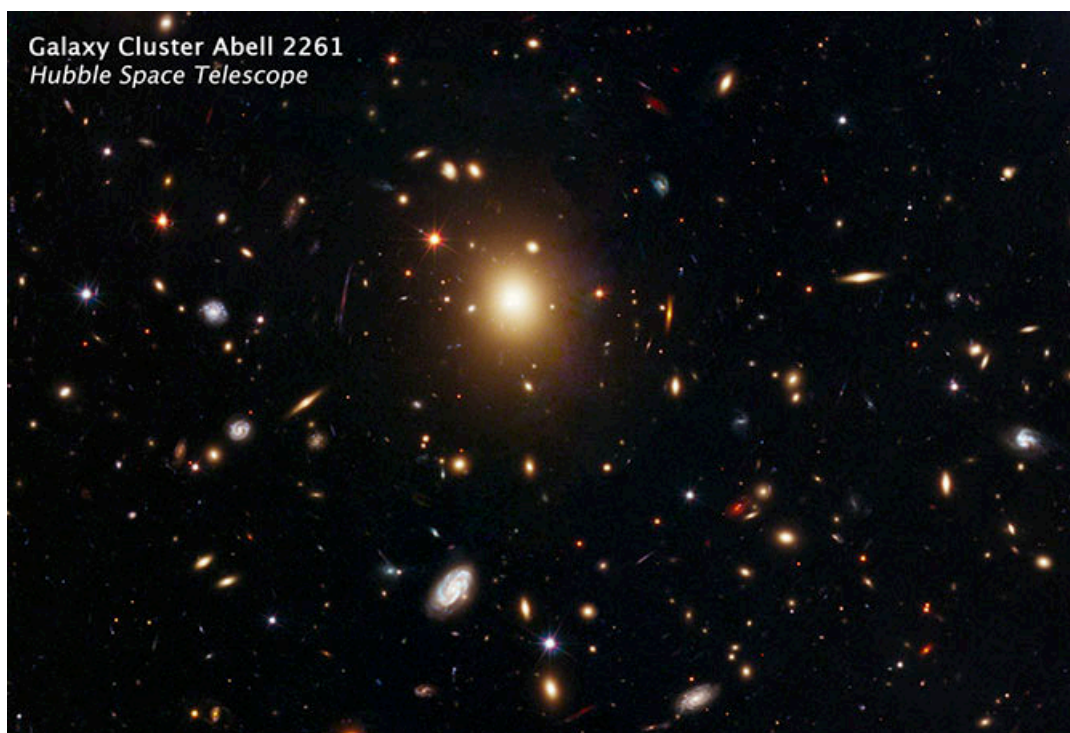
Figure 1.3: The brightest cluster galaxy (BCG) of galaxy cluster Abell 2261. Image credit: NASA; ESA; M. Postman, STScI; T. Lauer, NOAO, Tucson; CLASH team.
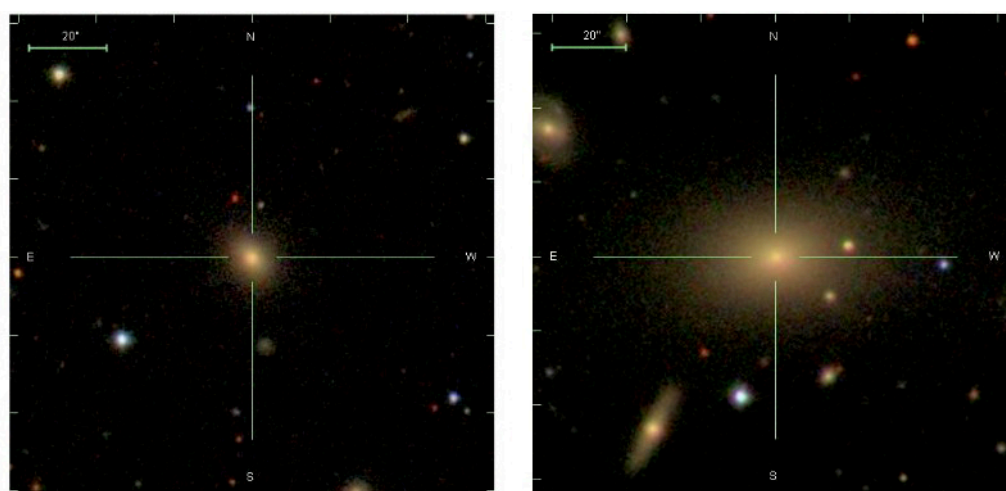
Figure 1.4: Example of an elliptical BCG (*left* panel) and a cD galaxy (*right* panel). The cD galaxy is surrounded by a large diffuse halo. The image is adapted from von der Linden *et al.* (2007).

be consistent with them being drawn simply as the brightest member of the standard luminosity function (Schechter & Peebles 1976) of elliptical galaxies (e.g., Tremaine & Richstone 1977; Dressler 1978; Bernstein & Bhavsar 2001). This implies that BCGs are not the extreme of normal elliptical galaxies, but belong to a special class of atypical galaxies which constitutes a unique sample in their own right.

Moreover, if BCGs would had been the brightest galaxies drawn from the general luminosity function, the dispersion of their luminosities should be larger (at the level of 2 mag). However, observational studies of BCG optical and near-infrared magnitudes demonstrated that the intrinsic scatter in the absolute magnitudes of BCGs is no more than 0.3 mag, much smaller when compared to other less massive galaxies (e.g. Sandage 1988; Aragón-Salamanca, Baugh & Kauffmann 1998; Collins & Mann 1998). The small dispersion in BCG luminosities also supports the uniqueness of the BCG population and suggests that they may have a different evolutionary history from the ordinary massive elliptical galaxies.

1.2.2   Morphology

Galaxy morphology is another important property to provide clues on galaxy formation and evolution. Originally, the most luminous galaxies in clusters were generally classified as giant elliptical (gE) galaxies which were distinct from other early-type galaxies by their large size. Some of them were classified specifically as D or cD galaxies (e.g., Matthews, Morgan & Schmidt 1964; Morgan, Kayser & White 1975; Albert, White & Morgan 1977). Matthews, Morgan & Schmidt (1964) outlined the definitions of these two specific morphological types. They defined a D galaxy as a system with an elliptical-like nucleus surrounded by a diffuse envelope. The "D", therefore, stands for "diffuse". cD galaxies, in their definitions, were the supergiant D galaxies which were much larger in size and observed in the core regions of rich galaxy clusters. Schombert (1987), on the other hand, defined D galaxies as being gE galaxies with a shallower slope of surface brightness profile, and cD galaxies as D galaxies but having large extended stellar haloes.

The exact meaning on the classification of D is often confusing and the classification of D and cD is often done loosely. Moreover, note that brighter elliptical galaxies

have shallower light profiles and galaxies with elliptical bulges can have disks (such as lenticular galaxies) and tidally stretched haloes, all of which satisfy the definition of a D galaxy. This implies that D galaxies are not a single class of new phenomenon and can be hardly regarded as a separate type of galaxy. Kormendy (1987) recommended that the term D galaxy should not be used. Since then BCGs have been usually classified into two main morphological types: cD galaxies containing a large visual extended envelope, and giant elliptical BCGs without an envelope in their outskirts (see Fig. 1.4). The questions that naturally arise are how to reasonably quantify the visual morphologies of BCGs, and whether the structures of BCGs are different from normal elliptical galaxies.

1.2.3   Structure

The unique morphologies of BCGs, especially those of cD galaxies, suggest that BCGs may have unique structures. Therefore, the comparison between the structures of BCGs and normal elliptical galaxies has drawn people's attention in order to probe their structural differences.

Oemler (1976) carried out the first comparative study of this by fitting the surface brightness profiles of galaxies with a Hubble surface brightness distribution (Hubble 1930) modified by an exponential cutoff. They found that, generally, normal elliptical galaxies can be well fitted by the model they used. In contrast, BCGs, especially those identified as cD galaxies, were shown to deviate from good fits by having a separate very diffuse envelope around the central bulge. Due to this envelope, there is an inflection in the profiles of BCGs which typically occurs between 24 and 26 mag arcsec^{-2} in the V-band.

Schombert (1986) conducted a study on the BCG light profile by employing the more general $r^{1/4}$ de Vaucouleurs model (de Vaucouleurs 1948). The structural differences between BCGs and elliptical galaxies was presented as well in their results. However, they found that the $r^{1/4}$ law provides a good description of the structure of elliptical galaxies only for surface brightness of $21 - 25$ mag arcsec^{-2}, and for most elliptical galaxies there is a flux excess displaced above the $r^{1/4}$ model at large radii, similar to BCGs. A more accurate model is required to confirm the structural differences of

BCGs and normal elliptical galaxies.

In more recent studies, a model profile called the Sérsic ($r^{1/n}$) law (Sérsic 1963) is used virtually by many authors to derive the structure of various kinds of galaxies. It is a more general power law model than the Hubble-Oemler model or $r^{1/4}$ de Vaucouleurs profile. The Sérsic model has the form

$$I(r) = I_{\mathrm{e}} \exp\{-b[(r/r_{\mathrm{e}})^{1/n} - 1]\}, \tag{1.1}$$

where $I(r)$ is the intensity at distance r from the centre, r_{e}, the effective radius, is the radius that encloses half of the total luminosity, I_e is the intensity at r_{e}, n is the Sérsic index representing concentration, and $b \simeq 2n - 0.33$ (Caon, Capaccioli & D'Onofrio 1993). Sérsic profiles with different Sérsic index n are illustrated in Fig. 1.5. The Sérsic function is able to properly describe the light profiles of galaxy bulges and normal elliptical galaxies. Graham *et al.* (1996) applied this law to BCG surface brightness profiles, finding that it is also an appropriate model to represent the BCG structure. They further showed that BCGs have larger values of Sérsic index n than ordinary elliptical galaxies.

However, many later studies claimed that a single Sérsic profile still cannot fully reproduce the BCG luminosity distributions. Gonzalez, Zabludoff & Zaritsky (2005) found that a sample of 30 BCGs were best fitted using a double $r^{1/4}$ de Vaucouleurs profile rather than a single Sérsic law. Furthermore, Donzelli, Muriel & Madrid (2011) suggested that a two-component model with an inner Sérsic and an outer exponential profile is required to properly decompose the light distribution of $\sim 48\%$ of the BCGs in their 430 galaxy sample. A similar conclusion was obtained by Seigar, Graham & Jerjen (2007). The interpretation of the deviation from single Sérsic model is that some BCGs are embedded in a dispersed stellar halo (see Fig. 1.6).

Since some of the BCGs can be well fitted by a single Sérsic model, and some of them deviate from the model by presenting a separate halo, it implies that even within the BCG population there are two structural types of galaxies. Apart from the studies on the difference between BCGs and normal galaxies, a few recent papers begin to focus on exploring the difference of these two BCG subsamples. For example, Donzelli, Muriel & Madrid (2011) split their BCG sample into two profile categories: single
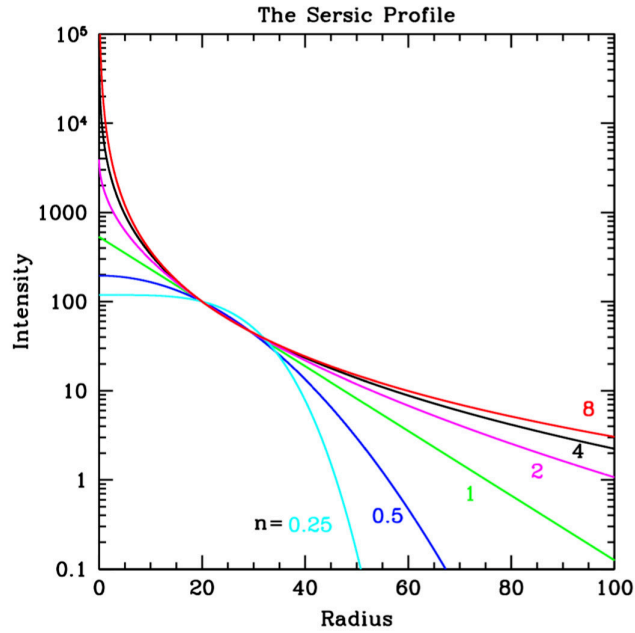
Figure 1.5: The Sérsic profile, where effective radius and intensity at the effective radius are fixed. The image is from https://users.obs.carnegiescience.edu/peng/work/galfit/README.pdf.
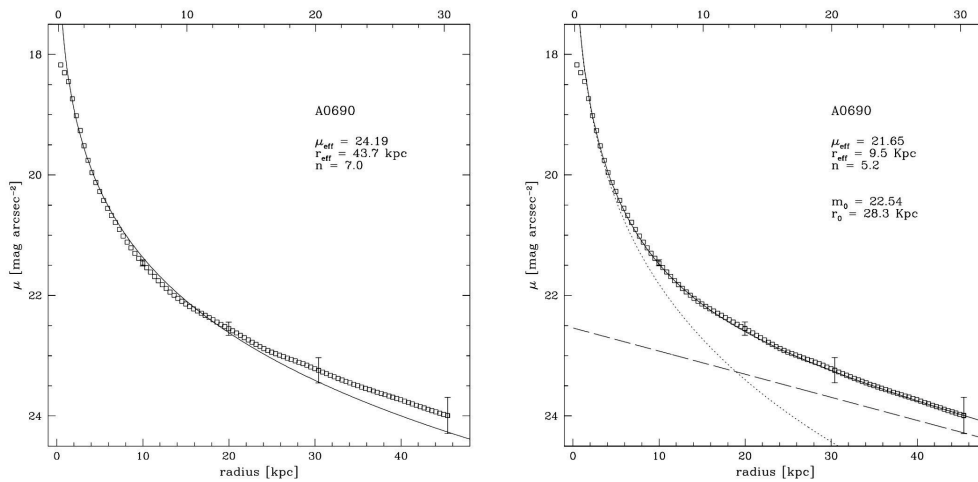
Figure 1.6: An example of BCG luminosity profile. The *left* panel shows that it is inconsistent with the single Sérsic model with a light excess in the outer regions of this BCG. The *right* panel illustrates that this profile can be well fitted by a Sérsic (dotted line) + exponential (dash line) model. The images are from Donzelli, Muriel & Madrid (2011).

(Sérsic) and double (Sérsic+Exponential) component profiles, according to the fitting model the BCG is consistent with. They found that double-profile BCGs are brighter than single profile BCGs, and that the extra-light of double profile BCGs comes from the outer regions of these galaxies. This suggests that the study on the subsample of BCGs could indeed provide more information on BCG evolution.

Most BCGs are visually classified as cD galaxies and elliptical BCGs, the two main classes of BCGs. However, there is no systematic study yet explicitly comparing the physical properties of these two types of BCGs. What is the relationship between BCG morphology and structure? Are elliptical BCGs and cD galaxies two clearly distinct and separated classes of galaxies? Are elliptical BCGs and cD galaxies formed by different processes or in different environments? Is there an evolutionary link between them? By carefully measuring the structure of cD and elliptical BCGs and relating their properties with cluster environments, we will try to answer these questions in Chapter 2 and Chapter 3.

1.2.4 Fundamental Plane

The properties of BCGs are often discussed in the scaling relations. On the Kormendy relation (Kormendy 1977) which is between effective radius (R_e) and mean surface brightness within effective radius ($\langle\mu\rangle_e$), BCGs are larger at a given mean effective surface brightness than normal elliptical galaxies (Schneider, Gunn & Hoessel 1983; Schombert 1987; Hoessel, Oegerle & Schneider 1987). The Kormendy relation can be expressed as a size–luminosity or size–mass relation which have a similar physical meaning. With more accurate measurements on the BCG structure, we will revisit the size-mass relation for BCGs in Chapter 3. Another scaling relation is the Faber–Jackson relation which can be expressed as $L \propto \sigma^\gamma$ where L is the luminosity and σ is the stellar velocity dispersion. BCGs have a much larger γ compared with that of normal elliptical galaxies (e.g., von der Linden *et al.* 2007; Liu *et al.* 2008). It implies that the velocity dispersion of BCGs increases less steeply with luminosity than predicted by the non-BCG Faber–Jackson relation.

Effective radius R_e, mean effective surface brightness $\langle\mu\rangle_e$, and stellar velocity dispersion σ are the three main global observables of elliptical galaxies. Elliptical galaxies do

not populate uniformly in this three dimensional parameter space, but are distributed along a narrow logarithmic plane which is called the fundamental plane (Dressler *et al.* 1987; Djorgovski & Davis 1987). The Kormendy relation and Faber–Jackson relation are interpreted as projection of the fundamental plane along the coordinate axes. There is a model fundamental plane predicted by theory for virialized stellar systems who are also in structural and dynamical homology and have constant mass-to-light ratio. Observations show that elliptical galaxies distribute on a plane deviating from this model fundamental plane. This is called the *tilt* problem. The inconsistency between theory and observation implies that at least one condition among the theoretical assumptions has to be dismissed. Either the variation in mass-to-light ratio, or the non-homology in elliptical galaxies is the possible solution for the tilt problem that many studies have argued, but there is no conclusion yet. Oegerle & Hoessel (1991) found that the fundamental plane of BCGs is consistent with the ordinary elliptical galaxies. However, more recently, von der Linden *et al.* (2007) demonstrated that BCGs lie on a different fundamental plane which is closer to the model fundamental plane predicted by theory. This implies that BCGs and normal elliptical galaxies have different formation histories.

1.2.5   Other Properties

In addition to the unique properties described above, BCGs are also special in other properties. von der Linden *et al.* (2007) found that BCGs have higher velocity dispersion than elliptical galaxies in similar stellar masses and derived that BCGs have higher dark matter fraction. BCGs often display double or multiple nuclei (Schneider, Gunn & Hoessel 1983; Laine *et al.* 2003). By using Integral Field Unit (IFU) spectroscopy, Oliva-Altamirano *et al.* (2015) showed that BCGs have high central metallicities and shallow metallicity gradients, and the ages of BCGs have a wide range, from 5 Gyr, which reflects an active accretion history, to 15 Gyr, which suggests no star formation since $z \sim 2$. The derived central stellar populations and stellar population gradients of BCGs are similar to the ones of early-type galaxies of similar mass. However, massive early-type galaxies have consistently old ages. Moreover, other studies (Giacintucci *et al.* 2007; von der Linden *et al.* 2007) find that BCGs have been frequently identified

as powerful radio sources and are more likely to host a radio-loud AGN. All of these properties provide clues on the mechanisms for BCG formation and evolution.

1.3   Environments and Host Clusters of BCGs

Since BCGs reside in the core of galaxy clusters, their unique properties are likely to tie to the properties of the host clusters. Studying the relationship of BCGs with their host galaxy clusters is important to better understand how BCG form and evolve.

BCGs were usually thought to reside in the centre of galaxy clusters. Early work on the X-ray morphology of galaxy clusters (Jones & Forman 1984) and their velocity structure (Quintana & Lawrie 1982) indeed found that BCGs are likely to be centrally located at the bottom of cluster gravitational potential. However, recent studies observed that some BCGs are displaced from the X-ray centre of clusters (e.g., Patel *et al.* 2006; Hashimoto, Henry & Boehringer 2014). Lauer *et al.* (2014) show specifically that the median offset from BCG to X-ray-defined cluster centre is ~ 10 kpc, but about 15% of their BCGs have offset larger than 100 kpc. Moreover, BCGs usually have significant peculiar velocities with respect to the mean velocity of their host clusters if they have an appreciable distance from cluster centres (Zabludoff, Huchra & Geller 1990; Malumuth 1992; Oegerle & Hill 2001; Coziol *et al.* 2009). The position and peculiar velocity of BCGs with respect to the centre of the cluster potential may correlate with the evolution of the cluster. For example, the BCG in the Coma cluster is not at the centre of X-ray potential and has large peculiar velocity dispersion, implying that Coma might be a recent merger of two clusters.

Another connection, the alignment observed between BCGs and their host clusters, also provides strong evidence that the evolution of BCGs is tied to the cluster assembly. In clusters with well-defined orientations in the optical, the elongation of the BCGs tends to align significantly with the host cluster's major axis (Carter & Metcalfe 1980; Binggeli 1982; Rhee & Nico 1989; Plionis *et al.* 2003). Porter (1988) also found a tendency for alignment of BCGs with cluster X-ray gas isodensity contours, and showed that BCGs tend to have larger ellipticities and smaller isophote twists than normal elliptical galaxies. Recently, with a new sample of local clusters and BCGs, Fasano

et al. (2010) observed that BCGs tend to be triaxial, with a much higher tendency towards prolateness, while non-BCG elliptical galaxies in clusters generally have a weak preference for prolateness, suggesting that the prolateness of the BCGs could closely follow the shape of dark matter haloes of the clusters.

In the core regions of galaxy clusters, a diffuse, low brightness stellar component, known as intra-cluster light (ICL), is observed in the intra-cluster space. The ICL is made up of stars which are thought to be gravitationally bound to the cluster potential well rather than any specific galaxy. In the nearby universe, the ICL in clusters is often found to be centred around the BCG (e.g., Rudick, Mihos & McBride 2011). Many studies have simulated the processes of ICL buildup and mergers in cluster cores, showing that a large fraction of the merging stellar mass ($30 - 80\%$, e.g. Conroy, Wechsler & Kravtsov 2007; Puchwein *et al.* 2010; Laporte *et al.* 2013) will end up as the extended halo of the BCGs or the ICL. It seems that the assembly of the ICL in clusters is probably intertwined with the evolution of BCGs, especially the cD galaxies.

How other intrinsic properties of BCGs are affected by the environments of clusters has also been studied by many works, providing more clues on the relationship of BCGs and their host clusters. Early work showed a weak relationship between the BCG luminosity and the richness of clusters (Sandage & Hardy 1973; Sandage 1976). This was supported by the later study of Postman & Lauer (1995). Hudson & Ebeling (1997) and Collins & Mann (1998) discovered a strong positive correlation of the BCG luminosity (or stellar mass) with the cluster X-ray luminosity. Other studies found that BCG luminosity in different bands always increases with the cluster dark matter halo mass (or cluster velocity dispersion) at $z < 0.8$ (Lin & Mohr 2004; Popesso *et al.* 2007; Brough *et al.* 2008; Whiley *et al.* 2008). Moreover, Brough *et al.* (2005) showed that the structures of the BCGs also correlate with the X-ray luminosity of their host clusters, with BCGs becoming more extended in more luminous clusters. The recent study of Ascaso *et al.* (2011) concluded that more luminous, larger, and centrally located BCGs are located in more massive galaxy clusters. However, whether the BCG properties relate with the properties of host clusters is still controversial. Guo *et al.* (2009) suggested that the DM halo mass of galaxy clusters is not a dominant property dictating the shape and size of BCGs. Hogg *et al.* (2004), Kauffmann *et al.*

(2004) and van der Wel *et al.* (2008) also reached similar conclusions. By using a well-defined large local BCG sample, with more accurate measurements of the BCG structures, and considering both local and global environments, we will revisit the relationship between BCG properties and their host clusters in Chapter 3 to examine whether nature and/or nurture are the important factors in BCG evolution.

1.4 Theories of BCG Formation and Evolution

The properties of BCGs are distinct from those of the other cluster galaxies, and tightly relate with their host galaxy clusters. All these properties indicate that BCGs may have quite an unusual formation history compared to ordinary elliptical galaxies. Any model for BCG formation and evolution has to acknowledge this. In the following, I review the main theories trying to explain the origin of BCGs.

1.4.1 Cooling Flows

One of the first theories on BCG origins proposed that they were formed from cooling flows in galaxy clusters (Cowie & Binney 1977; Fabian 1994). Current theories of structure formation involve the condensation of objects from a large cloud of gas which has cooled from an earlier hot state. As the cloud contracts under the influence of gravity, structures begin to form. In the cases of many large galaxies and clusters of galaxies, the gas envelope first cooled much more slowly. It then reached a quasi-hydrostatic equilibrium. From this point, the gas near the centre rapidly lost energy through the pairwise-interaction of thermal bremsstrahlung and was able to cool much more efficiently. The radiation observed from this cooling gas appears in the X-ray band. The cooling of the gas near the centre of the cluster reduces the amount of thermal support it provides to overlying layers. As a result, the outer regions collapse onto the cooling inner region. This collapse is called the "cooling flow". In the cooling flows scenario for BCGs, when the gas density in the cluster central regions becomes high enough, the intracluster gas becomes cool, leading to intense star forming out of the central cooling flow at the bottom of the potential well where BCGs form.

A few observations supported this idea. By studying the galaxy cluster of Abell 1795, McNamara *et al.* (1996) found blue- and ultraviolet-light excesses in its central galaxy. This indicates active star formation in the cluster core. More recently, molecular gas was detected directly in some of the central galaxies in clusters (Salomé & Combes 2003). Edwards *et al.* (2007) also claimed that cooling flow clusters are common in the local universe and BCGs are most often found at the centres of these systems.

However, many other observations have cast doubt over this theory. According to the cooling-flow scenario, a very large number of new stars should be created in the cluster cores, but there is no observational evidence for this population (McNamara & O'Connell 1989). Moreover, McNamara & O'Connell (1992) showed that the observed star formation can account for only a few percent of the material that is cooling and accreting on to the central galaxy. The cooling-flow theory also predicts colour gradients such that the halo around BCGs should become redder with increasing radius. However, such gradients have not been found (Andreon *et al.* 1992). Recently, observations have demonstrated that the X-ray gas does not cool enough (Kaastra *et al.* 2001; Peterson *et al.* 2001; Tamura *et al.* 2001; Jordán *et al.* 2004). Since central cluster galaxies are more likely to host radio-loud AGN (von der Linden *et al.* 2007), feedback from AGN may counteract the radiative cooling in cluster cores, making the BCG formation from cooling flows unlikely.

1.4.2   Galactic Cannibalism

Another BCG formation and evolution theory is known as "galactic cannibalism". It was initially proposed by Ostriker & Tremaine (1975) and developed by Ostriker & Hausman (1977). It suggests that existing galaxies are captured by the cluster potential and gradually sink to the centre through dynamical friction and tidal stripping. When the first galaxy arrives at the cluster centre, it subsequently grows in luminosity and mass to become a BCG by merging with other galaxies which come to the central regions later.

BCG growth through galactic cannibalism in galaxy clusters was once identified as a viable process using early analytical and numerical calculations (White 1976; Hausman & Ostriker 1978; Richstone & Malumuth 1983). However, the galactic canni-

balism scenario fails when worked out in detail. One the one hand, based on the fact that galaxy clusters have high velocity dispersion, which makes frequent merging of galaxies unlikely, studies such as Merritt (1985) and Tremaine (1990) argued that the dominance of BCGs in observations cannot be achieved via cannibalism of other cluster members. On the other hand, since the dynamical friction timescales are generally too long, the luminosity of BCGs predicted by galactic cannibalism is fainter by an order of magnitude than the observed luminosity (Merritt 1985; Tremaine 1990). The failure of this model implies that BCGs must have an earlier origin. A possible alternative scenario is galaxy merging during cluster collapse in a hierarchical cosmological model.

1.4.3   Galactic Merger during Cluster Collapse

Merritt (1983) suggested that rapid galactic mergers during cluster collapse could be the alternative formation mechanism for BCGs, particularly for cD galaxies. In this scenario, BCGs obtain most of their masses through mergers between several massive galaxies which take place in groups or low-mass clusters (Merritt 1985; Dubinski 1998) in the early times of the formation of big galaxy clusters, as expected in hierarchical cosmological models. BCGs continue to grow by late-time less-frequent accretion of smaller cluster members during the cluster collapse. Merritt (1983) also supposed that all galaxies had large haloes in the early collapse of the cluster. These haloes were stripped by the cluster tidal field during the initial collapse and then returned to the centre of the cluster potential well, forming the envelope around cD galaxies.

Although both the galaxy cannibalism and merging scenarios take into account the merging process for BCG formation, it is possible to differentiate these two theories by considering the formation period of the BCGs. In the cannibalism model, there are numerous small galaxies present in the evolved cluster, whereas in the merging model, galaxies follow the hierarchical cosmological model during the collapse of clusters. Moreover, as discussed in Section 1.4.2, the orbit decay of cluster galaxies in the galactic cannibalism scenario is not effective enough to account for the growth of BCGs.

Originally, the merging model during cluster collapse was generally accepted since it was supported by some observational evidence. The observed major-axis alignment

of BCGs with their host clusters (Carter & Metcalfe 1980; Binggeli 1982; West 1994) implies that the origin of BCGs coincides with hierarchical merging during cluster collapse (Niederste-Ostholt *et al.* 2010). Postman & Lauer (1995) demonstrated that the multiple nuclei observed in central cluster galaxies also favour the merging theory. By studying the surface brightness and colour profiles of a few cD galaxies and analysing their globular cluster systems, Jordán *et al.* (2004) concluded that cD galaxies appear to have formed rapidly at early times via hierarchical merging prior to cluster virialization. This is consistent with the scenario of rapid mergers during cluster collapse.

However, this theory still cannot explain some important observational properties of BCGs. Based on this theory, Dubinski (1998) performed the first N-body simulations of BCG formation in a massive halo formed within a CDM cosmology. He found that the extended envelope cannot be developed around the central galaxy, which is a characteristic of cD galaxies. Moreover, BCGs which formed in this scenarios are expected to be located near the host cluster centres and are expected to be at rest in the cluster cores. As reviewed in Section 1.3, observations show that the positions of some BCGs are away from the geometric cluster centre and there is an offset between the velocity of some BCGs and the mean velocity of their host clusters. (e.g. Oegerle & Hill 2001; Coziol *et al.* 2009). These facts poses problems for the mechanism of rapid mergers during cluster collapse for BCG formation, at least in some cases.

1.4.4 Two-phase Evolution

The BCG assembly within hierarchical growth of dark matter haloes has been well established using pure N-body simulations. However, due to the lack of detailed understanding of various baryonic processes, these hierarchical models ignore complex gas processes such as cooling, star formation and feedback during the formation and evolution of BCGs. With the improved knowledge of baryonic processes in galaxy evolution and with the development of semi-analytical techniques, a more promising scenario for BCG evolutionary history has been proposed by De Lucia & Blaizot (2007). They investigated the formation of BCGs by using both the Millennium simulation (Springel *et al.* 2005) and semi-analytic models (SAMs), providing the most complete quantitative prediction of the formation of BCGs in the nowadays standard

CDM model of structure formation.

By using their SAMs, De Lucia & Blaizot (2007) find that the stars that end up in the BCG today, started forming at very high redshifts in separate small galaxies. The star formation was quiescent triggered by rapid cooling rather than starbursts. Almost all of the star formation in these progenitors had been quenched before $z \sim 3$ by AGN activity. After that, BCGs grow through accretion of these small systems (see Fig. 1.7). De Lucia & Blaizot (2007) found that BCGs assemble rather late: half of the final stellar mass is built up on BCGs only at $z \lesssim 0.5$ (see the left panel of Fig. 1.8). Since the star formation in the satellite galaxies happened in a short period and had all been quenched in early time, the galaxies accreted on to BCGs have very low gas fractions and quite red colours, with an origin through minor mergers. De Lucia & Blaizot (2007) also find that there is a very small scatter in the formation histories of the stellar components of BCGs. Late mergers which is the accumulation of a large number of these old stellar populations yields the observed homogeneity of BCG properties. By analysing the formation and assembly histories of 125 BCGs in haloes more massive than 7×10^{14} M$_\odot$ at $z = 0$, they find that these BCGs have mean absolute magnitude $M_K = -26.58$ with a dispersion of 0.2 mag. These values appear to be in nice agreement with the observational results of Collins & Mann (1998). This agreement represents a success of the underlying galaxy formation model in their simulation.

Romeo *et al.* (2008) drew similar conclusion on the BCG formation by performing N-body and hydrodynamical simulations of the evolution of galaxy groups and clusters in a ΛCDM cosmology. Naab, Johansson & Ostriker (2009) and Laporte *et al.* (2012) confirmed this two-phase scenario in later simulations. Since many of these mergers take place very late, when most galaxies have converted their gas into stars, this theory claims that the merging events at low redshifts are very nearly dissipationless dry mergers and are not associated with significant star formation. They predicted that the stellar mass of BCGs grows by a factor of $3 - 4$, mainly via mergers, since $z = 1$.

This two-phase formation scenario avoids the need for cooling flows to provide the cold gas that would be necessary if BCGs had formed at later times. It also overcomes the problem caused by the merger rate in clusters being too low due to the high veloc-
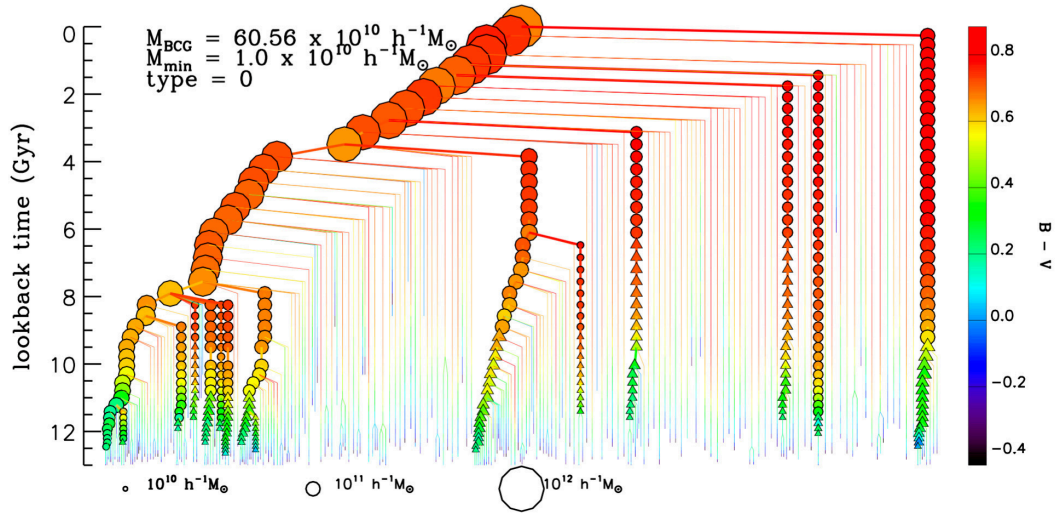
Figure 1.7: The merger tree for one BCG in the simulation of De Lucia & Blaizot (2007). Symbols are colour-coded as a function of B-V colour and their size scales with the stellar mass. The images are adapted from De Lucia & Blaizot (2007).
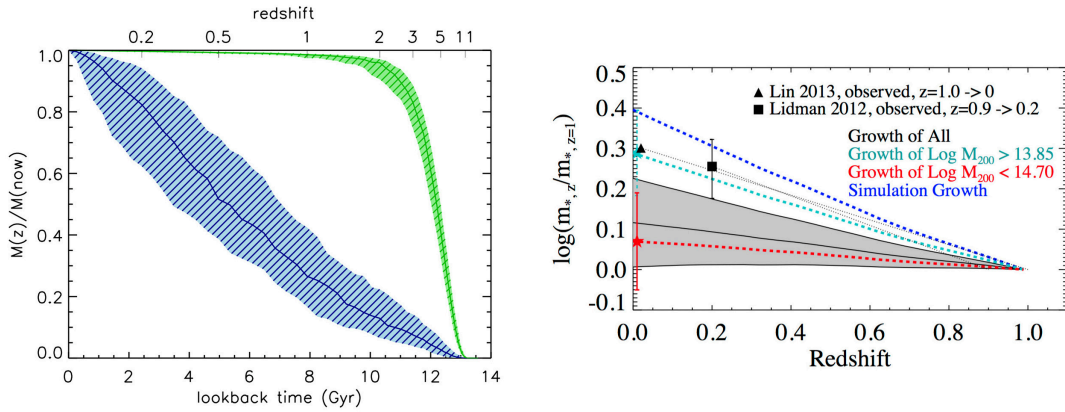
Figure 1.8: BCG mass growth. The *left* panel illustrates the assembly (blue) and formation (green) histories of BCGs at $z = 0$ from the simulation of De Lucia & Blaizot (2007). Thick lines show the median of the distributions, while the shaded regions show the 15th to 85th percentile range. It is clear that the stars that make up BCGs today are formed very early, and BCG assemble very late such that half of the final stellar mass is built up on BCGs through only at $z < 0.5$. The images are adapted from De Lucia & Blaizot (2007). The *right* panel shows the estimation of BCG stellar mass growth since $z \sim 1$ from both observations and simulations. The blue dash line shows the mass increase of BCG in the simulation of De Lucia & Blaizot (2007). Other lines are the observational results, in which the dash line with square is from Lidman *et al.* (2012), the dash line with triangle is from Lin *et al.* (2013), and other lines are from Zhang *et al.* (2016). It is clear that the measurements in observations show a slower BCG mass growth than in the simulation. The image is credited to Zhang *et al.* (2016).

ity dispersion in dynamically relaxed clusters. This model can also reproduce many other observational BCG properties. Colour evolution of the simulated BCGs is also consistent with a passively evolving stellar population which formed at $z = 2 - 5$. The predicted large BCG mass growth over $z = 0 - 1$ had been supported by Aragón-Salamanca, Baugh & Kauffmann (1998) who found a BCG mass growth by a factor of $2 - 4$ since $z = 1$ by examining the K-band Hubble diagram of BCGs. Moreover, dry mergers of red galaxies, apparently without significant merger-triggered star formation, have been observed at low redshift (e.g. van Dokkum 2005).

However, the prediction from this model is inconsistent with a number of recent observations on the BCG mass growth. Observations have reported a much slower mass growth since $z \sim 1$ (e.g., Whiley *et al.* 2008; Collins *et al.* 2009; Lin *et al.* 2013; Zhang *et al.* 2016). I will review the more recent observational studies of BCG evolution over a large redshift range in Section 1.5 in more detail.

1.5 Observations of BCG Evolution

To extend our understanding of BCG evolution and to test and improve the existent theoretical models, it is important to study how the properties of BCGs vary with cosmic time through observations. In this section, I will introduce briefly how BCGs at high redshifts are linked with local BCGs, and review the recent observational results of mass assembly and structure evolution of the BCGs.

1.5.1 Linking Local BCGs with High-z BCGs

Since BCGs reside only in galaxy clusters and groups, BCG samples are normally identified by using observations of clusters and groups at low and high redshifts. It is essential to link high-z and low-z BCGs in a meaningful way to ensure the correct comparison between their properties to probe the intrinsic BCG evolutions.

For instance, Collins *et al.* (2009) identified five BCGs in five X-ray clusters at $z = 1.2 - 1.5$, and a comparison sample of low-z ($z < 0.3$) BCGs was selected in clusters with similar dark matter halo masses. In the study of Whiley *et al.* (2008), the local

comparison sample was selected by matching the distribution of low-z cluster velocity dispersion to be the same as that of the high-z ($z < 1$) BCG sample.

In cosmological hierarchical models, the dark matter haloes of galaxy clusters grow with cosmic time, within which BCGs grow as well. Therefore, comparison between high-z and low-z BCGs whose host clusters have the same mass or velocity dispersion range cannot accurately probe the intrinsic evolution of BCGs since the cluster samples do not have direct evolutionary connections. Ideally, clusters at different redshifts should be selected in an evolutionary sequence, such that the higher-z clusters are the progenitors of the lower-z clusters. With such a sample, one could then meaningfully follow the evolution of the galaxy populations, including the mass growth of BCGs. Recent studies have developed empirical methods to connect BCG progenitors and their descendants at $z \lesssim 1 - 1.5$ in a more reasonable way. The basic idea of these methods is to trace BCG evolution depending on the halo mass growth history of clusters based on simulations. Using the full merger history of clusters, by either deriving correlation between the BCG stellar mass and cluster halo mass, or selecting BCGs directly from distant clusters which are in an evolutionary link with local clusters, the BCG mass assembly over $z = 0 \sim 1$ has been widely explored (e.g., Lidman *et al.* 2012; Lin *et al.* 2013; Shankar *et al.* 2015; Zhang *et al.* 2016).

However, these halo-mass-growth-based methods for linking local BCGs and their progenitors at $z \lesssim 1$ are difficult to apply beyond $z \gtrsim 1.5$. One reason is that the identification of clusters/proto-clusters at early times is very difficult. Another reason is that it is also difficult to define BCG progenitors in high-z clusters because the main progenitor may not be the most luminous galaxy, as it is the case for low-z BCGs. Although there is no good way so far to identify BCG progenitors at $z > 1.5$, a number of studies have been carried out to explore the build up of massive galaxies up to $z \sim 3$. To link galaxies at different redshifts, matching galaxy progenitors and descendants at a constant number density has been demonstrated to be a considerably improved approach for tracking the evolution of massive galaxies. Using SAMs Leja, van Dokkum & Franx (2013) showed that this technique is robust at directly tracking descendant and progenitor galaxies over cosmic time. Mundy, Conselice & Ownsworth (2015) further demonstrated that a constant number density selected sample (in the

range $-4.3 < \log n \, [h^3 \mathrm{Mpc}^{-3}] < -3.0$) is superior to a constant stellar mass selected sample, and can trace the true evolution of average stellar mass and average SFR of the progenitors and descendants of galaxies. However, these massive galaxies are not necessarily BCGs, and a clear correspondence between massive galaxies and BCGs at high redshifts ($z \gtrsim 1.5$) is still lacking. In order to obtain a better perspective of BCG assembly, it is critical to identify the progenitors of BCGs at $z \gtrsim 1.5$ through observations, and to explore their mass and structural evolution. In Chapter 4, taking into account abundance matching sorted by environment as well as the BCG stellar mass, I develop a new BCG progenitor selection method at $z \sim 2$ to probe the BCG evolution in the last 10 billion years.

1.5.2 Mass and Structure Evolution of BCGs

In the last two decades, many studies have been devoted to BCG formation and evolution by investigating several of their properties. Since one part of this thesis aims at exploring how the stellar mass and structure of BCGs evolve with cosmic time, in this section I focus on reviewing the main results of BCG mass and structure evolution from the studies so far.

Stellar mass is one of the fundamental galaxy properties whose assembly history is critical to understand galaxy evolution. Early studies found that $50 - 75\%$ of local BCG stellar mass was built up since $z \sim 1$ (Aragón-Salamanca, Baugh & Kauffmann 1998), consistent with the results from the simulation of De Lucia & Blaizot (2007). However, other studies demonstrated that this large mass growth is only for BCGs in low X-ray luminosity clusters. For BCGs in high X-ray luminosity clusters, BCGs have similar mass to local ones, illustrating a very small mass increase at $z \lesssim 1$ (e.g., Burke, Collins & Mann 2000; Nelson *et al.* 2002; Brough *et al.* 2002; Whiley *et al.* 2008). Part of the reason for the discrepency between earlier and later studies is the difference in cosmological model parameters.

More recently, by applying cluster-tracing techniques which try to link BCG progenitors at high redshifts with their local counterparts more accurately, many studies agree on a slow BCG mass assembly since $z \sim 1$ (see the right panel of Fig. 1.8). Lidman *et al.* (2012) demonstrated that BCGs have grown by a factor of 1.8 between

$z = 0.2 - 0.9$. Lin *et al.* (2013) found a similar growth such that the stellar mass of BCGs increases by a factor of 2.3 since $z \sim 1.4$. Moreover, Shankar *et al.* (2015) claimed an increase of a factor $2 - 3$ in BCG mean stellar mass at since $z < 1$. Zhang *et al.* (2016) showed a BCGs mass growth by a factor of ~ 2 since $z \sim 1.2$.

Observationally, the structure evolution of BCGs has also been explored at $z \lesssim 1$. By detecting progenitor-descendant pairs of BCGs, Shankar *et al.* (2015) suggest an increase in BCG effective radius by a factor of $2.5 - 4$ since $z \sim 1$. Ascaso *et al.* (2011), comparing local WINGS BCGs with high-z HST BCGs whose host clusters span the same range of X-ray luminosity, claim a BCG size growth of a factor of 2 within the last 6 Gyr (since $z \sim 0.6$). These results indicate that about 60% of the size of local BCGs has grown at $z < 1$. Ascaso *et al.* (2011) also find that the shape of BCGs has not changed significantly since $z \sim 0.6$.

Constrained by the techniques of selecting BCG progenitors at high redshifts, current studies on the BCG evolutionary history only concentrate on the redshift range of $0 \lesssim z \lesssim 1$. Reliable observational results on BCG evolution beyond $z \sim 1.5$ are still lacking. One important aim of this thesis is to develop a method to identify BCG progenitors at $z \sim 2$ and study the BCG assembly since that time. Our understanding of the BCG evolution could be broadened by extending the time baseline beyond $z \sim 2$.

1.6   Aims of the Thesis

This thesis focuses on both BCGs in the local universe and their progenitors at high redshifts to provide more observational insights on the BCG formation and evolution over the last 10 billion years. Specifically, this work concentrates on three topics: the properties of local cD and elliptical BCGs, the effect of the environment on the properties of present-day BCGs, and the evolution of the structure and stellar mass of BCGs since $z \sim 2$.

In Chapter 2 we explore the structural properties of cD and elliptical BCGs. Using the well-defined local BCG catalogue from von der Linden *et al.* (2007), we first visually classify BCGs into cD galaxies and ellipticals from SDSS images. The structure of cD and elliptical BCGs is then quantified from careful fits to their light profiles using

both one-component (Sérsic) and two-component (Sérsic+Exponential) models. We compare the structural parameters of cD and elliptical BCGs to analyse how distinct the haloes of cD galaxies are, and how different the cD and elliptical BCGs are in their structures. Based on the distinct structure of cD galaxies, we develop an automatic and objective technique to separate cD galaxies from the non-cD BCG population.

In Chapter 3 we examine how the environment affect the properties of local BCGs. Both local density and global halo mass are considered to represent different scales in the cluster environment. The relationship between the intrinsic properties of local BCGs (structure and mass) and their host environments (local and global) are studied carefully in order to probe the nature vs. nurture dilemma. In this chapter, we also complement our study of cD and elliptical BCGs by examining the difference in their stellar masses and environments. Linking the structure, stellar mass and environment of cD and elliptical BCGs allows us to have a clearer insight into the BCG assembly history.

We then move on to BCGs at high redshifts. We explore how BCG evolve since $z \sim 2$ in Chapter 4. By using simulations, we first develop a method to identify BCG progenitors at $z \sim 2$ depending on the environmental density and stellar mass of the galaxies. We apply this method to the CANDELS UDS data to obtain our observational progenitor sample at $z \sim 2$. Comparing BCG progenitors with their descendants at $z \sim 0$, we analyse BCG evolution since $z \sim 2$ considering properties such as structure, morphology, stellar mass and star formation rate. The implications of the results are extensively discussed in this chapter.

The overall conclusions of this work are presented in Chapter 5, along with prospects for future work.

Chapter 2

The Link Between Morphology and Structure of Brightest Cluster Galaxies: Automatic Identification of cDs

The work in this chapter is published in Zhao, Aragón-Salamanca & Conselice (2015a).

2.1 Introduction

The brightest cluster galaxies (BCGs) are the most luminous and massive galaxies in today's universe. Their stellar masses reach beyond $\sim 10^{11} M_\odot$, and they reside at the bottom of the gravitational potential well of galaxy clusters and groups. Their formation and evolution relate closely to the evolution of the host clusters (Whiley *et al.*, 2008) and further tie to the history of large-scale structures in universe (Conroy, Wechsler & Kravtsov 2007). BCGs are typically classified as elliptical galaxies (Lauer & Postman, 1992), but a fraction of them possess an extended, low surface brightness envelope around the central region. These are referred to as cD galaxies (e.g. Dressler 1984; Oegerle & Hill 2001).

The surface brightness profile of elliptical galaxies was originally modelled using the

empirical $r^{1/4}$ de Vaucouleurs law (de Vaucouleurs, 1948). However, Lugger (1984) and Schombert (1986) showed that the $r^{1/4}$ model cannot properly describe the flux excess at large radii for most elliptical galaxies, and an additional parameter n was introduced in the so-called Sérsic ($r^{1/n}$) law (Sérsic, 1963). For the most massive early-type galaxies, however, a single Sérsic profile still does not reproduce their luminosity distribution accurately. Gonzalez, Zabludoff & Zaritsky (2005) found that a sample of 30 BCGs were best fitted using a double $r^{1/4}$ de Vaucouleurs profile rather than a single Sérsic law. Furthermore, Donzelli, Muriel & Madrid (2011) suggested that a two-component model with an inner Sérsic and an outer exponential profile is required to properly decompose the light distribution of $\sim 48\%$ of the BCGs in their 430 galaxy sample. A similar conclusion was obtained by Seigar, Graham & Jerjen (2007).

The light profiles of BCGs need to be explained by any successful model of galaxy formation and evolution. In hierarchical models of structure formation, a two-phase scenario is currently favoured. Hopkins *et al.* (2009) proposed that a early central starburst could give rise to the bulge (elliptical) component of these galaxies, while the outer envelope was subsequently formed by the violent relaxation of stars originating in galaxies which merged with the central galaxy. Alternatively, Oser *et al.* (2010) and Johansson, Naab & Ostriker (2012) suggested that intense dissipational processes such as cold accretion or gas-rich mergers could rapidly build up an initially compact progenitor and, after the star formation is quenched, a second phase of slower, more protracted evolution is dominated by non-dissipational processes such as dry minor mergers to form the low-surface-brightness outskirts.

To shed light on the mechanism(s) leading to the formation of BCGs, especially of cD galaxies, we need to answer questions such as: are elliptical and cD BCGs two clearly distinct and separated classes of galaxies? if so, are elliptical and cD BCGs formed by different processes or in different environments? Are the extended envelopes of cD galaxies intrinsically different structures which formed separately from the central bulge? To help answer these questions, in this chapter we explore statistically how the visual classification of BCGs into different morphological classes (e.g., elliptical, cD; here referred to as "morphology"), relates to the quantitative structural properties of their light profiles (e.g., effective radius R_{e}, Sérsic-index n; generically called "struc-

ture" in this chapter). Moreover, finding an automatic and objective way to select cD BCGs is nontrivial for the future databases and study. Recent studies such as Liu *et al.* (2008) identified cD BCGs by Petrosian parameter profiles (Petrosian 1976), but their method does not give an unambiguous criterion to separate cD galaxies from non-cD BCGs.

In this work, we visually-classify 625 BCGs from the sample of von der Linden *et al.* (2007, hereafter L07) and fit accurate models to their light profiles. We find clear links between the visual morphologies and the structural parameters of BCGs, and these allow us to develop a quantitative and objective method to separate cDs galaxies from ellipticals BCGs. In Chapter 3 we will study how the visual morphology and structural properties of BCGs correlate with their intrinsic properties (stellar masses) and their environment (cluster mass and galaxy density), and explore the implications that such correlations have for the formation mechanisms and histories of cDs/BCGs.

This chapter is organized as follows. In Section 2.2 we introduce the BCG samples and the visual morphological classification of the BCGs. In Section 2.3 we describe the light distribution models and the fitting methods we use, and discuss how the results are affected by sky-subtraction uncertainties. This section also presents a quantitative evaluation of the quality of the fits. In Section 2.4 we present the structural properties of the BCGs in the sample. In Section 2.5 we introduce an objective diagnostic to separate cDs from non-cD BCGs using quantitative information from their light profiles. We summarise our main conclusions in Section 2.6.

2.2 Data

2.2.1 BCG Catalogue and Images

To study the structural properties of BCGs in galaxy groups and clusters, we use the BCG catalogue published by L07. The groups and clusters that host these BCGs come from the C4 cluster catalogue (Miller *et al.*, 2005) extracted from the Sloan Digital Sky Survey (SDSS; York *et al.*, 2000) third data release spectroscopic sample. The cluster-finding algorithm used to build the C4 catalogue identifies clusters as over-densities

in a seven-dimensional parameter space of position, redshift and colour, minimising projection effects. The C4 catalogue gives a very clean widely-used cluster and group sample which is well supported by simulations (no constraint on the dynamical state of clusters or groups). BCGs were identified by C4 catalogue as the brightest galaxy from the spectroscopic catalogue within $500h^{-1}$ kpc of the cluster centre (i.e., the peak of density field of C4 cluster) and without strong Hα emission. However, due to the problem of 55 arcsec "fiber collision", the true BCG is not included in the SDSS spectroscopic data for $\sim 30\%$ of the clusters and is missed by the C4 algorithm.

Based on the C4 catalogue, L07 applied an improved semi-automatic algorithm to identify BCGs as the brightest galaxy in the central region of the clusters. The catalogue finally contains 625 BCGs within $0.02 \leqslant z \leqslant 0.10$. L07 show that $\sim 85\%$ of them are the brightest galaxy in the cluster. In Section 1.3 we show that BCG may be displaced from the cluster centre. Therefore, L07 may misidentify few brightest "central" galaxies as BCGs and miss the true brightest galaxy in cluster. However, only 15% (94) of L07 BCGs may be misidentified. Based on our morphological classification (details are presented below), 46 L07 BCGs have disk morphology and 10 BCGs are in merging. These BCGs may be misidentified with higher probability. Excluding them with other 38 randomly-chosen early-type (E or cD) BCGs from our analysis, we find our conclusions are the same.

L07 also developed an iterative algorithm to measure the cluster velocity dispersion σ_{r200} within the virial radius R_{200}[1]. The systems hosting BCGs span a wide range of velocity dispersions, from galaxy groups ($\sigma_{r200} \leqslant 200$ km/s) to very massive clusters ($\sigma_{r200} \sim 1000$ km/s). 75% of the L07 BCGs are in dark matter haloes with $\sigma_{r200} \geqslant 309$ km/s, where the completeness of the haloes identified by the C4 algorithm is expected to be above 50%. Obviously, for larger halo masses the completeness is higher.

The images we use to classify the BCGs and analyse their structural properties come from the SDSS Seventh Data Release (DR7) r-band images. We also use SDSS-DR7 g-band images of the BCGs in Section 2.4.1. The BCG catalogue used in this chapter together with their main properties are presented in Appendix A.

---

[1]R_{200} is the radius within which the average mass density is $200\rho_c$, where ρ_c is the critical density of the universe.
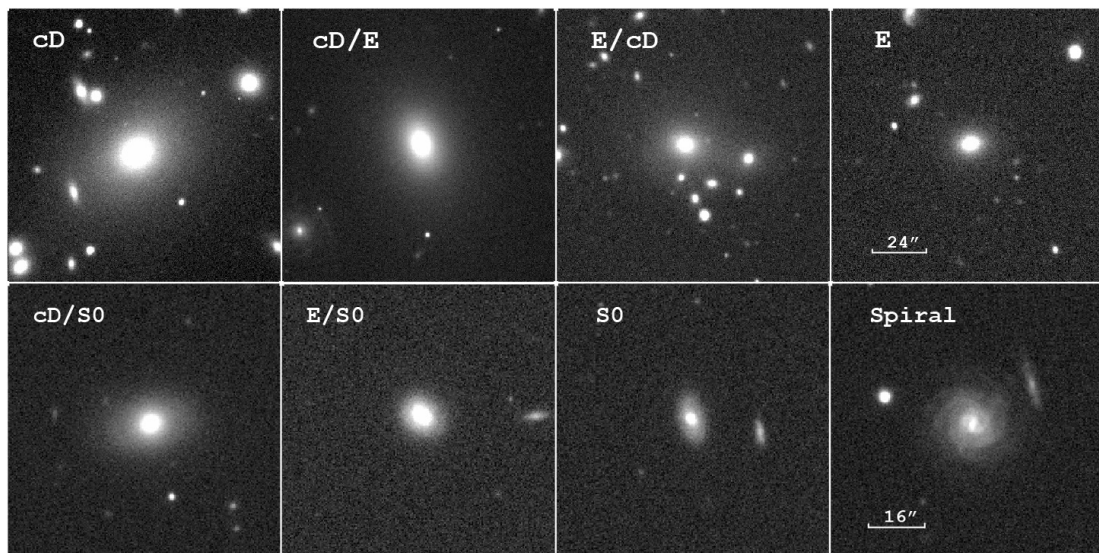
Figure 2.1: Examples of the main morphological classes of BCGs in our sample (cD, cD/E, E/cD, E, cD/S0, E/S0, S0, Spiral) illustrating the gradual transition between classes. The images are displayed using a logarithmic surface-brightness scale.

2.2.2 Visual Classification

The 625 BCGs in L07 sample were visually classified by careful inspection of the SDSS images by Alfonso Aragón-Salamanca. BCGs were displayed using a logarithmic scale between the sky level and the peak of the surface brightness distribution. The contrast was adjusted manually to ensure that the low-surface-brightness envelopes were revealed if present. cD galaxies are identified by a visually extended envelope, while the envelope is not visible in our elliptical BCGs. Finally the BCGs were classified into three main types: 414 cDs, including pure cD (356), cD/E (53) and cD/S0 (5); 155 ellipticals, including pure E (80), E/cD (72), and E/S0 (3); 46 disk galaxies, containing spirals (24) and S0s (22). The main morphological classes of BCGs are illustrated in Fig. 2.1. There are also 10 BCGs undergoing major mergers, but we will not discuss them in this chapter in any detail.

Over half of the BCGs in the sample are classified as cDs. Separating cD BCGs and non-cD elliptical BCGs is a very hard problem since there is no sharp distinction between these two classes (e.g., Patel *et al.* 2006; Liu *et al.* 2008). Detecting the extended stellar envelope that characterises cD galaxies depends not only on its dominance, but also on the quality and depth of the images, and on the details of the method(s) employed. We used intermediate classes such as cD/E (probably a cD, but could be E) and E/cD (probably E, but could be cD) to account for the uncertainty inherent in the visual classification.

Our careful inspection of the images clearly reveals that there is a wide range in the brightness and extent of the envelopes. There seems to be a continuous distribution in the envelope properties, ranging from undetected (pure E class) to clearly detected (pure cD class), with the intermediate classes (E/cD and cD/E) showing increasing degrees of envelope presence. This continuous distribution in envelope detectability will also be made evident in the structural analysis carried out later in this chapter. The classification we present here does not intend to be a definitive one since such a thing is probably unachievable. Our aim is to obtain a homogeneous and systematic visual classification of the BCGs and then study how such classification correlates with quantitative and objective structural properties of the BCGs. The visual morphological types of all the galaxies in the sample are presented in Appendix A.

We checked the effect that the redshift of BCGs may have on the visual classification. cDs might be mistakenly identified as elliptical if they are more distant since the extended low-surface-brightness envelope may be harder to resolve at higher redshifts. Fig. 2.2 illustrates the redshift distribution of the three main types. cD galaxies generally share the same redshift distribution with elliptical BCGs, especially at $z \geqslant 0.05$. At $z < 0.05$ we identify a slightly higher proportion (by $\sim 10\%$) of cD galaxies. However, if we compare the structural properties of cD and elliptical BCGs which are at $z \geqslant 0.05$, the results we obtain do not significantly differ from those using the full-redshift sample. As an additional check, we artificially redshifted some of the lowest redshift galaxies ($z \sim 0.02$–0.03) to $z = 0.1$, the highest redshift of the sample, taking into account cosmological effects such as surface-brightness dimming. Because the redshift range of the BCGs we study is very narrow, the effect on the images is minimal and does not have any significant impact on the visual classification. We are therefore confident that our visual classification is robust and that in the relatively narrow redshift range explored here any putative redshift-related biases will not affect our results.

We also test our visual classification by using SDSS Stripe 82 coadd r-band images. Stripe 82 is the SDSS stripe along the celestial equator in the Southern Galactic Cap, covering $-1.25 \leqslant \delta \leqslant 1.25$ and $-50° \leqslant \alpha \leqslant +60°$ with a total area of 275 deg^2. It was imaged multiple times through repeated scanning by the SDSS camera. The Stripe 82 images we use are from the SDSS Stripe 82 database, which are a completed coaddition including 123 runs and covering any given piece of the 275 deg^2 area scanned between 20 and 40 times (Annis *et al.* 2014). The Stripe 82 coadd image data thus reaches ~ 2 mag fainter than the SDSS DR7 single-pass data, which could help to examine the validity of our visual classification.

There are 32 BGCs in the L07 catalogue with Stripe 82 images, including 18 cDs (14 pure cD, 3 cD/E, and 1 cD/S0), 10 Es (5 pure E, and 5 E/cD), 2 S0s, and 2 Spirals. We compare the r-band images of Stripe 82 with those of SDSS DR7, finding that most of the galaxy morphologies derived from Stripe 82 images are consistent with the morphologies from SDSS DR7 image (see the first three rows of Fig. 2.3). We found only one exception: a BCG was classified as a pure E using the DR7 image, but
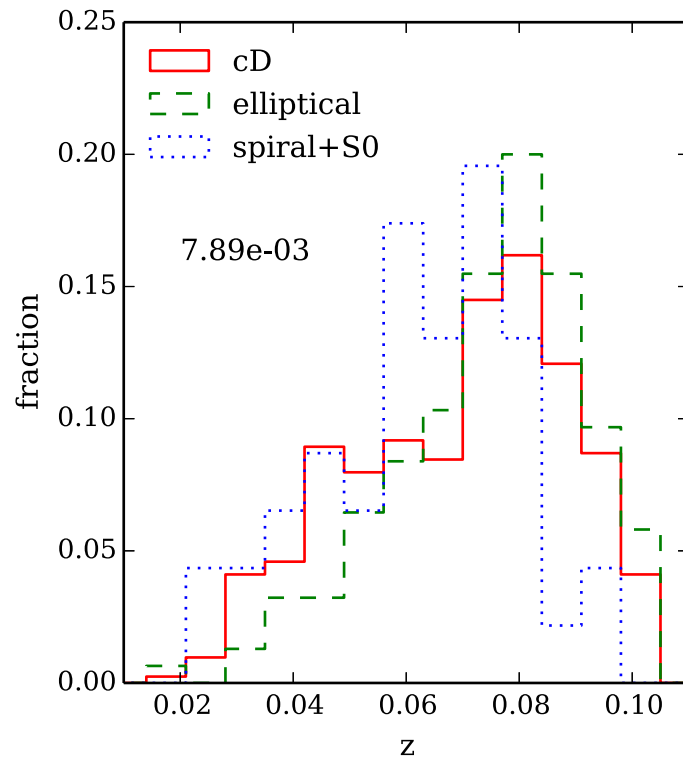
Figure 2.2: Redshift distribution for BCGs with different morphological types. The red solid line corresponds to cD BCGs, the green dashed line to ellipticals, and the blue dotted line to disk (spiral and S0) BCGs. A Kolmogorov-Smirnov test indicates that the redshift distributions of cD and elliptical BCGs are only different at the $\sim 2.4\sigma$ level (p-value $= 0.00789$). cD galaxies share the same redshift distribution with elliptical BCGs at $z \geqslant 0.05$, while there are proportionally $\sim 10\%$ more cD galaxies at $z < 0.05$.

exhibits a E/cD morphology in the Stripe 82 image (see the last row of Fig. 2.3). If what we find is true for all the L07 BCGs, the morphologies of only $\sim 3\%$ of them would be affected by the deeper images, with E morphologies probably being most likely affected. Nevertheless, deeper images would not make a significant change in morphology. Some pure E galaxies may change to E/cD, but it is unlikely that they would change as far as becoming pure cDs. Thus, we only expect relatively moderate changes in the morphological classification for a few cases due to the deeper images revealing the presence of the extended stellar envelope. Any change would always be in the same direction (moving galaxies along the E, E/cD, cD/E, cD sequence). Note that Alfonso and I carried out this comparison independently, reaching the same conclusions. This indicates that our visual classifications based on SDSS DR7 single-pass images are reasonably robust.

2.3   Quantitative Characterisation of BCG Structure

The surface brightness profiles of galaxies provide valuable information on their structure and clues to their formation. It has become customary to fit the radial surface brightness distribution using theoretical functions which have parameters that include a measurement of size (e.g., half-light radius or scale length), a characteristic surface brightness, and other parameter(s) describing the shape and properties of the surface brightness profiles. In this study we use GALFIT (Peng *et al.* 2002) to fit the 2-D luminosity profile of each BCG using two parametric models, and thus determine the best-fitted parameters of each model. GALFIT can simultaneously fit model profiles to several galaxies in one image, which is particularly important for BCGs since they usually inhabit very dense environments. In this way, the light contamination from nearby galaxies can be accounted for appropriately.

We explore two models to represent the luminosity profile of the BCGs. A model commonly used to fit a variety of galaxy light profiles is the generalization of the $r^{1/4}$ de Vaucouleurs (1948) law introduced by Sérsic (1963). The form of Sérsic function can be found in Section 1.2.3. This function provides a good model for galaxy bulges and massive elliptical galaxies. Since BCGs are mostly early-type galaxies,

Figure 2.3: Morphology comparison between images of Stripe 82 and SDSS DR7. Each panel shows one BCG morphology type, with the left image from DR7 and the right one from Stripe 82. Most of the BCGs keep the same morphology in the deeper Stripe 82 coadd images. Only one BCG change from pure E to E/cD, illustrated in the last row.

it is reasonable to fit their structure with single Sérsic models first. Subsequently, in order to explore the complexity introduced by the extended envelopes of cD galaxies, we will also fit the light profile of BCGs adding an additional exponential component to the Sérsic profile. Adding this exponential component is the simplest way to describe the "extra-light" from the extended envelope. Note that the exponential profile $I(r) = I_0 \exp(-r/r_{\rm s})$ is just a Sérsic model with $n = 1$. The models assume that the isophotes have elliptical shapes, and the ellipticity and orientation of each model component are parameters determined in the fitting process.

In order to run GALFIT, we require a postage stamp image for each BCG with appropriate size to measure its structure over the full extent of the object, a mask image with the same size as the stamp image, an initial guess for the fitting parameters, an estimate of the background sky level, and a point spread function (PSF). Details on how these ingredients are produced and the fitting procedures are given below.

2.3.1 Pipeline for One-Component Fits: GALAPAGOS

We run GALFIT using the GALAPAGOS pipeline (Barden *et al.*, 2012). GALAPAGOS has been successfully applied to a wide variety of ground- and space-based images (Häussler *et al.*, 2007a; van der Wel *et al.*, 2012, 2014; Huertas-Company *et al.*, 2013a; Lani *et al.*, 2013). We applied the version of GALAPAGOS 1.0 to fit the SDSS r-band images of the BCGs in our sample. The starting point are SDSS images with a size of 2047×1488 pixels. For each BCG, the pipeline carries out four main tasks before running GALFIT itself: (i) detection of all the sources present in the image; (ii) cutting out the appropriate postage stamp and preparing the mask image; (iii) estimation of the sky background; (iv) preparation of the input file for GALFIT. After completing these tasks, GALAPAGOS will run GALFIT using the appropriate images and input parameters. We describe now these tasks in detail.

(i) Source Detection: SExtractor (Bertin & Arnouts 1996) is used to detect galaxies in the SDSS images. A set of configuration parameters defines how SExtractor detects sources. The values of the SExtractor input parameters follows Guo *et al.* (2009): DETECT_MINAREA $= 25$, DETECT_THRESH $= 3.0$, and DEBLEND_MINCONT $= 0.003$. This set of parameters were tested to perform well on SDSS r-band images so

that the bright and extended BCGs were isolated from other sources without artificially deblending them into multiple components. SExtractor also provides estimates of several properties for the target BCGs and nearby objects such as their magnitude, size, axis ratio and position angle. These values are used to calculate the initial guesses of the model parameters that are needed as inputs by GALFIT.

(ii) Postage Stamp creation: GALAPAGOS cuts out a rectangular postage stamp centred on the target BCG which will be used by GALFIT as input image. We define the "Kron ellipse" for a galaxy image as an ellipse whose semi-major axis is the Kron radius[2] (R_{kron}), with the ellipticity and orientation determined by SExtractor. The postage stamp size is determined in such a way that it will fully contain an ellipse 3.5 times larger than the Kron ellipse, i.e., its semi-major axis is $3.5R_{\mathrm{kron}}$, and has the same ellipticity and orientation. The 3.5 factor represents a compromise between computational speed and ensuring that virtually all the BCG's light is included in the postage stamp. At this stage, a mask image is also created, identifying and masking out all pixels belonging to objects in the postage stamp which will not be simultaneously fitted by GALFIT. The aim is to reduce the computational time by excluding objects too far from the BCG or too faint to have any significant effect on the fit. Following Barden *et al.* (2012), an "exclusion ellipse" is defined for each galaxy with a semi-major axis $1.5R_{\mathrm{kron}} + 20\,\mathrm{pixels}$, and the same ellipticity and orientation as the Kron ellipse. GALAPAGOS masks out all objects whose exclusion ellipse does not overlap with the exclusion ellipse of the target BCG. These objects are deemed to be too far away from the BCG to require simultaneous fitting. Furthermore, all objects more than 2.5 magnitudes fainter than the BCG are also masked out since they are too faint to affect the BCG fit. The pixels that belong to these objects according to the SExtractor segmentation maps are masked out and excluded from the fits. All the remaining objects will be simultaneously fitted by GALFIT at the same time as the BCG. For a detailed description of this process and a justification of the parameter choice see Barden *et al.* (2012).

(iii) Sky Estimation: Accurate estimates of the sky background level is crucial when

---

[2]In this study we use the following definition of "Kron radius": $R_{\mathrm{kron}} = 2.5r_1$, where r_1 is the first moment of the light distribution (Kron, 1980; Bertin & Arnouts, 1996). For an elliptical light distribution, this is, strictly speaking, the semi-major axis.

fitting galaxy profiles, particularly when interested in the low-surface-brightness outer regions. Overestimating the sky level will result in the underestimation of the galaxy flux, size, and Sérsic index n, and vice-versa. GALAPAGOS uses a flux growth curve method to robustly estimate the local sky background around the target galaxy. SDSS DR7 also provides a global sky value for the whole 2047×1488 image frame and local sky values for each galaxy. The SDSS *PHOTO* pipeline estimates the sky background using the median flux of all the pixels in the image after 2.33σ-clipping. However, according to the SDSS-III website, the version of *PHOTO* used in DR7 and earlier data releases tended to overestimate both the global and local sky values. The sky measurement is improved by SDSS-III in later data releases, but since we use the images from DR7 we cannot use the SDSS sky value with enough confidence. Häussler *et al.* (2007a) demonstrated that the sky measurement that GALAPAGOS produces is highly reliable for single-band fits because it takes into account the effect of all the objects in the image. Therefore, in this study we use the local sky background estimated by GALAPAGOS. The accurate sky measurement provided by GALAPAGOS indicates that we can reach a surface brightness limit in the r-band of ~ 27 mag/arcsec^2. This is deep enough to study the faint extended structures of BCGs. For each galaxy, its local sky background is included in the GALFIT input file and is fixed during the fitting procedure. Given the importance of accurate sky subtraction, in Section 2.3.2 we will carry out an explicit comparison of our results using SDSS and GALAPAGOS sky estimates.

(iv) GALFIT Input: GALAPAGOS produces an input file which includes initial guesses for the fitting parameters based on the SExtractor output. As mentioned above, all objects which are not masked out are fitted simultaneously using a Sérsic model. The initial-guess model parameters for these nearby companions are also determined from SExtractor. In order to obtain reasonable results, we impose some constraints on the acceptable model parameter range. Our constrains on position, magnitude, axis ratio and position angle follow Häussler *et al.* (2007a). Additionally, the half-light radius R_{e} is constrained within $0.3 \leqslant R_{\mathrm{e}} \leqslant 800$ pixels. This prevents the code from yielding unreasonably small or large sizes. Since the pixel size of the SDSS images is 0.396 arcsec, R_{e} is constrained to be larger than 0.12 arcsec, which is much smaller than the PSF, and smaller than half the size of the original input images, reasonable for

the range of redshifts explored. In the original GALAPAGOS pipeline, the constraint on the Sérsic index is $0.2 \leqslant n \leqslant 8$. These are reasonably conservative limits, since normal galaxies with $n > 8$ are rarely seen and are often associated with poor model fits. However, some studies have shown that very luminous elliptical galaxies with $n > 8$ do exist (e.g., Graham *et al.*, 2005), therefore for the target BCGs we allow n to be as large as 14 to keep the fits as free as possible. For the companion galaxies, which are fitted simultaneously, we still keep the constraint $0.2 \leqslant n \leqslant 8$. The final ingredient needed by GALFIT is a PSF image appropriate for each BCG. These are extracted from the SDSS DR7 data products[3] according to the photometric band used and the position of the BCG on the SDSS image.

2.3.2 Effect of the Sky Background Subtraction: Comparing SDSS and GALAPAGOS Sky Estimates

As described in Section 2.3.1, in this study we rely on the sky measurements provided by GALAPAGOS. However, it is important to test the effect that the choice of sky background has on our results. We do this by comparing the fitted Sérsic model parameters n and R_e using the GALAPAGOS and SDSS sky estimates. As mentioned before, SDSS DR7 provides a global sky value for the whole 2047×1488 image and local sky values for each galaxy. Guo *et al.* (2009) found that the local background estimates are generally larger than the global ones due to contamination from the outskirts of extended and bright sources, making them unreliable. We therefore restrict our comparison to the global SDSS sky values. We fit the BCG light profiles twice using exactly the same procedure and input parameters (see Section 2.3.1) but changing only the sky background estimates. The first set of fits use the GALAPAGOS-determined sky values, while the second set use the SDSS DR7 global ones.

Fig. 2.4 shows the distribution of the difference between the SDSS DR7 global sky and the sky measured by GALAPAGOS. It is clear that the SDSS global sky is generally larger than the local sky from GALAPAGOS. The effect from different sky values on the best-fitted structural parameters (Sérsic index n and effective radius R_e) is shown in Fig. 2.5. It is clear that the SDSS larger sky values result in the values of n_{sdss} and

---

[3]http://www.sdss.org/DR7/products/images/read_psf.html
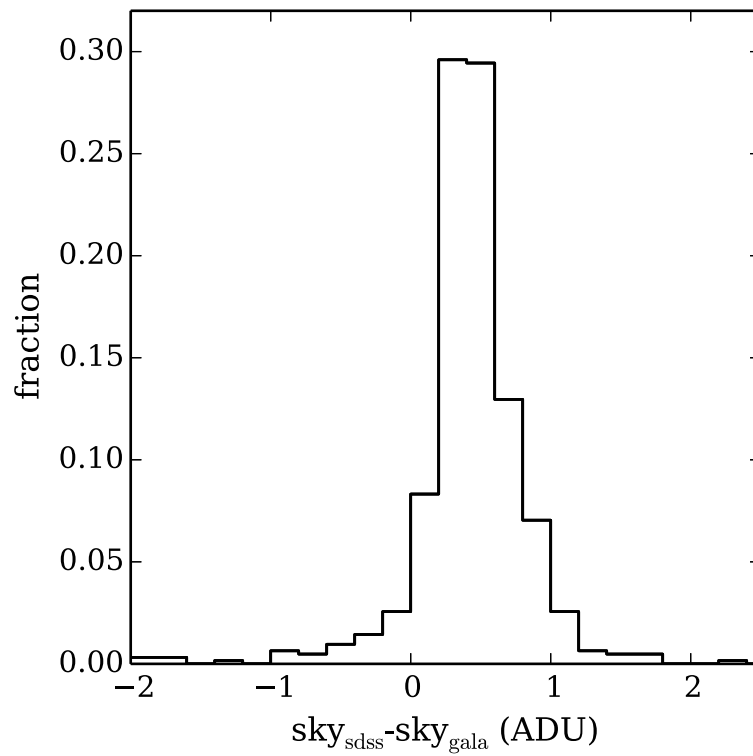
Figure 2.4: Distribution of the difference between the SDSS DR7 global sky and the GALAPAGOS-measured sky values. In general, SDSS overestimates the sky background. The average sky value measured by GALAPAGOS in the SDSS r-band BCG images is 140.8 ADU, corresponding to a surface brightness of ~ 20.9 mag/arcsec^2.
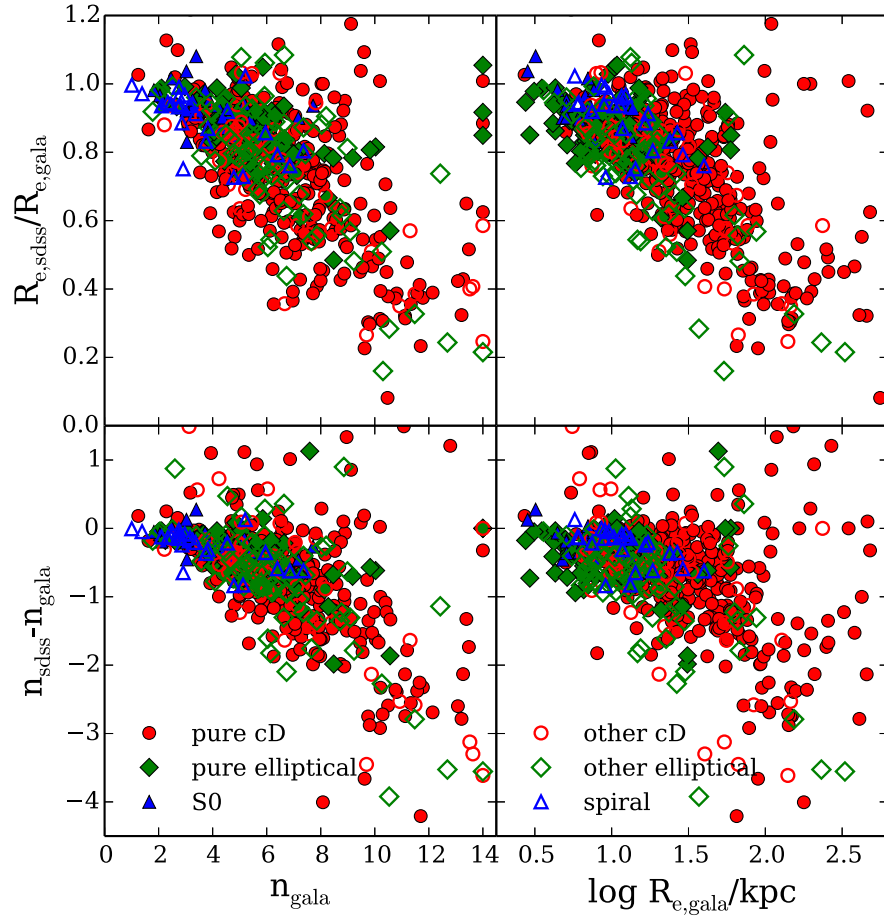
Figure 2.5: Comparison on the best-fit n and R_e from single Sérsic models using the SDSS and GALAPAGOS-measured sky estimates. Solid and open red circles correspond to pure cD and other cD galaxies (cD/E and cD/S0) respectively; solid and open green diamonds correspond to pure and other (E/cD and E/S0) elliptical BCGs respectively; solid blue triangles represent S0s and open ones are spirals. It shows that the SDSS overestimation of the global sky result in the values of n_{sdss} and $r_{e,sdss}$ being smaller than the corresponding GALAPAGOS ones. Moreover, the effect is more serious for the BCGs with large n and R_e which are mostly cDs.

$r_{\rm e,sdss}$ being smaller than the corresponding GALAPAGOS ones. The effect becomes more severe for those BCGs with large n and $R_{\rm e}$, most of which are cD galaxies. This means the overestimated sky values would particularly affect the measurements on the low-surface-brightness envelopes of cD galaxies. Although it is difficult to know *a priori* which the *true* value of the sky background is, based on the fact that the SDSS-III provides evidence that DR7 sky values are overestimated while Häussler *et al.* (2007a) showed reasonable proof of the reliability of the GALAPAGOS sky measurements, in what follows we will therefore trust and use the GALAPAGOS-determined sky values.

2.3.3 Two-Component Fits

Although the light profiles of many early-type galaxies can be reproduces reasonably well with single Sérsic models, the extended envelopes of cD galaxies may require an additional component. We therefore fitted all the BCGs by GALFIT using a two-component model consisting of a Sérsic profile plus an exponential. The input postage stamp, mask image, PSF, and sky values required by GALFIT remain the same as for the single-Sérsic fits. To ensure that we are fitting exactly the same light distribution, the location of the centre of the BCG is fixed to the X and Y coordinates determined in the single fit, and we also force the initial guesses of the model parameters to be the single-component fit results. The BCG companions are simultaneously fitted still with single-Sérsic profiles but with initial-guess parameters determined by the single profile fits.

Other than using the Sérsic+Exponential model, we also apply a more flexible two-component model to fit the BCG profiles which is Sérsic+Sérsic model. The input postage stamp, mask image, PSF, and sky values required by GALFIT remain the same as for the single-Sérsic fits. The X and Y coordinates determined in the single Sérsic fit are fixed for the centres of the two components to ensure the fitting is for the same galaxy. For the first Sérsic component, the initial guesses of the model parameters are the single-component fit results. For the second Sérsic component, the initial guesses of the parameters are set to be slightly different from the single-component fit results, to ensure GALFIT to distinguish the two Sérsic components. Same as the Sérsic+Exponential fits, the BCG companions are simultaneously fitted

with singleSérsic profiles with initial-guess parameters determined by the single profile fits.

2.3.4 Residual Flux Fraction and Reduced χ^2

Although the models we are fitting are generally reasonably good descriptions of the BCG light profiles, real galaxies can be more complicated, with additional features and structures such as star-forming regions, spiral arms, and extended haloes. It is therefore desirable to quantify how good the fits are and what residuals remain after subtracting the best-fit models. A visual inspection of the residual images can generally give a good feel for how good a fit is, and sometimes tell us whether an additional component or components are required. However, more quantitative, repeatable and objective diagnostics are also needed. The residual flux fraction (*RFF*; Hoyos *et al.*, 2011) provides one such diagnostic. It is defined as

$$RFF = \frac{\sum_{i,j \in A} |I_{i,j} - I_{i,j}^{\mathrm{model}}| - 0.8 \times \Sigma_{i,j \in A} \sigma_{i,j}^{\mathrm{bkg}}}{\Sigma_{i,j \in A} I_{i,j}}, \qquad (2.1)$$

where A is the particular aperture used to calculate *RFF*. Within A, $I_{i,j}$ is the original flux of pixel $(i.j)$, $I_{i,j}^{\mathrm{model}}$ is the model flux created by GALFIT, and $\sigma_{i,j}^{\mathrm{bkg}}$ is the *rms* of the background. The aperture A we use to calculate *RFF* is the "Kron ellipse" defined in Section 2.3.1 (an ellipse with semi-major axis R_{kron} and the ellipticity and orientation determined by SExtractor for the BCG). $\Sigma_{i,j \in A} I_{i,j}$, the denominator of Equation (2.1), is computed as the total BCG flux contained inside the Kron ellipse, which is one of the SExtractor outputs, and therefore independent of the model fit. Obviously, this diagnostic can be applied to both single-Sérsic and two-component profiles, or any other model.

The 0.8 factor before $\Sigma_{i,j \in A} \sigma_{i,j}^{\mathrm{bkg}}$ is derived from a hypothesis testing procedure. If the real galaxy had a pure Sérsic profile, GALFIT could find a model providing an exact fit to the galaxy. However, even in this optimal case, the errors associated with the readout noise and photon shot noise imply that the residual image will not be blank. In the case of independent errors, the properties of the residual image would be very similar to those of Gaussian white noise. For a pure Sérsic galaxy, *RFF* is expected to

be 0.0, so that the numerator of the *RFF* should deduct the effect of the noise in residual image. By using a residual image from GALFIT fit of a simulated pure Sérsic galaxy with background of Gaussian white noise, Hoyos *et al.* (2011) found that it should be $0.8 \times \Sigma_{i,j\in A}\sigma_{i,j}^{\mathrm{bkg}}$ to ensure the expectation value of the numerator of the *RFF* is 0.0. Since the denominator is a normalization factor, the expected value of the *RFF* then is 0.0 for pure Sérsic galaxy. *RFF* measures the fraction of the signal contained in the residual image that cannot be explained by background noise.

Since BCGs usually reside in dense environments, sometimes there are some faint nearby objects contained within the Kron ellipse that have not been fitted by GALFIT (those more than 2.5 mag fainter than the BCG, see Section 2.3.1). These objects will be present in the residual image. Moreover, brighter companions that have been simultaneously fitted may also leave some residuals due to inaccuracies in their fits. Therefore, even if the BCG light distribution has been accurately fitted, *RFF* can be affected by the residuals from the companion galaxies, failing to provide an accurate measure of the quality of the fit. To minimise the effect from companion galaxies on *RFF*, we mask out the pixels belonging to all companions within the Kron ellipse using SExtractor segmentation maps. The *RFF* will therefore measure the residuals from the BCG fit alone, excluding, as far as possible, those belonging to nearby galaxies.

An additional measurement of the fit accuracy is the reduced χ^2, which is minimised by GALFIT when finding the best-fit models. It is defined as

$$\chi_\nu^2 = \frac{1}{N_{\mathrm{dof}}} \sum_{i,j\in A} \frac{(I_{i.j} - I_{i,j}^{\mathrm{model}})^2}{\sigma_{i,j}^2}, \qquad (2.2)$$

where A is the aperture used to calculate χ_ν^2, N_{dof} is the number of degrees of freedom in the fit, $I_{i,j}$ is the original image flux of pixel (i, j). $I_{i,j}^{\mathrm{model}}$ represents, for each pixel, the sum of the flux of the models fitted to all the galaxies in the aperture, and $\sigma_{i,j}$ is the noise corresponding to pixel (i, j). This noise is calculated by GALFIT taking into account the contribution of the Poisson errors and the read-out-noise of the image (Peng *et al.*, 2002).

Similarly to *RFF*, χ_ν^2 also measures the deviation of the fitted model from the original light distribution. The value of χ_ν^2 that GALFIT minimises to find the best-fit model

is calculated over the whole postage stamp, and includes contributions from all the objects fitted. To make sure that we only take into account the contribution to χ_ν^2 from the BCG fit, we calculate it within the Kron ellipse of the BCG, masking out the nearby objects as we did when calculating *RFF*.

The choice of aperture (Kron ellipse with semi-major axis of R_{kron}) over which we evaluate *RFF* and χ_ν^2 represents a good compromise between covering a large fraction of the galaxy light while minimising the impact of close companions. We carried out several tests to evaluate the sensitivity of our results to the changes in aperture size. If we reduce the semimajor axis of the aperture by 20% or more we lose significant information on the extended halo of BCGs, which we must avoid. If we increase the semimajor axis of the aperture by 20% or more, we potentially increase the sensitivity to the galaxy haloes but in the crowded central cluster regions contamination from companion galaxies becomes a serious problem, generally increasing *RFF* and χ_ν^2. Changes in the aperture semimajor axis within $\pm 20\%$ would have no effect on the conclusions of this chapter.

2.3.5   Evaluating One-Component and Two-Component Fits

Since *RFF* and χ_ν^2 can quantify the residual images after subtracting the model fits, we attempt to use them to assess whether a one-component (Sérsic) fit or a two-component (Sérsic+Exponential) fit is more appropriate to describe the light profile of individual BCGs. In order to do this, we first evaluate the effectiveness of *RFF* and χ_ν^2 at quantifying the goodness-of-fit. We visually examine the fits and residuals obtained from both one- and two-component models for all the BCGs in our sample. In some cases, two of which are illustrated in Fig. 2.6, it is obvious which model is clearly favoured.

For those BCGs where such a clear distinction can confidently be made, we classify them into what we call 1C (one-component) BCGs and 2C (two-component) BCGs. Explicitly, 1C BCGs (e.g., galaxy 1 in the top panel of Fig. 2.6) are those for which a one-component Sérsic model represents their light distribution very well, and therefore the residuals left are small and show no significant visible structure. For these galaxies, adding a second component does not visibly improve the residuals. Conversely, 2C BCGs (e.g., galaxy 2 in the bottom panel of Fig. 2.6) are not well fitted by a one-
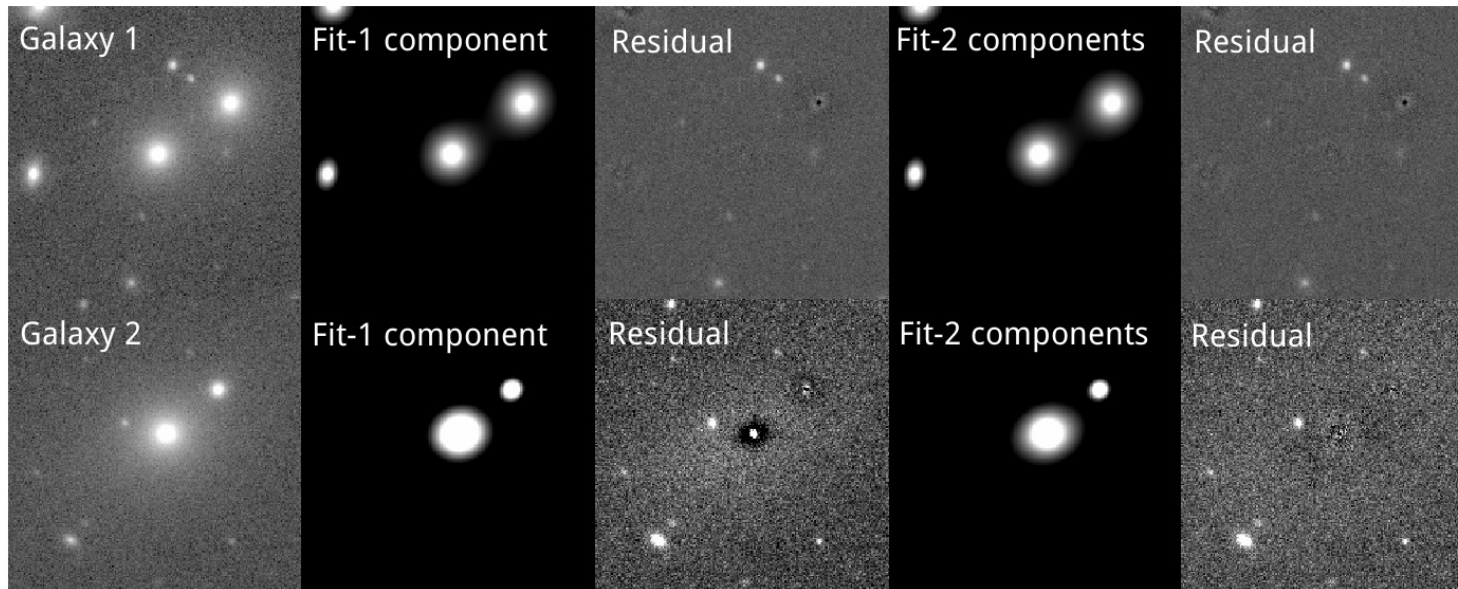
Figure 2.6: Example of one-component (Sérsic) fits and two-component (Sérsic+Exponential) fits for 1C and 2C BCGs, respectively. From left to right, the panels show the original image, the one-component model, the residuals after subtracting the one-component fit, the two-component model, and the residuals after subtracting the two-component fit. The upper panels show a 1C BCG where a one-component fit does a good job and adding a second component does not visibly improve the residuals. The lower panels show a 2C BCG, where the one-component residual exhibits clear excess light at large radii, suggesting that a second component is necessary. Indeed, the two-component residual is much better for this BCG.

component model, and the residuals are significant. These residuals often show excess light at large radii which can be identified as an exponential component or halo. Additionally, the fit to these galaxies visibly improves when using a two-component model. With these criteria we confidently identify 53 1C BCGs and 25 2C BCGs. Since we want to test the sensitivity of *RFF* and χ^2_ν, we concentrate for now on this small but robust subsample. The rest of the BCGs (537) cannot be confidently classified into 1C or 2C BCGs because it is too hard to tell visually due to the residuals containing significant structures which cannot be accurately fitted by such simple models.

Fig. 2.7 presents a comparison of the *RFF* and χ^2_ν values for the one- and two-component fits of the 53 1C BCGs and 25 2C BCGs. For 1C BCGs, the *RFF* and χ^2_ν distributions of one- and two-component fits are virtually indistinguishable. Neither *RFF* nor χ^2_ν improve significantly when the second component is added. However, *RFF* and χ^2_ν are significantly smaller for the two-component fits of 2C BCGs. It is clear therefore that the quantitative information that *RFF* and χ^2_ν provide agrees very well with the visual assessments of the fits. Both *RFF* and χ^2_ν are sensitive to changes in the residuals, but *RFF* appears to be more sensitive. As shown in the bottom panels of Fig. 2.7, the improvement in the two-component fit for 2C BCGs is around 40%–60% when measured by *RFF*, while it is only $\sim 20\%$ when measured by χ^2_ν. A further useful piece of information obtained from this test is that the typical values of $\log RFF$ and $\log \chi^2_\nu$ for fits deemed to be good by visual inspection are $\log RFF \simeq -1.7^{+0.11}_{-0.06}$, and of $\log \chi^2_\nu \simeq 0.042^{+0.033}_{-0.025}$ (median +/− 1st and 3rd quartiles of the parameter distributions).

As mentioned before, the majority of the BCGs cannot be visually classified into 1C or 2C BCGs with high certainty because their light distributions are too complex to be accurately represented by such simple models. Nevertheless, we can use the quantitative information provided by *RFF* and χ^2_ν to gauge to what extent the BCGs are better fit by a two-component model than by a one-component model. This will be discussed later.

We would like to point out that this is the first time that the residual flux is calculated considering *only* the contribution of the target galaxies when estimating both *RFF* and χ^2_ν, explicitly excluding the contribution due to the companion galaxies. For instance, Hoyos *et al.* (2011) also used *RFF* to evaluate the goodness-of-fit, but they measured
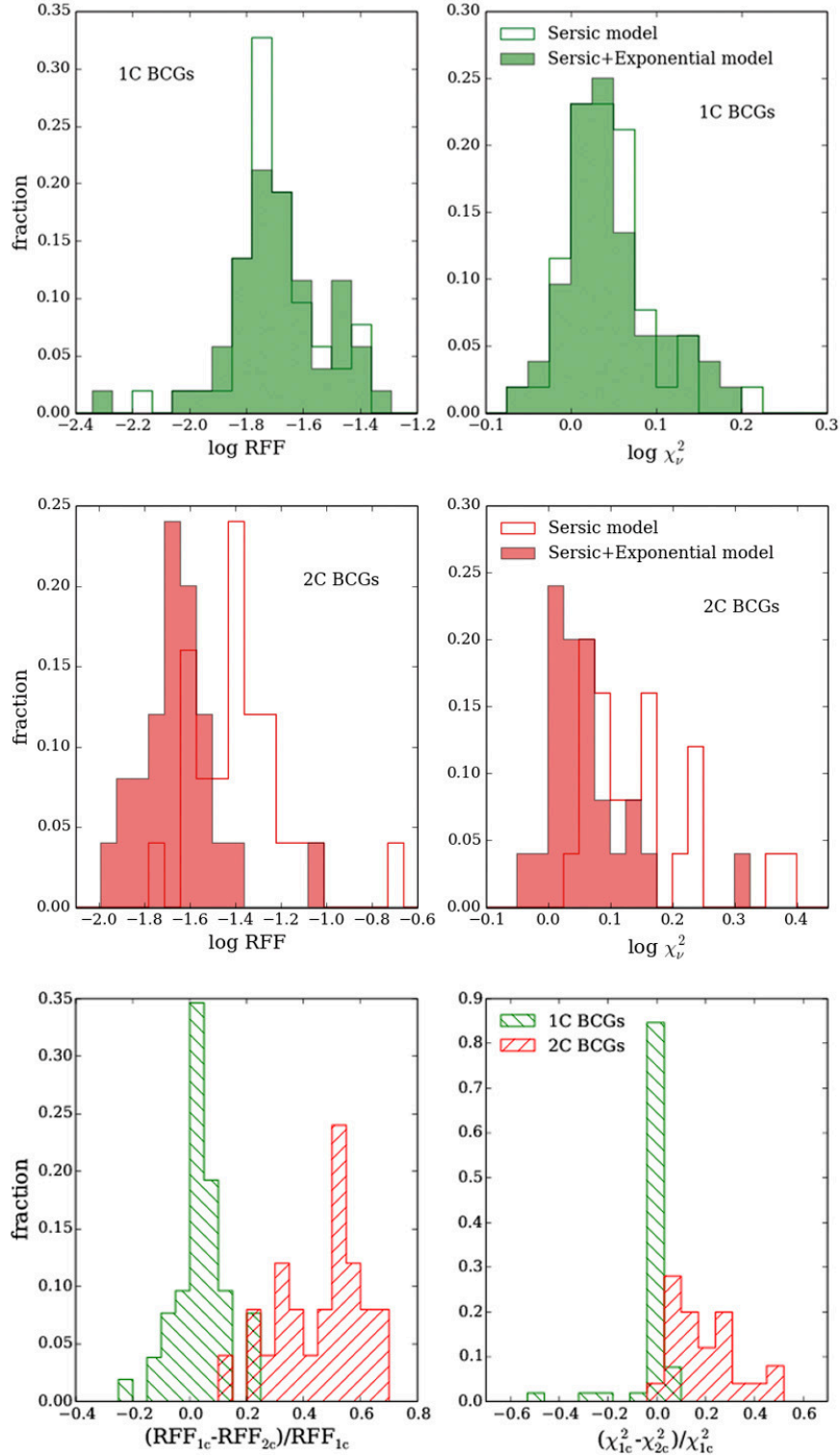
Figure 2.7: The top four panels show the distribution of $\log RFF$ (left) and $\log \chi_\nu^2$ (right) for single Sérsic (open histograms) and Sérsic+Exponential (solid histogram) fits. The two uppermost panels correspond to the 53 1C BCGs, while the middle panels correspond to the 25 2C BCGs. The two bottom panels show the difference in RFF and χ_ν^2 between one-component and two-component models for both sets of BCGs. RFF_{1c} (χ_{1c}^2) denotes RFF (χ_ν^2) for one-component models, and RFF_{2c} (χ_{2c}^2) denotes for two-component models. Clearly, the RFF and χ_ν^2 distributions of one- and two-component fits are virtually indistinguishable for 1C BCGs. However, RFF and χ_ν^2 tend to be significantly smaller for the two-component fits of 2C BCGs. Typical values for good fits are $\log RFF \simeq -1.7_{-0.06}^{+0.11}$, and $\log \chi_\nu^2 \simeq 0.042_{-0.025}^{+0.033}$ (median $+/-$ the 1st and 3rd quartiles of the parameters). Both RFF and χ_ν^2 are sensitive to the magnitude of the residuals, but RFF is appears to be significantly more sensitive.

the residuals over all pixels within a specific area around the target galaxies, without excluding nearby companions. Similarly, the χ_ν^2 values from GALFIT have also been applied to evaluate which fitting model is better (e.g., Bruce *et al.* 2012), but the effect of nearby objects on the χ_ν^2 values was also overlooked. Using the 2C BCG sample, we assessed the importance of this improvement. If the *RFF* and χ_ν^2 are calculated considering the residuals in all the pixels inside the relevant aperture, the *RFF* and χ_ν^2 distributions for the two-component fits of 2C BCGs cannot be distinguished from the one-component results. The effect of the contribution to the residuals from companion galaxies is so severe that it renders such a comparison useless. Our method therefore represents a significant step forward. It is extremely important to exclude the contibution of the companion galaxies when calculating *RFF* and χ_ν^2 in this kind of analysis.

2.4 Structural Properties of BCGs

Our morphologically-classified BCGs provide a large sample to statistically study their structural properties and link them to their morphological properties. In what follows we consider the three main morphological classes of BCGs: cDs (including all BCGs classified as pure cD, cD/E and cD/S0); ellipticals (including pure E, E/cD and E/S0) and disk (spiral and S0) BCGs. The 10 BCGs classified as mergers are excluded (see Section 2.2.2 for details). We decided to include the galaxies with "uncertain" morphologies (such as cD/E and E/cD) in our analysis to reflect the difficulties involved in visual classification. However, to ensure the robustness of our analysis, at every stage we have checked that considering only "pure" cD and elliptical BCGs (i.e., excluding the cD/E, cD/S0, E/cD and E/S0 classes) would not change our conclusions.

Since most BCGs are early-type galaxies, we will first consider and discuss single Sérsic models when fitting their SDSS r-band images. We will subsequently use Sérsic+Exponential models to see whether the fits are improved. But before embarking in the analysis of the parameters derived from these model fits, we first evaluate their uncertainties.
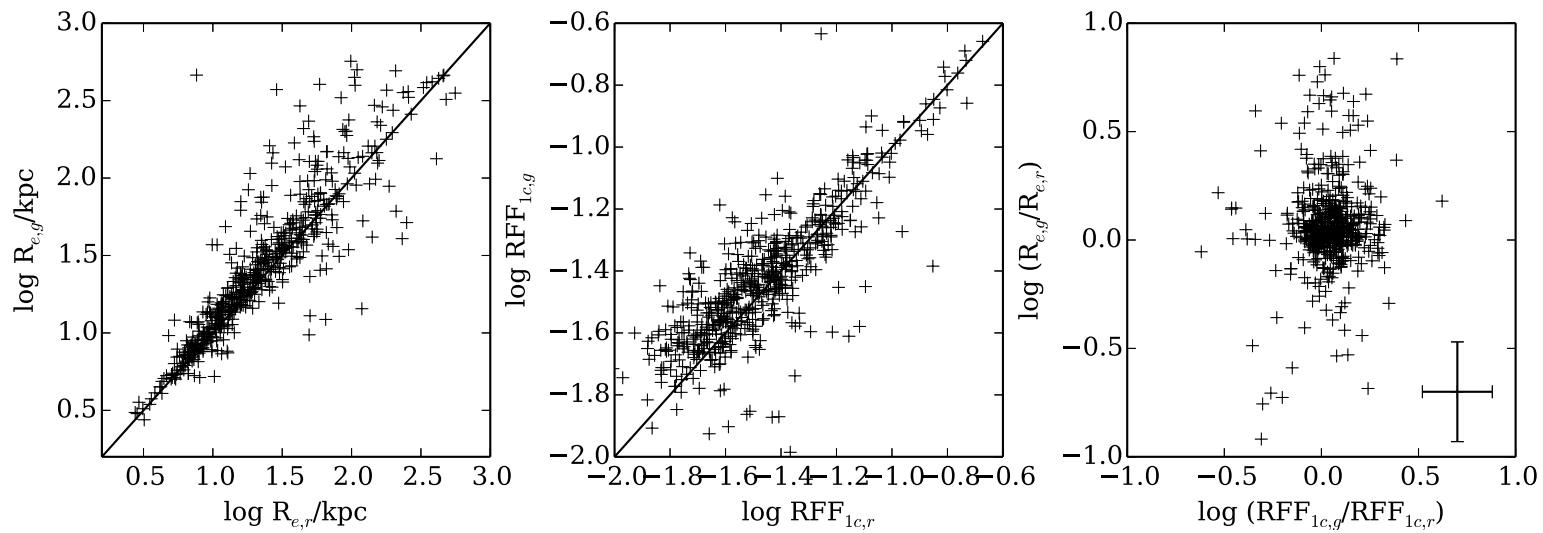
Figure 2.8: Comparison of the $R_{\rm e}$ (left panel) and $RFF_{\rm 1c}$ (middle panel) values obtained in both the SDSS g-band and r-bands. $RFF_{\rm 1c}$ denotes RFF for one-component (Sérsic) models. The solid lines correspond to the 1-to-1 relations. The right panel shows $\log(R_{\rm e,g}/R_{\rm e,r})$ vs. $\log(RFF_{\rm 1c,g}/RFF_{\rm 1c,r})$. The error bars in the bottom-right corner are derived from the *rms* scatter of each parameter.
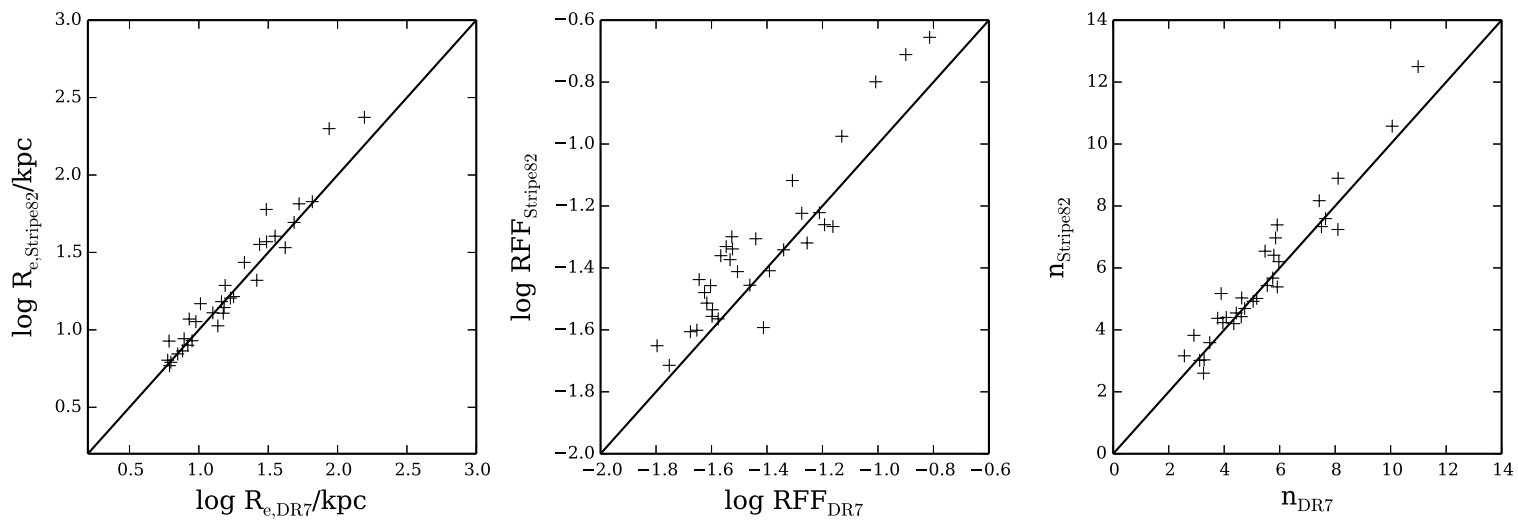
Figure 2.9: Comparison of the R_e (left panel), RFF_{1c} (middle panel), and n (right panel) values obtained from r-band images of Stripe 82 and DR7 for 32 L07 BCGs. The solid lines correspond to the 1-to-1 relations.

2.4.1   Structural Parameter Uncertainties

The parameter uncertainties that GALFIT reports are calculated using the covariance matrix derived from the Hessian matrix computed by the Levenberg-Marquardt algorithm that the program uses (Peng *et al.*, 2010). These formal uncertainties are only meaningful when the model provides a good fit to the image, in which case the fluctuations in the residual image are only due to Poisson noise. However, for real galaxy images the residual images contain not only Poissonian noise, but also systematics from non-stochastic and stochastic factors due to additional components not included in the fitting function (e.g., spiral arms, star-forming regions), asymmetries, shape mismatch, flat-fielding errors and so on. These non-random factors usually dominate the uncertainty of the parameters, and the uncertainties inferred from the covariance matrices are only lower-limit estimates (Peng *et al.*, 2010). Therefore, if we rely on the errors reported by GALFIT the uncertainties in the structural parameters of the BCGs could be severely underestimated. Indeed, these formal errors seem unrealistically small: typical GALFIT uncertainties for R_e and n are only $\sim$ 1–2%. A more robust and realistic way of determining these uncertainties is clearly needed.

We have measured the structural parameters of the BCGs in our sample by one-component (Sérsic) models using the SDSS r-band images. Independent measurements can also be obtained using the SDSS g-band images. In principle, the structural parameters could be wavelength-dependent. However, the $g - r$ colours of massive early-type galaxies with old stellar populations are quite spatially uniform and do not change much from galaxy-to-galaxy (e.g., Fukugita, Shimasaku & Ichikawa, 1995). Furthermore, morphological k-corrections are negligible for early-type galaxies between these two bands (e.g., Taylor-Mager *et al.* 2007), so it is reasonable to expect that the intrinsic structural parameters will not change much between g and r band. Therefore, any differences in the measured parameters between these two bands should be largely dominated by measurement errors. Moreover, if there are significant wavelength-dependent differences in the measured parameters that are driven by real physical differences, it is reasonable to expect that these may correlate with other galaxy properties such as their colour, morphology, redshift, cluster velocity dispersion, etc. No such correlations were found, so we are confident that the intrinsic differences are not significant

in these two bands.

We use GALAPAGOS to fit the SDSS g-band images of the BCGs in our sample by single-Sérsic models in exactly the same way as we did for the r-band images. Fig. 2.8 shows a comparison of the R_e and *RFF* values obtained in both bands. Similar comparisons were carried out for the rest of the structural parameters. The scatter around the 1-to-1 relations is due, in principle, to both intrinsic wavelength-dependent differences and measurement errors. Since, as we have argued, the intrinsic differences are not expected to be significant between these two bands, the measurement errors should dominate the scatter. We can thus use this scatter as an estimate of realistic, albeit perhaps marginally pessimistic, parameter uncertainties. The average errors are $\delta(n) \simeq 0.9$, $\delta(\log r_e) \simeq 0.16$, and $\delta(\log RFF) \simeq 0.13$.

Since there are 32 BCGs with both Stripe 82 and DR7 images in the r-band, we can also use the difference in the measured parameters from these two sets of images to directly explore the measurement uncertainties. In this comparison, both set of images are taken in the same band, so colour-induced differences are avoided. Once again, we use GALAPAGOS to fit the Stripe 82 r-band images with single-Sérsic models. The fitting procedure is entirely similar to the one used with DR7 images, using the appropriate PSF for Stripe 82. Fig. 2.9 shows a comparison of the R_e, *RFF*, and n values obtained from these two sets of images for these 32 BCGs. The parameter uncertainties are measured as the scatter around the 1-to-1 relations. The average errors from this method are $\delta(n) \simeq 0.5$, $\delta(\log r_e) \simeq 0.09$, and $\delta(\log RFF) \simeq 0.10$. As expected, these errors are smaller than the ones estimated when comparing the g- and r-band images because colour-related differences are not present. This exercise confirms that the errors we have derived for the whole sample are pessimistic.

The right-hand panel of Fig. 2.8 shows that the errors in R_e and *RFF* are not correlated. This is an important point since these two are the main parameters that we will use as diagnostics in our analysis in Section 2.5.
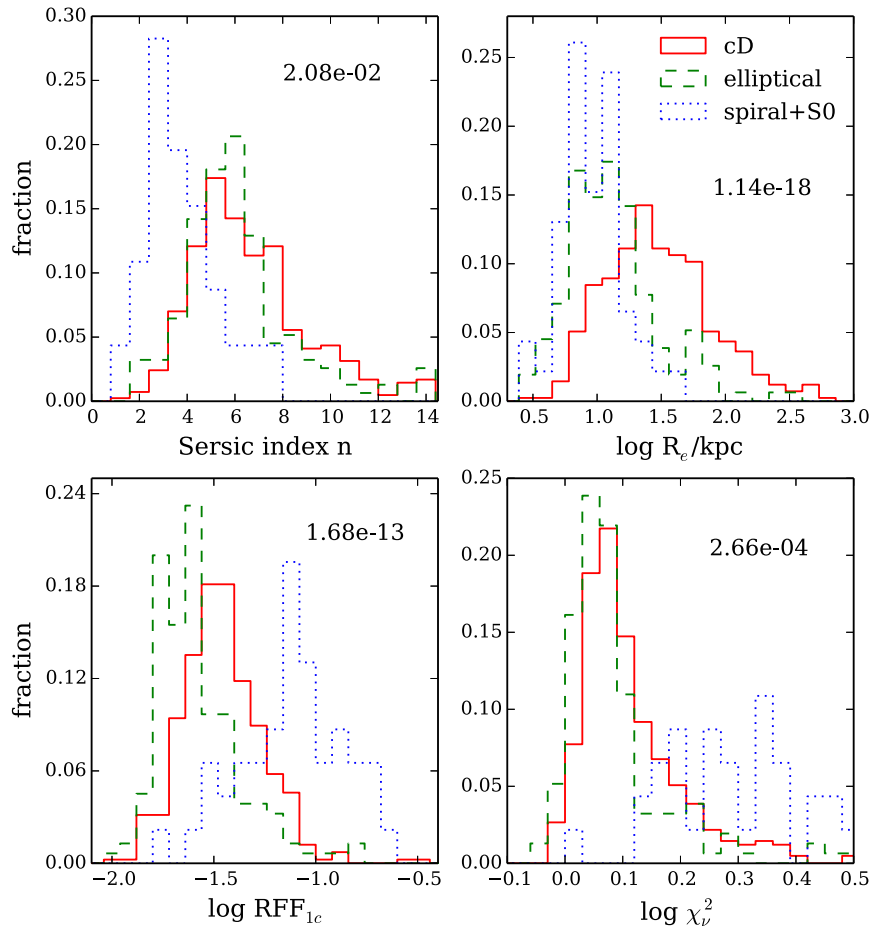
Figure 2.10: Distribution of the Sérsic index n (upper left), effective radius R_e (upper right), $\log RFF_\mathrm{1c}$ (lower left) and $\log\chi_\nu^2$ (lower right) from single Sérsic fits for the BCGs divided by morphology. The red solid line corresponds to cD galaxies, the green dashed line to ellipticals, and the blue dotted line to spirals and S0s. The p-value in each panel indicates the significance of the observed differences between the cD and elliptical BCG parameter distributions. These are derived from two-sample Kolmogorov-Smirnov tests.

2.4.2 Single Sérsic Models

We analyse now the behaviour of four parameters derived from the best-fitting single-Sérsic models along with the morphological classifications. Two of them, the Sérsic index n and the effective radius R_e, provide information on the intrinsic properties of the BCGs. The other two, *RFF* and χ^2_ν, show how well the models fit the real light distribution of the BCGs and also provide information about their detailed structure. The values of these parameters are listed in Appendix A. Fig. 2.10 shows the distribution of these parameters for the three main BCG morphologies. The σ value in each panel indicates the significance (confidence level) of the observed differences between the cD and elliptical BCG parameter distributions. These are derived from two-sample Kolmogorov-Smirnov tests.

2.4.2.1 Sérsic Index n

The Sérsic index n measures the concentration of the light profile, with larger n corresponding to higher concentration. The upper left panel of Fig. 2.10 presents the n distributions for the three main BCG morphologies. It is clear that disk (spiral and S0) BCGs tend to have smaller values of n, as expected. However, the n distribution for disk BCGs is skewed towards larger values ($n \gtrsim 3$) than those of the normal disk galaxy population (e.g., $n = 2.5$ in Shen *et al.*, 2003). This is because most disk BCGs are early-type bulge-dominated spirals and S0s. Elliptical and cD BCGs tend to have larger n values ($n \geq 4$). There are a few elliptical and cD BCGs (less than 5% of our BCG sample) have very high Sérsic index ($n > 12$). Their images show either double cores or very bright centre, causing GALFIT to use a very concentrated model to fit them. Nevertheless, they do not affect our conclusions. The n distributions of cD and elliptical BCGs are quite similar. A K–S test indicates that the distributions are not significantly different: the significance of any possible difference is just 2.04σ.

2.4.2.2 Effective Radius R_e

The effective radius R_e is a measurement of the extent (or size) of the light distribution. The upper right panel of Fig. 2.10 shows the distributions of $\log R_e$. Disk BCGs tend

to have relatively small sizes, and the vast majority of them ($\sim 85\%$) have $R_{\rm e}$ smaller than $\sim 15\,h^{-1}$kpc. About 75% of the elliptical BCGs also have $R_{\rm e} \lesssim 15\,h^{-1}$kpc, while cD galaxies tend to be significantly larger. More than 60% of cDs have $R_{\rm e} \gtrsim 15\,h^{-1}$kpc. A K–S test demonstrates that the difference in $R_{\rm e}$ distributions between cD and elliptical BCGs is very significant. This suggests that $R_{\rm e}$ could be a good discriminator to separate cD and elliptical BCGs.

2.4.2.3 Residual Flux Fraction and Reduced χ^2

The lower left panel of Fig. 2.10 presents the $RFF_{\rm 1c}$ distributions in a $\log_{10}$ scale, where $RFF_{\rm 1c}$ denotes *RFF* for one-component models. The $RFF_{\rm 1c}$ of disk BCGs has a much broader distribution and reaches significantly larger values than those of cDs and ellipticals. This reflects the fact that a single-Sérsic model is not a good representation of the light distribution of galaxies with clear disks, spiral arms and star-forming regions. Early-type BCGs have smoother light distributions that can be reasonably well reproduced with a Sérsic profile, and their $RFF_{\rm 1c}$ tend to be smaller. However, there are statistically significant differences between the $RFF_{\rm 1c}$ distributions of cD and elliptical BCGs. About 60% of elliptical BCGs have $RFF_{\rm 1c}$ values in the range corresponding to good fits (see Section 2.3.5 and Fig. 2.7), while just $\sim 25\%$ of cD galaxies do. This suggests that most elliptical BCGs can be well represented by single Sérsic models, while most cD galaxies are harder to model with such a simple profile. Since an extended envelope is a general property of cD galaxies, their deviation from a single Sérsic profile may be due, at least partially, to this extended envelope. This suggests that an additional model component may be required for them. We will re-visit two-component models in Section 2.4.3. The clear difference in *RFF* suggests that *RFF* could be another good discriminator to separate cD and elliptical BCGs.

Similar conclusions can be reached from the the distributions of χ^2_ν shown in the lower right panel of Fig. 2.10, albeit less clearly. This is not surprising since, as shown in Section 2.3.5, both *RFF* and χ^2_ν measure the strength of the residuals, but χ^2_ν is significantly less sensitive. Therefore, *RFF* is expected to be more efficient for separating cD and elliptical BCGs than χ^2_ν.

2.4.2.4   Axis Ratio b/a

The single Sérsic fits also provide information on the galaxies' axis ratio, represented by the ratio of semi-minor axis (b) and semi-major axis (a) of the best-fit model. This ratio provides information on the galaxies' ellipticity ($1 - b/a$). Fig. 2.11 presents the distribution of b/a for different BCG morphologies. The b/a values of disk BCGs span a wide range, from very small values to $b/a > 0.8$, with most disk BCGs having relatively small b/a ratios (peaking around $b/a \sim 0.5$). This distribution is characteristic of disk galaxies with a broad range of orientations. Elliptical and cD BCGs tend to have much larger values of b/a: almost all of them have $b/a > 0.6$. Interestingly, a K–S test demonstrates that the ellipticity distributions of elliptical and cD BCGs are different. Fig. 2.11 shows that elliptical BCGs tend to have a rounder profile than cD galaxies, which may partially due to the lack of the extended envelopes. Fasano *et al.* (2010) found that cDs tend to have prolate shapes, while elliptical BCGs do not show any preference of prolateness. Our results may support their finding, but a more detailed study of the 3D galaxy profiles is needed.

These results show a clear link between the visual morphologies of BCGs and their structural properties. Although cD galaxies tend to have similar shapes to elliptical BCGs, they usually have larger sizes and their structures generally deviate more from single Sérsic profiles. In contrast, elliptical BCGs tend to be smaller, and their light profiles are statistically more consistent with single Sérsic models. These structural differences, especially in R_e and *RFF*, could therefore provide quantitative ways to separate elliptical and cD BCGs without relying on visual inspection. We will explore these issues in Section 2.5.

2.4.3   Sérsic+Exponential Models

The *RFF* distributions shown in Section 2.4.2 indicate that elliptical BCGs are statistically better fitted by a single Sérsic model than cDs. Since a distinctive feature of cD galaxies is their extended luminous halo, two-component models may be more appropriate to describe accurately the light distributions of cD BCGs. Following Seigar,
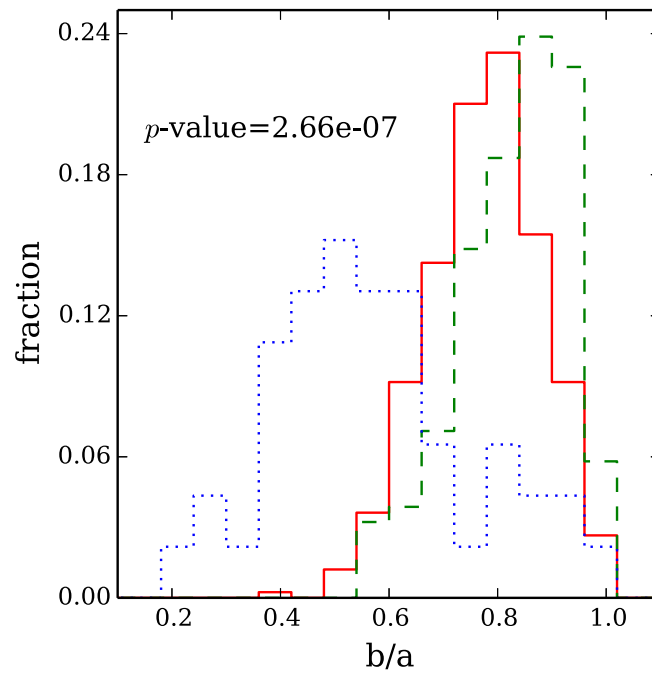
Figure 2.11: Distribution of the axis ratio (b/a) from single Sérsic fits for the BCGs divided by morphology. The red solid line corresponds to cD galaxies, the green dashed line to ellipticals, and the blue dotted line to spirals and S0s. The p-value is derived from two-sample Kolmogorov-Smirnov tests, indicating the significance of the observed differences between the cD and elliptical BCG parameter distributions. Elliptical BCGs tend to have a more spheroidal shape than cD galaxies.
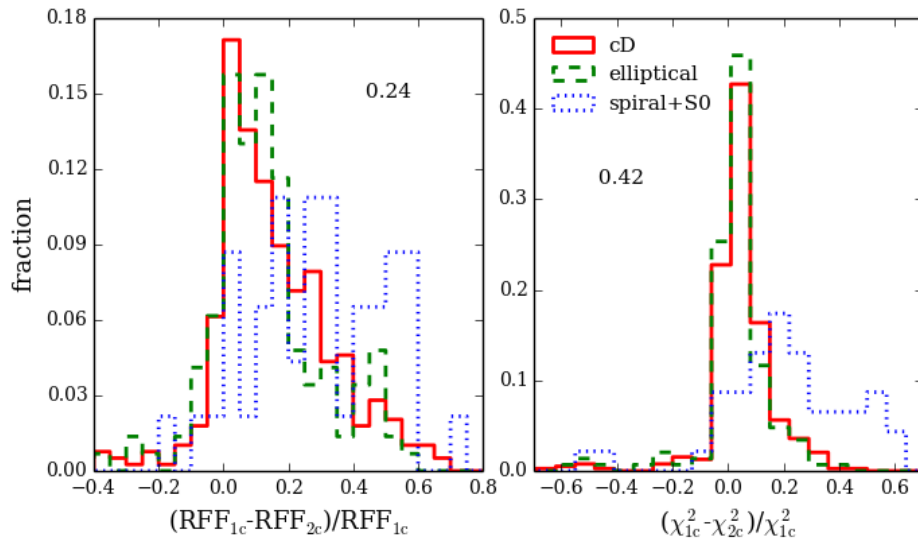
Figure 2.12: Comparison of the residuals between single Sérsic and Sérsic+Exponential models. The left panel shows the fractional differences in *RFF* obtained with two-component and one-component fits for cD (red solid line), elliptical (green dashed line), and disk (blue dotted line) BCGs. The right panel shows the corresponding fractional differences for χ^2_ν.

Graham & Jerjen (2007) and Donzelli, Muriel & Madrid (2011), we explore here how a model consisting of an inner Sérsic profile and an outer exponential envelope performs when fitting BCG images. The fitting process was described in detail in Section 2.3.3.

As shown in Section 2.3.5, both *RFF* and χ^2_ν can provide quantitative information to assess whether BCGs are better fitted by a two-component model than by a one-component model, at least in very clear cases. Fig. 2.12 shows a comparison of these parameters obtained for single Sérsic and Sérsic+Exponential models. In the left panel we show a histogram of the fractional differences in the *RFF* values ($RFF_{1c} - RFF_{2c})/RFF_{1c}$ for all three BCG types, where RFF_{2c} denotes *RFF* for two-component (Sérsic+Exponential) models. The right panel shows the corresponding χ^2_ν fractional differences $(\chi^2_{\nu,1c} - \chi^2_{\nu,2c})/\chi^2_{\nu,1c}$. It is clear that for disk BCGs, the Sérsic+Exponential model does a better job. This is not surprising since spiral and lenticular galaxies contain clearly distinct bulges and disks. For elliptical BCGs the improvement in *RFF* and χ^2_ν for two-component models is generally quite small, as expected: elliptical galaxies are known to be reasonably well fitted by Sérsic models, so the extra component does not improve the residuals significantly. Perhaps surprisingly, the improvement is also only marginally better for cDs: the typical fractional differences for cD galaxies are $(RFF_{1c} - RFF_{2c})/RFF_{1c} = 0.11^{+0.14}_{-0.08}$ and $(\chi^2_{\nu,1c} - \chi^2_{\nu,2c})/\chi^2_{\nu,1c} = 0.035^{+0.053}_{-0.029}$ (median $+/-$ 1st and 3rd quartiles of the parameter distributions). We checked that consistent results are obtained if we use Sérsic+Sérsic model fits instead of Sérsic+Exponential ones: no clear improvement in *RFF* or χ^2_ν is found for cD galaxies in this case either.

Since the distributions shown in Fig. 2.12 for ellipticals and cDs are statistically indistinguishable, there is no clear separation that could be used to distinguish elliptical and cD BCGs by comparing one-component and two-component fits. Moreover, on average, Sérsic+Exponential model (also Sérsic+Sérsic model) does not fit the profile of cD BCGs clearly better than single Sérsic model, implying that the light profiles of cD galaxies might be more complex and one model might not be good enough to represent all their profiles. Since there is no clear improvement in the two-component model, the model with the smallest number of parameters (i.e., single Sérsic model) will be preferred for simplicity. The following discussions are based on the results from the single Sérsic fits.

2.4.4 Summary of Section 2.4

In this section we have analysed the differences in the structural properties of BCGs as a function of morphology. These structural parameters have been derived from one-component (Sérsic) and two-component (Sérsic+Exponential) model fits. Disk BCGs (a small minority) have smaller Sérsic indices (n) than elliptical and cD BCGs, as expected. They also have different, generally broader, distributions of RFF and χ_ν^2. Elliptical and cD BCGs have similar n values, but cDs tend to have larger values of $R_{\rm e}$, RFF and χ_ν^2. These differences do not depend strongly on whether we use one- or two-component models.

The observed structural differences could provide quantitative ways to separate elliptical and cD BCGs without relying on visual inspection. We explore these in section 2.5. Furthermore, the differences we have found in the structural parameters suggest that the formation histories of elliptical and cD BCGs may be different. For instance, gas-rich major mergers and other dissipative processes may be responsible for building the inner (Sérsic-like) component, while dissipationless minor mergers may contribute to the build-up of the outer extended envelope and to the growth of galaxy sizes (e.g., Oser *et al.* 2010; Johansson, Naab & Ostriker 2012; Huang *et al.* 2013). We will explore in Chapter 3 whether the morphological and structural properties of BCGs are linked to other intrinsic BCG properties such as their stellar mass, and/or to the properties of their environment. These links will provide more clues to the formation history of cDs/BCGs.

2.5 Separating cD BCGs from non-cD BCGs

The results of Section 2.4.2 suggest that we may be able to use the different distributions of cD and non-cD BCGs on the $\log R_{\rm e}$–$\log RFF_{\rm 1c}$ plane to separate them in an objective, quantitative and automatic way. Fig. 2.13 shows that cDs are clearly segregated from other BCGs in this two-dimensional parameter space. We attempt to find a robust, well-defined way to separate, statistically, cD and non-cD BCGs using the information provided by this diagram. In other words, we suppose to find an "optimal border" that can separate them.

2.5.1 Method Description and the Optimal Border

Ideally, any process that selects cD galaxies from a sample of BCGs needs to have high completeness (i.e., select as many of the cDs present in the sample as possible), while avoiding contamination from non-cDs (i.e., maximising the purity of the sample). These two requirements compete with each other, and increasing completeness often results in a decrease in sample purity, and vice-versa. We need therefore to find the best compromise between these competing requirements. In general, the optimal solution will depend on the specific intent for the selected sample, and therefore on the decision of how much weight to give to completeness and to purity. It is useful to define a measurement on the quality of the selection method that combines both requirements in a well-defined way. The optimal solution will then be obtained by maximising this quality parameter.

Following Hoyos *et al.* (2012) the *sensitivity*, which is often known as *completeness* in astronomy, is defined as:

$$r = \frac{\#\text{TruePositives}}{\#\text{TruePositives} + \#\text{FalseNegatives}}.$$ (2.3)

Similarly, we define *specificity* as:

$$p = \frac{\#\text{TrueNegatives}}{\#\text{TrueNegatives} + \#\text{FalsePositives}}.$$ (2.4)

A "True Positive" is an object retrieved by the selection process with the required properties (i.e., a cD galaxy that is correctly selected as such). A "False Negative" is an item that is not retrieved by the selection process but does present the needed properties (a cD galaxy that is not selected). A "True Negative" is an item that is rightfully rejected by the selection process since it does not have the required properties (for instance, an elliptical galaxy that is not selected as a cD). A "False Positive" is an item that is incorrectly picked up by the selection process, but does not have the properties of interest (for example, an elliptical galaxy that is wrongly selected as a cD).

Sensitivity and *specificity* can be combined into a single number, known as the *F*-score (van Rijsbergen 1979), which provides a single measure on the quality of the selection

process. The general formula of *F*-score considers both the sensitivity and specificity of the selection to compute the score as a weighted harmonic average of r and p,

$$F_\beta = \frac{(1 + \beta^2) \times p \times r}{\beta^2 \times p + r},\tag{2.5}$$

where β is a control parameter that regulates the relative importance of completeness with respect to specificity. F_β measures the effectiveness of retrieval with respect to a user who attaches β times as much importance to sensitivity r as specificity p. β is a user-supplied value that depends on the particular goals of the study. We will explore later how the choice of β affects our selecting results. At this stage, a value of $\beta = 1.25$ is used, which can be thought of as weighing completeness more than the lack of contamination. For our BCG samples, the *F*-score is used to grade the performance of the diagnostics we use when separating cD galaxies from the parent population.

The selection process that we will apply to the parent population of BCGs in order to select cD galaxies will be defined by a "border" in the $\log R_\mathrm{e}$–$\log RFF_\mathrm{1c}$ plane (see Fig. 2.13). This border will be represented by a second-order polynomial in the horizontal coordinate. Higher-order polynomials (or more conplex functions) could be used, but the additional complexity is not required here. In our specific problem, the cD galaxies play the role of the "items presenting the required properties" discussed above, and the parent population is the complete sample of BCGs.

According to the definition of *sensitivity* and *specificity*, the BCGs in the parent sample are classified into four categories by their position relative to the border. In the $\log R_\mathrm{e}$–$\log RFF_\mathrm{1c}$ plane, cD galaxies dominate the region of large R_e and RFF_1c. We therefore define this region as the "cD side". Thus

- cD galaxies that fall on the cD side of the border are True Positives.

- cD galaxies that do not fall on the cD side of the border are called False Negatives.

- elliptical and disk (spiral and S0) BCGs that fall on the cD side are regarded as False Positives.

- elliptical and disk (spiral and S0) BCGs that do not fall on the cD side of the border are True Negatives.

The optimal border is found by maximising the *F*-score value. Following the method described in Hoyos *et al.* (2012), we use the Amoeba algorithm (Press & Spergel, 1988) to carry out this maximization and find the polynomial defining the border.

It is clear from Fig. 2.13 that the selected galaxy sample on the cD side of the optimal border will not contain only cD galaxies, and a degree of contamination will be present. We define contamination (Hoyos *et al.*, 2012) as:

$$C = \frac{\#\text{non-cDs tested as positive}}{\#\text{all positives}}. \tag{2.6}$$

The numerator are the non-cD BCGs which are on the cD side of the optimal border. The denominator of this fraction includes both cD galaxies and non-cD BCGs on the cD side.

Fig. 2.13 shows the $\log R_e$–$\log RFF_{1c}$ plane for the BCGs in our sample. The Amoeba algorithm requires a first guess for the border, shown by the black horizontal dotted line. The optimal border determined by the algorithm does not depend on the exact initial guess. The blue solid curve is the optimal border determined when we consider all cD galaxies (cD, cD/E and cD/S0) as cD galaxies. This border, computed using $\beta = 1.25$, has an *F*-score $= 0.69$. 75% of all the cD galaxies are above the border ($r = 0.75$), and thus selected from the parent sample. The remaining 25% are mixed with the elliptical and disk BCGs in the region below the border. This selection therefore yields 75% completeness. The galaxy sample above the border contains 311 cD galaxies and 79 non-cD BCGs resulting in a $\sim 20\%$ contamination in the selected cD samples. In the region below the border there are 103 cD galaxies and 122 and non-cD BCGs. Thus, the non-cD BGC sample has a contamination of 46% from cD galaxies. This indicates that this technique is more effective (cleaner) at selecting cD galaxies than at selecting non-cD BCGs.

Note that if we consider a "cleaner" sample that contains only pure cD and pure elliptical BCGs (excluding all cD/E, cD/S0, E/cD, E/S0, spiral and S0 BCGs), the optimal border (blue dashed curve in Fig. 2.13) does not change significantly, but the quality
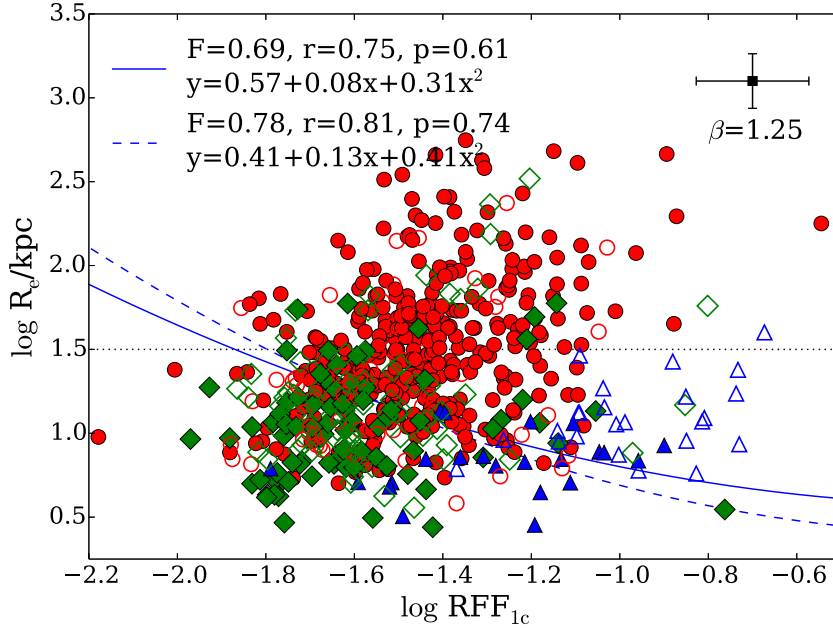
Figure 2.13: $\log R_e$ vs. $\log RFF_{1c}$ for the BCGs in our sample. We use this diagram to find the optimal border to separate cD from non-cD BCGs. The symbols are the same as in Fig. 2.5. The black dotted line is the "first guess" for the border. The blue solid curve is the optimal border determined when we consider all cD BCGs (cD, cD/E and cD/S0) as cD galaxies. The blue dashed curve is the optimal border determined when we consider only pure cD and pure elliptical BCGs (excluding all cD/E, cD/S0, E/cD, E/S0, spiral and S0 BCGs). The legend shows the maximum F-score for the optimal borders and the corresponding completeness r and specificity p. The equations defining the optimal borders are also shown. The error bar shows the mean error of each parameter. We used $\beta = 1.25$ in this case.
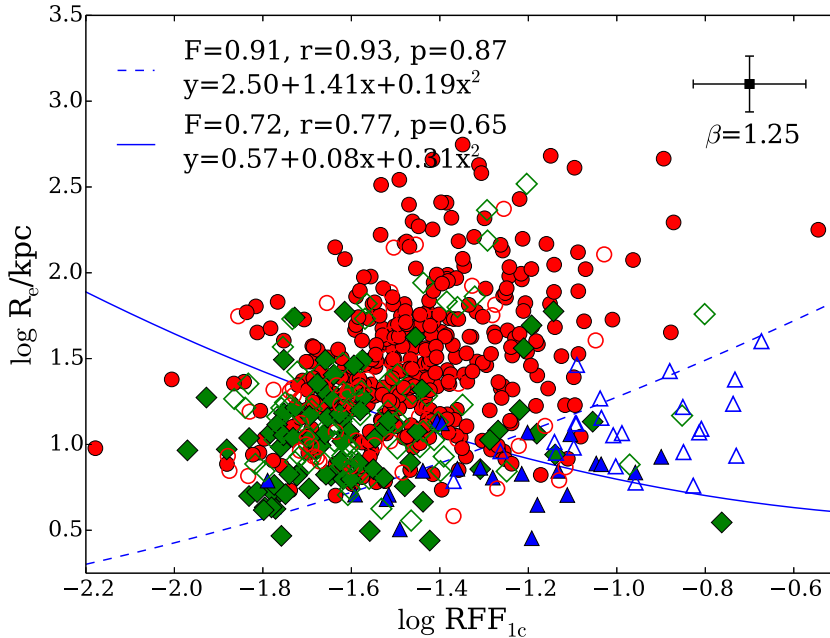
Figure 2.14: Two-step process to select cD BCGs. Symbols and legend are the same as in Fig. 2.13. Disk (spiral and S0) BCGs are separated from non-disk BCGs (cDs and ellipticals) first using the optimal border shown as the blue dashed curve. cD galaxies are then selected using the optimal border shown as the blue solid curve. See text for details.

of the selection as determined by the *F*-score value, the completeness r and the specificity p improves. This is not surprising: the identification of BCGs as pure cDs/Es (as opposed to the "dubious" ones) depends on more secure morphological characteristics which should be linked more clearly to the structural parameters. However, considering only this cleaner sample is not a realistic scenario since in practical cases we would like to start from a full sample of BCGs and find which ones are cDs. Nevertheless, it is reassuring that the border we determine does not depend very strongly on the exact training set used.

On the selected cD side, spiral BCGs are an important source of contamination. However, since most of them appear in the large RFF_{1c} region, it would be possible to go a step further to implement a simple further refinement in our method to separate spirals from the selected cDs: very few cD galaxies have $\log RFF_{1c}$ larger than ~ -1.1. This would significantly improve the purity of the cD sample at very little cost in terms of its completeness.

Moreover, it is clear from Fig. 2.13 that all disk BCGs (spirals and S0s) contribute significantly to the contamination of either the cD or the elliptical samples separated by the best border. However, we can use the fact that disk BCGs distribute over a distinct area on the $\log R_{e}$–$\log RFF_{1c}$ plane to apply a two-step process to exclude them from our cD selection. First, the disk BCGs can be separated from the elliptical and cD BCGs, and then the cD BCGs can be selected out of the rest BCG sample. Fig. 2.14 illustrates the results of this two-step selection. The blue dashed curve is the optimal border determined in the the first step. By excluding disk BCGs using this border, a very complete ($r = 0.93$) and pure ($p = 0.87$) non-disk BCG sample is built. The cDs can then be separated from the ellipticals using the optimal border shown by the blue solid curve with a completeness of 77% (305 cDs are selected), and a contamination of only 14%. Compared to the single-step cD selection (311 cDs were selected with 20% contamination), the two-step process clearly selects a very similar number of cDs but with better purity. The decision on whether the increase in purity is worth the additional complexity is left to the reader. In the reminder of this chapter we will use the single-step selection process for simplicity.

The automatic techniques we have developed can be applied to any BCG sample, but

the optimal border needs to be adapted and calibrated using the imaging data from which the parent sample was derived. The calibration can be performed using a sub-sample of visually-classified BCGs, and then automatically applied to the complete sample using the structural parameters determined from standard single-Sérsic fits.

A β value needs to be chosen depending on whether we are more interested in the completeness of the cD sample or in its purity, but we suggest that $\beta = 1.25$ represents a reasonable compromise (see section 2.5.3). Furthermore, it is important to remember that this method works better at selecting a sample of cD galaxies rather than a sample of non-cDs.

2.5.2 Distance to the Optimal Border

It is informative to explore the distribution of the points in the $\log R_{\mathrm{e}}$–$\log RFF_{1\mathrm{c}}$ plane (Fig. 2.13) in terms of their minimum (perpendicular) distance to the optimal border. We define the distance from each point to the optimal border as

$$D = \sqrt{\left(\frac{\Delta \log RFF_{1\mathrm{c}}}{\sigma_{\log RFF_{1\mathrm{c}}}}\right)^2 + \left(\frac{\Delta \log R_{\mathrm{e}}}{\sigma_{\log R_{\mathrm{e}}}}\right)^2}, \tag{2.7}$$

where $\Delta \log RFF_{1\mathrm{c}}$ is the difference in $\log RFF_{1\mathrm{c}}$ between the data point and the optimal border, and $\sigma_{\log RFF_{1\mathrm{c}}}$ is the dispersion in $\log RFF_{1\mathrm{c}}$ computed for all the points. $\Delta \log R_{\mathrm{e}}$ and $\sigma_{\log R_{\mathrm{e}}}$ have a similar meaning but for $\log R_{\mathrm{e}}$. Note that, because the units of the x and y axes are different, the distance is measured in units of the scatter of each parameter. For each point, the minimum distance D_{min} can be then determined. Fig. 2.15 shows the distribution of these minimum distances for the different morphologies. As expected, the vast majority ($> 80\%$) of the cDs show positive distances (they are above the optimal border line) while most of the ellipticals have negative ones. Under 20% of the cDs spill over to the negative region, severely contaminating the non-cD sample, while a few ellipticals weakly contaminate the cD region. The measurement errors in $\log R_{\mathrm{e}}$ (~ 0.16) and $\log RFF_{1\mathrm{c}}$ (~ 0.13) result in distance errors on the order of 0.7 in this metric. This contributes to the cDs' "spillover", but does not completely explain it. Reducing the measurement errors would certainly improve the performance of our method, but it would never make it perfect.
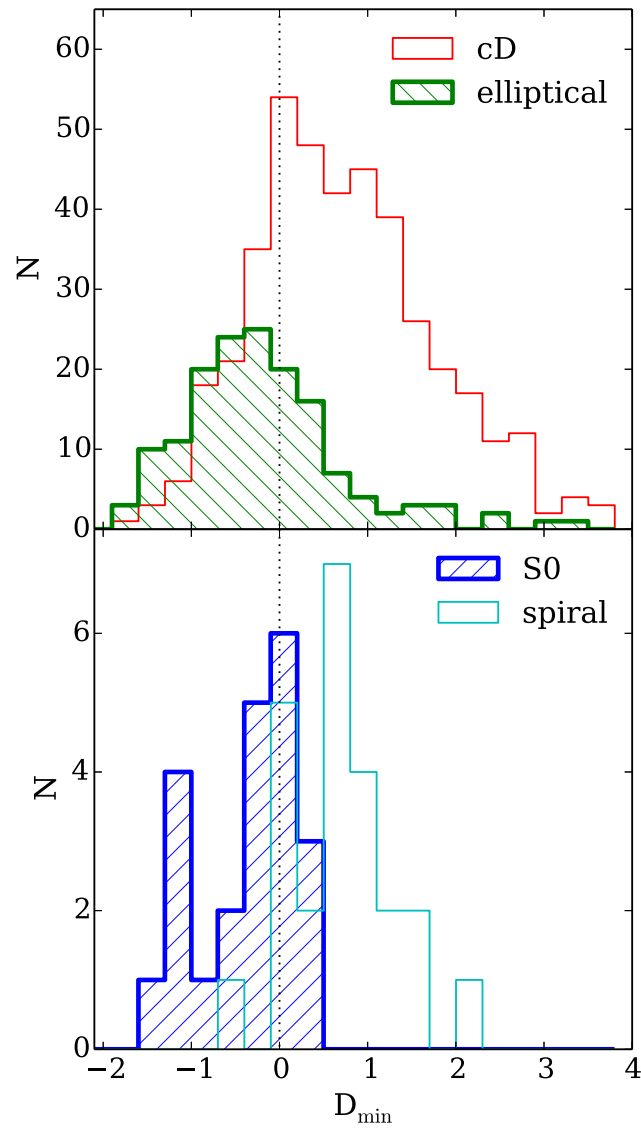
Figure 2.15: Distribution of the minimum distances to the optimal border shown in Fig. 2.13 for the cD and elliptical BCGs (top panel) and the spiral and S0 BCGs (bottom panel). Positive and negative distances correspond to points above and below the optimal border line respectively.
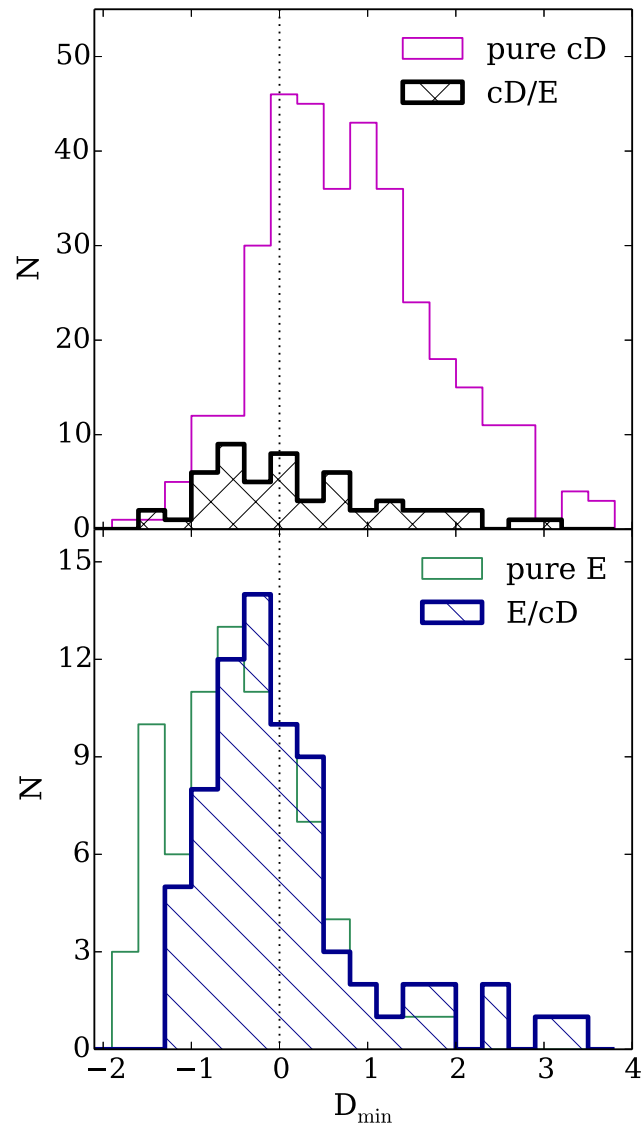
Figure 2.16: Distribution of the minimum distances to the optimal border shown in Fig. 2.13 for the pure cD BCGs and cD/E BCGs (top panel). The bottom panel shows the corresponding histograms for pure E BCGs and E/cD BCGs.

Interestingly, the spiral and S0 BCGs are quite well separated: the former show mostly positive distances while the later have mostly negative ones. This is mainly due to spirals having generally larger RFF_{1c} values because the spiral arms and star-forming regions are not included in the Sérsic models, while the S0s are smoother. This clear separation provides a possible way to separate spiral and S0 galaxies, but this needs to be further tested with large disk samples.

Another interesting result is that BCGs classified as pure and uncertain cDs (e.g., cD/E) have very different minimum distance distributions (Fig. 2.16, top panel). About half of the cD/E BCGs have negative distances (i.e., are on the wrong side of the border), but only $\simeq 20\%$ of the pure cDs do. Most of the spillover of the pure cDs into the negative region, however, can be explained by the measurement errors. It should be noticed that the difficulties inherit in the visual morphological classification are directly reflected in the structural parameters: when the visual classifier is certain that a BCG is a cD, its structural parameters almost always confirm it, while in uncertain cases (e.g., cD/E) the structural parameters reflect this uncertainty. Similar conclusions can also be obtained from the pure elliptical BCGs and uncertain ones (e.g., E/cD), as shown in the bottom panel of Fig. 2.16.

This analysis confirms the visual impression in terms of the BCG structure that there is a continuous distribution in the properties of the BCG extended envelopes, ranging from undetected (pure E class) to clearly detected (pure cD class), with the intermediate classes (E/cD and cD/E) showing increasing degrees of envelope presence. This continuous distribution in envelope detectability is reflected quantitatively in the structural parameters of the BCGs, by the minimum distance to the optimal border providing some indication of the relative importance of the envelope.

Our results from the visual classification and structure analysis confirm that there is a spectrum in the BCG envelope strength. Although, for convenience, our analysis often splits the majority of our BCGs into two separate populations (cDs and Es), we still consider that there are intermediate classes in each population in order to reflect the spectrum of BCG envelopes. Moreover, since in many ways cDs are the most interesting and special BCGs, the main purpose of our best-border method is to automatically select cD galaxies out of the parent sample in a way that is as complete and pure as we

possibly can. Although we cannot select a 100% pure cD sample due to the existence of a continuous envelope spectrum, the results presented in Section 2.5.1 show that the contamination in our selected cD sample is relatively low.

2.5.3   Effect of the β Parameter

In the F-score definition, the β parameter is used to apportion weight to the completeness and the specificity. For larger values of β the completeness is given a larger weight than the lack of contamination. Conversely, smaller values of β prioritise lack of contamination above completeness. To test how changing β affects the results of the selection process, we repeat the exercise carried out in Section 2.5.1 but using $\beta = 2.0$ and $\beta = 0.5$ in the determination of the optimal border.

Fig. 2.17 shows the optimal border for $\beta = 2.0$ (upper panel) and $\beta = 0.5$ (lower panel). It is clear that the β parameter has a decisive impact on the selection of potential cD galaxies. As shown in the upper panel, when compared to the $\beta = 1.25$ results, 11% more galaxies are correctly identified as cDs, significantly increasing the completeness. The price paid is that the specificity goes down from 61% to 46% since more non-cD BCGs are included. Conversely, in the lower panel ($\beta = 0.5$) the selected cD sample is purer ($p = 0.85$), but at the expense of completeness, with 20% fewer cD galaxies selected when compared with the $\beta = 1.25$ result.

With $\beta = 2.0$, the contamination of the cD sample by non-cDs is 23%, while the contamination of the non-cD sample by cDs is 39%. With $\beta = 0.5$, the corresponding values are 12% and 52% respectively. Therefore, for any value of β this selecting technique is cleaner and more effective at selecting cD galaxies than at selecting non-cD BCGs.

As before, if we consider a cleaner sample that contains only pure cD and pure elliptical BCGs, the optimal border (blue dashed curve) does not change significantly, but the F-score value, the completeness r and the specificity p improve. However, we have argued that this does not represent a realistic scenario.

We conclude that $\beta = 1.25$ represents a good compromise, as its optimal border picks up a cD galaxy sample reasonably complete, and with relatively small contamination.
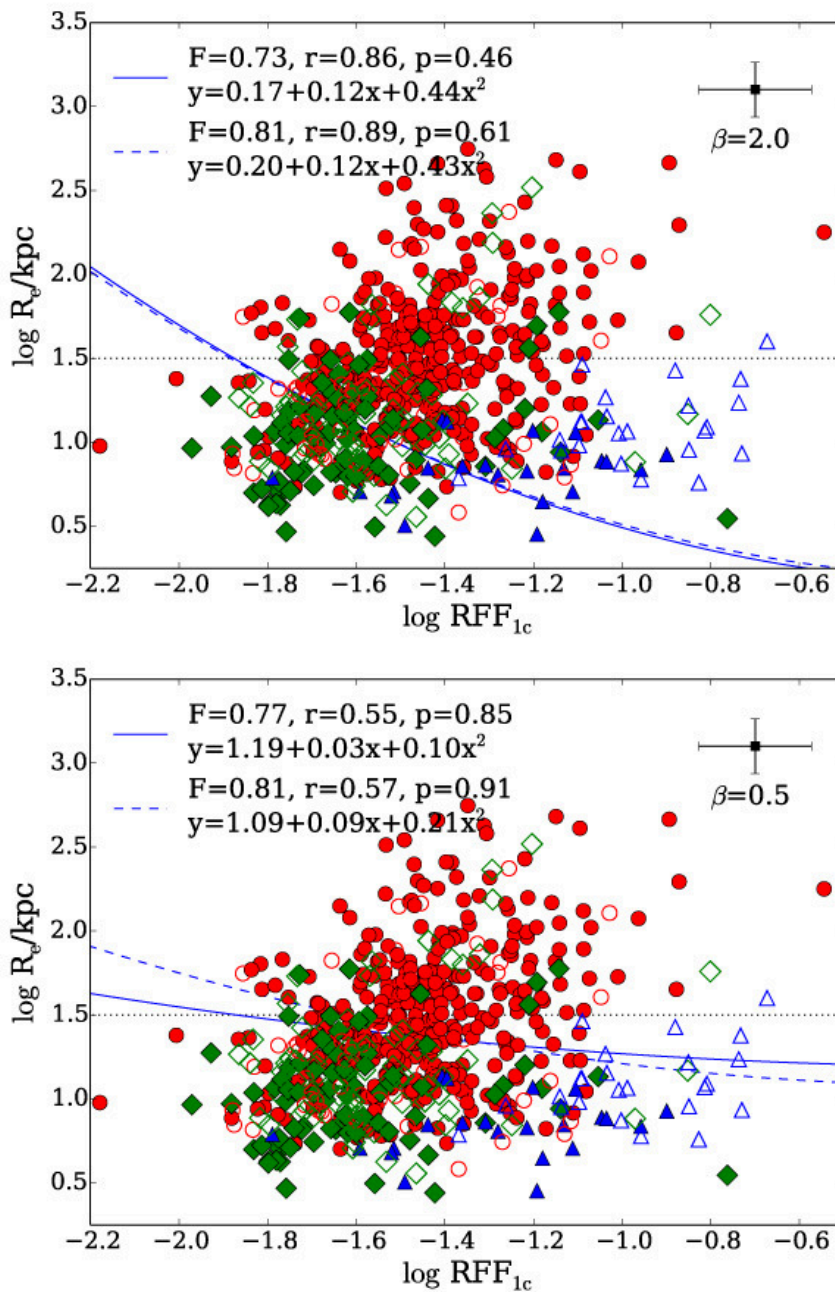
Figure 2.17: Illustration of the effect of β on the optimal border. The symbols, lines and legends have the same meaning as in Fig. 2.13 but we use $\beta = 2.0$ for the upper panel and $\beta = 0.5$ for the lower panel. With $\beta = 2.0$ we give more weight to the completeness than to the lack of contamination. When using $\beta = 0.5$, the lack of contamination is given more importance than achieving higher completeness. The choice on β depends on the aims of the specific research.

However, no single value of β can be considered to be "correct" and needs to be set according to the scientific goals of the study.

2.6 Conclusions

In this chapter we have analysed a well-defined sample of 625 low-redshift Brightest Cluster Galaxies published in von der Linden *et al.* (2007) with the aim of linking their morphologies to their structural properties. We morphologically classified the BCGs using SDSS r-band images and found that over half of them ($\sim 57\%$) are pure cD galaxies and pure elliptical BCGs constitute $\sim 13\%$ of the sample. The intermediate classes (mostly cD/E or E/cD) account for $\sim 21\%$. This suggests a continuous distribution in the properties of the BCG extended envelopes, ranging from undetected (pure E class) to clearly detected (pure cD class), with the intermediate classes (E/cD and cD/E) showing increasing degrees of envelope presence. We found this continuous distribution in envelope detectability is reflected quantitatively in the structural parameters of the BCGs. There is also a minority of BCGs that are neither cD nor elliptical. About 7% are disk galaxies (spirals and S0s, in similar proportions) and the rest ($\sim 2\%$) are in merging.

In order to link the morphologies of the BCGs to their structural properties, we have fitted the BCG's light distributions with the SDSS r-band images using one-component (Sérsic) and two-component (Sérsic+Exponential) models. We first characterised how well the models fit the target BCG by using two quantitative diagnostics. One diagnostic is the residual flux fraction (*RFF*), which measures the fraction of the galaxy flux present in the residual images after subtracting the models. The other diagnostic is the reduced χ_ν^2. We concluded that generally it is very difficult to find a robust diagnostic to decide, in a statistic way, whether a one-component or a two-component model is preferred for BCGs, especially for cD galaxies. Since there is no evident improvement by using two-component model fits, our other conclusions rely on the one-component Sérsic fits.

From simple one-component Sérsic profile fits, we have found a clear link between the BCGs morphologies and their structures, and claimed that a combination of the best-fit

parameters can be used to separate cD galaxies from non-cD BCGs. In particular, cDs and non-cDs show very different distributions in the $R_{\rm e}$–$RFF_{\rm 1c}$ plane, where $R_{\rm e}$ is the effective radius and $RFF_{\rm 1c}$ is the residual flux fraction, both determined from Sérsic fits. cDs have, generally, larger $R_{\rm e}$ and $RFF_{\rm 1c}$ values than ellipticals. Therefore we found, in a statistically robust way, a boundary to separate cD and non-cD BCGs in this parameter space. BCGs with cD morphology can be selected with reasonably high completeness ($\sim 75\%$) and low contamination ($\sim 20\%$).

This automatic and objective technique can be applied to any current or future BCG samples which have good quality images. The method needs to be adapted and calibrated using the imaging data from which the parent sample was derived. Once calibrated with a representative sub-sample of visually-classified BCGs, this technique can be applied to the complete sample using the structural parameters determined from standard single-Sérsic fits.

In Chapter 3 we will explore how the morphological and structural properties of BCGs are linked to other intrinsic BCG properties such as their stellar mass, and/or to the properties of their environments. These links will provide more clues to the formation history of cDs/BCGs.

Chapter 3

Evolution of the Brightest Cluster Galaxies: the influence of morphology, stellar mass and environment

The entirety of this chapter is published in Zhao, Aragón-Salamanca & Conselice (2015b).

3.1   Introduction

The brightest cluster galaxies (BCGs) are the most luminous and massive galaxies in the universe. They are found at the centres of galaxy clusters and groups, and exhibit many unique properties (see, e.g., Tonry 1987; Kormendy & Djorgovski 1989; Jordán *et al.* 2004; L07). Their origin and evolution is intimately linked with the evolution of their host clusters, and therefore can provide direct information on the formation and history of large-scale structures in universe (Conroy, Wechsler & Kravtsov 2007).

Many scenarios have been proposed to explain the formation and evolution of BCGs. One of them is galactic cannibalism (White, 1976; Ostriker & Hausman, 1977; Garijo, Athanassoula & Garcia-Gomez, 1997), where BCGs were formed as a result of hierarchical mergers of smaller galaxies. Other hypotheses include tidal stripping from cluster galaxies (Richstone, 1976; Merritt, 1985), and star formation in the cluster core,

where BCGs are formed through cooling flows (Fabian, 1994). Recently, numerical simulations and semi-analytic models suggest a two-phase process for BCGs formation. In these models, the stellar component of BCGs was initially formed through the collapse of cooling gas or gas-rich mergers at high redshifts; subsequently, BCGs continued to grow substantially by dissipationless processes such as dry mergers (De Lucia & Blaizot, 2007; Naab, Johansson & Ostriker, 2009; Laporte *et al.*, 2012). This inside-out formation scenario is broadly consistent with observations, avoiding the need for cooling flows to provide the cold gas that would be necessary if BCGs had formed at later times. It also overcomes the problem caused by the merger rate in clusters being too low due to the high velocity dispersion in dynamically relaxed clusters. However, some studies such as Ascaso *et al.* (2011) claimed that feedback rather than merging processes are the main mechanism affecting the evolution of the BCGs to the present epoch, ending the star formation within these systems. Therefore, many important details in the processes governing BCG formation and evolution are still unclear and deserve further investigation.

Since BCGs poses unique properties (e.g., distinct structures and morphologies, and very high stellar masses) and reside in special environments (the core of groups and clusters), studying the relationship between their properties and their environments will help to constrain the theories of BCG formation and evolution and tell us whether the intrinsic properties of BCGs or the environment play a dominant role in their history. In this context, it is important to bear in mind that, while both the location of BCGs at the bottom of the potential wells of clusters and their dominance at the massive end of the galaxy luminosity function may influence their properties, it is nonetheless very difficult to disentangle these two influences since it is hard to find equally massive non-BCGs for comparison. Therefore, when comparing BCGs and non-BCGs, differences in the mass range spanned by the samples may bias the results.

One key observational property of BCGs is that many of them show unique morphologies. The vast majority (but not all, see Chapter 2) BCGs are early-type galaxies. Most BCGs are classified as either elliptical or cD galaxies (Lauer & Postman, 1992; Fasano *et al.*, 2010; Zhao, Aragón-Salamanca & Conselice, 2015a). The defining characteristic separating these two morphological types is the presence of an extended, low-

surface-brightness stellar envelope in cDs that is absent in ellipticals (e.g. Dressler 1984; Oegerle & Hill 2001). Since cDs are not found outside the BCG galaxy population, it is very important to consider this unique galaxy class when studying BCGs. We will therefore use morphology as one of the main observables in this chapter, focusing on the different properties of elliptical and cD BCGs.

Many previous observational works usually study the BCG population as a whole, and compare it with the population of elliptical galaxies that are not BCGs (Bernardi *et al.* 2007; Lauer *et al.* 2007; L07; Liu *et al.* 2008). However, there has been some recent work exploring the structural differences between cluster ellipticals and BCGs with different morphologies. Fasano *et al.* (2010) found that, while non-BCG cluster ellipticals generally have triaxial shape with a weak preference for prolateness, BCGs are also triaxial but with a much higher tendency towards prolateness. Such a strong prolateness appears entirely due to the fact that cDs dominate the BCG population. In fact, while the shape of elliptical BCGs does not differ from other cluster ellipticals, cDs tend to have prolate shapes. Furthermore, they suggest that the prolateness of the cDs could reflect the shape of the associated dark matter haloes. In Chapter 2, we have studied in detail the morphology and structure of BCGs, demonstrating that the morphological distinction between ellipticals and cDs is accompanied by quantitative structural differences. cD BCGs generally have much larger sizes and their light profiles cannot be modelled accurately using single Sérsic functions. Conversely, elliptical BCGs are smaller and single Sérsic profiles provide better fits to their surface brightness distributions. These differences in morphology and structure suggest that cD and elliptical BCGs have followed different evolutionary paths. We investigate these possible scenarios in this chapter.

There has been a significant amount of work addressing the formation and evolution of BCGs. For example, Guo *et al.* (2009) studied how the structural parameters of central cluster galaxies correlate with their stellar masses and their host dark matter (DM) halo mass. They found that stellar mass is the dominant property dictating the shape and size of these galaxies, and suggest that the DM halo mass does not play a very significant role. Hogg *et al.* (2004), Kauffmann *et al.* (2004) and van der Wel *et al.* (2008) also reached similar conclusions. In contrast, other studies (e.g., Ascaso

et al. 2011) claimed that there is a significant correlation between the cluster mass and the properties of BCGs. Furthermore, Tovmassian & Andernach (2012) added the cluster richness to the halo/cluster mass as another environmental indicator. They found that the absolute K-band luminosity of cD galaxies (a good proxy for stellar mass) strongly depends on the cluster richness, but less strongly on the cluster velocity dispersion (a proxy for DM halo mass). Therefore, since the effects of the halo mass and the cluster richness could be different, it is necessary to take them into account as separate environmental parameters when studying BCG evolution.

Many other recent papers have studied the properties of BCGs in relation to other early-type galaxies, providing important clues to how they form and evolve. Some examples include Shankar *et al.* (2013, 2014a,b, 2015); Huertas-Company *et al.* (2013b,c); Bernardi (2009). For the sake of brevity, we will not describe their findings here but we will mention them in the following discussion when relevant.

In this chapter we use the well-defined local sample of 625 BCGs from L07 and carry out a comprehensive and systematic statistical study on the correlation between BCGs intrinsic properties (structure, morphology and stellar mass) and their environment. We consider two environmental measures, a global one (the DM cluster halo mass, characterised by its velocity dispersion) and a local one (the galaxy density). In doing so we will obtain very valuable additional information on how BCGs form and evolve.

The galaxy groups and clusters these BCGs inhabit span a very broad range of total masses, from $\sim 10^{13}\, M_\odot$ to $\sim 10^{15}\, M_\odot$. Since there is no clear boundary separating "clusters" from "groups" (although $10^{14}\, M_\odot$ could be taken as the transition mass), we will study group and cluster BCGs together. We will explore how the masses of the parent groups/clusters affect the properties and evolution of the BCGs.

This chapter is organized as follows. In Section 3.2 we introduce the BCG sample, and describe the observables we will use (morphologies, structural parameters, stellar masses, environmental densities, and DM halo virial masses). In Section 3.3 we show how the structural parameters of the BCGs relate to their stellar masses, and their global and local environment, and discuss the implications of the correlations we find on the formation of the BCG population. In Section 3.4 we go one step further and bring the galaxy morphologies into the general picture to learn about the distinct

evolutionary history of cD and elliptical BCGs. We summarise our main conclusions in Section 3.5. Throughout this chapter we have adopted the ΛCDM cosmology with $\Omega_{\mathrm{m}} = 0.3$, $\Omega_\Lambda = 0.7$, and $H_0 = 70 \, \mathrm{km \, s^{-1} \, Mpc^{-1}}$.

3.2 BCG Sample and Properties

The parent BCG sample we use in this chapter comes from the catalogue published by L07 which contains 625 BCGs residing in galaxy groups and clusters at $0.02 \leqslant z \leqslant 0.10$. See Chapter 2 for more description on this catalogue.

In Chapter 2 we also presented visual morphologies for these 625 BCGs. The BCGs were classified into three main types: 414 cD BCGs, 155 elliptical BCGs, and 46 disk BCGs. There are also 10 BCGs undergoing major mergers. The detailed description of our morphology classification can be found in Section 2.2.1. In this chapter we carry out our study on the three main types of BCGs, but not the 10 mergers. The sample therefore contains 615 BCGs.

The structural properties (Sérsic index n and effective radius R_{e}[1]) that we use in this chapter were also obtained in Chapter 2. These were derived from SDSS DR7 r-band images using two-dimensional single Sérsic (1963) model fits to the galaxies' light profiles. The detailed description of the fitting procedure and structural parameter estimation can be found in Chapter 2. The values of R_{e} and n that we obtained are broadly compatible with the ones published by Guo *et al.* (2009). However, there are some relatively minor systematic differences due to the improvements in the sky subtraction procedure implemented in Chapter 2. A direct comparison is presented in Appendix B.1.

The stellar masses we use come from "The MPA–JHU DR7 release of spectrum measurements" (see http://mpa-garching.mpg.de/SDSS/DR7/)[2]. Hereafter we call these "MPA–JHU masses". These stellar masses are obtained via spectral energy distribution (SED) fits to the DR7 photometric data using a Kroupa (2001) Initial Mass Function (IMF). More details on the stellar mass measurement can be found in Chapter 4.

---

[1] Strictly speaking, R_{e} is the effective semi-major axis of the single Sérsic model fit.

[2] In this work we use their updated stellar masses from http://home.strw.leidenuniv.nl/~jarle/SDSS/.

The number of BCGs in our sample which have MPA–JHU stellar mass information is 591, i.e., 96%. The very small minority of galaxies without stellar masses include 20 galaxies for which no spectroscopic redshift is available (essential to determine accurate distances) and 4 for which the MPA–JHU catalogue fails to provide a value for the mass, presumable because the SED fitting method does not yield a reliable solution. Since only 4% of the galaxies in the parent sample do not have stellar masses, we do not expect them to have any significant influence in our results. At this stage, and in order to ensure we have a stellar-mass-selected sample, we impose a minimum mass of $3 \times 10^{10} \, \mathrm{M_\odot}$, which reduces the sample to 535 BCGs. This limit also eliminates a few galaxies whose stellar masses, structural parameters and morphologies have larger uncertainties due to their faint magnitudes.

These MPA–JHU stellar masses are derived from SDSS Petrosian magnitudes. Petrosian magnitudes are measured by SDSS as the galaxy fluxes within a circular aperture whose radius is twice the Petrosian radius. In order to determine the Petrosian radius, SDSS first define the Petrosian ratio $R_P(r)$ at a radius r from the centre of an object to be the ratio of the local surface brightness in an annulus at r to the mean surface brightness within r. The Petrosian radius is then defined as the radius at which $R_P = 0.2$. The Petrosian flux is then defined as the flux within twice the Petrosian radius. The galaxy light profile used in the calculation of this flux is the galaxy's azimuthally averaged surface brightness profile. By definition, Petrosian magnitudes/fluxes are therefore not dependent on the fitting parameters that obtained from the single-Sérsic fits. This is important since it allows us to look for independent correlations between stellar mass and the fit parameters. Alternatively, Guo *et al.* (2009) estimated stellar masses using photometric fluxes derived from their single Sérsic fits of galaxy light profiles. Such a method results in model-dependent stellar masses, which may produce spurious correlations between the masses and the model parameters. We will discuss this in more detail in Section 3.3, and we will argue that for our study the MPA–JHU Petrosian-based stellar masses should be preferred.

The final key ingredients in our study are quantitative measurements of the environments where the BCGs reside. We will use two distinct descriptions of the environment, global and local. The "global environment" is governed by the properties of

the cluster/group that contains the BCG, and in particular its total mass (including the dark-matter halo). We use the velocity dispersion of the cluster (σ_{200}) published by L07 to estimate the halo virial mass M_{200} using the Equation 10 of Finn *et al.* (2005), which is

$$M_{200} = 1.2 \times 10^{15} \left(\frac{\sigma_{200}}{1000 \, \mathrm{km \, s^{-1}}} \right)^3$$
$$\times \frac{1}{\sqrt{\Omega_\Lambda + \Omega_0 (1+z)^3}} \, h_{100}^{-1} \, M_\odot. \tag{3.1}$$

The group and cluster sample studied here covers a broad range of masses, from $M_{200} \sim 10^{13} \, M_\odot$ to $M_{200} \sim 10^{15} \, M_\odot$, peaking at $M_{200} \sim 10^{14} \, M_\odot$ (see Fig. 3.6).

To characterise the "local environment" we use the environmental luminosity density introduced by Tempel, Tago & Liivamägi (2012). The environmental luminosity density is derived from the luminosity density field defined from a sample of galaxy groups. Tempel, Tago & Liivamägi (2012) first search for galaxy groups with a friends-of-friends method that uses a certain linking length (or neighbourhood radius) to find as many groups as possible and to ensure the group properties do not change with distance. To calculate the luminosity density field, the expected total luminosity of groups and isolated galaxies needs to be known. For each galaxy, they assume that it represents a related group of galaxies which lie outside the observational window of the survey. Therefore, the total luminosity is calculated for each galaxy but taking into account the luminosity of the unobserved galaxies. The luminosity density field is then calculated on a regular cartesian grid generated by using the SDSS angular coordinates. For each vertex, the luminosity density is calculated by a kernel sum which is a summation of the total luminosities of the galaxies within a kernel scale. Tempel, Tago & Liivamägi (2012) find the environmental density for all galaxies and groups by linearly interpolating the density field values in neighbouring vertices for the location of the galaxy or the group. The details of the calculation of the luminosity density field can be found in Tempel, Tago & Liivamägi (2012).

This is a good proxy for the environmental stellar mass density, which, as argued by Wolf *et al.* (2009), is a better and more robust measurement of the environment than galaxy number density. The main advantages of using stellar mass (or luminosity) density over galaxy number density are twofold. First, the environmental luminosity/mass

density does not depend strongly on the exact details of the galaxy sample used to define it, such as the magnitude limit, provided that it reaches significantly fainter than the "knee" of the luminosity function. And second, it represents better the strength of the interactions that a galaxy may experience from its neighbours: it is not the same to be surrounded by N faint low-mass galaxies than by N bright high-mass ones. Tempel, Tago & Liivamägi (2012) determined these environmental densities using SDSS r-band luminosities with a smoothing scale of $1\,\mathrm{h}^{-1}\mathrm{Mpc}$. The total number of BCGs in our mass-limited sample for which we have both stellar masses and environmental densities is 425. The galaxies for which environmental densities are not available are outside the footprint of the contiguous sky region covered by the work of Tempel, Tago & Liivamägi (2012), and therefore there is no reason to believe that their exclusion from our analysis will bias our conclusions. The BCG sample covers one order of magnitude in environmental density (see Fig. 3.6).

In what follows, we will consider the sample comprising the 425 $M_* > 3 \times 10^{10}\,\mathrm{M}_\odot$ BCGs with cD (275), elliptical (116), S0 (15) and spiral (19) morphologies for which we have obtained stellar masses, cluster masses and environmental densities.

3.3   Correlations between BCG Properties

In this section we analyse the correlations (or lack thereof) between the structural parameters, masses and environments (global and local) of the BCG population as a whole and discuss their implications. In Section 3.4 we will include morphology as an additional key property.

3.3.1   Stellar Masses and Structural Parameters

First we explore the relation between the BCGs structural parameters (Sérsic index n and effective radius R_e) and their stellar mass M_*. In the top panel of Fig. 3.1 we investigate whether there is a statistical correlation between the galaxies' profile shape, characterised by n, and their stellar mass. To guide the eye, we have binned the data in stellar mass bins 0.15 dex wide. The black squares with error bars show the median and
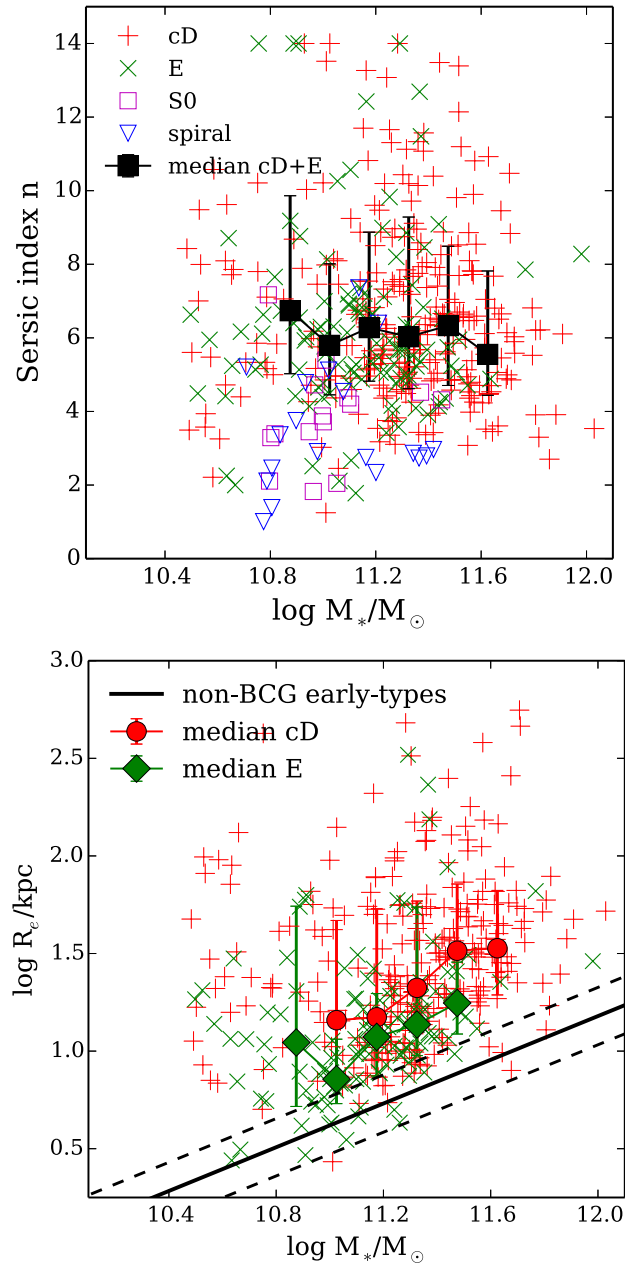
Figure 3.1: Comparison between the stellar masses and the structural parameters of the BCGs in our sample. Upper panel: Sérsic-index n vs. MPA–JHU stellar mass M_*. Lower panel: effective radius R_e vs. M_*. Red plus signs, green crosses, magenta open squares and blue open triangles correspond to cD, elliptical, S0 and spiral BCGs, respectively. Black solid squares with error bars in upper panel show the median and the 84 and 16 percentiles ($\sim 1\sigma$) of each parameter in 0.15 dex $\log M_*$ bins for the combined cD and elliptical BCGs. Red dots and green diamonds with error bars in lower panel are for cD and elliptical BCGs, respectively. Bins with fewer than 20 galaxies are excluded due to their large statistical uncertainties. The black solid line in the lower panel corresponds to the best-fit relation for the normal (non-BCG) early-type galaxy population, defined to have $n > 2.5$, from Shen *et al.* (2003). The dashed lines correspond to the 1σ scatter in this relation.

the 84 and 16 percentiles ($\sim 1\sigma$) of the n distributions for each mass bin, considering only the BCGs with cD and elliptical morphologies. In order to avoid large statistical uncertainties, we exclude bins with fewer than 20 galaxies.

We find no correlation between n and M_* for these galaxies. The median n for the elliptical and cD BCGs is 6.02, which indicates that, on average, these galaxies have both centrally-concentrated light profiles and extended envelopes, as expected for a population dominated by cDs (see Chapter 2 and references therein). Interestingly, as Chapter 2 pointed out, there is little separation between the n distributions of cD and elliptical galaxies. A Kolmogorov-Smirnov test indicates that the difference is only significant at the 2σ level. The median Sérsic index n is $6.12^{+2.76}_{-1.63}$ for cDs and $5.86^{+2.31}_{-1.42}$ for ellipticals[3]. The slightly larger median n value of the cD galaxies is driven by their extended envelope. As expected, disk BCGs (spirals and S0s) have significantly lower n values (2.91 and 3.88 respectively).

The lack of correlation between n and M_* for the BCGs in our sample contrasts with the findings of Guo *et al.* (2009), who claimed a clear positive correlation in the sense that more massive BCGs seem to have higher values of n. As we show in Appendix B.2, we believe this may be due to the fact that Guo *et al.* (2009) estimated stellar masses from total luminosities derived from single Sérsic model fits. These luminosities (and the derived stellar masses) depend on the value of n, and this dependency could drive an artificial correlation.

As an aside, we note that in the upper panel of Fig. 3.1 there is a small number of cD and elliptical BCGs whose n is quite large ($n > 12$). It is important to realise that for large n ($n > 6$ or so) very small changes in the light profile result in large changes in n, and thus all values of n above ~ 6 correspond essentially to the same profile. Furthermore, a visual inspection of the fits and the residuals indicate that these large n objects are usually surrounded by multiple close bright companions (or, in a few cases, a bright nearby star). This makes the fits less reliable. Furthermore, some of these objects have double cores, and therefore a single Sérsic profile is not a good model of their surface brightness distribution. In these cases, the derived model parameters should be taken with caution. Since the fraction of affected objects is quite small,

---

[3]The errors quoted for median values correspond to the 84 and 16 percentiles of the distributions ($\sim 1\sigma$ scatter).

they do not affect the statistical conclusions of this study. Removing them would have no significant statistical effect, and they are therefore kept in our analysis for completeness. Another reason for this that the high n systems are distributed over all stellar masses, and not just found within the high or low stellar mass systems.

We examine now the relationship between the effective radius R_e and the stellar mass of the BCGs shown in the lower panel of Fig. 3.1. For comparison, we show the relation found for normal non-BCG early-type galaxies by Shen *et al.* (2003) selected from the SDSS survey as system with $n > 2.5$. The sizes and stellar masses published by Shen *et al.* (2003) are directly comparable to the ones we use. Their effective radii are computed from single Sérsic fits to SDSS images, like ours, and their stellar masses are also derived using the method of Kauffmann *et al.* (2003). Note that the Shen *et al.* (2003) sample is dominated by field galaxies, although we will see below that similar conclusions are obtained for cluster early-types.

The effective radii of early-type BCGs is strongly correlated with their stellar masses: on average, R_e increases when M_* increases, but the scatter is large (about ~ 0.3 dex, or a factor of ~ 2 in R_e at a given mass). In agreement with Bernardi (2009), we find that almost all the BCGs are above the average relation for non-BCG early types, and the slope is similar (within a large uncertainty). The scatter is also larger for the BCGs than for the other early-type galaxies. Notwithstanding this large scatter, the median radius of BCGs is about twice as large as that of non-BCG early types of similar masses. This difference is largely due to the cD galaxies, which dominate the sample. As shown in the lower panel of Fig. 3.1, when we analyse the properties of BCGs separated by morphology, elliptical BCGs are, on average, significantly smaller than cDs. The minority of BCGs that have disk (spiral and S0) morphologies tend to populate the low end of the size distribution.

Fig. 3.1 also shows that the BCGs in our sample span a very broad range of stellar masses ($10^{10.5}$–$10^{12} M_\odot$). This is mainly due to the fact that these BCGs are hosted by galaxy groups and clusters with very different masses (Fig. 3.6), combined with the weak correlation between the galaxies' stellar masses and M_{200} (Fig. 3.4). Nevertheless, it is clear that at all stellar masses BCGs have larger radii than non-BCG early-type galaxies. This agrees with the findings of Valentinuzzi *et al.* (2010) and

Vulcani *et al.* (2014) for low-redshift BCG and non-BCG galaxies in the clusters of WIde-field Nearby Galaxy-cluster Survey (WINGS; see their Fig. 11). Although a detailed quantitative comparison is very difficult given the differences in methodology combined with the fact the the WINGS sample does not include groups, it is reassuring to see that compatible results are obtained independently. Note also that the stellar masses of the WINGS BCGs are all in the range 10^{11}–$10^{12}\,M_{\odot}$, where most of our BCGs lie, but we also have BCGs with lower stellar masses since our sample includes both clusters and groups.

3.3.2 Local Environment: the Effect of Galaxy Density

We explore now the relationship between the local environment that BCGs inhabit and their intrinsic properties (structural parameters and stellar masses). As discussed in Section 3.2, we use the environmental luminosity density of Tempel, Tago & Liivamägi (2012) to characterise the local environment. In the three panels of Fig. 3.2 we plot the Sérsic index n, the effective radius $R_{\rm e}$, and the MPA–JHU stellar mass M_* vs. this density. The left panel shows that there is no correlation between n and density (Pearson correlation coefficient 0.03). However, both $R_{\rm e}$ and M_* clearly correlate, on average, with density (correlation coefficients 0.32 and 0.49 respectively). Although there is significant scatter, larger and more massive BCGs tend to inhabit denser environments.

It appears that local density correlates with both the size and the stellar mass of the early-type BCGs. However, Fig. 3.1 shows that $R_{\rm e}$ correlates with M_*. It is therefore important to ascertain which of these two parameters is the intrinsic driver of the correlations with density. To do this, in the left panel of Fig. 3.3 we plot $R_{\rm e}$ vs. M_* binning the galaxies by density. We only include cD and elliptical BCGs. For a given stellar mass, the median $R_{\rm e}$ is the same for all densities. This suggests that density does not affect BCG size directly, but only through its dependence with stellar mass. In the right panel of this figure we show the M_*–density relation again, but now binning the galaxies by radius. For galaxies of all sizes, there is a clear correlation between stellar mass and environment: more massive BCGs tend to inhabit denser regions, regardless of their radius. This implies that the stellar mass–density correlation is the more funda-
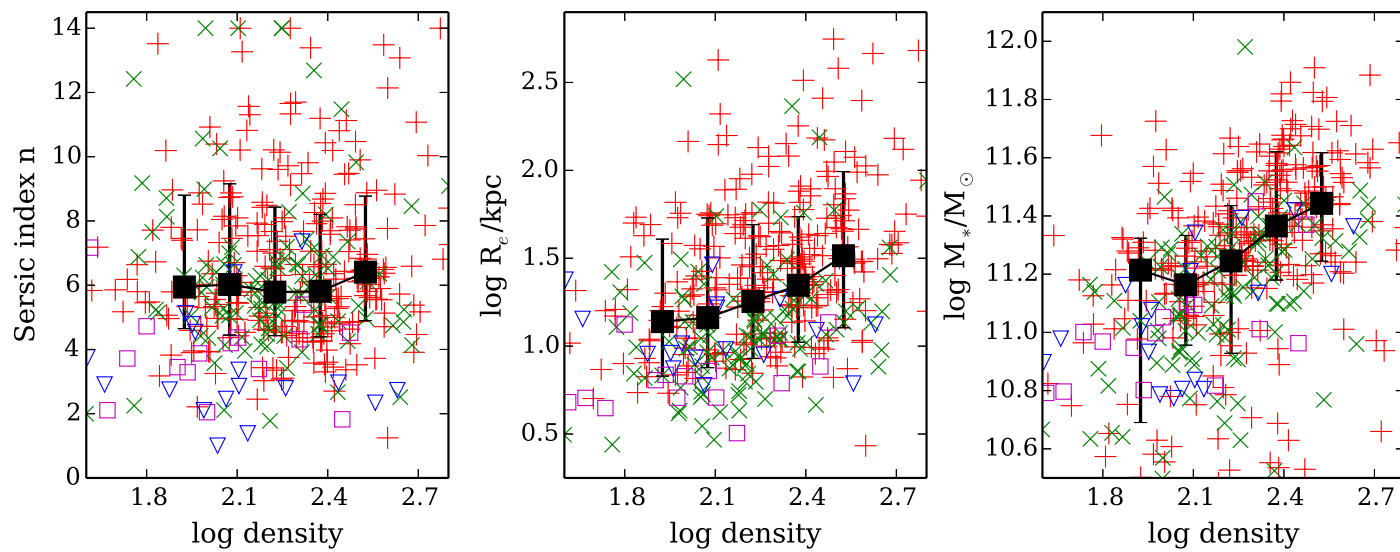
Figure 3.2: Relationship between environmental density and BCG properties. From left to right, these properties are the Sérsic index n, the effective radius R_{e}, and the stellar mass M_*. Symbols as in Fig. 3.1.
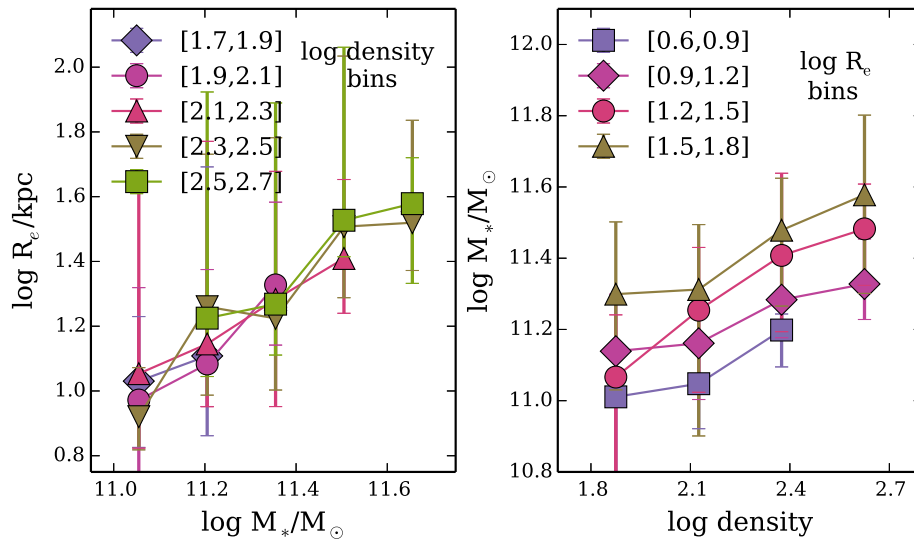
Figure 3.3: Left panel: R_e vs. M_* for cD and elliptical BCGs binned by environmental density. Right panel: M_* vs. environmental density binned by R_e. The points correspond to the median for each bin and error bars indicate the 84 and 16 percentiles ($\sim 1\sigma$). Bins containing fewer than 5 galaxies have been excluded due to their large statistical uncertainties. The legend shows the different symbols corresponding to each bin.

mental one, and that the environment affects the BCG stellar mass more directly than their sizes.

The fact that the mass-size relation for the general galaxy population does not depend significantly on environment (at least at low redshift) has been found in several recent studies (e.g., Shen *et al.*, 2003; Maltby *et al.*, 2010; Rettura *et al.*, 2010; Huertas-Company *et al.*, 2013b,c; Poggianti *et al.*, 2013). Our results reveal that this is also true for BCGs.

3.3.3   Global Environment: the Effect of the Cluster Mass

We now consider the effect of the global environment (characterised by the total mass of the host cluster M_{200}; see Section 3.2) on the properties of the BCGs. Fig. 3.4 shows the relation of M_{200} with the Sérsic index n, effective radius R_e, stellar mass M_* and environmental density (from left to right).

The Sérsic index does not show any dependence on the halo virial mass (Pearson correlation coefficient -0.04). Both effective radius and stellar mass show a small degree of correlation with M_{200}, albeit with large scatter (correlation coefficients 0.26 and 0.17 respectively)[4]. As before, we need to explore which of these two parameters is the driver of the observed correlations. The first panel of Fig. 3.5 shows that the stellar mass–size relation does not depend on the M_{200} (global environment), in agreement with the findings of Shankar *et al.* (2014b). Since we also found in Section 3.3.2 that the size of BCGs is not directly affected by the local environment (or galaxy density) we conclude that any apparent environmental effect on R_e is driven by the stellar mass–size relation combined with the environmental dependence (or dependencies) of stellar mass.

We now consider the effect of environment on the BCGs' stellar masses. Previous studies have found that the stellar masses of the BCGs correlate with the total mass (or velocity dispersion) of the host cluster (e.g., Whiley *et al.*, 2008; Ascaso *et al.*, 2011). One complication that plagues all environmental studies is the fact that the two characterisations of the environment that we use (local and global) are, not surprisingly,

---

[4]Note that R_e and M_* correlate more weakly with M_{200} than with the environmental density (compare Figs. 3.2 and 3.4).
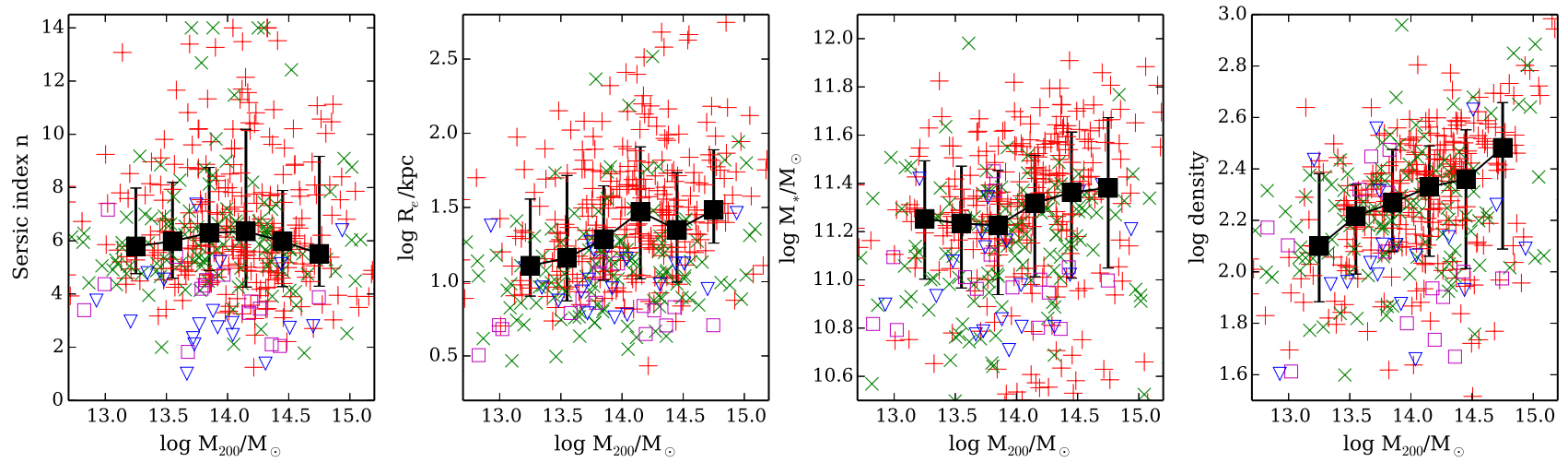
Figure 3.4: Relationship between M_{200} and other BCG properties. From left to right, these properties are the Sérsic index n, the effective radius R_{e}, the stellar mass M_* and the environmental density. Symbols as in Fig. 3.1
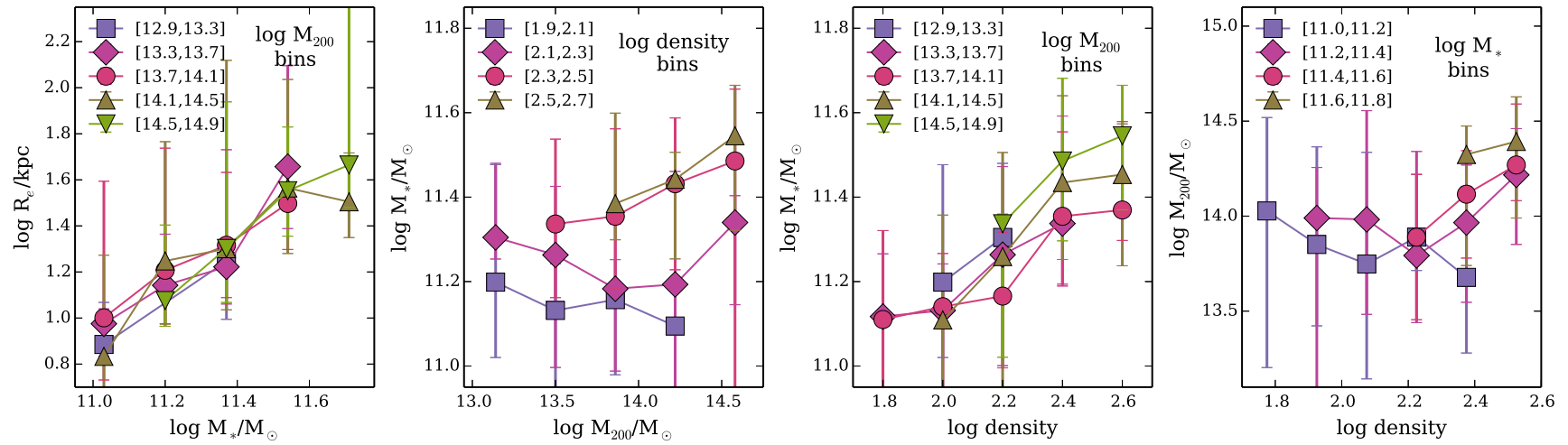
Figure 3.5: From left to right, the first panel shows R_e vs. M_* in M_{200} bins; the second panel M_* vs. M_{200} in density bins; the third panel M_* vs. density in M_{200} bins; and the fourth panel M_{200} vs. density in M_* bins. The points correspond to the median for each bin and error bars indicate the 84 and 16 percentiles ($\sim 1\sigma$). Bins containing fewer than 5 galaxies have been excluded due to their large statistical uncertainties. The legend shows the different symbols corresponding to each bin. Only cD and elliptical BCGs have been included.

correlated (see rightmost panel of Fig. 3.4), although not very tightly (correlation coefficient 0.33). However, these two measures of environment are clearly not representing the same physical scales or the same range of physical processes, and their evolution is largely decoupled (Poggianti *et al.*, 2010). There is also clear evidence that local and global environment do not have the same effect on galaxy evolution. For instance, Vulcani *et al.* (2012) found that the local environment has a strong effect on the galaxies' stellar mass function, while the same team showed that the global environment has no (or much weaker) effect (Vulcani *et al.*, 2013).

We find that the correlation between M_* and environmental density (Fig. 3.2 right panel; Pearson correlation coefficient 0.49) is much stronger than the M_*–M_{200} one (Fig 3.4 third panel; correlation coefficient 0.17), suggesting that the main driver of these correlations is the local density. This is confirmed by Fig. 3.5. The second panel shows that at fixed density the correlation between M_* and M_{200} largely disappears, except, perhaps, for the two highest density bins, although the statistical uncertainties are large. However, the third panel indicates that at fixed M_{200} the M_*–density relation is still present. The fourth panel shows that at fixed M_* most of the M_{200}–density correlation vanishes. We conclude that the M_*–environment correlations are really driven by the M_*–density correlation, while the weaker M_*–M_{200} correlation is secondary, and it originates on the M_{200}-density and M_*–density correlations.

It could be argued that the detected trend (more massive BGGs live in denser, more massive haloes) may be due, at least partially, to a pure statistical effect. If stellar masses are randomly drawn from the mass function of galaxies, massive haloes, which host a larger number of galaxies, have a higher probability to host more massive galaxies (see, e.g., Tremaine & Richstone 1977; Bhavsar & Barrow 1985; Lin, Ostriker & Miller 2010; Dobos & Csabai 2011; Paranjape & Sheth 2012; More 2012). However, we argue that this statistical effect cannot be the main driver of the correlation we find. There is quite a lot of evidence indicating that the luminosity of cluster BCGs is inconsistent with just statistical sampling of the cluster galaxy luminosity function: BCGs are generally too bright, and there is too large a gap between the luminosity of the first and second brightest galaxies (Sandage, 1976; Tremaine & Richstone, 1977; Bhavsar & Barrow, 1985; Dobos & Csabai, 2011; More, 2012; Hearin *et al.*, 2013,

among others)[5].

If BCGs are not governed by the luminosity/mass function of the rest of the cluster galaxies, the above statistical arguments do not apply. Things may be not so clear for the poorest groups, where the brightest galaxies seem to be compatible with being statistically drawn from the bright end of the galaxy luminosity function, as argued by some of these authors. However, the correlation between BCG mass and environment appears stronger for more massive and denser clusters (see, e.g., rightmost panel of Fig.3.2), where we argue this statistical effect should not apply, and weaker for poorer groups, where the statistical bias should be strongest. If the main driver of the correlation were just the statistical sampling of the luminosity function, we would expect the correlation to be strongest where this effect is most important (low mass and less dense clusters and groups). Since the effect we find is strongest for high-mass and denser clusters, we conclude that the correlation cannot be primarily driven by sampling statistics.

In summary, in this section we have found that BCGs follow a stellar mass–size relation that is independent of the environment, and that stellar mass is intrinsically correlated with the local environment (or environmental density). In Section 3.4 we will see how these correlations depend on the morphologies of the BCGs.

3.4   Evolutionary History of cD and Elliptical BCGs

3.4.1   Differences between cD and Elliptical BCGs

In Chapter 2 we found that the vast majority of BCGs (over 90%) have cD or elliptical morphologies, while only a small minority ($\sim 7\%$) are disk galaxies (spirals and S0s), and the remaining few are major mergers. The morphology of these galaxies is clearly linked to their quantitative structural parameters. cDs are generally larger than ellipticals, and their light distributions deviate significantly more from Sérsic profiles

---

[5]Note, however, that Paranjape & Sheth (2012) disagree, but More (2012) and Hearin *et al.* (2013) have argued against their results.

than those of ellipticals. With the additional information presented in this chapter we will now explore how morphology and structure are linked to the stellar masses and environments of the BCGs.

In Fig. 3.6 we present the distributions of the stellar masses, environmental densities and parent cluster total masses (M_{200}) for cD and elliptical BCGs. The left panel clearly shows that cDs have, statistically, larger stellar masses than elliptical BCGs. The median stellar mass of the cDs is $2.1^{+1.7}_{-1.1} \times 10^{11} \mathrm{M}_\odot$, $\sim 50\%$ larger than that of ellipticals ($1.4^{+0.9}_{-0.6} \times 10^{11} \mathrm{M}_\odot$). A two-sample Kolmogorov-Smirnov test shows that this difference is significant at the $\sim 4.6\sigma$ level. The disk galaxies (not shown in the figure for clarity) are even less massive: the median stellar mass for spirals and S0s is $1.0^{+1.0}_{-0.4} \times 10^{11} \mathrm{M}_\odot$.

With respect to environmental density (middle panel of Fig. 3.6), cDs seem to prefer marginally denser regions (by $\sim 20\%$ on average) than elliptical BCGs, although, statistically, this difference is only significant at the $\sim 2.4\sigma$ level. Disk galaxies tend to live in the regions with the smallest densities (a factor of ~ 2 smaller than cDs). Similarly (right panel of Fig. 3.6), cDs appear to be hosted by more massive clusters/groups than ellipticals, but once again the difference (a factor of ~ 1.7 in median M_{200}) is only barely significant ($\sim 2\sigma$).

These differences in the stellar masses and environments of BCGs with different morphologies suggest that their formation histories may be different. In Section 3.3 we found that there are intrinsic correlations between R_e and M_*, and between M_* and the environmental density. By exploring the relationship between these properties and the galaxies' morphologies we may be able to shed additional light on the issue of the formation and growth of BCGs. In Fig. 3.7 we show the R_e–density relation (left panel) and the M_*–density relation (right panel) for cD, elliptical, and disk BCGs. cD and elliptical BCGs show parallel correlations, in the sense that larger and more massive galaxies tend to prefer denser environments. However, at a fixed environmental density, cDs are, on average, a factor of ~ 2 larger and $\sim 40\%$ more massive than elliptical BCGs. Disk galaxies tend to be smaller and less massive, but clear correlations are not seen, perhaps due to the small number statistics. This correlation is also seen when investigating the relation with the the total mass of the cluster. These correla-
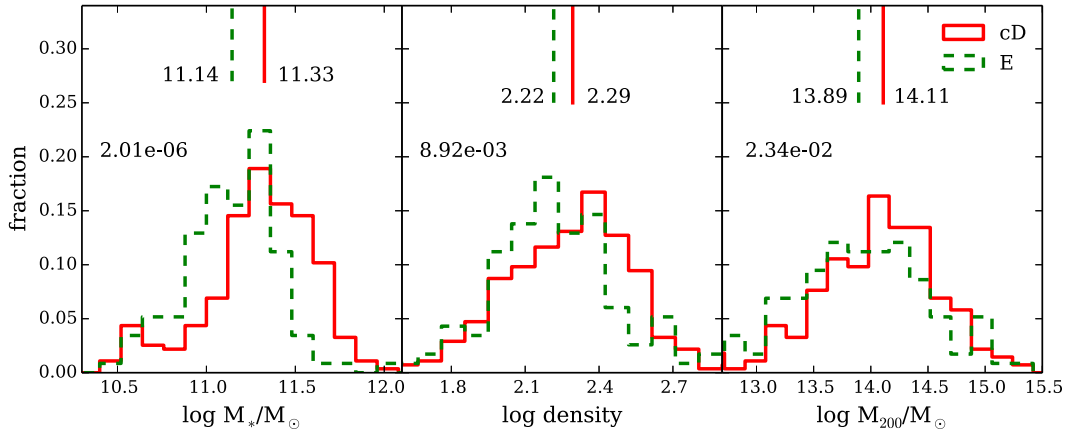
Figure 3.6: Distribution of M_*, environmental density and M_{200} for the 275 cD (red solid) and 116 elliptical (green dashed) BCGs in our sample. The p-value in each panel indicates the significance of the observed differences between the cD and elliptical BCG parameter distributions. These are derived from two-sample Kolmogorov-Smirnov tests. Statistically, compared with elliptical BCGs, cD galaxies are more massive, tend reside in denser environments, and tend to be hosted by more massive dark matter haloes. The median values of the different distributions are indicated by the vertical lines and adjacent numerical values.
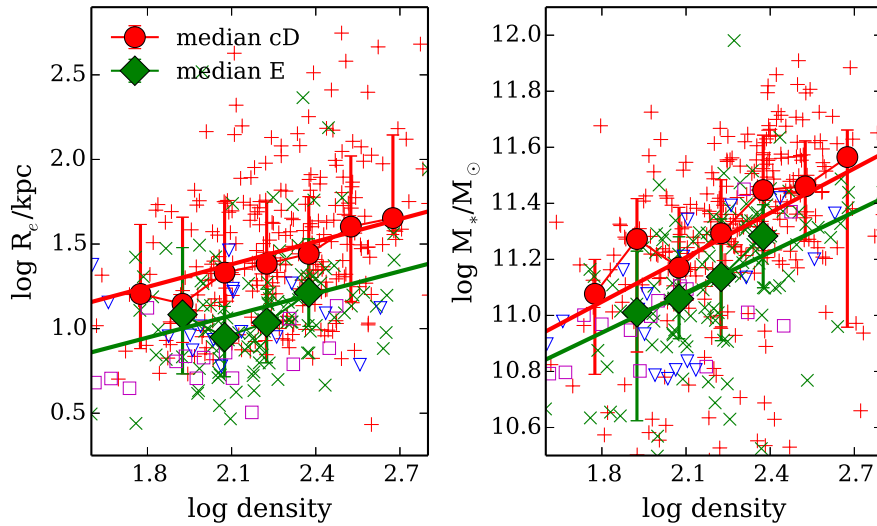
Figure 3.7: R_e–density and M_*–density relations for BCGs with different morphologies. Red plus signs, green crosses, magenta open squares and blue open triangles correspond to cD, elliptical, S0 and spiral BCGs, respectively (as in Fig. 3.1). Red filled circles with error bars show the median and the 84 and 16 percentiles for cD galaxies. Green filled diamonds show the same properties for elliptical BCGs. The red and green lines show a linear fit for cD and ellipical BCGs Respectively. It is clear that at the same density, cD galaxies are statistically larger by factor of ~ 2 than elliptical BDGs. The stellar mass of cDs is larger by a factor of ~ 1.4 than that of ellipticals. Disk BCGs tend to be smaller and less massive.

tions are futhermore certainly due to the fact that there is a different relation between the stellar mass and radius for ellipticals and cD. This effect is driven by the stellar mass being higher, which then increases the radius.

Note that the observational results presented in this chapter, including the differences found between cDs and elliptical BCGs, do not depend on whether the morphological classification is done visually (as shown here) or automatically (based on the structural parameter method described in Chapter 2). Fig. 3.8 and Fig. 3.9 show the results obtained using the cD and elliptical BCGs classification defined by the optimal border of Fig. 2.13 (the blue solid curve). Fig. 3.10 and Fig. 3.11 show the results by using the cD and elliptical BCGs selected by the two-step process (i.e., the best border presented as blue solid curve in Fig. 2.14). These figures show that using the automatic cD/elliptical classification yields very consistent results. We are therefore confident that our results are robust, and do not depend significantly on the details of the morphological classification.

3.4.2 Implications

Our empirical results, together with the findings of previous works, suggest a possible scenario linking the evolution of elliptical and cD BCGs. Whiley *et al.* (2008), Burke & Collins (2013), Burke, Hilton & Collins (2015) and Zhang *et al.* (2016), among others, suggest that the stellar mass of BCGs has experienced some (but relatively moderate) growth in the last ~ 6–8 Gyrs. Although measuring BCG growth is notoriously difficult due to progenitor bias (see Shankar *et al.* 2015 for a recent discussion), it seems to be due, mostly, to the effect of minor and major mergers (Burke & Collins, 2013), with minor mergers dominating at later times (Shankar *et al.*, 2013; Burke, Hilton & Collins, 2015). At most, BCGs may have grown by a factor ~ 1.8 in stellar mass since $z \sim 1$, although this factor could have been as small as ~ 1.2 if about half of the accreted stellar mass from the merging companions became part of the intra-cluster light (Burke, Hilton & Collins, 2015). This mass growth seems to have been faster in the past, when both minor and major mergers were more common (Burke & Collins, 2013), but these authors also found that BCGs in similar mass clusters can have very different merging histories. Furthermore, Ascaso *et al.* (2011) reported that BCGs have
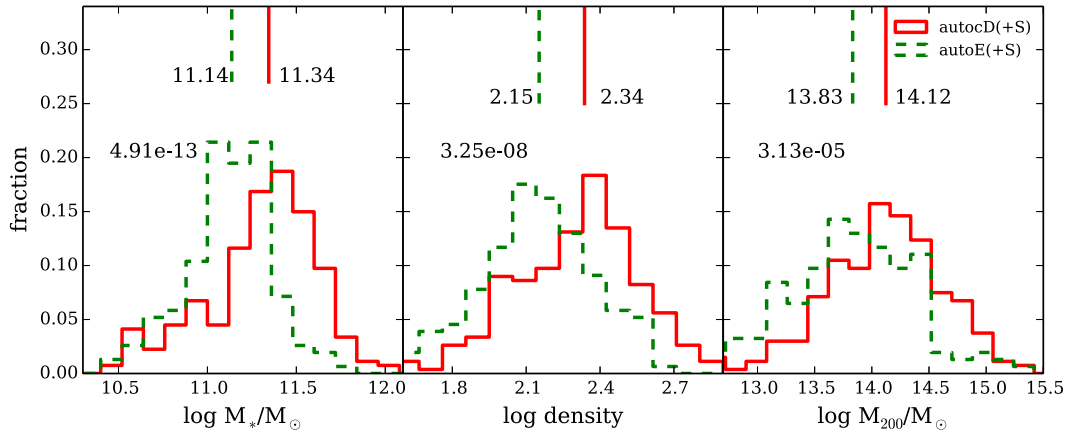
Figure 3.8: Distribution of M_*, environmental density and M_{200} for the automatically selected cD (red solid) and elliptical (green dashed) BCGs by using the best border in Fig. 2.13.
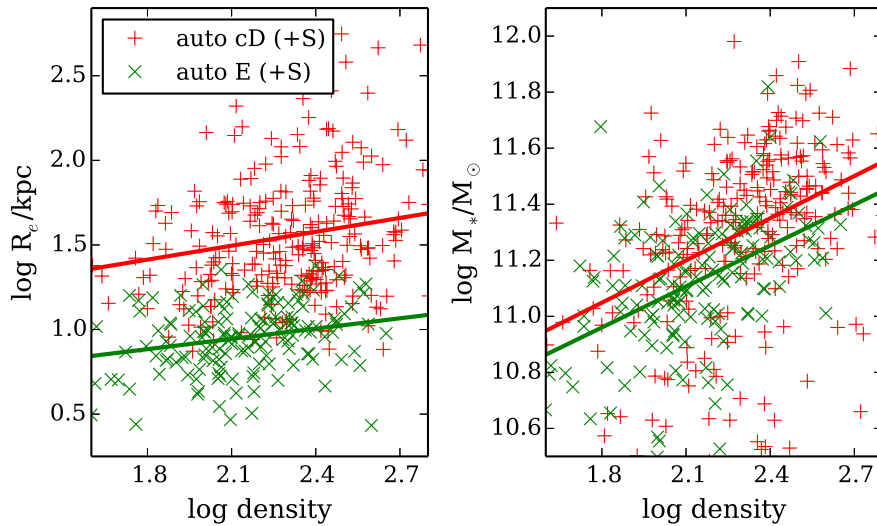
Figure 3.9: R_e–density and M_*–density relations for BCGs with different morphologies which are selected automatically by the best border in Fig. 2.13 . Red plus signs are automatically identified cD galaxies, and green crosses correspond to automatically selected elliptical BCGs. The red and green lines show a linear fit for these cD and elliptical BCGs, respectively. It is clear that at the same density, cD galaxies are statistically larger and more massive than elliptical BDGs.
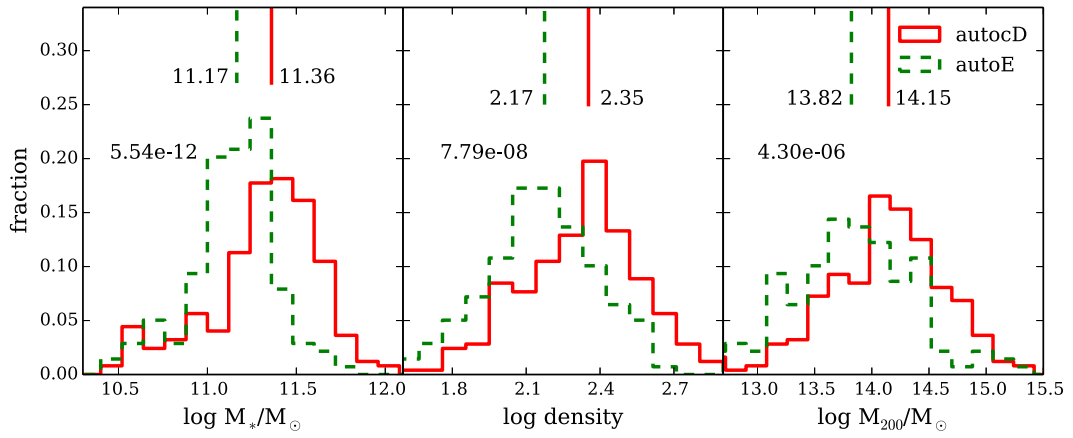
Figure 3.10: Distribution of M_*, environmental density and M_{200} for the two-step automatically selected cD (red solid) and elliptical (green dashed) BCGs by using the best border in Fig. 2.14..
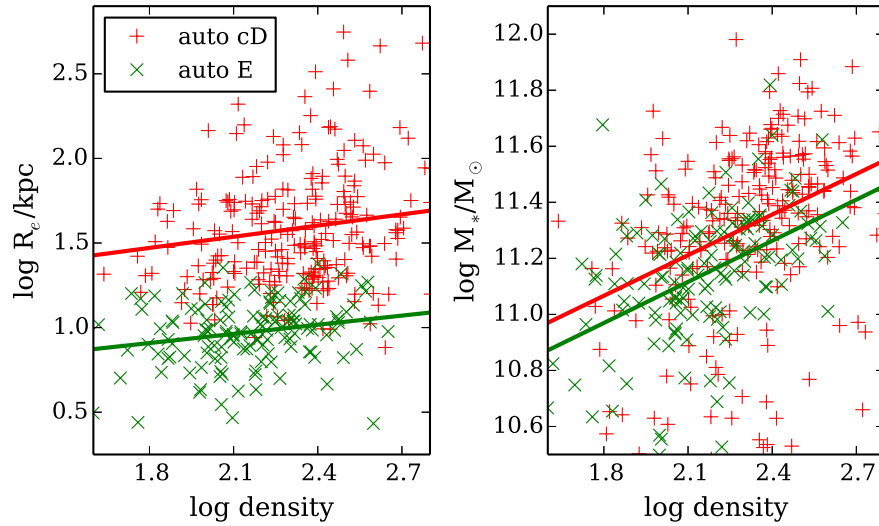
Figure 3.11: R_e–density and M_*–density relations for BCGs with different morphologies which are selected automatically by the two-step best border in Fig. 2.14 . Red plus signs are automatically identified cD galaxies, and green crosses correspond to automatically selected elliptical BCGs. The red and green lines show a linear fit for these cD and elliptical BCGs, respectively. It is clear that at the same density, cD galaxies are statistically larger and more massive than elliptical BDGs.

grown in size by a factor of ~ 2 over a similar period. Interestingly, the difference in mass between cDs and elliptical BCGs in similar environments is of the order of 40% (i.e., comparable with the measured mass growth), and we find that the difference in size is a factor of ~ 2 (again, compatible with the measured size growth), but with a very large scatter in both cases. Additionally, in Chapter 2 we found that, when it could be reliably measured, the fraction of the light (stellar mass) contained in the cD envelopes is of the order of ~ 40–60%, with significant galaxy-to-galaxy variations.[6] It is therefore plausible that most present-day BCGs started their life as ellipticals, and they subsequently grew, in stellar mass and size, due to mergers to become cDs. In this process, the characteristic cD envelope developed. The large scatter in the stellar masses and sizes of the cDs is explained by their different merger histories. Furthermore, the growth of the BCGs in mass and size seems to be linked to the hierarchical growth of the structures they inhabit: as the groups and clusters become denser and more massive, the BCGs at their centres also grew.

By the present time, most BCGs seem to be well advanced in this process. In Chapter 2 we found that the majority ($\sim 57\%$) of the BCGs are cDs, $\sim 21\%$ have intermediate cD/E or E/cD morphologies, while ellipticals are a minority ($\sim 13\%$). The presence of intermediate morphological classes suggests that this process is still ongoing. Present-day elliptical BCGs may (or may not) develop cD-type envelopes in the future, depending on whether the current merger rate is sufficient. With the limited statistical evidence that we have, we can only speculate about the origin of the few ($\sim 7\%$) BCGs with spiral and S0 morphologies, but perhaps these are the ones which avoided major mergers in their past history and retained their disks.

If the evolutionary framework we propose is correct, one would expect the morphological mix of BCGs to change with redshift: at earlier times, the fraction of elliptical BCGs should be higher than today, with cDs showing the opposite trend. We have visually examined the images of the 13 BCGs in the ESO Distant Survey (White *et al.*, 2005) clusters and groups for which deep HST images are available (Desai *et al.*, 2007), and morphologically classified them following the same criteria used for the

---

[6]Note that the galaxies for which this fraction could be reliable measured are the ones whose profiles are better modelled using two-component Sérsic+Exponential profiles. Since these tend to be the ones with more prominent envelopes, the average fraction of light in cD envelopes is probably closer to $\sim 40\%$, the bottom end of the measured range.

low-redshift sample. The average redshift of these galaxies is $z \sim 0.6$. Although cosmological surface-brightness and resolution effects would have to be properly accounted for in a more systematic study, we feel that these HST images have enough resolution and depth (4 orbit exposure) for this purpose. They compare favourably with the SDSS images of the lower-redshift galaxies. Notwithstanding these possible caveats, we find that 4 of the BCGs are ellipticals, 3 cDs, 4 E/cD or cD/E, one is a spiral, and one is a merger. Although the sample is pitifully small, the trend seems to go in the right direction: the fraction of ellipticals more than doubles when compared with the local sample, while the fraction of cDs halves. There is also a significant fraction of galaxies with intermediate morphologies, suggesting that the transformation process is also happening at these redshifts. Of course, with a such small sample, no firm conclusions can be obtained, but at least these findings are compatible with our hypothesis. A systematic study of a large, well-defined sample of BCGs with deep HST images, reaching $z \sim 1$, would be required to obtain a definitive answer.

Numerical simulations and semi-analytic models (see, e.g., De Lucia & Blaizot 2007 and references therein) provide a plausible inside-out scenario for the growth of BCGs which is broadly compatible with our findings. At early times ($z \sim 1$–3), dissipative processes similar to the ones proposed for the formation of normal giant elliptical galaxies were responsible for the building of the BCGs' inner (elliptical-like) stellar component, whose light profile can be well represented by a Sérsic model. Subsequently, as the structures around BCGs grew hierarchically, the mass and size of these galaxies continued to increase, mainly due to dissipationless (dry) mergers, and the cD envelopes were formed as a result. This picture is also largely consistent with other observations. For example, dry mergers have been directly observed in cluster environments (e.g., van Dokkum 2005), and it has been suggested that the accreted stars could have built up the extended stellar haloes observed in BCGs (Abadi, Navarro & Steinmetz, 2006; Murante *et al.*, 2007).

3.5   Conclusions

Using a large well-defined sample of 425 nearby Brightest Cluster Galaxies from the catalogue of L07, we have carried out a study of the relationships between their internal properties (stellar masses, structural parameters, sizes and morphologies) and their environment. The stellar masses M_* are based on the MPA–JHU SDSS DR7 measurements. The structural parameters (effective radius R_e and Sérsic-index n) were derived in Chapter 2 using single Sérsic profile fits. The visual morphologies were also obtained in Chapter 2. The majority ($\sim 57\%$) of the BCGs are cDs, $\sim 13\%$ are ellipticals, $\sim 21\%$ belong to intermediate cD/E or E/cD classes, and $\sim 7\%$ have disk morphologies, with spirals and S0s in similar proportions. We use two separate measurements of the environment, the local environmental density (Tempel, Tago & Liivamägi, 2012), and the global dark-matter halo virial mass M_{200} derived from the cluster velocity dispersions of L07. The main conclusions of this chapter are:

- The Sérsic-index n does not correlate with the stellar mass M_* or the environment of the galaxies.

- The effective radius R_e of the BCGs correlates with their stellar mass M_*, but the scatter is large (~ 0.3 dex in effective radius at a given mass). This correlation does not depend significantly on the environment.

- Almost all BCGs have larger R_e than non-BCG early-type galaxies of similar M_*. The median radius of the BCGs is about twice as large as that of non-BCG early types of similar masses. This difference is largely due to the cD galaxies, which dominate the sample. Moreover, the scatter in the M_*–R_e relation is significantly larger for the BCGs than for the other early-type galaxies, suggesting a more complex formation history.

- More massive BCGs tend to inhabit denser regions and more massive clusters, but M_* correlates significantly more strongly with environmental density than with the cluster dark-matter halo mass M_{200}. Indeed, the apparent correlation between M_* and M_{200} can be explained by the correlations between M_{200} and M_* with environmental density.

- The median stellar mass of cD BCGs is $2.1 \times 10^{11} M_\odot$, $\sim 50\%$ larger than that of ellipticals ($1.4 \times 10^{11} M_\odot$). BCGs with disk morphologies have even smaller stellar masses (median $1.0 \times 10^{11} M_\odot$).

- cDs seem to prefer marginally denser regions (by $\sim 20\%$ on average) than elliptical BCGs. Disk galaxies tend to live in the regions with the smallest densities. Similarly, cDs appear to be hosted by more massive clusters/groups than ellipticals (by factor of ~ 1.7 in median M_{200}). However, these differences are only significant at the 2–2.4σ level.

- cD and elliptical BCGs show parallel correlations between their stellar masses and environmental densities: larger and more massive galaxies tend to prefer denser environments. However, at a fixed environmental density, cDs are, on average, $\sim 40\%$ more massive than elliptical BCGs. Due to the correlation between R_e and M_*, cDs and ellipticals also exhibit positive and parallel correlations between their effective radii and the environmental density. cDs are, statistically, twice as large as elliptical BCGs at a given density. Disk BCGs tend to be smaller and less massive.

Our results, together with the findings of previous observational and theoretical studies, suggest an evolutionary link between elliptical and cD BCGs. We suggest that most present-day BCGs started their life as ellipticals, and they subsequently grew in stellar mass and size, due to mergers, to become cDs. In this process, the characteristic cD envelope developed. The large scatter in the stellar masses and sizes of the cDs is explained by their different merger histories occurring at $z < 1$. Furthermore, the growth of the BCGs in mass and size seems to be linked to the hierarchical growth of the structures they inhabit: as the groups and clusters became denser and more massive, the BCGs at their centres also grew.

This process is nearing completion by the present time, since the majority of the BCGs in the local universe have cD morphology. However, the presence of intermediate morphological classes (cD/E and E/cD) suggests that the growth and morphological transformation of some BCGs is still ongoing. It is also possible that today's elliptical BCGs may develop cD-type envelopes in the future, depending on the merger activity

they may experience.

This scenario is broadly compatible with hierarchical inside-out models for the formation and growth of BCGs. Early dissipative processes were responsible for the building of the BCGs' inner elliptical-like stellar component. As the structures around BCGs grew hierarchically, the mass and size of these galaxies continued to increase, mainly due to dissipationless mergers, and the cD envelopes were thus formed.

The evolutionary framework we propose seems to be able to explain the observed properties of BCGs, including the differences between the morphological classes. The obvious next step to test this scenario is to carry out a study of the morphology, mass, structure and environment for a large and statistically robust sample of BCGs as a function of redshift, reaching $z \sim 1$. A key piece of evidence would be the evolution of the fraction of cD BCGs with time, and its links with the growth of their masses, sizes and environments.

Chapter 4

Exploring the progenitors of brightest cluster galaxies at $z \sim 2$

This chapter is published in Zhao et al. (2016, submitted).

4.1   Introduction

Brightest cluster galaxies (BCGs) are the most luminous and massive galaxies in local universe. They reside at the bottom of the gravitational potential well of galaxy clusters, and are surrounded by a population of satellite galaxies. The special regions they reside in, and the unique properties they exhibit (e.g., distinct structures and morphologies, very high stellar masses) set them apart from the general galaxy population. Their origin and evolution also tightly link with the evolution of their host clusters and provide direct information on the history of large-scale structures in universe (e.g., Conroy, Wechsler & Kravtsov 2007). Even though much attention has been dedicated to the study of BCG formation and evolution, understanding when these most massive galaxies formed and how they evolve with time are still controversial issues.

Early N-body simulations studying BCG formation through merging in a cold matter (CDM) cosmology, find that BCG growth through early merging of few massive galaxies dominates over late-time accretion of many smaller systerms (e.g., Dubinski 1998). The modern context of BCG assembly through hierarchical growth within

networks of dark matter haloes is now well established. For example, by using nine high-resolution dark matter-only simulations of galaxy clusters in a ΛCDM universe, Laporte *et al.* (2013) claim that BCGs can grow mainly through dissipationless dry mergers of quiescent galaxies from $z = 2$ to the present day, producing BCG light profiles and stellar mass growth in good agreement with observations. However, pure N-body models ignore mechanisms such as gas cooling and star formation in BCG evolution which are also likely important processes.

Taking into account hydrodynamical processes such as infalling gas and AGN feedback, recent semi-analytic models (SAMs) suggest that the stellar component of today's BCGs was initially formed through the collapse of cooling gas or gas-rich mergers at high redshift, and consequently BCGs continued to grow, but assemble substantially very late (50% of the final mass is assembled at $z \lesssim 0.5$) through dissipationless processes such as dry mergers of satellite galaxies (De Lucia & Blaizot 2007; Naab, Johansson & Ostriker 2009; Laporte *et al.* 2012). This two-phase evolution for BCG growth successfully reproduces many observations, however, it has been questioned by a number of studies which find a much slower stellar mass growth in BCGs at $z \lesssim 1$ in observations (e.g., Whiley *et al.* 2008; Collins *et al.* 2009; Lin *et al.* 2013; Zhang *et al.* 2016). More observational studies of BCGs at higher redshifts will help to constrain these models and give us a better idea of their evolution.

To understand how BCGs evolved and assembled their stellar masses, and which mechanisms drive these changes, it is important to properly connect today's BCGs to their progenitors at earlier times observationally. This requires the non-trivial task of linking BCG descendants with their progenitors through cosmic time, which in turn requires assumptions for how BCGs evolve.

At lower redshift ($z \lesssim 1 - 1.5$), BCG progenitor-descendant pairs are selected by an empirical approach through constructing a sample based on finding distant clusters, and using the correlation between BCG stellar mass and cluster mass. Employing this method, many studies have characterized the assembly of BCGs at $z \lesssim 1$. Lidman *et al.* (2012) demonstrated that BCGs have grown by a factor of 1.8 between $z = 0.2 - 0.9$. While Lin *et al.* (2013) found a similar growth such that the stellar mass of BCGs increases by a factor of ~ 2.3 since $z \sim 1.4$. Shankar *et al.* (2015) claimed an increase

of a factor $\sim 2 - 3$ in BCG mean stellar mass, and $\sim 2.5 - 4$ factor increase in BCG mean effective radius, since $z \sim 1$. Zhang *et al.* (2016) showed a BCGs mass growth by a factor of ~ 2 since $z \sim 1.2$ using a similar approach.

However, the techniques for linking local BCGs and their progenitors at $z \lesssim 1$ are difficult to apply at higher redshifts ($z \gtrsim 1.5$). On the one hand, it is difficult to identify clusters/proto-clusters at early times. On the other hand, it is also difficult to define BCG progenitors in high-z clusters since the main progenitor may not be the most luminous/massive galaxy as the low-z BCGs. Nonetheless, a number of studies have been carried out to explore the build-up of massive galaxies up to $z \sim 3$.

Among the solutions for linking galaxies at different redshifts, matching galaxy progenitors and descendants at a constant number density has been demonstrated to be a considerably improved approach for tracking the evolution of galaxies (e.g., Leja, van Dokkum & Franx 2013; Mundy, Conselice & Ownsworth 2015). By applying this method, van Dokkum *et al.* (2010) claim a mass growth of a factor of ~ 2, and a size growth of a factor of ~ 4 for massive galaxies since $z = 2$. Ownsworth *et al.* (2014), using a variety of number density selections with $n \leqslant 1 \times 10^{-4} \mathrm{Mpc}^{-3}$ at $0.3 < z < 3$, find that about 75% of the total stellar mass in massive galaxies at $z = 0.3$ is created at $z < 3$, and the sizes of massive galaxy progenitors is a factor of 1.8 smaller than local early-type galaxies of similar mass. Marchesini *et al.* (2014) investigate ultra-massive galaxy evolution by using progenitors from $z = 3$ which are selected with both a fixed cumulative number density and an evolving number density. They find that the stellar content of ultra-massive galaxies have grown by a factor of $2 - 3.6$ since $z = 3$. However, these systems are not necessarily BCGs, and a clear correspondence between massive galaxies and BCGs at high redshifts ($z \gtrsim 1.5$) is still lacking. In order to obtain better perspective of BCG assembly, it is critical to identify the progenitors of BCGs at $z \gtrsim 1.5$, and to explore their mass and structural evolution.

In this chapter we investigate the issue of how to find and trace the evolution of BCGs at $z < 3$. Using our method, we also investigate the formation processes for BCGs. Mergers are potentially a significant process in BCG formation, as they are predicted to be a major mechanism in the hierarchical picture of galaxy formation. Apart from the dominant role of minor mergers in BCG mass assembly at low redshift (e.g., Burke,

Hilton & Collins 2015), observations suggest that at high redshifts BCG evolution is also largely driven by mergers through both major and minor events (e.g., Lidman *et al.* 2013; Burke & Collins 2013).

Since mergers closely relate to the environmental density around galaxies, in this work, we use a method to identify BCG progenitors at $z \sim 2$, which depends on galaxy local densities as well as galaxy stellar masses. We will first examine what fraction of true BCG progenitors are selected by our method using simulation data, and then apply this method on observational data using the CANDELS UDS survey. Our method to probe BCG progenitors at $z \gtrsim 1.5$ is easier, since it avoids the difficulty of identifying clusters at high redshifts. Comparing high-z BCG progenitors with their local SDSS descendants, we also discuss the evolution of BCG structure, morphology, stellar mass and star formation since $z \sim 2$.

The rest of this chapter is organized as follows. In Section 4.2, we present the observational data employed in this work. We also introduce necessary quantities which will be used in selecting our BCG progenitors and for comparing BCG properties in this section. The description and simulation tests of our selection of BCG progenitors are presented in Section 4.3. Although the BCG progenitors selected by our method are contaminated by non-BCG progenitors, in Section 4.3.3, we demonstrate that our selected progenitors sample, and their local descendants, can be used to trace BCG evolution since $z \sim 2$. We then describe our results of BCG assembly in Section 4.4. In Section 4.5 we first discuss the possible mechanisms for BCG evolution implied by our results, and then we compare our results with other studies of BCG evolution at $z \lesssim 1$ as well as massive galaxy growth since $z \sim 2$. Finally, we summarise our results in Section 4.6. Throughout this study we have adopted the ΛCDM cosmology with $\Omega_m = 0.3$, $\Omega_\Lambda = 0.7$, and $H_0 = 70 \ \mathrm{km \ s^{-1} \ Mpc^{-1}}$.

4.2 Observational Data and Quantities

In this section, we first describe the galaxy catalogues for our local samples and high-z galaxies. We also provide information on their properties, such as stellar masses, star formation rates (SFRs) and specific star formation rates (sSFRs). The environmental

density measured at high redshifts in observations is introduced in a following separate subsection. We then explain how we use the constant number density to trace galaxy evolution. The structural properties of galaxies from profile fitting are described in the final subsection.

4.2.1 Local Sample

The local BCG sample in this chapter, which we compare with the high-z progenitors to study BCG evolution, comes from the L07 BCG catalogue. A detailed description on this catalogue can be found in Section 2.

The stellar masses we use for the L07 BCGs are the MPA–JHU stellar masses. These masses are computed by multiplying the dust-corrected luminosity of the galaxy by the stellar mass-to-light ratio (M_*/L). The M_*/L for SDSS galaxies was initially derived by fitting the observed values of the $D_n(4000)$ and $H\delta_A$ indices with a library of models from Bruzual & Charlot (2003) (Kauffmann *et al.* 2003). A Kroupa IMF is assumed. MPA–JHU group then used broad-band u, g, r, i, z photometry of SDSS DR7 for the fits instead of the spectral features. Although the method is not identical to that of Kauffmann *et al.* (2003), the results agree very well. A detailed discussion and comparison of the methods can be found in http://mpa-garching.mpg.de/SDSS/DR7/mass_comp.html. Each model is then weighted by its likelihood, and a probability distribution for M_*/L is computed. The MPA–JHU mass is the median of this distribution. Compared with the stellar mass obtained from the M_*/L of the best χ^2 model, median stellar mass is ~ 0.1 dex smaller (Brinchmann *et al.* 2004; Cid Fernandes *et al.* 2005). When we compare the stellar mass between local sample and their high-z progenitors, we convert the MPA–JHU stellar masses to those with a Chabrier IMF.

As we discuss in detail later in this chapter, the high-z progenitor sample selected by our method will contain both true BCG progenitors and non-BCG progenitors (see Section 4.3.2.3). This is due to there being no perfect way to only select true BCG progenitors at high redshift. Thus, at $z \sim 0$, we construct a counterpart sample which is a mixture of local BCGs and local non-BCGs as the descendants of our high-z progenitors (see Section 4.3.3.2). Therefore, in addition to the L07 BCG catalogue, we also employ SDSS DR7 data as our parent galaxy catalogue to select local non-BCGs

to match the high-z inevitable contamination. Since the non-BCGs are selected based on their stellar mass (see Section 4.3.3.2), the parent galaxy catalogue is the MPA–JHU DR7 stellar mass catalogues. We select our "contamination" galaxies within the redshift range of $0.02 \leq z \leq 0.10$, the same as our BCG sample.

The SFR and sSFR for both the pure BCGs and the contaminant non-BCGs are taken from the MPA–JHU SFR catalogue (http://mpa-garching.mpg.de/SDSS/DR7/sfrs.html). The total SFRs (dust-corrected) for star-forming galaxies are derived by Brinchmann *et al.* (2004) based on a Hα emission line modelling technique. Salim *et al.* (2007) demonstrated that these "Hα" SFRs are very consistent with the dust-corrected SFRs constrained by the UV luminosity of local star-forming galaxies. For local galaxies without Hα detections which belong almost exclusively in the red sequence, the dust-corrected SFRs are obtained from SED fitting of SDSS photometry (details could be found in Salim *et al.* 2007). The SFRs for SDSS galaxies are measured by assuming a Kroupa IMF. They are divided by 1.06 when compared with the SFRs of high-z galaxies which are derived by assuming a Chabrier IMF. 1.06 is the conversion factor to convert SFRs which are calculated for Kroupa IMF to Chabrier IMF. sSFRs of SDSS galaxies are calculated by using the SFRs described here and the MPA–JHU masses. When compared with high-z sSFR, they are also converted to the values for Chabrier IMF.

4.2.2 High-z Sample

The Cosmic Assembly Near-infrared Deep Extragalactic Legacy Survey (CANDELS; PIs: Faber and Ferguson; Grogin *et al.* 2011; Koekemoer *et al.* 2011) provides excellent data to study galaxy properties at high redshift. CANDELS is a 902-orbit Multi-Cycle Treasury program on the *Hubble Space Telescope (HST)* with imaging by the Wide Field Camera 3 (WFC3) and the Advanced Camera for Surveys (ACS) on five different fields: GOODS-N, GOODS-S, COSMOS and UDS. The galaxy catalogue on which we apply our selection of BCG progenitors is from the CANDELS UDS (Mortlock *et al.* 2015).

CANDELS UDS covers a part of the field of UKIRT Infrared Deep Sky Survey (UKIDSS, Lawrence *et al.* 2007) Ultra Deep Survey (UDS). Its image has a pixel scale of 0.06

arcsec/pixel and a 5σ depth of $H = 26.3$ in a 1 arcsec aperture. The photometry of the CANDELS UDS includes *U*-band data from the CFHT (Foucaud et al. in prep), *B, V, R, i', z'*-band data from the Subaru/XMM-Newton Deep Survey (SXDS; Furusawa *et al.* 2008), *J, H* and *K*-band data from UKIDSS UDS, *F*606*W* and *F*814*W* data from the ACS, H_{160} and J_{125}-band WFC3 data, *Y* and *Ks* bands taken as part of the Hawk-I UDS and GOODS Survey (HUGS; VLT large programme ID 186.A-0898, PI: Fontana; Fontana *et al.* 2014).

The photometric redshifts for the high-z galaxies of CANDELS UDS are calculated by Mortlock *et al.* (2015) with the method described in Hartley *et al.* (2013). In brief, the SED templates are fit to the photometry described above, and the best-fitting redshift is used. We constrain our high-z galaxy sample within the redshift range of $1 \leq z \leq 3$, to ensure a statistically large number of high-z progenitors selected by our method.

The stellar masses of our high-z galaxies are calculated by Mortlock *et al.* (2015) for the CANDELS UDS. The method used to compute the stellar masses is described in detail in Mortlock *et al.* (2013, 2015), Hartley *et al.* (2013) and Lani *et al.* (2013). Briefly, the stellar masses are measured through a multi-colour stellar population fitting technique. With a Chabrier IMF, a large grid of synthetic SEDs from the stellar population models of Bruzual & Charlot (2003) are used to fit the multi-band photometry of the CANDELS UDS. They obtained two kinds of stellar mass. One is the best-fit stellar mass whose template has the smallest χ^2 value. Another one is the mode stellar mass. By binning the stellar masses of the 10% of templates with the lowest χ^2 in bins of 0.05 dex, they determine the mode stellar mass which corresponds to the stellar mass bin with the largest number of templates. In this work we use the mode stellar masses in the catalogue as these masses are less likely to be affected by the bad fitting through templates (Mortlock *et al.* 2013).

We find that for all the CANDELS UDS galaxies, the mode stellar mass is statistically consistent with the best-fit stellar mass. Mode mass is only ~ 0.01 dex smaller than the best-fit one. For our selected 38 progenitors (selection is described in Section 4.3) which are more massive, we find that the difference between mode and best-fit mass becomes larger, such that the best-fit stellar mass is ~ 0.1 dex larger than the mode mass. Note that in local universe the best-fit mass for SDSS galaxies is ~ 0.1 dex larger

than the MPA–JHU mass. Although the methods used to determine stellar masses at low and high redshift are not exactly the same, given the differences in the datasets, the principles applied–SED fitting of rest-frame optical data–are very similar. We acknowledge that a detailed comparison of the stellar masses of the low- and high-z galaxy samples carries considerable uncertainty, but given the large size of the evolution we measure (a factor of ~ 2.5 in stellar mass; see below), it is not unreasonable to assume that such a large effect cannot be solely explained by systematic differences in the stellar mass determination. Nevertheless, these difficulties need to be taken into account when interpreting our results.

Since CANDELS UDS is a subset of the UDS field, it benefits from the same wealth of the UDS data set, such as the SFR. The SFRs we use for our high-z galaxies are calculated by Ownsworth *et al.* (2014) for the full UDS field. They are obtained from the rest-frame near UV luminosities which trace the presence of young and short-lived stellar populations produced by recent star formation. First, Ownsworth *et al.* (2014) determine dust-uncorrected SFRs with a Chabrier IMF. Since the UV light is very susceptible to dust extinction, they then apply a careful dust correction to obtain the final dust-corrected SFRs. For the full description of the dust correction and SFR calculation see Ownsworth *et al.* (2014). The sSFRs are calculated by taking these SFRs and the stellar masses described above.

In Section 4.4, we find that BCG progenitors at $z \sim 2$ have much higher SFRs (by almost two orders of magnitude) than their local quiescent descendants. Although the techniques for measuring SFRs of high-z and local galaxies are not exactly the same, since the Hα and UV SFRs are very similar (e.g., Salim *et al.* 2007; Twite *et al.* 2012) and all SFRs are carefully dust-corrected, we think our statistical results are still reliable and reasonably robust. Explicitly, we do not think the uncertainty introduced by the different SFR measurements used at high- and low-z is responsible for the clear SFR evolution that we detect.

4.2.3   Density Measurement in Observations

One important property we use in this work to select the BCG progenitors is the local environmental density around the high-z galaxies. Lani *et al.* (2013) compute the

environmental density for UDS galaxies which can be also used for the CANDELS UDS sample. The detailed discussion of the density measurement can be found in their paper. In brief, the densities we use in this work are measured by galaxy counts in a fixed physical aperture.

Lani *et al.* (2013) construct a cylinder with a projected radius of 400 kpc and depth of 1 Gyr around each galaxy within which they count the number of neighbouring galaxies. The radius of 400 kpc represents the typical "radius" of galaxy clusters at high redshifts. The depth of 1 Gyr is several times greater than the 1σ measured uncertainty on the photometric redshifts. This depth avoids diluting the number of galaxies in the cylinder by minimising the exclusion of sources due to the large photometric redshift errors. Moreover, with accounting for holes and edges in the field, the number of real galaxies in an aperture ($N_{\mathrm{g}}^{\mathrm{aper}}$) is normalised. The equation to calculate the density for every galaxy in the UDS catalogue is

$$\rho_{\mathrm{aper}} = \frac{N_{\mathrm{g}}^{\mathrm{aper}}}{N_{\mathrm{mask}}^{\mathrm{aper}}} \times \frac{N_{\mathrm{mask}}^{\mathrm{tot}}}{N_{\mathrm{z}}}, \tag{4.1}$$

where $N_{\mathrm{mask}}^{\mathrm{aper}}$ is the number of good pixels which are not masked within the chosen aperture, $N_{\mathrm{mask}}^{\mathrm{tot}}$ is the total number of non-masked pixels in the UDS, and N_{z} is the total number of galaxies over the entire field which lie within the 1 Gyr redshift interval we consider.

The galaxies employed in Lani *et al.* (2013) to calculate the environmental density are taken from the UDS K-band selected catalogue. A magnitude completeness cut of $K_{\mathrm{AB}} = 24.4$ was also applied, producing a completeness of $\sim 99\%$. This magnitude cut corresponds to a stellar mass cut of $M_{*}^{\mathrm{cut}} = 10^{9.76} M_{\odot}$ at $z \sim 2$, assuming a Chabrier IMF. For more details we refer the reader to Hartley *et al.* (2013) and Mortlock *et al.* (2015).

4.2.4 Constant Number Density Selection

In this section we discuss how to connect our low redshift sample of BCGs to the galaxies at high redshifts.

The main method we use to identify BCG progenitors and study BCG evolution is to match the abundance of BCG environments at low and high redshift. In other words, we will assume a constant number density of "BCG environments" (i.e., a constant number density of clusters or highest-density regions). Since BCGs reside in some of the densest environments and most massive halos in the local universe, it is reasonable to assume that at high-z each BCG progenitor will also reside in one of the most overdense regions. Each high-z overdensity hosting the BCG progenitor may accrete galaxies from other less dense regions, and finally evolve into one galaxy cluster hosting a BCG in the local universe. Thus we assume that the comoving number density of local galaxy clusters and that of high-z most overdense regions that host the BCG progenitors are approximately the same. Note that because we are dealing with a special class of galaxies, of which there is only one per cluster, it is reasonable to assume that the number density of present-day and high-z structures that harbour them remains roughly the same: we expect mergers among massive clusters (the most massive halos) to be much rarer than among normal galaxies (or much less massive halos). Therefore, for BCGs, assuming an unevolving number density is reasonable, while it may not be so for other galaxy populations (cf. Marchesini *et al.* 2014).

The BCG progenitor is identified as the most massive galaxy in each high-z overdensity. The cluster number density used in our study corresponds to that of the clusters in L07. We consider the clusters whose velocity dispersions are $\sigma_{200} \geq 309$ km/s, and DM halo masses are $M_{200} \geq 10^{13.55} h^{-1} M_{\odot}$, corresponding to a cumulative comoving number density of $10^{-4.06} h^3 \mathrm{Mpc}^{-3}$. Applying this number density to the observational data, we need to select 38 high-z progenitors at $1 \leq z \leq 3$ from the CANDELS UDS data, and 469 local galaxies at $0.02 \leq z \leq 0.10$ from SDSS DR7. Detailed descriptions on how we choose our 38 high-z and 469 local sample are presented in Section 4.3.1 and Section 4.3.3.2. Note that by using this method, not all of the selected massive galaxies are true BCG progenitors. In Section 4.3 we will look at the fraction of true BCG progenitors in the selected progenitor sample obtained using different selection methods, including using a fixed galaxy number density. We conclude that that environment matching is a better way to identify true BCG progenitors at high redshifts. Our main results are therefore obtained using this method.

We consider also the effect of using an evolving number density of BCG environments in our selection of BCG progenitors. In the simulation, we find that there are on average 1.4 overdensities at $z \sim 2$ whose most massive galaxies will end up in one single BCG at $z \sim 0$. Therefore, applying an evolving environment number density of $1.4 \times 10^{-4.06} h^3 \, \mathrm{Mpc}^3$ at the $z = 2.07$ snapshot in the simulation (i.e., 1.4 times larger than the non-evolving one), we find that the fraction of true BCG progenitors in the selected sample is comparable (actually, marginally smaller) than the one found using constant number density. Therefore, using an evolving number density does not improve the success rate of the BCG progenitor selection; on the contrary, the sample is contaminated by a slightly higher fraction of non-BCG progenitors. Furthermore, translating an evolving number density of structures from the simulations into the observational domain at $z \sim 2$ is likely to introduce further uncertainties. Since the additional complications inherent in considering evolving number densities do not seem to improve the results, we opt for the simpler constant-density of structures selection method.

4.2.5   Shifting Local Galaxies to High Redshift

One aspect of BCG evolution we study in detail is the connection between local BCGs and their high-z progenitors based on their structural evolution. The high spatial resolution and the high-quality images of the CANDELS UDS data allow for a good assessment of the structural properties (e.g., galaxy size and shape) of high-z galaxies. However, a given galaxy will look different when observed with different instruments or at different redshifts. The extracted structural parameters are also wavelength dependent due to bandpass shifting and cosmological dimming. Therefore, a direct comparison of structural parameters from the original SDSS images and the CANDELS UDS images cannot be done without understanding these biases.

In order to explore the intrinsic structural evolution of BCGs, the images from the SDSS and CANDELS UDS need to be calibrated to allow comparisons between redshifts, ensuring similar resolutions and imaging depth. This can be achieved by using the code FERENGI (Full and Efficient Redshifting of Ensembles of Nearby Galaxy Images; Barden, Jahnke & Häußler 2008). This code takes into account the cosmo-
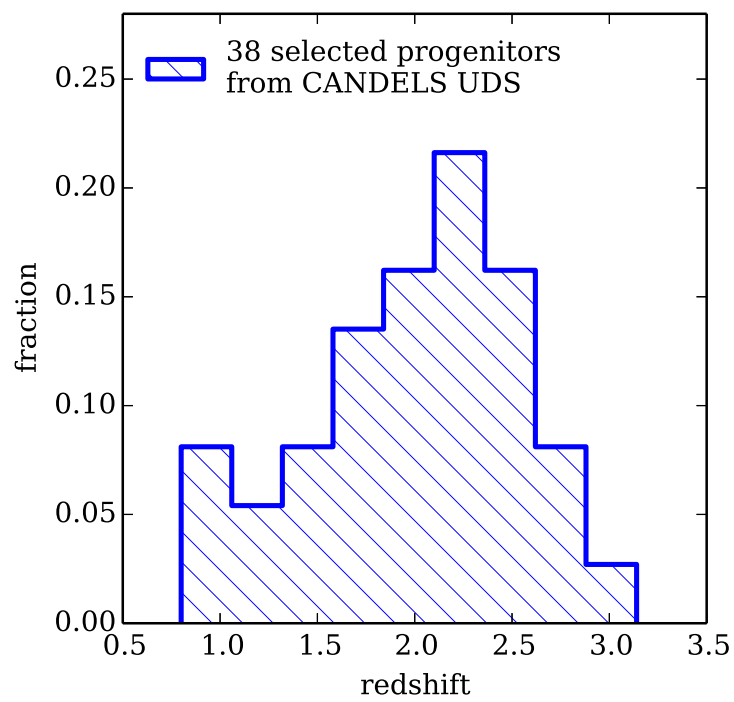
Figure 4.1: Redshift distribution of the 38 progenitors selected by our method as the most massive galaxies in the densest environments from CANDELS UDS. The median redshift of this distribution is $z = 2.06$.
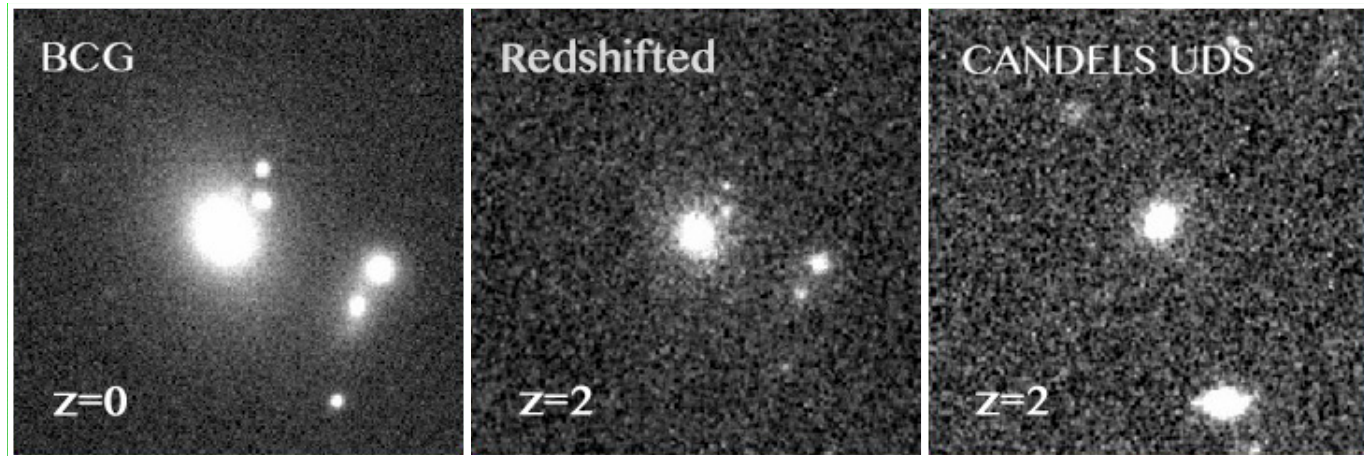
Figure 4.2: An example of a simulated galaxy created by using the FERENGI code (middle panel) after shifting one local BCG in the SDSS g-band (left panel) to $z = 2$ as observed in the CANDELS UDS H_{160}-band data. The right panel is an original H_{160}-band image of a random galaxy at $z \sim 2$. This shows that the input we use in the FERENGI code is able to create a reasonable simulated image compared to an actual $z \sim 2$ image within the CANDELS H_{160}-band.

logical corrections for size, surface brightness and bandpass shifting when simulating low redshift galaxies to high redshift. Simulated images are produced when the input galaxy images are simulated to appear as higher redshift images using the output redshift and instrumental properties. For a full description about the code see Barden, Jahnke & Häußler (2008).

By applying our proposed BCG progenitor selection (detailed description in Section 4.3) on the CANDELS UDS data, the selected 38 progenitors at $z = [1, 3]$ have a redshift distribution as shown in Fig. 4.1. To compare with this, the SDSS images therefore need to be simulated to $z = [1, 3]$ following a similar redshift distribution shown in Fig. 4.1 after taking into account the k-correction in the FERENGI code. To be efficient when running FERENGI, we only simulate SDSS g-band images to CANDELS UDS H_{160}-band at $z = 2$. This also allows us to account for the major k-correction because the g-band at $z \sim 0$ is in the same rest-frame wavelength as the H_{160}-band at $z = 2$.

Fig. 4.1 illustrates that $z \sim 2$ is the median redshift of our 38 selected high-z progenitors, and $\sim 90\%$ of them are at $z < 2.5$, implying that the k-correction differences are not a significant factor in the simulation. Furthermore, we know that high-z galaxies look very similar at wavelengths which are greater than the Balmer break (e.g., Conselice *et al.* 2011) which is the case for our entire sample. Testing on a small number of galaxies, we find that morphologies of the simulated SDSS galaxies placed at $z = 2$ look very similar to the high-z galaxies. We further demonstrate that galaxy structures (shape and size) measured from simulated images placed at $z = 2$ do not have a large differential from the structures of their original galaxies. We therefore only simulate SDSS g-band images to CANDELS UDS H_{160}-band at $z = 2$ without a full k-correction.

One important input in the simulation code is the high redshift sky background image, whose size needs to be larger than the local input images. The size of our input SDSS galaxy images is 500×500 pixels which is too large to cut out a corresponding clean sky area within the CANDELS UDS image. Therefore we create simulated CANDELS UDS sky images which are large enough to be applied in the FERENGI code. First, we randomly choose 10 clean sky areas within the CANDELS imaging that contain no

bright objects nearby. Within each of the sky areas, a patch of size 200×200 pixels is cut out. Then for each patch we create the simulated sky image in 1000×1000 pixels by copying and pasting the patch. Ultimately, we create 10 simulated CANDELS UDS sky images for these simulations. Each of the SDSS galaxies are then redshifted within one of the simulated sky images which is randomly chosen from the ten.

Since the stellar populations in galaxies at higher redshifts are brighter and younger, simply shifting the local galaxies out to high redshift without considering the brightness increase due to stellar evolution will make them look fainter compared to the real average galaxies at such distances. In the FERENGI code, a brightness evolution is put in as an option to account for this evolution. It is introduced by a crude mechanism such that the magnitude evolves as $M_{\mathrm{evo}} = x \times z + M$. By studying the luminosity function from present to $z = 2$, Ilbert *et al.* (2005) found that the characteristic magnitude M^* of the Schechter function in B rest-frame band strongly evolves with redshift, such that M^* at $z = 2$ is ~ 2 magnitude smaller than that in local universe. Since the SDSS g-band is similar with the B band in rest-frame, we set $x = -1$, making a galaxy 2 mag brighter at redshift $z = 2$ than it would be without luminosity evolution.

The middle panel of Fig. 4.2 shows one example of the output image from the FERENGI code after redshifting one local BCG in the SDSS g-band (left panel) to $z = 2$ observed in CANDELS UDS H_{160}-band. The far right panel is the original H_{160}-band image of one random CANDELS UDS galaxy at $z = 2$. This demonstrates that the input we use in the FERENGI code is able to create a reasonable simulated image which appears similar to galaxies seen in the original H_{160}-band image at $z \sim 2$.

4.2.6 Quantitative Characterisation of Galaxy Structure

The surface brightness profiles of galaxies provide valuable information on their structure and their morphology. In addition to measuring galaxy structural parameters by light profile fitting, we also introduce the *RFF* to quantify how good the model fit is and how far the galaxy profile deviates from the model profile.

4.2.6.1 Structure Parameters

The structural properties (effective radius R_e and Sérsic index n) of simulated local galaxies and high-z progenitors are measured using 2D single Sérsic model fits. The fits are carried out with GALFIT through the GALAPAGOS pipline in which the target galaxy and its near neighbours are fitted simultaneously, yielding more accurate results.

For local SDSS galaxies, these fits are carried out on their $z = 2$ simulated images created by the FERENGI code. For each target galaxy, the background level is fixed in GALFIT which is the mean sky value of the created CANDELS sky image used in the image simulation. The point spread function (PSF) employed in GALFIT is the output simulated PSF created by the FERENGI code. For the high-z galaxies we study in the CANDELS UDS, the structural parameters are measured from the HST WFC3 H_{160} images with the PSF of this band, and with the sky value measured by GALAPAGOS. GALAPAGOS uses a flux growth curve method to improve the sky subtraction and produces a highly reliable measure of the background for single-band fits (Häussler *et al.* 2007b).

4.2.6.2 Residual Flux Fraction

The light profiles of real galaxies are often complicated with features such as disturbances, merger remnants, or other structures such as star-forming regions and spiral arms which cannot be fitted by a single Sérsic model. Although we can do visual inspection on the residual images which will give us a good idea whether the galaxy profile can be explained by the single Sérsic model, a more quantitative, repeatable, and objective diagnostic is desired to quantify how large the offset is after subtracting the single Sérsic model from the original image. The *RFF* provides one such diagnostic. Detailed discussion on the *RFF* calculation can be found in Chapter 2. We compute *RFF* on the residual images of both the simulated local galaxies and the high-z progenitors. The comparison of these will show at which epoch the galaxies are more disturbed, which we discuss later in this chapter.

4.3 Selecting BCG Progenitors at $1 < z < 3$

In this section we introduce our basic procedure for the BCG progenitor selection. This is a critical aspect and thus a major part of this chapter. In summary, we investigate several methods to match high-z BCG progenitors with their $z = 0$ counterparts. We ultimately selected a method which depends on the environments of galaxies at high redshifts to locate the most likely BCG progenitors. We test and fine-tune our method using the output of the Millennium Simulation.

4.3.1 Basic Assumption

In order to trace the formation and evolution of BCGs, statistically large samples of BCGs are needed over a broad redshift range. In many other recent studies, BCG samples at higher redshifts are selected through the detection of galaxy clusters in either the X-ray band (Collins *et al.* 2009, Burke & Collins 2013, Zhang *et al.* 2016) or the infrared band (Lin *et al.* 2013), and BCG evolution can be traced back to $z \sim 1$. Unfortunately, the observational constraint on BCG evolutionary scenarios is still poor at $z \gtrsim 1 - 1.5$, and is limited by the difficulty of identifying large samples of galaxy clusters beyond $z \sim 1$. However, due to the fact that environment can be measured at high redshifts with observables which are relatively easy to obtain (albeit the high calibre data of observables is vital), we develop a density-dependent selection criteria to obtain a statistically large sample of BCG progenitors beyond $z \sim 1$.

Our basic idea for selecting BCG progenitors at high redshifts is to select the most massive galaxies in the densest environments. For a complete observational galaxy sample at high redshifts, environmental density can be measured for each galaxy through galaxy counts within a fixed physical aperture. Once the densest environments are located, we select the most massive galaxy in each cylinder as the BCG progenitor candidate. Since we find that a simple fixed galaxy number density approach failed to find the correct progenitors, based on the Millennium simulation, we ultimately employ this method to identify the progenitor galaxies of BCGs.

The summary of this method is that once the environmental densities for all galaxies are obtained, they are ranked from the largest overdensity down to the smallest over-

density. Given the volume of the CANDELS survey and using the number densities of BCGs in the local universe, there will be a number of N BCG progenitors that need to be selected as the most massive galaxies in the top N densest regions.

We apply our method to the observational data of the CANDELS UDS. At a constant number density of $10^{-4.06}h^3\mathrm{Mpc}^{-3}$, 38 progenitors need to be selected at $z = 1 - 3$, as we discussed in Section 4.2.4. The environmental densities have already been measured by Lani *et al.* (2013) for the UDS which covers the CANDELS UDS. Therefore, the densities are known for CANDELS UDS galaxies. By ranking them from the most overdense to the least overdense, we select 38 progenitors as the most massive galaxies in the top 38 densest regions. We then compare this sample with the 469 local descendants from our SDSS DR7 sample.

Although we can obtain a progenitor sample this way, it is possible that a fraction of these galaxies are not the true BCG progenitors but are the progenitors of non-BCGs at $z \sim 0$. Important questions are how many true BCG progenitors are in our selected high-z samples and what fraction of the true BCG progenitors are selected. We carry out a series of tests in the simulations to answer these questions.

4.3.2   Test of Method in Simulations

To test our assumption of the BCG progenitor selection, we use the output of the Millennium Simulation and their respective SAM realisations. The Millennium Simulation uses 2160^3 particles of mass $8.6 \times 10^8 h^{-1} M_\odot$ to follow the evolution of the DM distribution within a comoving box of side $500h^{-1}\mathrm{Mpc}$ from $z = 127$ to $z = 0$ in 64 snapshots. Using the assumption of the ΛCDM cosmological model, the cosmological parameters are $\Omega_\mathrm{m} = 0.25$, $\Omega_\mathrm{b} = 0.045$, $\Omega_\Lambda = 0.75$, $h = 0.73$, $\sigma_8 = 0.9$ and $n_\mathrm{s} = 1$. The SAM used in this work is from De Lucia & Blaizot (2007). They study the formation and evolution of BCGs by applying their model to the output of the Millennium Simulation with the updated treatments for stellar populations, dust attenuation and cooling flow suppression via AGN feedback.

We employ the simulation data at two redshift snapshots. One is $z = 0$ (snapshot=63) at which we identify a sample of BCGs. All of their progenitors can be traced easily

at any higher redshift. The other epoch we study is $z = 2.07$ (snapshot=32) at which we select the progenitor sample by using the same method that we use on our data. Although the 38 progenitors from the CANDELS UDS are chosen from $z = 1 - 3$, their average redshift is $z = 2.06$ (see Fig. 4.1). Thus the simulation comparison is carried out at the SAM snapshot at $z = 2.07$. In the following, we describe in detail how we define the galaxy sample used in the tests at $z = 0$ and $z = 2.07$. We then discuss the fraction of true BCG progenitors which are selected by our method. We also examine and discuss the fraction of BCGs recovered when densities measured with different parameters are used, or when the top three most massive galaxies are identified as the BCG progenitor candidates. The implication of these results will be discussed briefly.

4.3.2.1 Simulation Snapshot at z=0 Sample Selection

In the full simulation box at $z = 0$ BCGs are identified as the most massive galaxy within the virial radius of their DM haloes whose mass $M_{\mathrm{vir}} \geq 10^{13.55} h^{-1} M_{\odot}$. This halo mass criteria is employed to be consistent with the observational halo mass which is $M_{200} \geq 10^{13.55} h^{-1} M_{\odot}$ corresponding to $10^{-4.06} h^3 \mathrm{Mpc}^{-3}$ (see Section 4.2.4). There are 8490 BCGs identified at $z = 0$ in the simulation through this method.

Once the BCGs at $z = 0$ are selected, it is straightforward to trace their progenitors at any higher redshift. For the full comparison between observations and simulations, we use the observational constraints in the simulations. There is a stellar mass cut of $M_*^{\mathrm{cut}} = 10^{9.76} M_{\odot}$ at $z \sim 2$ for the galaxies used in Lani *et al.* (2013) to calculate the density for galaxies in the UDS survey (see Section 4.2.3). To be consistent with this, at $z = 2.07$ in the simulation, we only consider galaxies whose mass $M_* \geqslant 10^{9.76} M_{\odot}$. At each redshift snapshot, every galaxy with $M_* \geqslant 10^{9.76} M_{\odot}$ which ends up as one of our local 8490 BCGs is counted as a true BCG progenitor. At $z = 2.07$ there are $78,454$ true BCG progenitors in total for the whole 8490 BCGs, comprising a "true BCG progenitor catalogue". These progenitors however are not only the most massive progenitors, but include all the individual objects that grow and merge to form the BCGs in the local universe within the simulation.
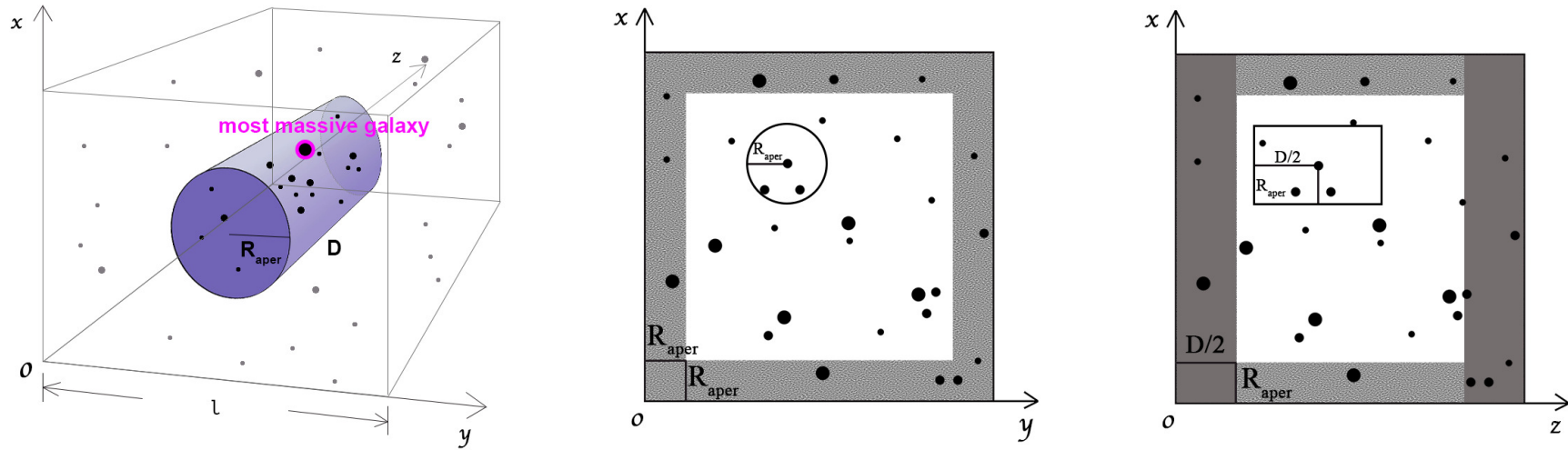
Figure 4.3: Left panel illustrates how density is measured through galaxy counts (black dots) in a cylinder of fixed aperture R_{aper} and depth D (coloured in purple) for the central galaxy. Larger dots show the more massive galaxies. The most massive galaxy in the cylinder, with a magenta circle, is selected as the BCG progenitor candidates in this example. The density is measured in the z-direction of the box in the simulation. The grey dots are the galaxies outside the cylinder. Middle panel shows a cross section perpendicular to the z-axis. Density is not calculated for those galaxies in the shaded area whose vertical distance to the box edges of the x-axis or y-axis is less than the aperture radius R_{aper}. Right panel shows a cross section perpendicular to the y-axis. Density is not calculated for those galaxies in the dark shaded area whose distance in z direction to the x-y surface is less than $D/2$. In all, galaxies in the dark and light shaded area in the right panel are excluded from the density catalogue in the simulation. The density of galaxies in the inner white region is measured within a fixed aperture, as shown in the left panel.

4.3.2.2 Snapshot of z=2.07

In order to apply our observational method on the simulation data to select BCG progenitor candidates, we first calculate the environmental density for galaxies in the full simulation box at $z = 2.07$ by using galaxy counts in a fixed physical aperture, with some modification of Equation 4.1. In the simulations, there are no bad pixels that need to be masked as in the observations. Thus the $N_{\mathrm{mask}}^{\mathrm{aper}}$ term is the area of the chosen aperture, and $N_{\mathrm{mask}}^{\mathrm{tot}}$ is the area of one side of the full box. The term $N_{\mathrm{mask}}^{\mathrm{tot}}/N_{\mathrm{mask}}^{\mathrm{aper}}$ then reduces to $l^2/(\pi R_{\mathrm{aper}}^2)$, where l is the box length of one side (i.e., 500 h^{-1}Mpc) and R_{aper} is the aperture radius. We use a density contrast in our test defined as

$$\delta = \frac{N_{\mathrm{g}}^{\mathrm{aper}}}{N_{\mathrm{z}}} \times \frac{l^2}{\pi R_{\mathrm{aper}}^2} - 1, \qquad (4.2)$$

where $N_{\mathrm{g}}^{\mathrm{aper}}$ is, as before, the number of galaxies in the chosen aperture. N_{z} is the total number of galaxies within $l^2 \times D$, following the definition in Lani *et al.* (2013), where D is the depth of the cylinder. The cylinder we use is in the direction of the z-axis. The left panel of Fig. 4.3 illustrates how the density is measured within a fixed aperture. The most massive galaxy in the cylinder (circled in magenta) is a BCG progenitor candidate as we discuss in Section 4.3.1.

The values of the aperture radius R_{aper}, and the depth of the cylinder D, are chosen to be similar to the ones adopted in Lani *et al.* (2013) who construct a cylinder with an aperture radius of 400 kpc, and depth of 1 Gyr to measure UDS densities. In the simulation, the value of $R_{\mathrm{aper}} = 400$ kpc can be employed easily. However, it is difficult to apply a 1 Gyr depth as the cylinder depth in one single box. Unfortunately, the 1σ uncertainty of the UDS photometric redshifts $\Delta z \sim 0.1$ at $z \sim 2$ corresponds to $\pm 300 h^{-1}$Mpc ($\Delta v \sim \pm 30000$ km/s). This is already larger than the box size in each redshift snapshot. The depth of 1 Gyr is thus several times greater than the 1σ uncertainty of the UDS photometric redshift. Since we are limited by the simulation box, we are more generous in considering the photometric redshift errors at high redshift. Additionally, to ensure a large sample of galaxies in the simulation box being eligible to have a reliable density measurement, we use $D = 120 h^{-1}$Mpc as the cylinder depth.

As we mention in Section 4.3.2.1, only galaxies whose mass $M_* \geqslant 10^{9.76} M_\odot$ will be

considered within the $z = 2.07$ selection in the simulation. However, density is not measured for galaxies too close to the box edges, as a full measure of environment cannot be done. Therefore, there is no measurement of environmental density for galaxies whose perpendicular distance to the box edges in the x-axis or y-axis is less than the chosen aperture radius. The middle panel of Fig. 4.3 shows a cross section perpendicular to the z-axis. The galaxies in the shaded area are excluded from the density catalogue.

On the other hand, if the distance in the z direction from one galaxy to the x-y surface is less than $D/2$, the density measurement will not be employed on this galaxy for the same reason that no galaxy information can be traced in the space outside the simulation box. A cross section perpendicular to the y-axis in the right panel of Fig. 4.3 illustrates this requirement on distance in the z-direction. Finally, a density catalogue which is ranked from the largest densities to the smallest densities is created for galaxies with $M_* \geqslant 10^{9.76} M_\odot$ at $z = 2.07$ in the simulation. The most massive galaxy is known in each density and is taken as the BCG progenitor candidate in our selection.

In the simulation, fixed number density tracing is applied as well. Since there are 8490 BCGs at $z = 0$ in the simulation, we need to select 8490 progenitors within the $z = 2.07$ snapshot. Based on our assumption for BCG progenitors, the progenitor sample galaxies are identified as the most massive galaxies in the top 8490 densest environments in the simulation. Finally, the number of true BCG progenitors within our observationally based selection sample can be known by matching our 8490 progenitors with the $78,454$ true BCG progenitors the simulation gives us.

4.3.2.3 Fraction of the Selected True BCG Progenitors

In order to show explicitly how many true BCG progenitors can be found with our observationally based selection method, we define

$$f_{\mathrm{tot}} = N_{\mathrm{tot}}^{\mathrm{match}}/N_{\mathrm{tot}}, \tag{4.3}$$

which is a fraction of the true BCG progenitors in our selected high-z progenitors. The term $N_{\mathrm{tot}} = 8490$ is the total number of the progenitor galaxy sample identified

through our method as the most massive galaxies in the densest environments. $N_{\text{tot}}^{\text{match}}$ is the number of true BCG progenitors found within these $N_{\text{tot}} = 8490$ progenitors. Note that we allow more than one BCG progenitors to end up in the same local BCG.

In the end, we find $f_{\text{tot}} = 45\%$, indicating that the progenitor sample selected by our density-dependent method at $z \sim 2$ is not a pure sample of true BCG progenitors, but is contaminated by 55% of progenitors of local non-BCG galaxies (we call these systems non-BCG progenitors hereafter). This is a much higher fraction of successful progenitor selection than we would get using a simple fixed galaxy number density on the most massive galaxies (35%). In the 3780 (45%) true BCG progenitors of our selected sample, 2042 of them are the most massive progenitors of BCGs. In Section 4.3.3.1, we will examine how different the properties are between our true BCG progenitors and the non-BCG progenitors, as well as discuss whether the progenitor sample we select can be used to trace BCG evolution and how to account for this contamination when comparing high and low redshifts.

4.3.2.4 Effect of Density Measurement Method

The f_{tot} value we measure is based on the density measurement with a cylinder size of $R_{\text{aper}} = 400$ kpc and $D = 120h^{-1}$Mpc. In this section, we examine whether the cylinder size can significantly effect the fraction of the selected true BCG progenitors using our method. We thus apply different apertures and depths to calculate the environmental density.

First, with a fixed depth of $D = 120h^{-1}$Mpc, we employ different aperture radii from the local scale $R_{\text{aper}} = 250$ kpc, to the global scale $R_{\text{aper}} = 1$ and 2 Mpc. The total fraction of selected true BCG progenitors is then $f_{\text{tot}} = 47\%$, 42% and 39%, respectively for these different scenarios. It thus appears that f_{tot} increases at smaller aperture radii, however the aperture size is not a major factor in significantly increasing the number of selected true BCG progenitors.

We also measure galaxy number densities within cylinders with a fixed aperture of $R_{\text{aper}} = 400$ kpc and with different depths of $D = 250, 30,$ and $4h^{-1}$Mpc. $250h^{-1}$Mpc represents the largest photometric redshift uncertainty which we have in the data.

$30h^{-1}$Mpc is of the same order of redshift accuracy measured by narrow-band imaging, and $4h^{-1}$Mpc is the spectroscopic redshift measuring error. The corresponding total fractions are then: $f_{\text{tot}} = 36\%$, 51% and 56%, respectively. This implies that if spectroscopic redshifts for a large sample of galaxies in the early universe could be measured accurately in observations, the fraction of selected true BCG progenitors could increase by $> 10\%$ compared to using SED-fitted photometric redshifts. However, the fraction of true BCG progenitors selected as the most massive galaxies in the densest environments cannot exceed 70% even if we use a cylinder with very small aperture (e.g., $R_{\text{aper}} = 250$ kpc) and a spectroscopic redshift uncertainty (e.g., $4h^{-1}$Mpc). This suggests that there is a natural limit in how well we can trace BCG progenitors with this method.

The length of the cylinder used to measure density in the observations is equivalent to 1 Gyr of look-back-time (or $\sim 1000h^{-1}$ Mpc around $z \sim 2$), which is significantly larger than the one we have used in the simulations due to the size of the simulation box. In order to use a cylinder with a more similar length to the one used in the observations, we have replicated the $z = 2.07$ simulation box on all sides, taking advantage of the periodic boundary conditions. This allows us to measure environmental density with cylinder whose length is more than $500h^{-1}$ Mpc. By using cylinder lengths of $500h^{-1}$ Mpc and $1000h^{-1}$ Mpc, the fraction of the true BCG progenitors in our selected high-z sample is $\sim 41\%$ in both cases, a number that is very similar to what was found with smaller cylinders. We are thus reassured that our results on BCG evolution do not depend on the exact size of the cylinder used in the simulation tests.

4.3.2.5 Effect of Galaxy Stellar Mass

De Lucia & Blaizot (2007) show in simulations that BCG progenitors have a wide stellar mass distribution from $10^{10} M_{\odot}$ to $10^{12} M_{\odot}$, and there is a good overlap between the mass distribution of high-z massive galaxies and the massive progenitors of local BCGs. This implies that the most massive galaxy in a dense region could be a non-BCG progenitor and we could miss out those true BCG progenitors whose stellar masses are slightly smaller.

Therefore, in the simulation, we select the candidates of BCG progenitors from a larger

pool that includes the second and third most massive galaxies in the densest regions to examine the possible effect from stellar mass differentials. We carry out this test through a method of iterative matching. We first test if the most massive galaxy in a given environment is a BCG progenitor. If this most massive galaxy is matched as the true BCG progenitor then we do not further match the 2nd and 3rd massive galaxies. However, if the top massive galaxy is a not a BCG progenitor then we match the 2nd most massive galaxy in that environment with the true BCG progenitors. No further matching will be done on the 3rd galaxy as long as the 2nd one is the true BCG progenitor. If neither the 1st or 2nd massive galaxies are BCG progenitors then we match the 3rd most massive one. This selection down to the 3rd most massive galaxy increases the total fraction of the true BCG progenitors we select to $f_{\mathrm{tot}} = 55\%$.

Combined with the results of Section 4.3.2.4 this indicates that a large fraction of massive galaxies in very dense environments at high redshift do not end up in $z = 0$ BCGs but in local normal massive galaxies. Both overdensity and stellar mass are not unique tracers for identifying true BCG progenitors at $z \sim 2$. Other than using environmental density, we also examine the fraction of true BCG progenitors in the simulation if our progenitors are selected based on their host DM subhalo masses. Muldrew, Pearce & Power (2011) demonstrate that in simulations the maximum circular velocity of the subhalo is a better property to represent the subhalo mass than the virial mass of subhalo. We thus examine the selection that the BCG progenitors are selected as the 8490 most massive galaxies in the top 8490 subhaloes sorted by their maximum circular velocity. If we use this method, the total fraction of the selected true BCG progenitors increases to $f_{\mathrm{tot}} = 65\%$. Although dark matter is a more promising tracer to find BCG progenitors at $z \sim 2$, it is hard to apply it on observation data since measuring the maximum circular velocity of subhalo cannot be done observationally at the moment. However, ultimately this may be a better method of finding BCG progenitors in the future.

4.3.3   Effect of Contaminants in Our Selected Sample

Since our final aim is to apply our BCG progenitor selection on the CANDELS UDS data by employing the UDS density catalogue, the following discussion will be based

on the results of the simulation tests in Section 4.3.2.3. We show that using the density measured as in Lani *et al.* (2013) within the UDS, our selected progenitors at $z \sim 2$ are not pure BCG progenitors, but consist of 45% true BCG progenitors and 55% non-BCG progenitors as contaminants. This means that within the 38 progenitors selected from the CANDELS UDS at $1 \leqslant z \leqslant 3$, about 17 of them are BCG progenitors and the rest are contaminants. It is, however, impossible to know from the available data which are the real BCG progenitors and which are not.

In the following we first show, based on simulations, that the properties of our entire selected progenitor sample and the 45% true BCG progenitors within them are not significantly different. Next, in order to trace BCG evolution down to $z \sim 0$, our selected progenitors at high redshifts need to be compared with their counterparts in the local universe, which will be a mixture of BCGs and non-BCGs. We demonstrate below that the local non-BCGs which are the descendants of those 55% non-BCG progenitors statistically share similar properties of local BCGs. We find that the uncertainty resulting from the contamination in our samples does not erase the BCG evolution signal. The comparison, at the same number density, between the progenitors we select at high redshift with their local counterparts can therefore give us an accurate measurement of BCG evolution.

4.3.3.1 Contamination at High-z

From the test we carry out in Section 4.3.2, we know that the 38 progenitors that we select from the CANDELS UDS by our method is a mixed sample with 45% true BCG progenitors and 55% non-BCG progenitors. The question we need to answer is how the contaminant non-BCG progenitors differ from the true BCG progenitors. Ideally, the comparison should be carried out in observational data between the whole 38 progenitors and the 17 true BCG progenitors within them. However, there is no method that can identify the true BCG progenitors in our selected high-z sample. Therefore, we carry out our comparison in simulation by using the 8490 progenitors selected through the observationally based selection. They are compared with the 3780 (45%) true BCG progenitors, and 4710 (55%) non-BCG progenitors within them (see Section 4.3.2.2 and Section 4.3.2.3). The properties within the simulation we discuss are
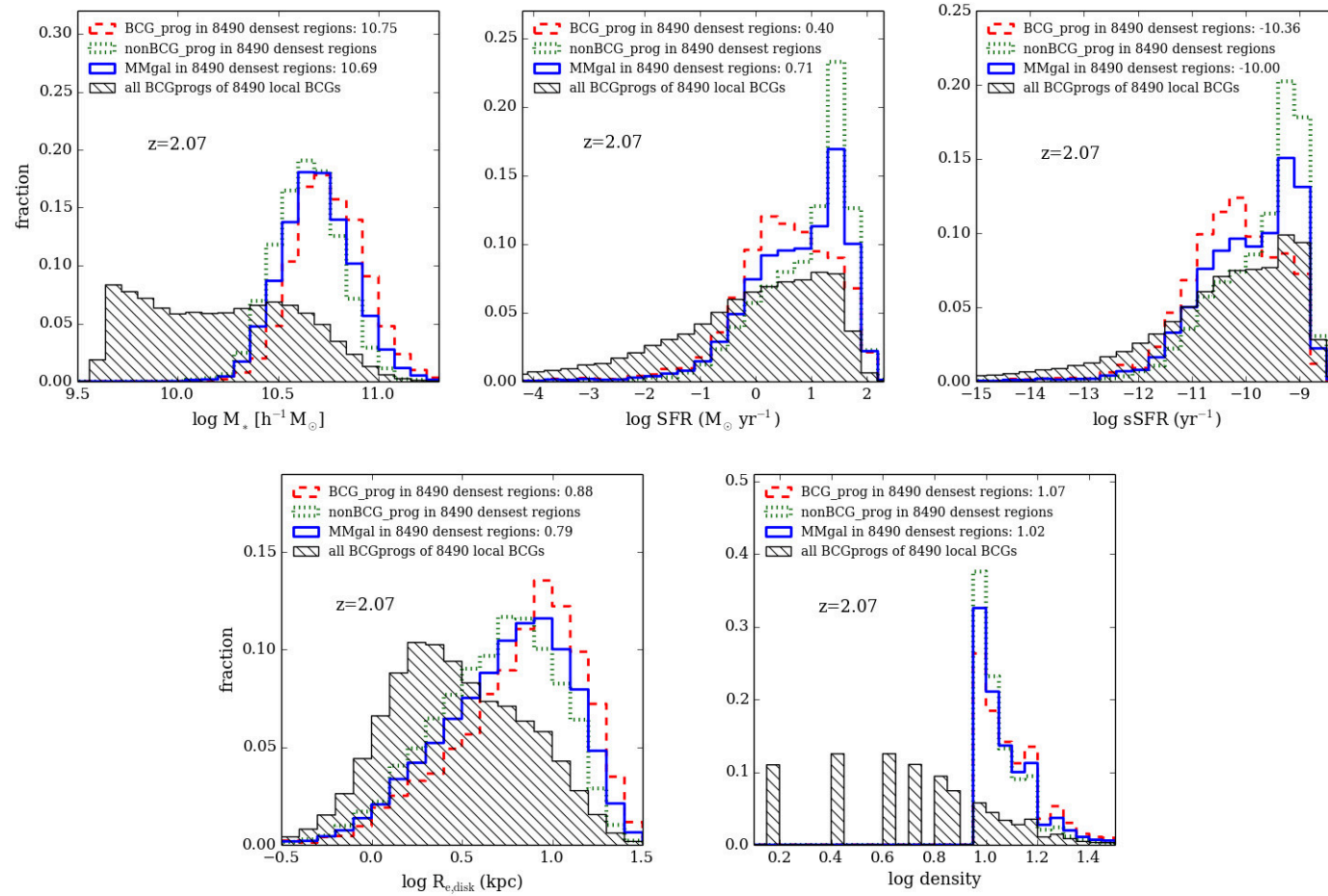
Figure 4.4: Property distributions of the 8490 most massive galaxies in the top 8490 densest regions (blue solid) at $z = 2.07$ from the Millennium simulation. In the upper-row, stellar mass, SFR, and sSFR are shown in panels from left to right, respectively. In the lower-row, the left panel is the disk radius distribution, and the right panel is for density measured within a fixed aperture. In each panel, distribution of the 45% true BCG progenitors within these 8490 galaxies is illustrated as the red dash line. The remaining 55% non-BCGs progenitors are presented in the green dotted line. The black line with shadow presents the distribution of the entire 78,454 progenitors of local 8490 BCGs in the simulation. The numbers in legend show the median value of the corresponding distributions. Detail discussions can be found in text.

stellar mass, SFR/sSFR, disk radius, and density and position of galaxies.

First, we examine the differences in galaxy masses. The left panel in the upper-row of Fig. 4.4 illustrates the stellar mass distribution of our selected 3780 true BCG progenitors (red dash line) and the 4710 non-BCG progenitors (green dotted line) in the simulation. It illustrates that the true BCG progenitors selected by our method are slightly more massive than those selected which are non-BCG progenitors. The non-BCG progenitors make the entire 8490 progenitors (shown blue solid line) have on average a somewhat smaller stellar mass. The median stellar mass of true BCG progenitors is $10^{10.75}h^{-1}$ M$_\odot$, and it is $10^{10.69}h^{-1}$ M$_\odot$ for all the 8490 progenitors. The effect of non-BCG progenitors on the stellar mass distribution is thus to make it 0.06 dex smaller. Moreover, we also plot the mass distribution of the entire $z = 2.07$ progenitor population of the 8490 $z = 0$ BCGs (i.e., the 78,454 true BCG progenitors. See Section 4.3.2.1). This is shown in Fig. 4.4 as the black shaded area. It is clear that our method selects those BCG progenitors at the most massive end.

The next two properties we examine are SFR and sSFR, whose distributions are shown in the middle and right panels in the upper-row of Fig. 4.4. As can be seen, the non-BCG progenitors, which make up 55% of the selected sample (green dotted line), and the entire selected samples (blue solid line) have a different distribution from the 45% true BCG progenitors (red dash line). The actual BCG progenitors distribute relatively evenly over $\log SFR = [0, 2]$ ($\log sSFR = [-11, -9]$), with a larger fraction found towards the low SFR and low sSFR values. If we take the median SFR of the 8490 progenitors as a threshold, the majority of the true BCG progenitors have a SFR lower than $\log SFR = 0.71$ and a similar fraction for sSFR selection. In contrast, the selected non-BCG progenitors and the whole progenitor sample are dominated by galaxies with high SFR (high sSFR). The non-BCG progenitor population makes the SFR (sSFR) distribution of the entire selected progenitors larger by a factor of ~ 0.3 dex (~ 0.4 dex) than the true BCG progenitors.

The left panel in the lower-row of Fig. 4.4 shows the distribution of disk radius which is derived by De Lucia & Blaizot (2007) from halo radius following the relationship in Mo, Mao & White (1998). We find that non-BCG progenitors (green dotted line) in our selected sample tend to have smaller disk radii, making the entire sample of

selected progenitors (blue solid line) more compact in disk size by a factor of 0.1 dex than the true BCG progenitors (red dash line). At the same time, it is clear that the true BCG progenitors we select from the densest environments have much larger radii compared with the entire 78,454 true BCG progenitors of the 8490 $z = 0$ BCGs (black shaded area).

Moreover, we also check the environments of our selected samples in the simulation. The distribution of density where our selected progenitors reside is presented in the right panel in the lower-row of Fig. 4.4. We find that the environments of the 45% true BCG progenitors (red dash line) are only marginally denser than the environments which host the 55% non-BCG progenitors (green dotted line). About 10% more non-BCG progenitors are in the less dense regions. Nevertheless, a K-S test demonstrates that the entire sample of our selected progenitors (blue solid line) are within the same local density as the 45% true BCG progenitors. This result is partially by design given that we only select our progenitors based on being in dense environments. However it might be the case that the BCG progenitors are more likely to be found in the densest environments among this selection, but this appears to not be the case as presented by the black shaded area which shows environments of the entire 78,454 true BCG progenitors of the 8490 $z = 0$ BCGs. It is clear that majority of the true BCG progenitors reside in less dense regions.

In addition to the environmental density, the location of the galaxy in the host dark matter halo is examined as well. The simulation gives the central galaxy of its FOF group as type 0, the central galaxy of a subhalo is type 1, and satellite galaxy as type 2. In the 3780 true BCG progenitors we select, 71% of them are type 0 galaxies while 19% are type 1 galaxies and the rest 10% are type 2 galaxies. In the 4710 non-BCG progenitors, we find that 72% are type 0 galaxies, 23% are type 1 galaxies and other 5% are type 2 galaxies. There is thus not much difference in terms of galaxy position within their respective groups and clusters between BCG progenitors and non-BCG progenitors.

Based on the simulation, we find that the properties of the entire progenitor population selected by our method are very similar to the properties of the actual BCG progenitors within them. These properties include: stellar mass, disk radius and environment. The

non-BCG progenitors do however appear to influence the distribution of SFR/sSFR, driving the SFR/sSFR of the entire selected progenitors higher by a factor of $0.3 - 0.4$ dex larger.

We apply these findings on our 38 observational progenitors, supposing that their stellar masses and effective radii represent the true BCG progenitor at $z \sim 2$ but with a ~ 0.4 dex larger SFR/sSFR. In Section 4.3.3.3 we demonstrate that the evolution of BCGs over $z = 0 - 2$ is intrinsic, and still evident, even if the systematic raising of the star formation from the non-BCG progenitors is considered.

We mentioned in Section 4.3.2.3 that in the 3780 (45%) true BCG progenitors of our selected sample, 2042 of them are the most massive progenitors of BCGs. If only these most massive progenitors are considered as the true BCG progenitors, we examine again the difference in properties between the 2042 most massive BCG progenitors and our whole 8490 selected progenitor sample. We find that the stellar mass of our 8490 selected progenitors is 0.15 dex less than the stellar mass of 2042 most massive BCG progenitors, and the SFR/sSFR of our entire selected progenitors is still ~ 0.4 dex larger. There is not much difference in effective radius in this case. We will discuss in 4.3.3.3 that how BCG evolution could be affected if only the most massive BCG progenitors are considered.

4.3.3.2 Contamination in the Local Universe

Since the progenitor population selected by our method is a mixture of real BCG progenitors and non-BCG progenitors, in order to trace evolution down to $z \sim 0$, the local comparison should be the $z \sim 0$ counterparts of our high-z progenitors rather than a pure local BCG sample. In this section, we discuss how we construct an observational local mixed sample which consists of the descendants of both our selected high-z non-BCG progenitors and the BCG progenitors. We also examine whether the properties of a locally mixed sample are different from a pure BCG sample due to the non-BCG contamination. At our constant number density selection of $10^{-4.06}h^3\text{Mpc}^{-3}$, we calculate that 469 local descendants should be selected from SDSS DR7. We must populate these descendants with both real BCGs and other non-BCG galaxies.

In the simulation, we find that within the $z = 0$ descendants of the $z = 2.07$ 8490 selected progenitors found using our observational method, 38% of them are BCGs and the remaining 62% are non-BCGs. There is no 1-to-1 correspondence between high-z progenitor and local descendant, which is due to the fact that more than one progenitors could merge to end up in the same local descendant. Therefore the fraction (38%) of BCGs in the local mixed sample is not necessarily the same as the fraction (45%) of true BCG progenitors in high-z selected progenitor sample. Applying the fractions of local BCGs and non-BCGs to the 469 local observational sample, there are thus 291 non-BCGs and 178 BCGs we should identify to build up a mixed counterpart sample at $z \sim 0$.

In order to ensure that the 291 local non-BCGs we identify in SDSS DR7 catalogue are likely the descendants of our selected high-z contaminants from CANDELS UDS, they are chosen according to their distribution within the whole $z = 0$ galaxy population in terms of stellar mass. This distribution can be determined based on our simulation results. In the simulation, at $z = 2.07$, 4710 galaxies (55%) selected by our method in the top 8490 densest regions evolve into non-BCGs at $z = 0$. In terms of stellar mass, how these non-BCGs distribute in the whole $z = 0$ galaxies can be known. By ranking galaxies by stellar mass from large to small in the $z = 0$ box, descendants of our non-BCG progenitors are located by their stellar masses (hereafter we call the mass-ranked whole local galaxy population as the "galaxy pool").

Therefore, down to a specific stellar mass $M_{*,\text{threshold}}$ in the galaxy pool, we could know how many non-BCGs whose $M_* \geqslant M_{*,\text{threshold}}$ are there. Note that, in the galaxy pool, a specific stellar mass $M_{*,\text{threshold}}$ corresponds to a number of galaxies whose $M_* \geqslant M_{*,\text{threshold}}$. Taken into account the local comoving volume, a specific stellar mass $M_{*,\text{threshold}}$ then corresponds to a cumulative number density $ND(> M_{*,\text{threshold}})$. Since we use the number density of $ND = 10^{-4.06} h^3 \text{Mpc}^{-3}$ in this work, to be convenient, we take this value as a unit. When we explore the mass distribution of non-BCGs in the galaxy pool, we choose a number of $M_{*,\text{threshold}}$ whose converted cumulative number densities are $m \times ND$ where $m = 1/2, 1, 2, 4, 8, 16, 32, 64$. In Fig. 4.5, the upper tick labels of x-axis show the stellar masses $M_{*,\text{threshold}}$ we choose in the $z = 0$ simulation box, and the lower tick labels of x-axis show the corresponding
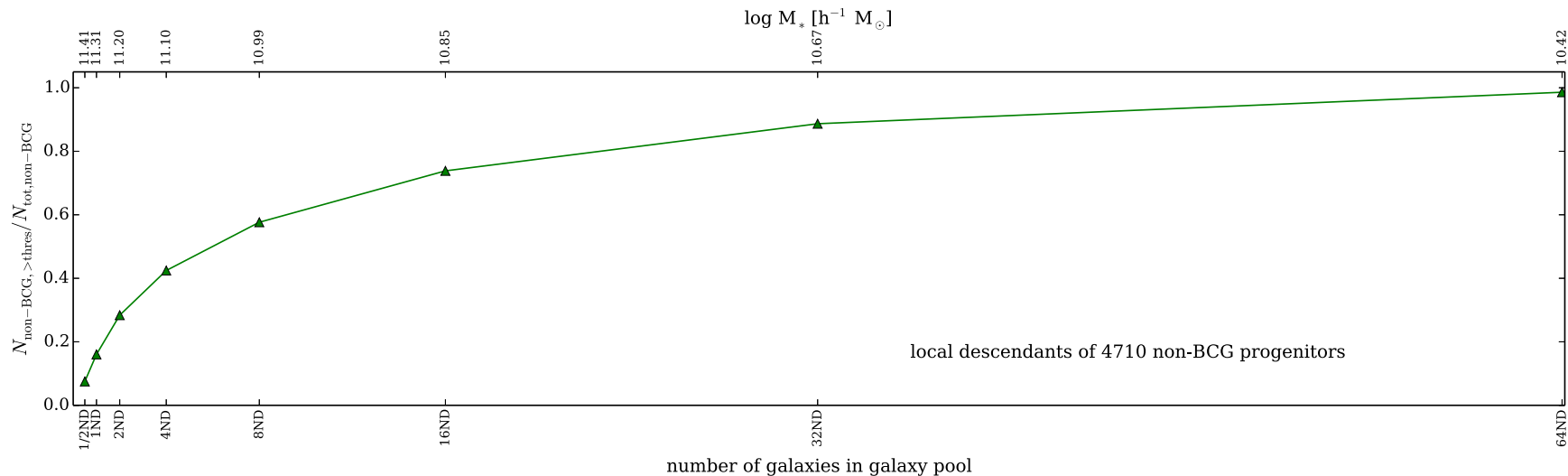
Figure 4.5: Cumulative fraction of local non-BCGs which are the descendants of the 4710 $z = 2.07$ non-BCG progenitors in the simulation. These galaxies are plotted as a function of galaxy number in the "galaxy pool" (see text) from our simulation. Galaxies in the galaxy pool are ranked by their stellar masses, from large to small. Note that the galaxy number in the galaxy pool can easily be converted to a number density by dividing the volume of the $z = 0$ simulation box ($500^3 h^{-3} \text{Mpc}^3$). At the number density of $ND = 10^{-4.06} h^3 \text{Mpc}^{-3}$, we choose the numbers, such that they can be converted as $m \times ND$ where $m = 1/2, 1, 2, 4, 8, 16, 32, 64$. The tick label of the x-axis is thus expressed in terms of $m \times ND$. Searching from the most massive galaxy down to a chosen number of galaxies (i.e., $m \times ND$), the number of descendants we retrieve from our selected non-BCG progenitors is obtained, which is expressed as $N_{\text{non-BCG},>\text{thres}}$. This number $N_{\text{non-BCG},>\text{thres}}$ can be converted into a cumulative fraction defined as $f_{\text{non-BCG},>\text{thres}} = N_{\text{non-BCG},>\text{thres}}/N_{\text{tot,non-BCG}}$ where $N_{\text{tot,non-BCG}}$ is the total number of $z = 0$ descendants of the 4710 non-BCG progenitors. When the y-axis reaches $= 1$ this is when all of the descendants of non-BCG progenitors have been recovered.

cumulative number density.

Down to each $M_{*,\text{threshold}}$, the number of descendants of our selected non-BCG progenitors can be obtained (we express this as $N_{\text{non}-\text{BCG},>\text{thres}}$). This number can be converted to a cumulative fraction defined as $f_{\text{non}-\text{BCG},>\text{thres}} = N_{\text{non}-\text{BCG},>\text{thres}}/N_{\text{tot,non}-\text{BCG}}$ where $N_{\text{tot,non}-\text{BCG}}$ is the total number of $z = 0$ descendants of our 4754 non-BCG progenitors. This fraction is the y-axis of Fig. 4.5. Fig. 4.5 finally shows the distribution of the $z = 0$ descendants of our selected non-BCG progenitors in the galaxy pool in terms of stellar mass. If the total number of non-BCGs is known (i.e., $N_{\text{tot,non}-\text{BCG}}$ is known), this figure essentially tells us how many non-BCGs are between two adjacent cumulative number densities of galaxy pool. This figure also tells us we need to go down to $64ND$ in the galaxy pool to retrieved almost all the descendants of our non-BCG progenitors.

We apply this distribution to the SDSS DR7 galaxies to select the observational descendants of our high-z non-BCG progenitors. In observation, the galaxy pool is comprised of the SDSS DR7 galaxies which are at $0.02 \leqslant z \leqslant 0.1$ and are ranked by stellar mass from large to small. The cumulative number densities $m \times ND$ where $m = 1/2, 1, 2, 4, 8, 16, 32, 64$ are also used for the SDSS DR7 data. For each cumulative number density, the corresponding number of SDSS DR7 galaxies (counted from the most massive galaxy) is known, from which the non-BCGs are selected. Since we need to obtain 291 non-BCGs to contaminate our pure BCGs (i.e., $N_{\text{tot,non}-\text{BCG}} = 291$), how many non-BCGs should be selected between two adjacent cumulative number densities could be known according to Fig. 4.5. The non-BCGs are then selected randomly from galaxies which are not BCGs.

There is also the caveat that the galaxy distribution in our simulation cannot fully represent the observational one due to the unclear baryon physics in galaxy formation and evolution. However, the distribution of local descendants of high-z non-BCG progenitors from this simulation is currently the best method we can take for selecting non-BCG descendants in observations. Moreover, since the formation and evolution of non-BCGs may involve fewer hydrodynamical mechanisms such as inflows/outflows at $z < 3$, the simulation results for non-BCGs could be better than the results for BCGs.
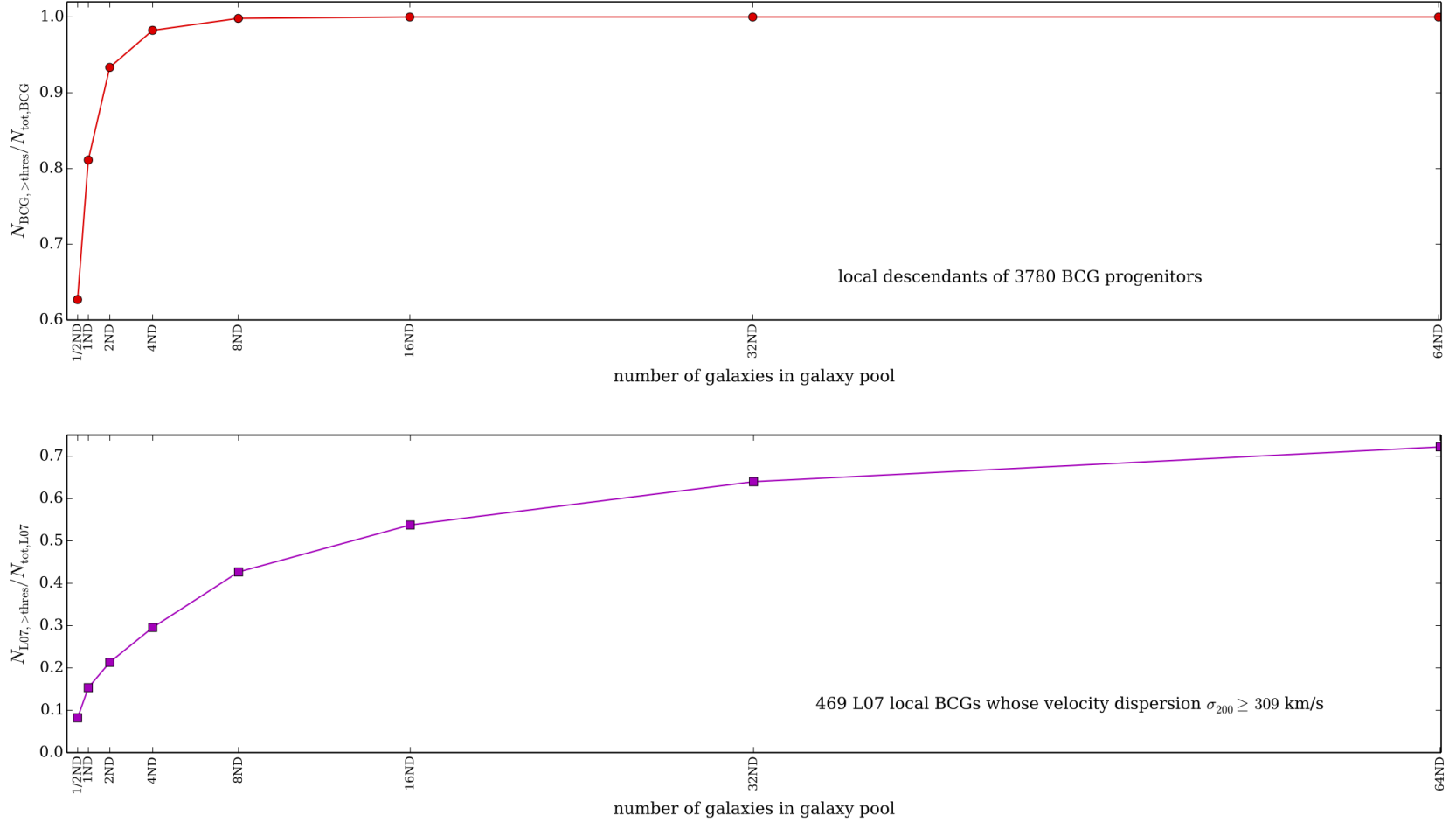
Figure 4.6: *Upper* panel: cumulative fraction of simulated $z = 0$ BCGs which are the descendants of the 3780 $z = 2.07$ BCG progenitors as a function of galaxy number density in the simulated galaxy pool. *Lower* panel: Real data for BCGs, showing the cumulative fraction of local L07 BCGs as a function of galaxy number in the SDSS DR7 galaxy pool.

The question now is: how do we select the BCG themselves at low redshifts? Similar to Fig. 4.5 for local non-BCGs, the upper panel of Fig. 4.6 shows the distribution of $z = 0$ BCGs which are the descendants of our selected 3780 $z = 2.07$ BCG progenitors in the simulation. However, this simulation and others create too many massive galaxies compared with observations at $z \sim 0$ (e.g., Lin *et al.* 2013), such that the simulation distributions of local massive galaxies does not represent the real observational ones correctly. This is shown clearly by comparing the upper panel of Fig. 4.6 with the lower panel which illustrates the L07 BCG distribution in the SDSS DR7 galaxy population. Therefore, we select 178 BCGs from the L07 catalogue according to the L07 BCG distribution. The BCGs within every bin are selected randomly from those galaxies which are L07 BCGs whose host clusters have velocity dispersion $\sigma_{200} \geq 309$ km/s.

Combining the 178 BCGs and the 291 non-BCGs, the final local mixed sample is created. We run this process 10 times to get 10 sets of local mixed sample avoiding biases from selecting a single sample. In order to examine the effect of non-BCG properties, we compare the 469 local mixed sample with the 178 pure local BCGs within them.

In Fig. 4.7, the dotted colour lines present the property distributions of our 10 sets of mixed samples at $z \sim 0$, and the magenta solid lines are for our one set of 178 pure BCGs (the properties of 10 sets pure BCGs are very similar, therefore we plot only one set pure BCGs to keep the plots clean). We find very little effect from the non-BCGs on the BCG properties, such that the mixed sample have very similar structures (n and R_{e}), *RFF*, stellar mass and SFR/sSFR as pure BCGs. Note that the stellar mass distribution of the local mixed sample has a relatively evident offset from the pure BCGs by a factor of 0.08 dex. Nevertheless, the uncertainty derived from the descendants of our selected non-BCG progenitors is no larger than ~ 0.1 dex for all the properties we explore.

4.3.3.3 Can Contaminants erase BCG Evolution?

In Section 4.3.3.1 we find that the effect of contamination from non-BCG progenitors is very small on BCG progenitor stellar mass and size (< 0.1 dex), but is more evident on SFR/sSFR by increasing them by a factor of ~ 0.4 dex. In Section 4.3.3.2 we
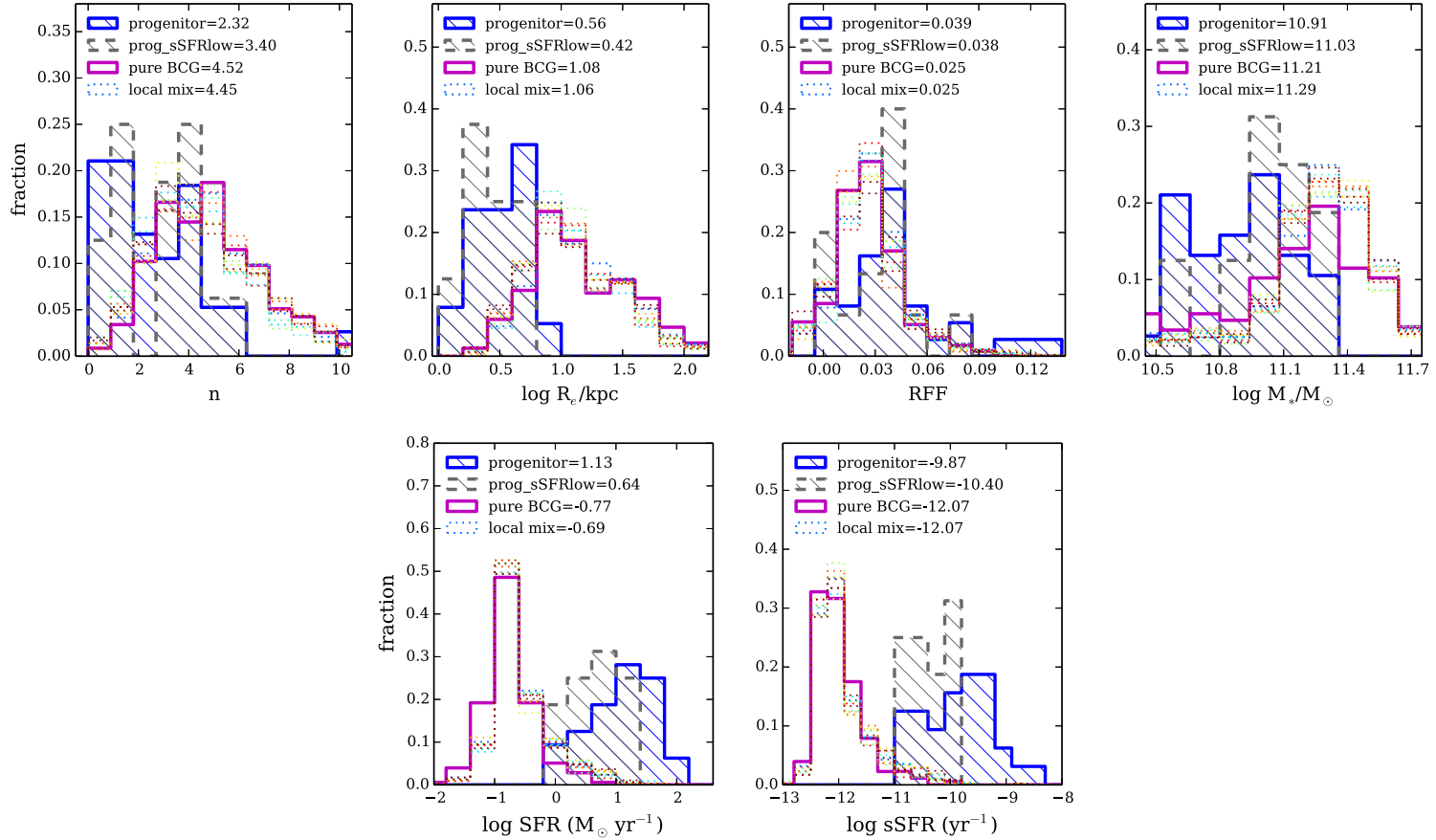
Figure 4.7: Distribution of Sérsic index n, effective radius, *RFF*, stellar mass, SFR and sSFR from our observations. The blue solid line with shadow in each panel shows the property distribution of the 38 high-z progenitors selected by our method from CANDELS UDS. Specifically, the grey dashed lines with shadow illustrate the distributions of our selected progenitors whose sSFR is lower than the median value (i.e., $\log sSFR < -9.87$). The several colour dotted lines show the distributions of the 10 sets of local mixed sample each of which contains 291 non-BCGs and 178 BCGs. Magenta solid line is for the 178 pure BCGs in one set of the local mixed sample. The legends indicate the median value of each distribution. The value for the local mixed sample in the legend is the average median value of the 10 sets. Detailed discussions are in the text.

demonstrate that the effect of the descendants of non-BCG progenitors is no more than ~ 0.1 dex on local BCG structure, stellar mass or SFR/sSFR properties. In this section, we will examine whether the uncertainty introduced by both non-BCG progenitors and local non-BCGs will erase the BCG evolution since $z \sim 2$ and whether the BCG evolution we find by our method is intrinsic.

The properties of our 38 selected progenitors are plotted in Fig. 4.7 in blue solid lines with shadow. Note that there is one progenitor has very bad original CANDELS UDS image which results in unreliable fitting result (see Fig. 4.9). Therefore, we do not take into account its shape, size, and morphology in our discussions. Comparing the properties of our high-z progenitors with the properties of the $z \sim 0$ mixed sample (colour dotted lines), we find that BCG evolution is evident since $z \sim 2$ even if uncertainties are taken into account. We discuss this for stellar mass, SFR/sSFR and size specifically below.

We find that even if the BCG mass growth decreases when the 0.06 dex uncertainty from non-BCG progenitors and the 0.08 dex uncertainty from local non-BCGs are considered, the mass build-up in BCGs remains clear, growing by a factor of 0.24 dex over $z = 0 - 2$. The systematic contamination cannot erase the change of BCG SFR/sSFR either since the difference in SFR/sSFR between high-z progenitors and their local counterparts (~ 1.8 dex for SFR; ~ 2.2 dex for sSFR) is much larger than the 0.4 dex uncertainty from non-BCG progenitors. In respect of effective radius, 0.4 dex size growth still remains even if the 0.1 dex systematic contamination from non-BCG progenitors is considered.

If we only consider that the most massive BCG progenitors are the true BCG progenitors, in Section 4.3.3.1, we find that the contamination makes the stellar mass of our high-z progenitors ~ 0.15 dex less than those of the most massive BCG progenitors. Taking into account the 0.08 dex uncertainty from local non-BCGs, we find that BCGs grow in mass by a factor of 0.15 dex over $z = 0 - 2$ in this case. Previous discussion shows that the BCG mass growth is 0.24 dex when all the selected true BCG progenitors are considered. It implies that the stellar mass evolution we find by considering all the selected true BCG progenitors is an upper limit. The evolutions of effective radius and SFR/sSFR, however, are not affected if only the most massive BCG progenitors

are considered.

In Section 4.3.3.1 we find that our selected progenitors whose SFR/sSFR is less than the median value are more likely to be the true BCG progenitors. Since a low-SFR/-sSFR subsample may be more likely the true BCG progenitors, we examine their properties specifically. In Fig. 4.7, the grey dashed lines with shadow represents the property distribution of our selected progenitors with low star formation rate whose $\log sSFR < -9.87$. These lower star forming systems have a much lower SFR and sSFR than the entire selected progenitor sample (by design), and are slightly more compact, more concentrated, and more massive. Nevertheless, the evolution in our selections from $z \sim 2$ to $z \sim 0$ remains statistically evident.

In all, we demonstrate that BCG evolution based on our selection of high-z progenitors and the local descendants must intrinsically be true. The uncertainties introduced by the contaminant non-BCG progenitors and local non-BCGs have relatively little effect, and cannot account for the evident evolution since $z \sim 2$. Even considering the low-sSFR subsample of high-z selected progenitors, the evolution we find for BCGs remains. Since there is no good way to separate true BCG progenitors from our high-z non-BCG progenitors in observations, the main results in the following sections are based on the entire 38 selected progenitors and the 10 sets of local mixed samples.

4.4   BCG Evolution since $z \sim 2$

In order to explore BCG evolution since $z \sim 2$, we have selected 38 progenitors at $1 \lesssim z \lesssim 3$ from the CANDELS UDS and created 10 sets of their local counterparts from SDSS DR7 as explained in detail in Section 4.3. We have demonstrated in Section 4.3.3 that the evolution between these two samples can represent the BCG evolution from $z \sim 2$ to $z \sim 0$. In this section using Fig. 4.7 and Fig. 4.8, we describe in detail the evolution of BCG structure (Sérsic index and effective radius), morphology (visual morphology and *RFF*), stellar mass and SFR/sSFR. Fig. 4.7 presents the distributions of galaxy properties. Specifically, our main results of BCG evolution is shown by the blue solid lines with shadow (i.e., selected progenitors) and the colour dotted lines (i.e., local descendants).

Fig. 4.8 explicitly illustrates how the BCG properties vary as a function of redshift. In Fig. 4.8, the cyan diamond shows the mean value of each property, at our two different redshifts, by averaging the median value of the 10 sets constructed from the local samples (see Section 4.3). The error bars are the 84 and 16 percentiles ($\sim 1\sigma$) of each property distribution which are from averaging the error bars of 10 sets from the local samples. The median redshift of our local descendants is 0.074. The blue triangle presents the median property value of our selected high-z progenitors. The error bars are also the 84 and 16 percentiles of each property distribution. Our 38 selected progenitors distribute around $z = 2.06$. In the following, we call our selected high-z systems the BCG progenitors, and call their local counterparts BCGs, for simplicity.

4.4.1 Structure Evolution

Since the photometric images from the CANDELS survey are at high resolution, we can examine the structures of the galaxies in our sample by fitting their light profiles. We use the pipeline of GALAPAGOS and GALFIT to fit each galaxy's profile with a single-Sérsic model. The sky value in the CANDELS imaging is determined by GALAPAGOS, and for the simulated BCG images the sky is fixed as the sky value obtained from the CANDELS sky patch used in the simulation. We analyse the behaviour of the two structural parameters derived from the best-fitting single-Sérsic model. They are the Sérsic index n, and the effective radius R_{e}, which provides information on the intrinsic structural properties of these galaxies.

4.4.1.1 Sérsic index n

The Sérsic index n measures the concentration of the light profile, with larger n values corresponding to higher concentrations. The first panel in the upper row of Fig. 4.7 clearly shows that the high-z BCG progenitors have, statistically, much smaller values of n than their local descendants. About 55% of BCG progenitors have n smaller than 2.5, which we define as late-type galaxies. In contrast, less than 20% of the local BCGs have $n < 2.5$. A K-S test indicates that the difference in the Sérsic index n is significant at the 4.2σ level. The first panel in the upper row of Fig. 4.8 shows that the median
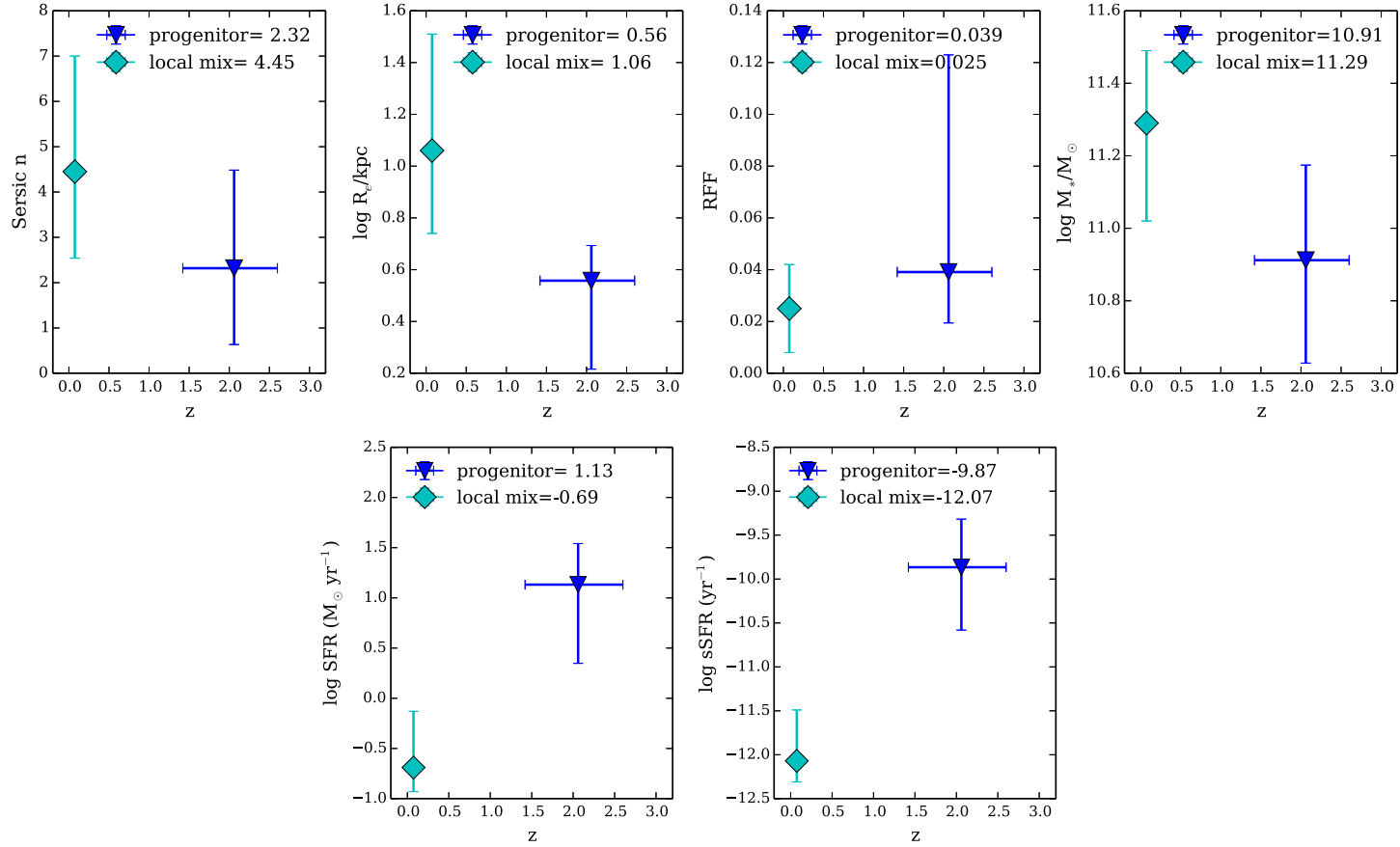
Figure 4.8: The evolution of BCG properties as a function of redshift. The cyan diamonds show the median value of each property for the local descendants (obtained by averaging the medians of the 10 sets of local mixed samples simulated to $z = 2$). The error bars are the 84 and 16 percentiles ($\sim 1\sigma$ of the distributions shown in Fig. 4.7), also averaged for the 10 sets local mixed samples. The blue triangle in each panel presents the median value of each property for our 38 high-z progenitors. Clear evolution between $z \sim 2$ and $z \sim 0$ is observed for all the BCG properties presented (i.e., shape, size, morphology, stellar mass and SFR/sSFR). Note that the error bars represent the width of the distributions, and not the error in the median values, which are given in the text.

n of BCG progenitors is $2.32^{+0.44}_{-0.34}$, while the median n of their local descendants is $4.45^{+0.15}_{-0.11}$.

In previous work, Buitrago *et al.* (2013) also find an enormous change for galaxy structures with cosmic time. They find that at $z \sim 2$, $\sim 70\%$ of the massive galaxy population have late-type Sérsic profiles ($n < 2.5$), while early-type galaxies ($n > 2.5$) have been the predominant morphological class for massive galaxies since only $z \sim 1$. Our result suggests that the shape evolution is also true for the most massive galaxy population, the BCGs.

4.4.1.2 Effective radius R_{e}

The effective radius R_{e} is a measurement of the size of the light distribution. The second panel in the upper row of Fig. 4.7 shows the distribution of $\log R_{\mathrm{e}}$ for the high-z BCG progenitors (blue solid lines with shadow), and their local descendants (dotted colour lines). It is clear that the BCG progenitors at $z \sim 2$ are much more compact than their descendants at $z \sim 0$. Almost all the high-z progenitors ($> 90\%$) have radii smaller than $R_{\mathrm{e}} \sim 6.3$ kpc, while there are $\sim 80\%$ of local BCGs whose radii are larger than this value. The difference in $\log R_{\mathrm{e}}$ distribution is very significant, based on a K-S test. The second panel in the upper row of Fig. 4.8 shows that the median radius of local BCGs is 11.5 kpc (i.e., $\log R_{\mathrm{e}} = 1.06^{+0.03}_{-0.02}$), which is a factor of ~ 3.2 larger than the size of the high-z BCG progenitors ($\log R_{\mathrm{e}} = 0.56^{+0.03}_{-0.07}$). This is also similar to what is found when just selecting massive galaxies at high and low redshifts (Buitrago *et al.* 2013).

Laporte *et al.* (2013) investigated the size growth of BCGs by using a suite of nine high-resolution dark matter-only simulations of galaxy clusters in a ΛCDM universe tracing a $z = 2$ population of quiescent elliptical galaxies to $z = 0$. They found that BCGs grow on average in size by a factor of $5 - 10$. This is much faster than the size growth we find from observational data, such that BCGs grow in size only by a factor of 3.2 since $z \sim 2$. Laporte *et al.* (2013) set the sizes of their high-z galaxies according to the observed size-mass relation for $z \sim 2$ massive quiescent galaxies which have a steeper size–mass relation and experience faster size evolution (e.g., Trujillo *et al.* 2007; Buitrago *et al.* 2008; van der Wel *et al.* 2014). In contrast, a large fraction

of the BCG progenitors in our study are Sérsic defined late-type galaxies (median $n = 2.32$, see Section 4.4.1.1) which have slower size evolution (e.g., Buitrago *et al.* 2008; Bruce *et al.* 2012; van der Wel *et al.* 2014). Therefore, it is not surprise that the size growth in Laporte *et al.* (2013) is larger than our results. Since Buitrago *et al.* (2013) demonstrate in observations that the late-type galaxies ($n < 2.5$) dominate the massive galaxy population at $z > 1$ (see also Bruce *et al.* 2012), simulations need further improvement on exploring the size evolution of massive galaxies.

4.4.2 Morphological Evolution

The single-Sérsic model is a generally reasonably good description of the local BCG light profiles since the majority of them are early-type galaxies. However, the high-z BCG progenitors may be more complicated, with distorted features, or star forming regions and spiral arms, due to an intense early evolutionary phase. Therefore, inspection of the residuals that remain after subtracting the best-fit Sérsic model is valuable for understanding whether a galaxy has a symmetric profile, or is in merger/star forming state.

We first carry out a visual inspection of the residual images which can generally give a good feel of whether the profiles of BCG progenitors and their local descendants are smooth or distorted. Then we demonstrate the quantitative differences by using the objective diagnostic of *RFF*.

4.4.2.1 Visual Inspection of Residual Images

Fig. 4.9 shows the single-Sérsic fits for all the 38 BCG progenitors selected by our method. Each row presents three BCG progenitors, each of which shows in the left panel the original image from the CANDELS UDS, the middle panel is the best-fitted single-Sérsic model, and the right panel is the residual image. The first galaxy from right in the third row from bottom is excluded from our discussion since it has a bad original image.

Inspecting the residual images, about 5 of these systems have strong asymmetric/distorted profiles, or stretched structures, suggesting mergers are ongoing. Another 7 progeni-
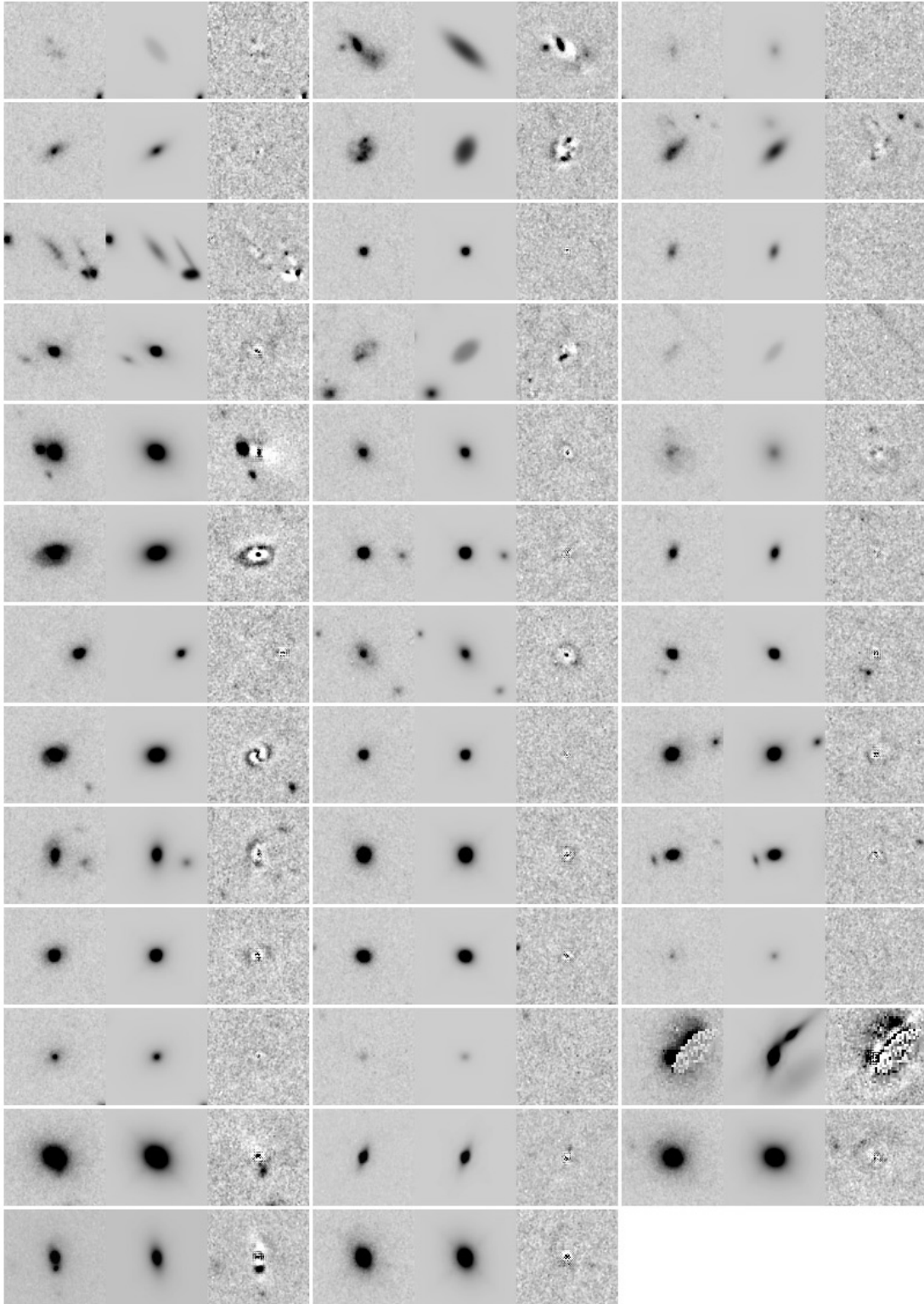
Figure 4.9: Single-Sérsic fits of the 38 BCG progenitors selected by our method from the CAN-DELS UDS. Each row presents three BCG progenitors, for each of which the left panel is the original image within the CANDELS UDS, the middle panel is the best-fit model, and the right panel is the residual image. The scale of each image is 5.2" × 5.0". The first galaxy from right in the third row from bottom has very bad original image which results in unreliable fitting result. We do not take it into account in our discussions. Inspecting the residual images, 68% of the BCG progenitors have regular light profiles, the majority of which can be fitted by a single-Sérsic model. In contrast, the remaining 32% of the progenitors are asymmetric, distorted, or have a close nearby companion. These imply that at $z \sim 2$ many BCG progenitors are undergoing or will undergo interactions and mergers.
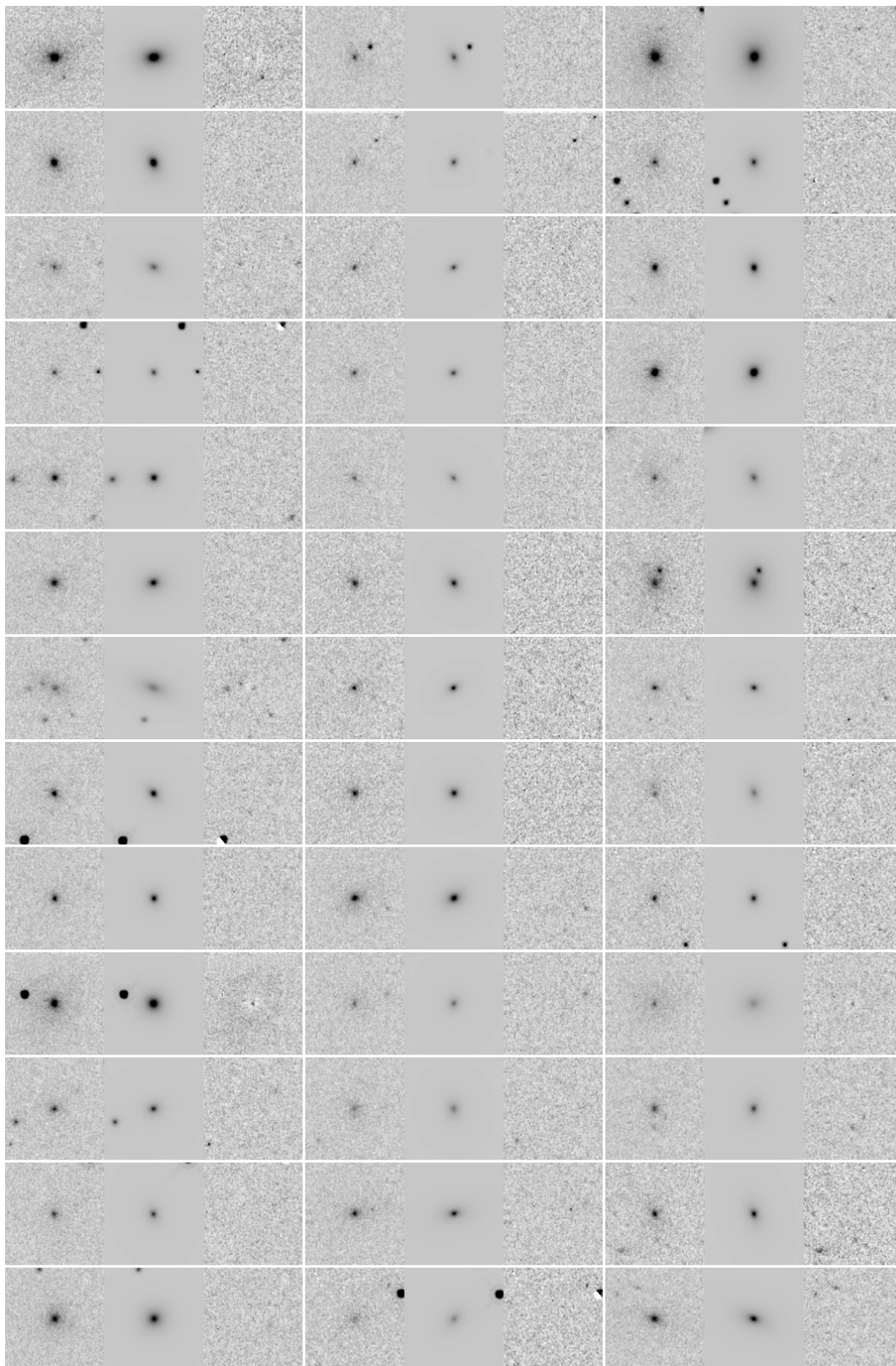
Figure 4.10: Single-Sérsic fits of 39 local descendants which are simulated to $z = 2$. They are randomly selected from one set of the local mixed BCG sample. As in Fig. 4.9, each row presents three local descendants. The left panel is the original simulated image obtained from shifting the local SDSS BCG to $z = 2$ by running the FERENGI code. The middle panel is the best-fit model, and the right panel is the residual image. The scale of each image is 7.1" × 7.3", corresponding to 59×61 kpc^2 at $z = 2$. It is clear that the local descendants have smooth and symmetric profiles, most of which can be well represented by a single-Sérsic model.

tors show a close nearby object which implies that they might be undergo early stages of a merger. The remaining 25 progenitors have regular profiles, 6 of which show clear symmetric disc or spiral arms, while the others (19) can be well fit by a single-Sérsic model. The single-Sérsic fitting results in Fig. 4.9 indicate that more than half of the BCG progenitors seem to be in a quiescent evolutionary state which may already evolve as elliptical galaxies. Nonetheless, there is still a large fraction of progenitors ($\sim 32\%$) which are undergoing, or will undergo, more intense interactions at $z \lesssim 2$ with the responsible mechanism is most likely merging.

Fig. 4.10 shows the single-Sérsic fits of 39 local descendants which are randomly selected from one set of our local mixed sample. As in Fig. 4.9, each row shows three local descendants. The left panel is the original simulated image obtained from shifting the local BCG to $z = 2$ by running the FERENGI code. The middle panel is the best-fitted single-Sérsic model, and the right panel is the residual image. It is clear that all the local BCGs have smooth and symmetric profiles, most of which can be well represented by a single-Sérsic model. None of these galaxies have an asymmetric or distorted morphology which can be found in the progenitor sample. This indicates that local BCGs are already well evolved into elliptical BCGs or cD galaxies (see also Chapter 2).

4.4.2.2   Residual Flux Fraction (*RFF*)

Visual inspection of the residual images shows evident differences in light profile shapes between high-z BCG progenitors and local BCGs, such that the high-z ones are interacting while the nearby ones already possess smooth profiles. In this section, we demonstrate this difference quantitatively through the *RFF* values whose calculation is in Section 4.2.6.2.

The *RFF* distributions, measured on the residual images of both the high-z progenitors and the 10 sets of local descendants, are shown in the third panel in the upper row of Fig. 4.7. Local BCGs, whose residual images are visually clean with little obvious residuals, have a smaller *RFF* such that about $\sim 75\%$ of them have $RFF \lesssim 0.03$. In contrast, *RFF* of the BCG progenitors distributes towards larger values, indicating that a fraction of them deviate further from the single-Sérsic model. This is consistent with

their light profiles. A K-S test shows a significant difference between these two *RFF* distributions at the level of 4.9σ.

The difference of *RFF* between local BCGs and their progenitors is also shown in the third panel in the upper row of Fig. 4.8, with the median *RFF* for BCGs at $z \sim 0$ being $0.025^{+0.001}_{-0.001}$, and for the high-z progenitors it is $0.039^{+0.017}_{-0.004}$. Note that the *RFF* distribution of high-z progenitors has a significant tail towards high values. From visual inspection on Fig. 4.9, a fraction of progenitors are merging or have very close companions, creating a variety of unsmooth galaxy profiles. These profiles may result in *RFF* scattering towards larger values.

4.4.3 Stellar Mass Evolution

In this section, we probe BCG mass growth since $z \sim 2$. Since star formation is one potential mechanism for the increase of BCG stellar masses, we also compare SFR and sSFR of BCG progenitors at $z \sim 2$ and their descendants at $z \sim 0$ to determine how star formation contributes to BCG mass growth.

4.4.3.1 Stellar Mass Growth

The fourth panel in the upper row of Fig. 4.8 illustrates the average stellar mass difference of high-z BCG progenitors and their $z \sim 0$ descendants. BCG stellar mass has grown by a factor of ~ 2.5 since $z \sim 2$ from $\log M_* = 10.91^{+0.05}_{-0.06}$ to $\log M_* = 11.29^{+0.01}_{-0.02}$. The fourth panel in the upper row of Fig. 4.7 shows that at $z \sim 2$ about 80% of BCG progenitors have stellar masses smaller than $10^{11} M_\odot$, while in local universe $\sim 90\%$ of descendants have grown into massive galaxies with masses larger than $10^{11} M_\odot$. The mass distributions of high-z progenitors and local BCGs have significant differences at the 6.4σ level as demonstrated by a K-S test.

The stellar mass growth predicted in simulations can be examined by comparing the stellar masses of our selected 3780 true BCG progenitors at $z = 2$ with the mass of their BCG descendants at $z = 0$. We find that the $z = 0$ BCG stellar mass is about 5 times larger than their $z = 2$ progenitors. There is more BCG growth in simulations than in the observational results. This offset between simulation and observation may

be due to the higher galaxy stellar mass predicted in De Lucia & Blaizot (2007) at low redshifts which is discussed in more detail in Lin *et al.* (2013). Laporte *et al.* (2013) also predicts BCG evolution in simulations, but by adopting the dark matter-only simulations of galaxy clusters. They claim that the stellar mass of BCGs increase by a factor of $2-3$ since $z \sim 2$, which is consistent with our results.

4.4.3.2   SFR and sSFR

The left panel in the lower row of Fig. 4.7 presents two clearly distinct distributions of SFR for BCG progenitors and local descendants. Almost all the BCG progenitors are forming more than 1 $M_\odot$ yr^{-1} through star formation. The same panel in Fig. 4.8 indicates that their median SFR is $13.5^{+4.3}_{-2.3}$ $M_\odot$ yr^{-1}. In the local universe, as BCGs have become elliptical BCGs or cD galaxies, $\sim 85\%$ of them have very low SFR that produce less than one solar mass per year. The median value of SFR for local BCGs from Fig. 4.8 is $0.20^{+0.03}_{-0.01}$ $M_\odot$ yr^{-1}.

The right panel in the lower row of Fig. 4.7 shows the distributions of sSFR for BCG progenitors and their $z \sim 0$ descendants. Like SFRs, the sSFRs clearly separate as well. From the right panel in the lower row of Fig. 4.8, the high-z BCG progenitors have a much higher sSFR concentrating on $\log \mathrm{sSFR} = -9.90^{+0.12}_{-0.14}$, while the sSFR of their descendants distributes around a very small value of $\log \mathrm{sSFR} = -12.10^{+0.03}_{-0.01}$.

4.4.3.3 M_*–SFR relationship

Fig. 4.11 illustrates the M_*–SFR relation (*upper* panel) as well as the M_*–sSFR relation (*lower* panel) for our high-z BCG progenitors and their local descendants. Since the SFR/sSFR distributions are similar between the 10 sets of local descendants (see the lower row of Fig. 4.7), we plot only one set of the local sample in Fig. 4.11 to keep the figure clear. In each panel, the green solid line is the relation found in Daddi *et al.* (2007) for star-forming galaxies at $z = 2$, and the brown dashed line is the M_*–SFR relation from Bauer *et al.* (2011) for star-forming galaxies at $2.0 < z < 2.5$.

It is evident that the BCG progenitors have lower SFR/sSFR values than the general star-forming galaxies, but still distribute in a relatively higher SFR/sSFR region dif-
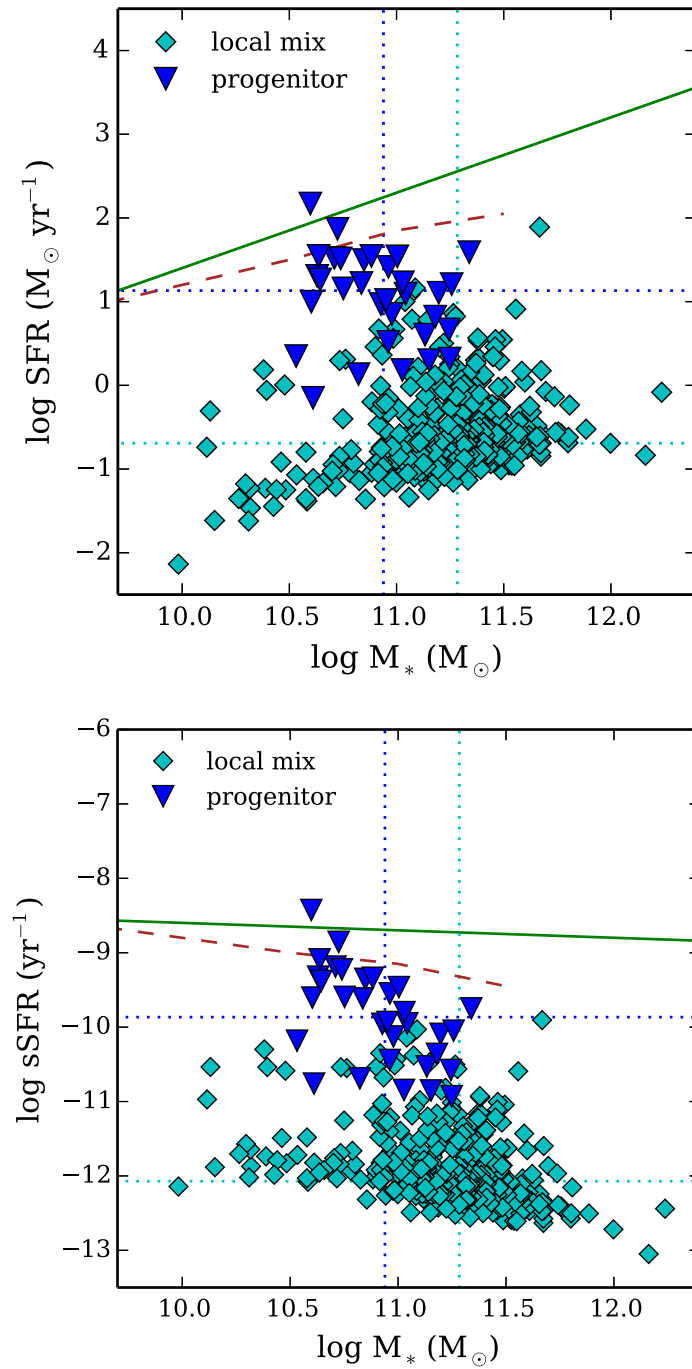
Figure 4.11: *Upper* panel: The M_*–SFR relation in log units for our 38 selected progenitors (blue triangles), and one set of local mixed sample (cyan diamonds). The vertical dotted lines show the median values of log stellar mass, and the horizontal dotted lines indicate the median $\log SFR$. The green solid line is the relation found in Daddi *et al.* (2007) for star-forming galaxies at $z = 2$. The brown dashed line is the M_*–SFR relation from Bauer *et al.* (2011) for star-forming galaxies at $2.0 < z < 2.5$. *Lower* panel: The M_*–sSFR relation in log units. The markers and lines have the same meaning as in the *upper* panel. It is clear that the BCG progenitors at $z \sim 2$ have a higher SFR and sSFR distributing separately from majority of their quiescent local descendants in either the M_*–SFR or M_*–sSFR diagram, although the SFR and sSFR of BCG progenitors are lower than that of the general star-forming galaxies.

ferentiating from the majority of their local quiescent descendants. This implies that the BCG progenitors at $z \sim 2$ already passed through their most active star-forming phase, and have begun a quiescent phase. Nevertheless their less-intense star formation still keeps them in a relatively higher SFR/sSFR. In the local universe, however, their descendants have already long been quenched. Moreover, the morphologies of BCG progenitors (see Section 4.4.2.1) have no strong correlation with their SFRs or stellar masses.

4.5 Discussion

4.5.1 Mechanisms Driving BCG Mass Growth

The processes that increase the stellar masses and sizes of massive galaxies are still an open question. There are two primary mechanisms: star formation and merging. Mergers are important since massive galaxies very likely form through the merging together of smaller galaxies in the hierarchical picture of galaxy formation. Star formation is also essential for massive galaxies in building up stellar mass, particularly at high redshifts where massive galaxies experience a much higher SFR than in the local universe (e.g., van Dokkum *et al.* 2004; Papovich *et al.* 2006; Ownsworth *et al.* 2012). In this section, we will discuss the contribution of these two processes to the evolution of BCGs and their importance at different epochs.

Our study shows that BCG progenitors at $z \sim 2$ have a relatively high SFR, and a large fraction of them have either close companions or an asymmetric and distorted morphology. These results suggest that both star formation and (major) mergers may be key mechanisms in BCG evolution at $z \sim 2$. Here we carry out a simple estimate to determine how much these two mechanisms contribute to the BCG mass growth at high redshift. Note that the in-situ stellar mass of BCG progenitors at $z \sim 2$ already accounts for $\sim 40\%$ of the total mass of BCGs at $z \sim 0$.

With the assumption that the SFR of our BCG progenitors is constant over $z = 1 - 2$, and taking into account the 0.4 dex uncertainty in SFR from contaminants, the mass increase during this period via star formation is $0.07 - 0.18 M_{*,z=0}$ where $M_{*,z=0}$ is the

stellar mass of BCGs at $z \sim 0$. On the other hand, we estimate the possible BCG mass growth through mergers by employing the major merger rate for massive galaxies at high redshifts. Conselice, Rajgor & Myers (2008) use the CAS parameters (structural concentration, asymmetry and clumpiness) to estimate major merger rates for galaxies at $1 < z < 3$. Since the median redshift of our BCG progenitors is $z \sim 2$ and 80% of them have stellar mass less than $10^{11} M_\odot$, we use their major merger rate for galaxies with stellar masses $> 10^{10} M_\odot$ at $z = 2$. Assuming the major merger rate is constant over $z = 1 - 2$, we find that BCG mass growth is about $0.12 M_{*,z=0}$ through major mergers. A similar mass increase is found by employing the major merger rate of Hopkins *et al.* (2010), such that for $z = 2$ massive galaxies ($M_* > 10^{10} M_\odot$) $0.09 M_{*,z=0}$ is built up through merging with other objects whose mass ratios are $> 1/3$. The star formation and major mergers thus seem to contribute approximately equally to BCG mass build-up at high redshifts.

Our results show that the local BCGs are quite quiescent, where the mass added via star formation is only $0.2 M_\odot$ per year on average. Since the SFR of massive galaxies decreases quickly with cosmic time (e.g., Daddi *et al.* 2007; van Dokkum *et al.* 2010; Ownsworth *et al.* 2012; Ownsworth *et al.* 2014), the contribution from star formation to BCG mass growth since $z \sim 1$ should be very small. By studying the number of mergers onto BCGs, as well as the mass ratio of infalling companions, Burke & Collins (2013) find that both major and minor mergers are common at $z \sim 1$, and cause a significant BCG mass growth. At much lower redshifts, some observational studies conclude that minor mergers dominate mass growth, and the rarity of major mergers (e.g., Liu *et al.* 2009; Edwards & Patton 2012). Others point out that some BCGs continue to grow through major mergers at $z \sim 0$. Nevertheless, mergers (either major or minor) is the dominant process at $z \lesssim 1$.

4.5.2   **Links with BCG Evolution at** $z < 1$

In this chapter, we extend the observational study of BCG structural evolution and mass growth to $z \sim 2$.

In observations, BCG size evolution has been explored at $z < 1$. By tracing host halo masses to link BCG progenitors and descendants, Shankar *et al.* (2015) suggest

a noticeable increase in BCG mean effective radius by a factor of $\gtrsim 2.5$ since $z \sim 1$. By comparing local WINGS BCGs with high-z HST BCGs whose host clusters span the same range of X-ray luminosity, Ascaso *et al.* (2011) claim a BCG size growth of a factor of ~ 2 within the last 6 Gyr (since $z \sim 0.6$). These results indicate that about 60% of the size growth of local BCGs has occured at $z \lesssim 1$. Considering the size increase in our study (by a factor of 3.2 from $z \sim 2$), it seems that BCG size increases only moderately during $z = 1 - 2$.

Galaxy shape also reveals important information on galaxy evolution. We find that the Sérsic index n of BCGs has a clear evolution, such that BCG progenitors are consistent with Sérsic late-type galaxies at $z \sim 2$, which evolve into local BCGs as early-type galaxies. Moreover, the morphology of our BCG progenitors indicates that a fraction of them are undergoing morphological transformations at $z \sim 2$ through merging, or will undergo mergers at $z < 2$. However, at $z < 1$, Ascaso *et al.* (2011) find that the shape of BCGs has not changed significantly after $z \sim 0.6$. Since the single Sérsic model mainly represents the shape of the central bulge, it probably implies that the morphological transformation of BCG bulges is still going on at $z \sim 2$, and is complete before $z \sim 0.6$, during which mergers may play an important role. After that the size and mass growth is focused on the outer regions of BCGs. More observational studies on the shape evolution of BCGs are needed during $z = 0 - 1$ to determine if this scenario is likely.

Moreover, many studies explore the build-up of BCG stellar mass at $z \lesssim 1 - 1.5$ in observations. Some of them claim that there is little change in BCG mass since $z \sim 1$ (Burke, Collins & Mann 2000; Whiley *et al.* 2008; Collins *et al.* 2009). In contrast, other papers (e.g., Lidman *et al.* 2012; Lin *et al.* 2013; Shankar *et al.* 2015; Zhang *et al.* 2016) find a generally consistent BCG mass growth by a factor of ~ 2 over $z = 0 - 1$. In Section 4.5.1, we did a simple estimation of BCG mass growth from $z \sim 2$ to $z \sim 1$, reporting that, in this period, at most 18% of the total mass of local BCGs will be added through star formation, and $\sim 12\%$ via major mergers. Since SFR and major merger rate decrease with cosmic time (e.g., Bridge, Carlberg & Sullivan 2010; Bluck *et al.* 2012; Ownsworth *et al.* 2014), this mass growth is more likely an upper limit. Considering the stellar mass BCG progenitors already have at $z \sim 2$ ($\sim 40\%$ of the

total mass of local BCGs), our estimate shows that by $z \sim 1$ the BCG stellar mass will be no more than 70% of the total mass at $z = 0$, suggesting that there has to be an additional mass build-up in BCGs after $z \sim 1$. The BCG mass will increase by a factor of no less than ~ 1.4 from $z \sim 1$ to $z \sim 0$.

Although we discuss the BCG evolution by combining our work over $z = 0 \sim 2$ with other studies at $z \lesssim 1$, it is dangerous to do so since the BCG progenitor selections we use are different. Homogeneous BCG data over large range of redshift from future observations is necessary for better understanding the BCG evolution since high redshifts.

4.5.3 Comparison with Massive Galaxy Evolution

Many studies have examined the properties of massive galaxies at high redshifts, broadening our understanding of massive galaxy evolution over a large redshift range. Here we compare our results on BCGs with the evolution of massive galaxies over $z = 0 - 2$. Since constant number density is applied in our study, the comparison is carried out with papers which also use constant number density to trace massive galaxies at different redshifts.

van Dokkum *et al.* (2010) study the growth of massive galaxies from $z = 2$ using a fixed galaxy number density selection of 2×10^{-4} Mpc^{-3}. They find that at this number density the stellar mass of galaxies has increased by a factor of ~ 2, and size has grown by a factor of ~ 4 since $z = 2$. They verify that their results are not sensitive to the exact number density by repeating key parts of the analysis for a number density of 1×10^{-4} Mpc^{-3}. Ownsworth *et al.* (2014) study the growth of massive galaxies from $z = 3$ by adopting a fixed number density of $\sim 10^{-4}$ Mpc^{-3}, similar to the one used in this study. Their results show that the stellar mass of galaxies at $z \sim 0.3$ is ~ 2.5 times larger than their progenitors at $z \sim 2$, and the size of massive galaxies increases by a factor of ~ 2.3 by comparing the average galaxy size within the redshift bin $0.3 < z < 0.5$ with the bin at $2.0 < z < 2.5$. Compared with BCG stellar mass growth (a factor of ~ 2.5) and size growth (by a factor of ~ 3.2), the evolution of massive galaxies appears similar to the BCG evolution from $z \sim 2$.

Specifically, at high redshift, we examine whether our selected BCG progenitors have different properties from normal massive galaxies which are in the same redshift and stellar mass range. The normal massive galaxies are selected from the CANDELS UDS catalogue whose redshifts and stellar masses have a similar distribution as our 38 selected BCG progenitors. We find that our BCG progenitors are very similar to the normal massive galaxies in many properties such as structure, morphology, and SFR/sSFR. This implies that the BCG progenitors do not show any specific differences with other massive galaxies at $z \sim 2$. Since local BCGs are different from the control samples of local non-BCGs which match in stellar mass, redshift and colour (von der Linden *et al.* 2007), BCG progenitors must experience some specific mechanism(s) at $z \lesssim 2$ (probably more minor mergers) which results in the specific properties of BCGs at $z \sim 0$. These mechanisms are likely responsible for the characteristic cD envelope observed in many local BCGs (see Chapter 2 and Chapter 3).

4.6   Summary

In this chapter, we carry out a study of BCG evolution beyond $z = 1$ to explore how structure, morphology and stellar mass of BCGs vary with cosmic time since $z \sim 2$.

By proposing a BCG progenitor selection which identifies BCG progenitors as the most massive galaxies in the densest local environments, we select our BCG progenitor sample at $z \sim 2$ from the CANDELS UDS data. Testing our method in simulations we find that 45% of our selected progenitors are true BCG progenitors. Although the high-z progenitors selected by our method are a mixed sample of BCG and non-BCG progenitors, the properties of our high-z progenitors can be used to trace BCG evolution because they are similar to the properties of the pure BCG progenitors within the sample. We use a constant number density of $10^{-4.06} h^3 \text{Mpc}^{-3}$ to select our samples.

At this density the descendants of the high-z selected sample are taken from the SDSS DR7 galaxy catalogue. To ensure the galaxy sample at $z \sim 0$ are the descendants of our selected progenitors, based on simulations, we construct a local mixed sample which contains 38% BCGs and 62% non-BCGs. We demonstrate through several methods that the contamination from non-BCGs and non-BCG progenitors do not erase the

intrinsic BCG evolution. Comparing properties between our high-z BCG progenitors and their local descendants, we find a clear BCG evolution since $z \sim 2$ in structure, morphology and stellar mass. Our major results on BCG evolution at $z \lesssim 3$ are:

- At $z \sim 2$, less than 50% of the most massive galaxies in the densest environments are the true BCG progenitors.

- Although the environmental density is not a strong tracer, the method we propose to identify BCG progenitors at $z \sim 2$ can be applied to observational data to derive BCG evolution since they have similar properties to the pure BCG progenitors.

- The size of BCGs has grown by a factor of ~ 3.2 since $z \sim 2$. The BCG progenitor profiles are mainly Sérsic late-type galaxies with median Sérsic index of $n = 2.3$, while their local BCG descendants are early-type galaxies whose median Sérsic index is $n = 4.5$.

- The residual images after subtracting single Sérsic fits illustrate that BCG progenitors at $z \sim 2$ are more distorted, whereas the local BCGs have smoother profiles. This difference in morphology is verified quantitatively by *RFF* measures, such that BCG progenitors have larger *RFF* values than their local counterparts. About 32% of BCG progenitors at $z \sim 2$ are undergoing mergers, or will undergo mergers at $z < 2$.

- The stellar mass of BCGs has grown by a factor of ~ 2.5 since $z \sim 2$. The median SFR of BCG progenitors at $z \sim 2$ is still relatively high, at $\sim 14\ M_\odot$ yr^{-1}. In contrast, their local descendants are very quiescent, with a median SFR of only $0.2\ M_\odot$ yr^{-1}. We find that over the $z = 1 - 2$ period, star formation and merging contribute approximately equally to BCG mass growth. However, since the SFR decreases with time, merging must play a more important role in BCG assembly at $z \lesssim 1$.

- We find that BCG progenitors at high-z are not significantly different than other galaxies of similar mass at the same redshift range. This suggests that the processes which differentiate BCGs from normal massive elliptical galaxies must occur at $z \lesssim 2$.

Chapter 5

Conclusions

This thesis has been devoted to shedding light on the formation and evolution of BCGs through a careful study of local BCGs from SDSS as well as BCG progenitors at high reshifts from the CANDELS UDS. The work presented in this thesis addresses three main problems in some detail: 1) the relationship between morphology and structure for local BCGs, focusing on the structural differences between cD galaxies and elliptical BCGs; 2) the influence of environment on the properties and evolution of local BCGs; 3) the identification of BCG progenitors beyond $z \sim 1.5$, together with the study of BCG structure and stellar mass growth since $z \sim 2$. In the first part of this chapter, I summarise and discuss the conclusions from this work on the evolution of BCGs. I end by discussing some possible ways in which this work can be extended in the future.

5.1   Summary of the Thesis

5.1.1   cD Galaxies and Elliptical BCGs

In Chapter 2, I analysed 625 BCGs in the local universe using SDSS DR7 images to investigate the relationship between their morphologies and their structural properties. Considering the presence or absence of the extended stellar envelope, we morphologically classify the BCGs visually into pure cD galaxies ($\sim 57\%$), pure elliptical BCGs ($\sim 13\%$), and intermediate classes which are mostly cD/E or E/cD ($\sim 21\%$).

These classes represent a continuous transition in the properties of the BCG extended envelopes, ranging from undetected (pure E class) to clearly detected (pure cD class), with the intermediate classes (E/cD and cD/E) showing increasing degrees of envelope presence. By fitting the BCGs light profiles with single Sérsic models, I find a clear link between BCG morphologies and their structures, in such a way that cD galaxies are typically larger than elliptical BCGs, and the extended envelope of cD galaxies is clearly a distinct structure differing from the central bulge. This local BCG morphology–structure correlation indicates that cD galaxies and elliptical BCGs not only have different morphologies but also have intrinsic structural difference. This study on cD galaxies and elliptical BCGs is complemented in Chapter 3 by further exploring their stellar masses and environments. I demonstrated that local cD galaxies are typically $\sim 40\%$ more massive than elliptical BCGs, and they are hosted in denser and more massive clusters compared to elliptical BCGs.

My study reveals a morphological transition within the BCG population which is closely related to the cluster environments. Together with the findings of previous studies, I suggest an evolutionary link between elliptical BCGs and cD galaxies. I propose that most present-day cD galaxies started their life as elliptical BCGs at $z \sim 1$, which subsequently grew in stellar mass and size due to (dry) mergers. In this process, the envelope of cD galaxies developed. This process is nearing completion by the present time, since the majority of BCGs in the local universe have cD morphology. However, the presence of intermediate morphological classes (cD/E and E/cD) suggests that the growth and morphological transformation of some BCGs is still ongoing. Furthermore, the growth of the BCGs in mass and size seems to be linked to the hierarchical growth of the structures they inhabit: as the groups and clusters became denser and more massive, the BCGs at their centres also grew.

In Chapter 2, I also find that cD galaxies and non-cD BCGs show very different distributions in the R_{e}–RFF_{1c} plane, where R_{e} is the effective radius and RFF_{1c} is the residual flux fraction, both determined from single Sérsic fits. cD galaxies have, generally, larger R_{e} and RFF_{1c} values than elliptical BCGs. Based on this BCG morphology–structure correlation, I develop a statistically robust way to separate cD galaxies from non-cD BCGs. Our diagnostic is able to automatically select cD galaxies

with high completeness ($\sim 75\%$) and low contamination ($\sim 20\%$). Our cD selection is more objective and time-saving compared to the more subjective and time-consuming visual classification. It can be applied to any BCG sample.

5.1.2 Effect of the Environment on BCGs

In Chapter 3, I probe the effect of environment on the properties of local BCGs by investigating the relationship between BCG structure, stellar mass, and cluster environment (local environmental density and global cluster dark matter halo mass).

I found that the Sérsic-index n does not correlate with the stellar mass or the environment of BCGs. The effective radius R_{e} of the BCGs correlates with their stellar mass. However, this correlation does not depend significantly on the environment. Almost all BCGs have larger R_{e} than non-BCG early-type galaxies of similar mass. The median radius of the BCGs is about twice as large as that of non-BCG early types of similar masses. Moreover, the scatter in the M_*–R_{e} relation is significantly larger for BCGs than for the other early-type galaxies, suggesting a more complex formation history. Additionally, more massive BCGs tend to inhabit denser regions and more massive clusters, but BCG mass correlates much more strongly with environmental density than with the cluster dark matter halo mass.

These results imply that the environment of BCGs, specially the local density, directly affects the growth of the BCG stellar mass. The BCG size, which is independent of environment, is mostly determined by the intrinsic stellar mass of the BCGs.

5.1.3 BCG Evolution since $z \sim 2$

In Chapter 4, I present a new method for tracing the evolution of BCG structure, morphology, stellar mass, and star formation from $z \sim 2$ to $z \sim 0$. By discussing various ways to construct a BCG progenitor sample at high redshift in numerical simulations, I conclude that the best method to identify BCG progenitors at $z \sim 2$ is a hybrid environmental density and stellar mass ranking approach. I find that 45% of BCG progenitors can be retrieved by using this approach. Although the high-z progenitors identified by our method are a mixed sample of BCG and non-BCG progenitors, the properties of

our high-z progenitors can be used to trace BCG evolution. The observational BCG progenitors at $z \sim 2$ are then selected by applying our method on the CANDELS UDS data. I also construct a local comparison sample which is likely to contain the descendants of our high-z progenitors. This ensures a fair comparison between high-z and low-z samples in order to trace BCG evolution.

Using the progenitor and descendant samples, I demonstrate that the sizes of BCGs have grown by a factor of ~ 3.2 since $z \sim 2$, and the BCG progenitors are mainly Sérsic late-type galaxies, exhibiting less concentrated profiles than their early-type local counterparts. I also find that the BCG progenitors at $z \sim 2$ have more disturbed morphologies, and $\sim 32\%$ of them are undergoing mergers or will undergo mergers at $z < 2$. In contrast, local BCGs have much smoother morphologies, almost all of which can be fitted by a single, high concentration Sérsic profile. Moreover, our results indicate that the stellar masses of BCGs have grown by a factor of ~ 2.5 since $z \sim 2$. The SFR of BCG progenitors has a median value of ~ 14 $M_\odot \mathrm{yr}^{-1}$, which is much higher than their quiescent local descendants whose median SFR is only 0.2 $M_\odot \mathrm{yr}^{-1}$. I demonstrate that between $z \sim 2$ and $z \sim 1$ star formation and merging contribute approximately equally to BCG mass growth. However, merging plays a dominant role in BCG assembly at $z \lesssim 1$. I also show that BCG progenitors at high-z are not significantly different from other galaxies of similar mass at the same epoch. This suggests that the processes which differentiate BCGs from normal massive elliptical galaxies must occur at $z \lesssim 2$ (probably due to more minor mergers) to form the specific properties of BCGs at $z \sim 0$. These mechanisms are probably responsible for the characteristic cD envelope observed in many local BCGs.

Combined with the results observed for cD galaxies and elliptical BCGs in Chapter 2 and Chapter 3, I propose an overall scenario for BCG evolution in the last 10 billion years. At $z \sim 2$, BCGs grow through both merging and star formation, which contribute approximately equally to the BCG mass build-up over $z = 1 - 2$. After $z \sim 1$, dry mergers became more and more important for BCG assembly, triggering the formation of the envelope of cD galaxies and driving the transformation of elliptical BCGs into cD galaxies. Moreover, BCGs may experience relatively more minor mergers, making their properties distinct from those of the normal massive galaxy population.

5.2 Future Work

In this final section, I consider some of the potential directions in which this work may be complemented and extended in future studies.

The results presented in this thesis suggest a morphological transformation at $z \lesssim 1$ within the BCG population, such that BCGs evolve from ellipticals to cDs with the growth of an extended envelope. However, the BCG morphological transition is still poorly understood and highly under-constrained by observational data. One reason is that the photometric images from current imaging surveys are too shallow to allow detailed statistical analysis on the cD envelopes at high redshifts since the envelopes have an extremely low surface brightness (< 25 mag arcsec^{-2}). In our work, we only study the morphology of ~ 10 BCGs at $z \sim 0.6$. Needless to say, a large sample of cD galaxies and elliptical BCGs at $z \gg 0$ is needed to extensively examine the evolution of the envelope of cD galaxies. The Subaru Hyper Suprime-Cam (HSC) survey could help in achieving this.

The Subaru HSC (Miyazaki *et al.* 2012), the largest camera ever built for an 8-metre class ground-based telescope, is, at the moment, the most powerful instrument for both wide and deep imaging surveys. The HSC imaging survey, started in March 2014, is on-going with 300 nights approved over 5 years (more details can be found at http://www.naoj.org/Projects/HSC/surveyplan.html). It will cover a field of view of 1400 deg^2, and is expected to observe more than 10,000 galaxy clusters to $z = 1$. The excellent images from the survey are expected to reach a magnitude limit of 26 mag in the r-band, more than one magnitude fainter than other on-going or complete ground-based wide surveys (e.g., Dark Energy Survey, CFHT, SDSS). It provides an unprecedented homogeneous sample of galaxies and galaxy clusters with extremely high-quality images, allowing a deep statistical study on the faint structures in galaxies and clusters over a large redshift range which would be difficult to achieve before the Subaru HSC survey. Therefore, it would become possible to explore the envelope properties of high-z cD galaxies and to analyse how BCG morphologies evolve from $z \sim 1$ to $z \sim 0$.

With the advent of Integral Field Units (IFUs) on large ground based telescopes (e.g.,

MaNGA project in SDSS-III; MUSE at the VLT), the spectroscopic properties of the different parts of the BCGs can be observed. The IFU data can measure, for example, the stellar populations, ages, metallicities and kinematics of the bulges and envelopes of cD galaxies, and therefore provide information on the evolutionary history of the inner and outer regions of cD galaxies. This will allow us to further address, in great detail, the question of how the morphology of BCGs and their assembly histories are linked.

Simulations have predicted that mergers are a critical mechanism in BCG evolution (e.g., Laporte *et al.* 2013). Observational studies have also reported the importance of mergers in BCG growth at $z < 1$ (Brough *et al.* 2011; Burke & Collins 2013). However, it is still unclear how mergers correlate with the formation and evolution of the cD envelopes. Moreover, BCG assembly and morphological evolution may also be affected by the formation of the ICL (see Chapter 1). It is still difficult to measure the ICL over a large redshift range using current observational data due to its low surface brightness. With Subaru HSC survey data, it will be possible to probe the interplay between mergers, the ICL, and BCG formation and evolution since $z \sim 1$. This will provide much needed evidence to clarify the interactions between the growth of BCGs and the assembly of their host clusters.

Appendices

Appendix A

Data Table

Table A.1 contains the main properties of the BCGs discussed in this paper. The full table is published electronically. It can be obtained from http://adsabs.harvard.edu/abs/2015yCat..74482530Z.

ID2 (1)	ID3 (2)	RA deg (3)	DEC deg (4)	z (5)	σ_{cl} km s^{-1} (6)	$\log R_{e,1c}$ kpc (7)	n_{1c} (8)	RFF_{1c} (9)	χ^2_{1c} (10)	Type (11)	Comments (12)
1011	1013	227.107346	−0.266291	0.091	748	1.527	5.38	0.08190	1.752	cD	Clear halo; perhaps interacting
1023	1025	153.409478	−0.925413	0.045	790	1.908	6.25	0.05052	1.374	cD	Clear halo; interacting with fainter galaxies
1064	1075	153.437067	−0.120224	0.094	875	1.312	4.49	0.02648	1.086	E/cD	
–	1027	191.926938	−0.137254	0.088	1020	1.063	4.42	0.06594	1.903	E	Interacting/merging with bright early-type
–	1389	202.337884	0.749685	0.080	853	1.044	6.02	0.01990	1.087	E/cD	Faint/small halo
2040	2050	17.513187	13.978117	0.059	759	2.408	9.77	0.04122	1.224	cD	Several bright-ish companions
1052	1058	195.719058	−2.516350	0.083	749	1.627	4.89	0.04694	1.455	cD	Multiple merger
1034	1036	192.308670	−1.687394	0.085	771	0.977	4.86	0.02102	1.115	E	
1041	1044	194.672887	−1.761463	0.084	771	2.318	5.64	0.05023	1.280	cD	Very large, elongated halo; some faint companions
–	1126	192.516071	−1.540383	0.084	878	2.039	9.12	0.04520	1.348	cD	Interacting with faint companions
3002	3004	258.120056	64.060761	0.080	1156	1.667	4.81	0.02561	0.991	cD	
3096	3283	135.322540	58.279747	0.098	756	1.866	6.96	0.05535	1.144	cD	Merging with bright companion
1045	1048	205.540176	2.227213	0.077	828	0.883	2.52	0.10689	11.280	E/cD	Multiple merger
1003	1004	184.421356	3.655806	0.077	966	1.753	4.75	0.05233	1.225	cD/E	Interacting/merging with early-type
–	1456	173.336242	2.199054	0.099	746	1.696	8.09	0.02573	1.128	cD	
1053	1061	228.220703	4.514004	0.038	789	0.875	7.54	0.01749	1.074	cD	
2163	2074	314.975446	−7.260758	0.079	765	1.231	8.03	0.04481	1.315	E/cD	
2002	2002	358.557007	−10.419200	0.076	812	2.660	11.12	0.03832	1.201	cD	Many faint and bright-ish companions
2006	2013	10.460272	−9.303146	0.056	903	1.433	1.62	0.04140	1.477	cD	Several faint companions
1355	1460	175.554108	5.251709	0.097	1074	0.952	5.30	0.01557	1.052	cD	Interacting with faint galaxy; faint but clear halo
1058	1069	184.718166	5.245665	0.076	721	1.988	7.98	0.04144	1.251	cD	Interacting with faint galaxies
1002	1002	159.777581	5.209775	0.069	800	1.740	8.40	0.03838	1.321	cD/E	Clear halo
–	1276	183.271286	5.689677	0.081	729	0.995	5.30	0.02142	1.151	E	
1039	1042	228.808792	4.386210	0.098	857	1.800	8.77	0.04365	1.205	E/cD	Some halo? faint companions
–	3332	124.471428	40.726395	0.063	802	1.463	6.40	0.08125	2.639	SB0	
3011	3028	204.034694	59.206401	0.070	872	2.120	7.86	0.08172	1.556	cD	Several faint companions
1001	1001	208.276672	5.149740	0.079	746	1.820	7.85	0.02720	1.128	E/cD	
3004	3012	255.677078	34.060024	0.099	1127	1.717	3.54	0.08433	1.949	cD	Late merger?
–	3094	254.933115	32.615319	0.098	875	1.291	3.50	0.02878	1.069	cD	Very faint companions
–	1066	202.795126	−1.730259	0.085	814	1.942	9.09	0.03653	1.161	E/cD	Interacting/merging with bright galaxy and fainter one
–	2214	321.599487	10.777511	0.095	741	0.818	3.98	0.02260	1.199	E	
2096	2109	359.836166	14.670211	0.093	786	1.161	6.56	0.03572	1.242	cD/E	
2085	2085	334.197449	−9.724778	0.094	806	0.779	3.43	0.02861	1.348	cD	
2027	2035	4.177309	−0.445436	0.065	1084	1.436	8.89	0.02417	1.168	cD	Several companions
–	3084	118.360820	29.359459	0.061	781	1.584	3.95	0.06632	1.382	cD	Several faint and bright companions
–	3347	119.679733	30.773809	0.076	902	1.354	6.04	0.01470	1.019	E/cD	
–	1283	125.745443	4.299105	0.095	754	2.747	10.47	0.04483	1.094	cD	Several faint-ish companions
–	1039	186.878093	8.824560	0.090	846	1.962	6.94	0.06100	1.965	cD	Clear halo, bright companion (dumbbell galaxy)

Table A.1: Properties of the BCG sample. Columns (1) and (2) provide galaxy identifications, where ID2 is the SDSS-C4 number <SDSS-C4 NNNN> and ID3 is the SDSS C4_2003 number, <SDSS-C4-DR3 NNNN>, as given in Simbad (von der Linden *et al.*, 2007). Columns (3) and (4) give the right ascension and declination in degrees. Column (5) gives the redshift and column (6) the velocity dispersion of the cluster. Columns (7), (8), (9) and (10) contain the effective radius, Sérsic index, residual flux fraction and reduced χ^2 derived from the single Sérsic fits (see text for details). Column (11) gives the visual morphological classification of the BCGs. Column (12) contains some comments from the classifier.

Appendix B

Comparison with Guo+09

B.1 Structural Parameters

There are 104 galaxies in common between our sample and that of Guo *et al.* (2009). A comparison between the measurements of the effective radius R_e and the Sérsic index n for these galaxies is presented in Fig. B.1. Although the measurements correlate very well, there are some relatively small systematic differences. The median offset between our R_e measurements and those of Guo *et al.* (2009) is 0.15dex. The median offset in n is 0.47. The larger values we obtain are due to the improvements in the sky subtraction implemented in Chapter 2 in which we showed that the sky values provided by SDSS DR7 were overestimated due to the presence of extended objects. This is particularly important in crowded fields such as the centres of groups and clusters. We used GALAPAGOS (Barden *et al.*, 2012) to obtain a more reliable estimate of the sky after removing contamination from neighbouring objects. Although the reduction in the sky values is quite small (typically ~ 0.4 counts, or 0.3%), the effect on R_e and n can be significant for extended objects such as BCGs. More details are provided in Section 2.3.2 of Chapter 2.

B.2   Stellar Masses

In Section 3.3.1, we found no correlation between n and M_* for the BCGs in our sample. This contrasts with the findings of Guo *et al.* (2009), who show a clear positive correlation in the sense that more massive BCGs seem to have higher values of n. In this Appendix we explore the possibility that the correlation found by Guo *et al.* (2009) may be due to the fact that these authors estimated stellar masses from the total luminosity derived from single Sérsic model fits. These luminosities (and the derived stellar masses) are therefore model dependent, and, in particular, they will depend on the value of n. Since there is a direct relation between the best-fit total flux and n for a Sérsic profile (see Equations 4 and 6 in Peng *et al.* 2010), this dependency could drive the observed correlation.

In order to confirm this, we have derived stellar masses for the BCGs in our sample following the same method as Guo *et al.* (2009) using our own single Sérsic fits. Since we have 104 BCGs in common with Guo *et al.* (2009), we can check that the values of M_* derived in this way for the galaxies in common agree well with theirs: the scatter in this comparison is below 0.1 dex and there is no bias. In Fig. B.2 we show that, using these model-dependent M_* values, a positive correlation between n and M_* is indeed found (Pearson correlation coefficient 0.38). The correlation we find is qualitatively similar to the one shown in Fig. 6 of Guo *et al.* (2009) when considering the same mass range.

This indicates that the correlation claimed by Guo *et al.* (2009) may be the consequence of assuming that a Sérsic model fit provides an accurate representation of the total light distribution of BCGs. This assumption is clearly not correct, particularly for cD galaxies, as demonstrated by previous studies (see Chapter 2 and references therein). Measuring the total luminosity of a galaxy is far from trivial and, of course, the Petrosian magnitudes used to derive MPA–JHU masses are not without their problems (see, e.g., Graham *et al.* 2005). We do not claim that the stellar masses we use are better than the ones used by Guo *et al.* (2009), but they are, at least, model independent and not directly linked to the models used to derive the structural parameters that we study. For these reasons we prefer to use the MPA–JHU masses in this chapter. Nevertheless, bearing in mind this uncertainty, we have checked and confirmed that
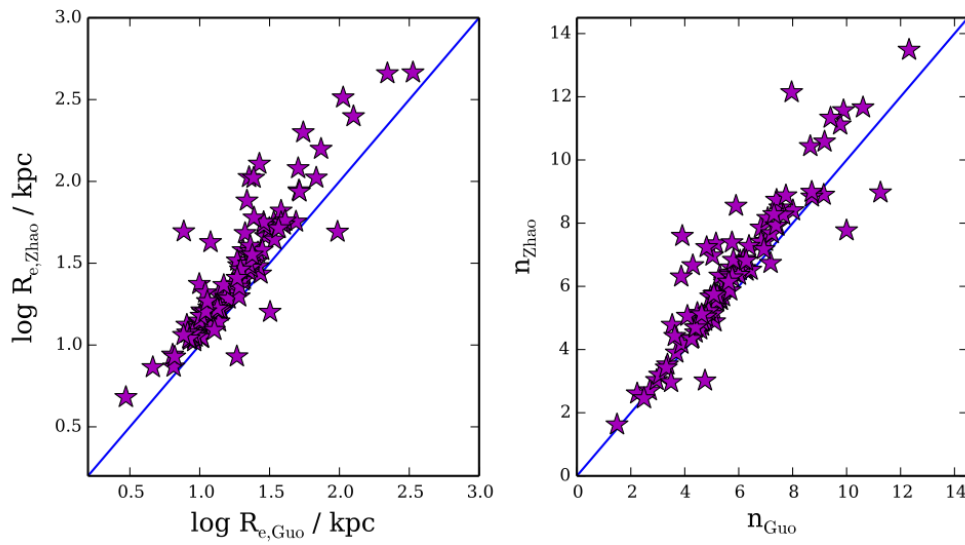
Figure B.1: Comparison between the values of the effective radius R_e and Sérsic index n obtained in Chapter 2 and Guo *et al.* (2009) for the 104 galaxies in common. The solid lines correspond to the 1-to-1 relation.
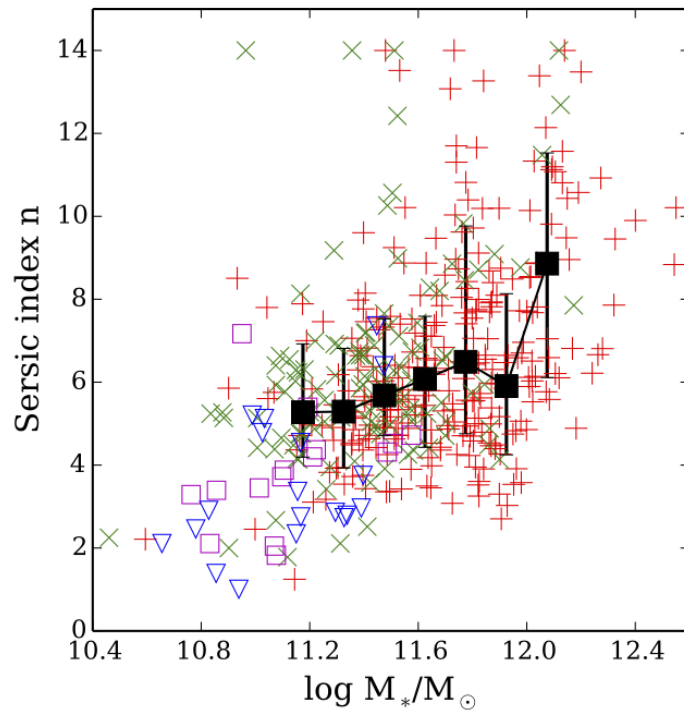
Figure B.2: Sérsic index n vs. stellar mass for the BCGs in our sample, similar to Fig. 3.1, but with the stellar mass M_* is derived following the method described in Guo *et al.* (2009). Symbols as in Fig. 3.1. See text for details.

all our conclusions (with the exception of the lack of correlation between M_* and n) remain the same if we use Sérsic-model based luminosities/stellar masses instead of the MPA–JHU ones.

Bibliography

Abadi M. G., Navarro J. F., Steinmetz M., 2006. *MNRAS*, **365**, 747.

Albert C. E., White R. A., Morgan W. W., 1977. *ApJ*, **211**, 309.

Andreon S., Garilli B., Maccagni D., Gregorini L., Vettolani G., 1992. *A&A*, **266**, 127.

Annis J., Soares-Santos M., Strauss M. A., Becker A. C., Dodelson S., Fan X., Gunn J. E., Hao J., Ivezić Ž., Jester S., Jiang L., Johnston D. E., Kubo J. M., Lampeitl H., Lin H., Lupton R. H., Miknaitis G., Seo H.-J., Simet M., Yanny B., 2014. *ApJ*, **794**, 120.

Aragón-Salamanca A., Baugh C. M., Kauffmann G., 1998. *MNRAS*, **297**, 427.

Ascaso B., Aguerri J. A. L., Varela J., Cava A., Bettoni D., Moles M., D'Onofrio M., 2011. *ApJ*, **726**, 69.

Balogh M. L., Baldry I. K., Nichol R., Miller C., Bower R., Glazebrook K., 2004. *ApJL*, **615**, L101.

Barden M., Häußler B., Peng C. Y., McIntosh D. H., Guo Y., 2012. *MNRAS*, **422**, 449.

Barden M., Jahnke K., Häußler B., 2008. *ApJS*, **175**, 105.

Bauer A. E., Conselice C. J., Pérez-González P. G., Grützbauch R., Bluck A. F. L., Buitrago F., Mortlock A., 2011. *MNRAS*, **417**, 289.

Bernardi M., Hyde J. B., Sheth R. K., Miller C. J., Nichol R. C., 2007. *AJ*, **133**, 1741.

Bernardi M., 2009. *MNRAS*, **395**, 1491.

Bernstein J. P., Bhavsar S. P., 2001. *MNRAS*, **322**, 625.

Bertin E., Arnouts S., 1996. *A&AS*, **117**, 393.

Bhavsar S. P., Barrow J. D., 1985. *MNRAS*, **213**, 857.

Binggeli B., 1982. *A&A*, **107**, 338.

Bluck A. F. L., Conselice C. J., Buitrago F., Grützbauch R., Hoyos C., Mortlock A., Bauer A. E., 2012. *ApJ*, **747**, 34.

Bridge C. R., Carlberg R. G., Sullivan M., 2010. *ApJ*, **709**, 1067.

Brinchmann J., Charlot S., White S. D. M., Tremonti C., Kauffmann G., Heckman T., Brinkmann J., 2004. *MNRAS*, **351**, 1151.

Brough S., Collins C. A., Burke D. J., Mann R. G., Lynam P. D., 2002. *MNRAS*, **329**, 53.

Brough S., Collins C. A., Burke D. J., Lynam P. D., Mann R. G., 2005. *MNRAS*, **364**, 1354.

Brough S., Couch W. J., Collins C. A., Jarrett T., Burke D. J., Mann R. G., 2008. *MNRAS*, **385**, L103.

Brough S., Tran K.-V., Sharp R. G., von der Linden A., Couch W. J., 2011. *MNRAS*, **414**, L80.

Bruce V. A., Dunlop J. S., Cirasuolo M., McLure R. J., Targett T. A., Bell E. F., Croton D. J., Dekel A., Faber S. M., Ferguson H. C., Grogin N. A., Kocevski D. D., Koekemoer A. M., Koo D. C., Lai K., Lotz J. M., McGrath E. J., Newman J. A., van der Wel A., 2012. *MNRAS*, **427**, 1666.

Bruzual G., Charlot S., 2003. *MNRAS*, **344**, 1000.

Buitrago F., Trujillo I., Conselice C. J., Bouwens R. J., Dickinson M., Yan H., 2008. *ApJL*, **687**, L61.

Buitrago F., Trujillo I., Conselice C. J., Häußler B., 2013. *MNRAS*, **428**, 1460.

Burke C., Collins C. A., 2013. *MNRAS*, **434**, 2856.

Burke D. J., Collins C. A., Mann R. G., 2000. *ApJL*, **532**, L105.

Burke C., Hilton M., Collins C., 2015. *MNRAS*, **449**, 2353.

Caon N., Capaccioli M., D'Onofrio M., 1993. *MNRAS*, **265**, 1013.

Carter D., Metcalfe N., 1980. *MNRAS*, **191**, 325.

Cid Fernandes R., Mateus A., Sodré L., Stasińska G., Gomes J. M., 2005. *MNRAS*, **358**, 363.

Collins C. A., Mann R. G., 1998. *MNRAS*, **297**, 128.

Collins C. A., Stott J. P., Hilton M., Kay S. T., Stanford S. A., Davidson M., Hosmer M., Hoyle B., Liddle A., Lloyd-Davies E., Mann R. G., Mehrtens N., Miller C. J., Nichol R. C., Romer A. K., Sahlén M., Viana P. T. P., West M. J., 2009. *Nature*, **458**, 603.

Conroy C., Wechsler R. H., Kravtsov A. V., 2007. *ApJ*, **668**, 826.

Conselice C. J., Bluck A. F. L., Ravindranath S., Mortlock A., Koekemoer A. M., Buitrago F., Grützbauch R., Penny S. J., 2011. *MNRAS*, **417**, 2770.

Conselice C. J., Rajgor S., Myers R., 2008. *MNRAS*, **386**, 909.

Cowie L. L., Binney J., 1977. *ApJ*, **215**, 723.

Coziol R., Andernach H., Caretta C. A., Alamo-Martínez K. A., Tago E., 2009. *AJ*, **137**, 4795.

Daddi E., Dickinson M., Morrison G., Chary R., Cimatti A., Elbaz D., Frayer D., Renzini A., Pope A., Alexander D. M., Bauer F. E., Giavalisco M., Huynh M., Kurk J., Mignoli M., 2007. *ApJ*, **670**, 156.

De Lucia G., Blaizot J., 2007. *MNRAS*, **375**, 2.

de Vaucouleurs G., 1948. *Annales d'Astrophysique*, **11**, 247.

Desai V., Dalcanton J. J., Aragón-Salamanca A., Jablonka P., Poggianti B., Gogarten S. M., Simard L., Milvang-Jensen B., Rudnick G., Zaritsky D., Clowe D., Halliday C., Pelló R., Saglia R., White S., 2007. *ApJ*, **660**, 1151.

Djorgovski S., Davis M., 1987. *ApJ*, **313**, 59.

Dobos L., Csabai I., 2011. *MNRAS*, **414**, 1862.

Donzelli C. J., Muriel H., Madrid J. P., 2011. *ApJS*, **195**, 15.

Dressler A., Lynden-Bell D., Burstein D., Davies R. L., Faber S. M., Terlevich R., Wegner G., 1987. *ApJ*, **313**, 42.

Dressler A., 1978. *ApJ*, **223**, 765.

Dressler A., 1984. *ApJ*, **281**, 512.

Dubinski J., 1998. *ApJ*, **502**, 141.

Edwards L. O. V., Hudson M. J., Balogh M. L., Smith R. J., 2007. *MNRAS*, **379**, 100.

Edwards L. O. V., Patton D. R., 2012. *MNRAS*, **425**, 287.

Ellis R. S., Abraham R. G., Dickinson M., 2001. *ApJ*, **551**, 111.

Fabian A. C., 1994. *ARA&A*, **32**, 277.

Fasano G., Bettoni D., Ascaso B., Tormen G., Poggianti B. M., Valentinuzzi T., D'Onofrio M., Fritz J., Moretti A., Omizzolo A., Cava A., Moles M., Dressler A., Couch W. J., Kjærgaard P., Varela J., 2010. *MNRAS*, **404**, 1490.

Finn R. A., Zaritsky D., McCarthy, Jr. D. W., Poggianti B., Rudnick G., Halliday C., Milvang-Jensen B., Pelló R., Simard L., 2005. *ApJ*, **630**, 206.

Fontana A., Dunlop J. S., Paris D., Targett T. A., Boutsia K., Castellano M., Galametz A., Grazian A., McLure R., Merlin E., Pentericci L., Wuyts S., Almaini O., Caputi K., Chary R.-R., Cirasuolo M., Conselice C. J., Cooray A., Daddi E., Dickinson M., Faber S. M., Fazio G., Ferguson H. C., Giallongo E., Giavalisco M., Grogin N. A., Hathi N., Koekemoer A. M., Koo D. C., Lucas R. A., Nonino M., Rix H. W., Renzini A., Rosario D., Santini P., Scarlata C., Sommariva V., Stark D. P., van der Wel A., Vanzella E., Wild V., Yan H., Zibetti S., 2014. *A&A*, **570**, A11.

Fukugita M., Shimasaku K., Ichikawa T., 1995. PASP, **107**, 945.

Furusawa H., Kosugi G., Akiyama M., Takata T., Sekiguchi K., Tanaka I., Iwata I., Kajisawa M., Yasuda N., Doi M., Ouchi M., Simpson C., Shimasaku K., Yamada T., Furusawa J., Morokuma T., Ishida C. M., Aoki K., Fuse T., Imanishi M., Iye M., Karoji H., Kobayashi N., Kodama T., Komiyama Y., Maeda Y., Miyazaki S., Mizumoto Y., Nakata F., Noumaru J., Ogasawara R., Okamura S., Saito T., Sasaki T., Ueda Y., Yoshida M., 2008. *ApJS*, **176**, 1.

Garijo A., Athanassoula E., Garcia-Gomez C., 1997. *A&A*, **327**, 930.

Giacintucci S., Venturi T., Murgia M., Dallacasa D., Athreya R., Bardelli S., Mazzotta P., Saikia D. J., 2007. *A&A*, **476**, 99.

Gonzalez A. H., Zabludoff A. I., Zaritsky D., 2005. *ApJ*, **618**, 195.

Graham A., Lauer T. R., Colless M., Postman M., 1996. *ApJ*, **465**, 534.

Graham A. W., Driver S. P., Petrosian V., Conselice C. J., Bershady M. A., Crawford S. M., Goto T., 2005. *AJ*, **130**, 1535.

Grogin N. A., Kocevski D. D., Faber S. M., Ferguson H. C., Koekemoer A. M., Riess A. G., Acquaviva V., Alexander D. M., Almaini O., Ashby M. L. N., Barden M., Bell E. F., Bournaud F., Brown T. M., Caputi K. I., Casertano S., Cassata P., Castellano M., Challis P., Chary R.-R., Cheung E., Cirasuolo M., Conselice C. J., Roshan Cooray A., Croton D. J., Daddi E., Dahlen T., Davé R., de Mello D. F., Dekel A., Dickinson M., Dolch T., Donley J. L., Dunlop J. S., Dutton A. A., Elbaz D., Fazio G. G., Filippenko A. V., Finkelstein S. L., Fontana A., Gardner J. P., Garnavich P. M., Gawiser E., Giavalisco M., Grazian A., Guo Y., Hathi N. P., Häussler B., Hopkins P. F., Huang J.-S., Huang K.-H., Jha S. W., Kartaltepe J. S., Kirshner R. P., Koo D. C., Lai K., Lee K.-S., Li W., Lotz J. M., Lucas R. A., Madau P., McCarthy P. J., McGrath E. J., McIntosh D. H., McLure R. J., Mobasher B., Moustakas L. A., Mozena M., Nandra K., Newman J. A., Niemi S.-M., Noeske K. G., Papovich C. J., Pentericci L., Pope A., Primack J. R., Rajan A., Ravindranath S., Reddy N. A., Renzini A., Rix H.-W., Robaina A. R., Rodney S. A., Rosario D. J., Rosati P., Salimbeni S., Scarlata C., Siana B., Simard L., Smidt J., Somerville R. S., Spinrad H., Straughn A. N., Strolger L.-G., Telford O., Teplitz H. I., Trump J. R., van der Wel A., Villforth C., Wechsler R. H., Weiner B. J., Wiklind T., Wild V., Wilson G., Wuyts S., Yan H.-J., Yun M. S., 2011. *ApJS*, **197**, 35.

Guo Y., McIntosh D. H., Mo H. J., Katz N., van den Bosch F. C., Weinberg M., Weinmann S. M., Pasquali A., Yang X., 2009. *MNRAS*, **398**, 1129.

Hartley W. G., Almaini O., Mortlock A., Conselice C. J., Grützbauch R., Simpson C., Bradshaw E. J., Chuter R. W., Foucaud S., Cirasuolo M., Dunlop J. S., McLure R. J., Pearce H. J., 2013. *MNRAS*, **431**, 3045.

Hashimoto Y., Henry J. P., Boehringer H., 2014. *MNRAS*, **440**, 588.

Hausman M. A., Ostriker J. P., 1978. *ApJ*, **224**, 320.

Häussler B., McIntosh D. H., Barden M., Bell E. F., Rix H.-W., Borch A., Beckwith S. V. W., Caldwell J. A. R., Heymans C., Jahnke K., Jogee S., Koposov S. E., Meisen-heimer K., Sánchez S. F., Somerville R. S., Wisotzki L., Wolf C., 2007a. *ApJS*, **172**, 615.

Häussler B., McIntosh D. H., Barden M., Bell E. F., Rix H.-W., Borch A., Beckwith S. V. W., Caldwell J. A. R., Heymans C., Jahnke K., Jogee S., Koposov S. E., Meisenheimer K., Sánchez S. F., Somerville R. S., Wisotzki L., Wolf C., 2007b. *ApJS*, **172**, 615.

Hearin A. P., Zentner A. R., Newman J. A., Berlind A. A., 2013. *MNRAS*, **430**, 1238.

Hoessel J. G., Oegerle W. R., Schneider D. P., 1987. *AJ*, **94**, 1111.

Hogg D. W., Blanton M. R., Brinchmann J., Eisenstein D. J., Schlegel D. J., Gunn J. E., McKay T. A., Rix H.-W., Bahcall N. A., Brinkmann J., Meiksin A., 2004. *ApJL*, **601**, L29.

Hopkins P. F., Cox T. J., Dutta S. N., Hernquist L., Kormendy J., Lauer T. R., 2009. *ApJS*, **181**, 135.

Hopkins P. F., Bundy K., Hernquist L., Wuyts S., Cox T. J., 2010. *MNRAS*, **401**, 1099.

Hoyos C., den Brok M., Verdoes Kleijn G., Carter D., Balcells M., Guzmán R., Peletier R., Ferguson H. C., Goudfrooij P., Graham A. W., Hammer D., Karick A. M., Lucey J. R., Matković A., Merritt D., Mouhcine M., Valentijn E., 2011. *MNRAS*, **411**, 2439.

Hoyos C., Aragón-Salamanca A., Gray M. E., Maltby D. T., Bell E. F., Barazza F. D., Böhm A., Häußler B., Jahnke K., Jogee S., Lane K. P., McIntosh D. H., Wolf C., 2012. *MNRAS*, **419**, 2703.

Huang S., Ho L. C., Peng C. Y., Li Z.-Y., Barth A. J., 2013. *ApJL*, **768**, L28.

Hubble E. P., 1925a. *Popular Astronomy*, **33**.

Hubble E. P., 1925b. *ApJ*, **62**.

Hubble E. P., 1926. *ApJ*, **64**.

Hubble E. P., 1930. *ApJ*, **71**.

Hudson M. J., Ebeling H., 1997. *ApJ*, **479**, 621.

Huertas-Company M., Mei S., Shankar F., Delaye L., Raichoor A., Covone G., Finoguenov A., Kneib J. P., Le F. O., Povic M., 2013a. *MNRAS*, **428**, 1715.

Huertas-Company M., Mei S., Shankar F., Delaye L., Raichoor A., Covone G., Finoguenov A., Kneib J. P., Le F. O., Povic M., 2013b. *MNRAS*, **428**, 1715.

Huertas-Company M., Shankar F., Mei S., Bernardi M., Aguerri J. A. L., Meert A., Vikram V., 2013c. *ApJ*, **779**, 29.

Ilbert O., Tresse L., Zucca E., Bardelli S., Arnouts S., Zamorani G., Pozzetti L., Bottini D., Garilli B., Le Brun V., Le Fèvre O., Maccagni D., Picat J.-P., Scaramella R., Scodeggio M., Vettolani G., Zanichelli A., Adami C., Arnaboldi M., Bolzonella M., Cappi A., Charlot S., Contini T., Foucaud S., Franzetti P., Gavignaud I., Guzzo L.,

Iovino A., McCracken H. J., Marano B., Marinoni C., Mathez G., Mazure A., Meneux B., Merighi R., Paltani S., Pello R., Pollo A., Radovich M., Bondi M., Bongiorno A., Busarello G., Ciliegi P., Lamareille F., Mellier Y., Merluzzi P., Ripepi V., Rizzo D., 2005. *A&A*, **439**, 863.

Johansson P. H., Naab T., Ostriker J. P., 2012. *ApJ*, **754**, 115.

Jones C., Forman W., 1984. *ApJ*, **276**, 38.

Jordán A., Côté P., West M. J., Marzke R. O., Minniti D., Rejkuba M., 2004. *AJ*, **127**, 24.

Kaastra J. S., Ferrigno C., Tamura T., Paerels F. B. S., Peterson J. R., Mittaz J. P. D., 2001. *A&A*, **365**, L99.

Kauffmann G., Heckman T. M., White S. D. M., Charlot S., Tremonti C., Brinchmann J., Bruzual G., Peng E. W., Seibert M., Bernardi M., Blanton M., Brinkmann J., Castander F., Csábai I., Fukugita M., Ivezic Z., Munn J. A., Nichol R. C., Padmanabhan N., Thakar A. R., Weinberg D. H., York D., 2003. *MNRAS*, **341**, 33.

Kauffmann G., White S. D. M., Heckman T. M., Ménard B., Brinchmann J., Charlot S., Tremonti C., Brinkmann J., 2004. *MNRAS*, **353**, 713.

Koekemoer A. M., Faber S. M., Ferguson H. C., Grogin N. A., Kocevski D. D., Koo D. C., Lai K., Lotz J. M., Lucas R. A., McGrath E. J., Ogaz S., Rajan A., Riess A. G., Rodney S. A., Strolger L., Casertano S., Castellano M., Dahlen T., Dickinson M., Dolch T., Fontana A., Giavalisco M., Grazian A., Guo Y., Hathi N. P., Huang K.-H., van der Wel A., Yan H.-J., Acquaviva V., Alexander D. M., Almaini O., Ashby M. L. N., Barden M., Bell E. F., Bournaud F., Brown T. M., Caputi K. I., Cassata P., Challis P. J., Chary R.-R., Cheung E., Cirasuolo M., Conselice C. J., Roshan Cooray A., Croton D. J., Daddi E., Davé R., de Mello D. F., de Ravel L., Dekel A., Donley J. L., Dunlop J. S., Dutton A. A., Elbaz D., Fazio G. G., Filippenko A. V., Finkelstein S. L., Frazer C., Gardner J. P., Garnavich P. M., Gawiser E., Gruetzbauch R., Hartley W. G., Häussler B., Herrington J., Hopkins P. F., Huang J.-S., Jha S. W., Johnson A., Kartaltepe J. S., Khostovan A. A., Kirshner R. P., Lani C., Lee K.-S., Li W., Madau P., McCarthy P. J., McIntosh D. H., McLure R. J., McPartland C., Mobasher B., Moreira H., Mortlock A., Moustakas L. A., Mozena M., Nandra K., Newman J. A., Nielsen J. L., Niemi S., Noeske K. G., Papovich C. J., Pentericci L., Pope A., Primack J. R., Ravindranath S., Reddy N. A., Renzini A., Rix H.-W., Robaina A. R., Rosario D. J., Rosati P., Salimbeni S., Scarlata C., Siana B., Simard L., Smidt J., Snyder D., Somerville R. S., Spinrad H., Straughn A. N., Telford O., Teplitz H. I., Trump J. R., Vargas C., Villforth C., Wagner C. R., Wandro P., Wechsler R. H., Weiner B. J., Wiklind T., Wild V., Wilson G., Wuyts S., Yun M. S., 2011. *ApJS*, **197**, 36.

Kormendy J., Djorgovski S., 1989. *ARA&A*, **27**, 235.

Kormendy J., 1977. *ApJ*, **218**, 333.

Kormendy J., 1987. In: *Structure and Dynamics of Elliptical Galaxies*, p. 17, ed. de Zeeuw P. T.

Kron R. G., 1980. *ApJS*, **43**, 305.

Kroupa P., 2001. *MNRAS*, **322**, 231.

Laine S., van der Marel R. P., Lauer T. R., Postman M., O'Dea C. P., Owen F. N., 2003. *AJ*, **125**, 478.

Lani C., Almaini O., Hartley W. G., Mortlock A., Häußler B., Chuter R. W., Simpson C., van der Wel A., Grützbauch R., Conselice C. J., Bradshaw E. J., Cooper M. C., Faber S. M., Grogin N. A., Kocevski D. D., Koekemoer A. M., Lai K., 2013. *MNRAS*, **435**, 207.

Laporte C. F. P., White S. D. M., Naab T., Ruszkowski M., Springel V., 2012. *MNRAS*, **424**, 747.

Laporte C. F. P., White S. D. M., Naab T., Gao L., 2013. *MNRAS*, **435**, 901.

Lauer T. R., Postman M., 1992. *ApJL*, **400**, L47.

Lauer T. R., Faber S. M., Richstone D., Gebhardt K., Tremaine S., Postman M., Dressler A., Aller M. C., Filippenko A. V., Green R., Ho L. C., Kormendy J., Magorrian J., Pinkney J., 2007. *ApJ*, **662**, 808.

Lauer T. R., Postman M., Strauss M. A., Graves G. J., Chisari N. E., 2014. *ApJ*, **797**, 82.

Lawrence A., Warren S. J., Almaini O., Edge A. C., Hambly N. C., Jameson R. F., Lucas P., Casali M., Adamson A., Dye S., Emerson J. P., Foucaud S., Hewett P., Hirst P., Hodgkin S. T., Irwin M. J., Lodieu N., McMahon R. G., Simpson C., Smail I., Mortlock D., Folger M., 2007. *MNRAS*, **379**, 1599.

Leja J., van Dokkum P., Franx M., 2013. *ApJ*, **766**, 33.

Lidman C., Suherli J., Muzzin A., Wilson G., Demarco R., Brough S., Rettura A., Cox J., DeGroot A., Yee H. K. C., Gilbank D., Hoekstra H., Balogh M., Ellingson E., Hicks A., Nantais J., Noble A., Lacy M., Surace J., Webb T., 2012. *MNRAS*, **427**, 550.

Lidman C., Iacobuta G., Bauer A. E., Barrientos L. F., Cerulo P., Couch W. J., Delaye L., Demarco R., Ellingson E., Faloon A. J., Gilbank D., Huertas-Company M., Mei S., Meyers J., Muzzin A., Noble A., Nantais J., Rettura A., Rosati P., Sánchez-Janssen R., Strazzullo V., Webb T. M. A., Wilson G., Yan R., Yee H. K. C., 2013. *MNRAS*, **433**, 825.

Lin Y.-T., Mohr J. J., 2004. *ApJ*, **617**, 879.

Lin Y.-T., Brodwin M., Gonzalez A. H., Bode P., Eisenhardt P. R. M., Stanford S. A., Vikhlinin A., 2013. *ApJ*, **771**, 61.

Lin Y.-T., Ostriker J. P., Miller C. J., 2010. *ApJ*, **715**, 1486.

Lintott C. J., Schawinski K., Slosar A., Land K., Bamford S., Thomas D., Raddick M. J., Nichol R. C., Szalay A., Andreescu D., Murray P., Vandenberg J., 2008. *MNRAS*, **389**, 1179.

Liu F. S., Xia X. Y., Mao S., Wu H., Deng Z. G., 2008. *MNRAS*, **385**, 23.

Liu F. S., Mao S., Deng Z. G., Xia X. Y., Wen Z. L., 2009. *MNRAS*, **396**, 2003.

Lugger P. M., 1984. *ApJ*, **286**, 106.

Maltby D. T., Aragón-Salamanca A., Gray M. E., Barden M., Häußler B., Wolf C., Peng C. Y., Jahnke K., McIntosh D. H., Böhm A., van Kampen E., 2010. *MNRAS*, **402**, 282.

Malumuth E. M., 1992. *ApJ*, **386**, 420.

Marchesini D., Muzzin A., Stefanon M., Franx M., Brammer G. G., Marsan C. Z., Vulcani B., Fynbo J. P. U., Milvang-Jensen B., Dunlop J. S., Buitrago F., 2014. *ApJ*, **794**, 65.

Matthews T. A., Morgan W. W., Schmidt M., 1964. *ApJ*, **140**, 35.

McNamara B. R., O'Connell R. W., 1989. *AJ*, **98**, 2018.

McNamara B. R., O'Connell R. W., 1992. *ApJ*, **393**, 579.

McNamara B. R., Wise M., Sarazin C. L., Jannuzi B. T., Elston R., 1996. *ApJL*, **466**, L9.

Merritt D., 1983. *ApJ*, **264**, 24.

Merritt D., 1985. *ApJ*, **289**, 18.

Miller C. J., Nichol R. C., Reichart D., Wechsler R. H., Evrard A. E., Annis J., McKay T. A., Bahcall N. A., Bernardi M., Boehringer H., Connolly A. J., Goto T., Kniazev A., Lamb D., Postman M., Schneider D. P., Sheth R. K., Voges W., 2005. *AJ*, **130**, 968.

Miyazaki S., Komiyama Y., Nakaya H., Kamata Y., Doi Y., Hamana T., Karoji H., Furusawa H., Kawanomoto S., Morokuma T., Ishizuka Y., Nariai K., Tanaka Y., Uraguchi F., Utsumi Y., Obuchi Y., Okura Y., Oguri M., Takata T., Tomono D., Kurakami T., Namikawa K., Usuda T., Yamanoi H., Terai T., Uekiyo H., Yamada Y., Koike M., Aihara H., Fujimori Y., Mineo S., Miyatake H., Yasuda N., Nishizawa J., Saito T., Tanaka M., Uchida T., Katayama N., Wang S.-Y., Chen H.-Y., Lupton R., Loomis C., Bickerton S., Price P., Gunn J., Suzuki H., Miyazaki Y., Muramatsu M., Yamamoto K., Endo M., Ezaki Y., Itoh N., Miwa Y., Yokota H., Matsuda T., Ebinuma R., Takeshi K., 2012. In: *Ground-based and Airborne Instrumentation for Astronomy IV*, 84460Z.

Mo H. J., Mao S., White S. D. M., 1998. *MNRAS*, **295**, 319.

More S., 2012. *ApJ*, **761**, 127.

Morgan W. W., Kayser S., White R. A., 1975. *ApJ*, **199**, 545.

Mortlock A., Conselice C. J., Hartley W. G., Ownsworth J. R., Lani C., Bluck A. F. L., Almaini O., Duncan K., van der Wel A., Koekemoer A. M., Dekel A., Davé R., Ferguson H. C., de Mello D. F., Newman J. A., Faber S. M., Grogin N. A., Kocevski D. D., Lai K., 2013. *MNRAS*, **433**, 1185.

Mortlock A., Conselice C. J., Hartley W. G., Duncan K., Lani C., Ownsworth J. R., Almaini O., Wel A. v. d., Huang K.-H., Ashby M. L. N., Willner S. P., Fontana A., Dekel A., Koekemoer A. M., Ferguson H. C., Faber S. M., Grogin N. A., Kocevski D. D., 2015. *MNRAS*, **447**, 2.

Muldrew S. I., Pearce F. R., Power C., 2011. *MNRAS*, **410**, 2617.

Mundy C. J., Conselice C. J., Ownsworth J. R., 2015. *MNRAS*, **450**, 3696.

Murante G., Giovalli M., Gerhard O., Arnaboldi M., Borgani S., Dolag K., 2007. *MNRAS*, **377**, 2.

Naab T., Johansson P. H., Ostriker J. P., 2009. *ApJL*, **699**, L178.

Nelson A. E., Gonzalez A. H., Zaritsky D., Dalcanton J. J., 2002. *ApJ*, **566**, 103.

Niederste-Ostholt M., Strauss M. A., Dong F., Koester B. P., McKay T. A., 2010. *MNRAS*, **405**, 2023.

Oegerle W. R., Hill J. M., 2001. *AJ*, **122**, 2858.

Oegerle W. R., Hoessel J. G., 1991. *ApJ*, **375**, 15.

Oemler, Jr. A., 1976. *ApJ*, **209**, 693.

Oliva-Altamirano P., Brough S., Jimmy, Kim-Vy T., Couch W. J., McDermid R. M., Lidman C., von der Linden A., Sharp R., 2015. *MNRAS*, **449**, 3347.

Oser L., Ostriker J. P., Naab T., Johansson P. H., Burkert A., 2010. *ApJ*, **725**, 2312.

Ostriker J. P., Hausman M. A., 1977. *ApJL*, **217**, L125.

Ostriker J. P., Tremaine S. D., 1975. *ApJL*, **202**, L113.

Ownsworth J. R., Conselice C. J., Mortlock A., Hartley W. G., Buitrago F., 2012. *MNRAS*, **426**, 764.

Ownsworth J. R., Conselice C. J., Mortlock A., Hartley W. G., Almaini O., Duncan K., Mundy C. J., 2014. *MNRAS*, **445**, 2198.

Papovich C., Moustakas L. A., Dickinson M., Le Floc'h E., Rieke G. H., Daddi E., Alexander D. M., Bauer F., Brandt W. N., Dahlen T., Egami E., Eisenhardt P., Elbaz D., Ferguson H. C., Giavalisco M., Lucas R. A., Mobasher B., Pérez-González P. G., Stutz A., Rieke M. J., Yan H., 2006. *ApJ*, **640**, 92.

Paranjape A., Sheth R. K., 2012. *MNRAS*, **423**, 1845.

Patel P., Maddox S., Pearce F. R., Aragón-Salamanca A., Conway E., 2006. *MNRAS*, **370**, 851.

Peebles P. J. E., 1980. *The large-scale structure of the universe*.

Peng C. Y., Ho L. C., Impey C. D., Rix H.-W., 2002. *AJ*, **124**, 266.

Peng C. Y., Ho L. C., Impey C. D., Rix H.-W., 2010. *AJ*, **139**, 2097.

Peterson R. C., Terndrup D. M., Sadler E. M., Walker A. R., 2001. *ApJ*, **547**, 240.

Petrosian V., 1976. *ApJL*, **209**, L1.

Plionis M., Benoist C., Maurogordato S., Ferrari C., Basilakos S., 2003. *ApJ*, **594**, 144.

Poggianti B. M., De Lucia G., Varela J., Aragón-Salamanca A., Finn R., Desai V., von der Linden A., White S. D. M., 2010. *MNRAS*, **405**, 995.

Poggianti B. M., Calvi R., Bindoni D., D'Onofrio M., Moretti A., Valentinuzzi T., Fasano G., Fritz J., De Lucia G., Vulcani B., Bettoni D., Gullieuszik M., Omizzolo A., 2013. *ApJ*, **762**, 77.

Popesso P., Biviano A., Böhringer H., Romaniello M., 2007. *A&A*, **464**, 451.

Porter A. C., 1988. *PhD thesis*, California Institute of Technology, Pasadena.

Postman M., Lauer T. R., 1995. *ApJ*, **440**, 28.

Press W. H., Spergel D. N., 1988. *ApJ*, **325**, 715.

Puchwein E., Springel V., Sijacki D., Dolag K., 2010. *MNRAS*, **406**, 936.

Quintana H., Lawrie D. G., 1982. *AJ*, **87**, 1.

Rettura A., Rosati P., Nonino M., Fosbury R. A. E., Gobat R., Menci N., Strazzullo V., Mei S., Demarco R., Ford H. C., 2010. *ApJ*, **709**, 512.

Rhee G., Nico R., 1989. Ap&SS, **157**, 201.

Richstone D. O., Malumuth E. M., 1983. *ApJ*, **268**, 30.

Richstone D. O., 1976. *ApJ*, **204**, 642.

Romeo A. D., Napolitano N. R., Covone G., Sommer-Larsen J., Antonuccio-Delogu V., Capaccioli M., 2008. *MNRAS*, **389**, 13.

Rudick C. S., Mihos J. C., McBride C. K., 2011. *ApJ*, **732**, 48.

Salim S., Rich R. M., Charlot S., Brinchmann J., Johnson B. D., Schiminovich D., Seibert M., Mallery R., Heckman T. M., Forster K., Friedman P. G., Martin D. C., Morrissey P., Neff S. G., Small T., Wyder T. K., Bianchi L., Donas J., Lee Y.-W., Madore B. F., Milliard B., Szalay A. S., Welsh B. Y., Yi S. K., 2007. *ApJS*, **173**, 267.

Salomé P., Combes F., 2003. *A&A*, **412**, 657.

Sandage A., Hardy E., 1973. *ApJ*, **183**, 743.

Sandage A., 1976. *ApJ*, **205**, 6.

Sandage A., 1988. *ARA&A*, **26**, 561.

Schawinski K., Urry C. M., Virani S., Coppi P., Bamford S. P., Treister E., Lintott C. J., Sarzi M., Keel W. C., Kaviraj S., Cardamone C. N., Masters K. L., Ross N. P., Andreescu D., Murray P., Nichol R. C., Raddick M. J., Slosar A., Szalay A. S., Thomas D., Vandenberg J., 2010. *ApJ*, **711**, 284.

Schechter P. L., Peebles P. J. E., 1976. *ApJ*, **209**, 670.

Schneider D. P., Gunn J. E., Hoessel J. G., 1983. *ApJ*, **268**, 476.

Schombert J. M., 1986. *ApJS*, **60**, 603.

Schombert J. M., 1987. *ApJS*, **64**, 643.

Seigar M. S., Graham A. W., Jerjen H., 2007. *MNRAS*, **378**, 1575.

Sérsic J. L., 1963. *Boletin de la Asociacion Argentina de Astronomia La Plata Argentina*, **6**, 41.

Shankar F., Marulli F., Bernardi M., Mei S., Meert A., Vikram V., 2013. *MNRAS*, **428**, 109.

Shankar F., Guo H., Bouillot V., Rettura A., Meert A., Buchan S., Kravtsov A., Bernardi M., Sheth R., Vikram V., Marchesini D., Behroozi P., Zheng Z., Maraston C., Ascaso B., Lemaux B. C., Capozzi D., Huertas-Company M., Gal R. R., Lubin L. M., Conselice C. J., Carollo M., Cattaneo A., 2014a. *ApJL*, **797**, L27.

Shankar F., Mei S., Huertas-Company M., Moreno J., Fontanot F., Monaco P., Bernardi M., Cattaneo A., Sheth R., Licitra R., Delaye L., Raichoor A., 2014b. *MNRAS*, **439**, 3189.

Shankar F., Buchan S., Rettura A., Bouillot V. R., Moreno J., Licitra R., Bernardi M., Huertas-Company M., Mei S., Ascaso B., Sheth R., Delaye L., Raichoor A., 2015. *ApJ*, **802**, 73.

Shen S., Mo H. J., White S. D. M., Blanton M. R., Kauffmann G., Voges W., Brinkmann J., Csabai I., 2003. *MNRAS*, **343**, 978.

Springel V., White S. D. M., Jenkins A., Frenk C. S., Yoshida N., Gao L., Navarro J., Thacker R., Croton D., Helly J., Peacock J. A., Cole S., Thomas P., Couchman H., Evrard A., Colberg J., Pearce F., 2005. *Nature*, **435**, 629.

Strateva I., Ivezić Ž., Knapp G. R., Narayanan V. K., Strauss M. A., Gunn J. E., Lupton R. H., Schlegel D., Bahcall N. A., Brinkmann J., Brunner R. J., Budavári T., Csabai I., Castander F. J., Doi M., Fukugita M., Győry Z., Hamabe M., Hennessy G., Ichikawa T., Kunszt P. Z., Lamb D. Q., McKay T. A., Okamura S., Racusin J., Sekiguchi M., Schneider D. P., Shimasaku K., York D., 2001. *AJ*, **122**, 1861.

Tamura T., Kaastra J. S., Peterson J. R., Paerels F. B. S., Mittaz J. P. D., Trudolyubov S. P., Stewart G., Fabian A. C., Mushotzky R. F., Lumb D. H., Ikebe Y., 2001. *A&A*, **365**, L87.

Taylor-Mager V. A., Conselice C. J., Windhorst R. A., Jansen R. A., 2007. *ApJ*, **659**, 162.

Tempel E., Tago E., Liivamägi L. J., 2012. *A&A*, **540**, A106.

Tonry J. L., 1987. In: *Structure and Dynamics of Elliptical Galaxies*, p. 89, ed. de Zeeuw P. T., D. Reidel Publishing Co., Princeton, NJ.

Tovmassian H. M., Andernach H., 2012. *MNRAS*, **427**, 2047.

Tremaine S. D., Richstone D. O., 1977. *ApJ*, **212**, 311.

Tremaine S., 1990. In: *Dynamics and Interactions of Galaxies*, p. 394, ed. Wielen R.

Trujillo I., Conselice C. J., Bundy K., Cooper M. C., Eisenhardt P., Ellis R. S., 2007. *MNRAS*, **382**, 109.

Twite J. W., Conselice C. J., Buitrago F., Noeske K., Weiner B. J., Acosta-Pulido J. A., Bauer A. E., 2012. *MNRAS*, **420**, 1061.

Valentinuzzi T., Fritz J., Poggianti B. M., Cava A., Bettoni D., Fasano G., D'Onofrio M., Couch W. J., Dressler A., Moles M., Moretti A., Omizzolo A., Kjærgaard P., Vanzella E., Varela J., 2010. *ApJ*, **712**, 226.

van der Wel A., Holden B. P., Zirm A. W., Franx M., Rettura A., Illingworth G. D., Ford H. C., 2008. *ApJ*, **688**, 48.

van der Wel A., Bell E. F., Häussler B., McGrath E. J., Chang Y.-Y., Guo Y., McIntosh D. H., Rix H.-W., Barden M., Cheung E., Faber S. M., Ferguson H. C., Galametz A., Grogin N. A., Hartley W., Kartaltepe J. S., Kocevski D. D., Koekemoer A. M., Lotz J., Mozena M., Peth M. A., Peng C. Y., 2012. *ApJS*, **203**, 24.

van der Wel A., Franx M., van Dokkum P. G., Skelton R. E., Momcheva I. G., Whitaker K. E., Brammer G. B., Bell E. F., Rix H.-W., Wuyts S., Ferguson H. C., Holden B. P., Barro G., Koekemoer A. M., Chang Y.-Y., McGrath E. J., Häussler B., Dekel A., Behroozi P., Fumagalli M., Leja J., Lundgren B. F., Maseda M. V., Nelson E. J., Wake D. A., Patel S. G., Labbé I., Faber S. M., Grogin N. A., Kocevski D. D., 2014. *ApJ*, **788**, 28.

van Dokkum P. G., Franx M., Förster Schreiber N. M., Illingworth G. D., Daddi E., Knudsen K. K., Labbé I., Moorwood A., Rix H.-W., Röttgering H., Rudnick G., Trujillo I., van der Werf P., van der Wel A., van Starkenburg L., Wuyts S., 2004. *ApJ*, **611**, 703.

van Dokkum P. G., Whitaker K. E., Brammer G., Franx M., Kriek M., Labbé I., Marchesini D., Quadri R., Bezanson R., Illingworth G. D., Muzzin A., Rudnick G., Tal T., Wake D., 2010. *ApJ*, **709**, 1018.

van Dokkum P. G., 2005. *AJ*, **130**, 2647.

van Rijsbergen C. J., 1979. *Information Retrieval (2nd ed.)*, Butterworth-Heinemann, Newton, MA, USA.

von der Linden A., Best P. N., Kauffmann G., White S. D. M., 2007. *MNRAS*, **379**, 867.

Vulcani B., Poggianti B. M., Fasano G., Desai V., Dressler A., Oemler A., Calvi R., D'Onofrio M., Moretti A., 2012. *MNRAS*, **420**, 1481.

Vulcani B., Poggianti B. M., Oemler A., Dressler A., Aragón-Salamanca A., De Lucia G., Moretti A., Gladders M., Abramson L., Halliday C., 2013. *A&A*, **550**, A58.

Vulcani B., Bundy K., Lackner C., Leauthaud A., Treu T., Mei S., Coccato L., Kneib J. P., Auger M., Nipoti C., 2014. *ApJ*, **797**, 62.

West M. J., 1994. *MNRAS*, **268**, 79.

Whiley I. M., Aragón-Salamanca A., De Lucia G., von der Linden A., Bamford S. P., Best P., Bremer M. N., Jablonka P., Johnson O., Milvang-Jensen B., Noll S., Poggianti B. M., Rudnick G., Saglia R., White S., Zaritsky D., 2008. *MNRAS*, **387**, 1253.

White S. D. M., Rees M. J., 1978. *MNRAS*, **183**, 341.

White S. D. M., Clowe D. I., Simard L., Rudnick G., De Lucia G., Aragón-Salamanca A., Bender R., Best P., Bremer M., Charlot S., Dalcanton J., Dantel M., Desai V., Fort B., Halliday C., Jablonka P., Kauffmann G., Mellier Y., Milvang-Jensen B., Pelló R., Poggianti B., Poirier S., Rottgering H., Saglia R., Schneider P., Zaritsky D., 2005. *A&A*, **444**, 365.

White S. D. M., 1976. *MNRAS*, **174**, 19.

Wolf C., Aragón-Salamanca A., Balogh M., Barden M., Bell E. F., Gray M. E., Peng C. Y., Bacon D., Barazza F. D., Böhm A., Caldwell J. A. R., Gallazzi A., Häußler B., Heymans C., Jahnke K., Jogee S., van Kampen E., Lane K., McIntosh D. H., Meisenheimer K., Papovich C., Sánchez S. F., Taylor A., Wisotzki L., Zheng X., 2009. *MNRAS*, **393**, 1302.

York D. G., Adelman J., Anderson, Jr. J. E., Anderson S. F., Annis J., Bahcall N. A., Bakken J. A., Barkhouser R., Bastian S., Berman E., Boroski W. N., Bracker S., Briegel C., Briggs J. W., Brinkmann J., Brunner R., Burles S., Carey L., Carr M. A., Castander F. J., Chen B., Colestock P. L., Connolly A. J., Crocker J. H., Csabai I., Czarapata P. C., Davis J. E., Doi M., Dombeck T., Eisenstein D., Ellman N., Elms B. R., Evans M. L., Fan X., Federwitz G. R., Fiscelli L., Friedman S., Frieman J. A., Fukugita M., Gillespie B., Gunn J. E., Gurbani V. K., de Haas E., Haldeman M., Harris F. H., Hayes J., Heckman T. M., Hennessy G. S., Hindsley R. B., Holm S., Holmgren D. J., Huang C.-h., Hull C., Husby D., Ichikawa S.-I., Ichikawa T., Ivezić Ž., Kent S., Kim R. S. J., Kinney E., Klaene M., Kleinman A. N., Kleinman S., Knapp G. R., Korienek J., Kron R. G., Kunszt P. Z., Lamb D. Q., Lee B., Leger R. F., Limmongkol S., Lindenmeyer C., Long D. C., Loomis C., Loveday J., Lucinio R., Lupton R. H., MacKinnon B., Mannery E. J., Mantsch P. M., Margon B., McGehee P., McKay T. A., Meiksin A., Merelli A., Monet D. G., Munn J. A., Narayanan V. K., Nash T., Neilsen E., Neswold R., Newberg H. J., Nichol R. C., Nicinski T., Nonino M., Okada N., Okamura S., Ostriker J. P., Owen R., Pauls A. G., Peoples J., Peterson R. L., Petravick D., Pier J. R., Pope A., Pordes R., Prosapio A., Rechenmacher R.,

Quinn T. R., Richards G. T., Richmond M. W., Rivetta C. H., Rockosi C. M., Ruthmansdorfer K., Sandford D., Schlegel D. J., Schneider D. P., Sekiguchi M., Sergey G., Shimasaku K., Siegmund W. A., Smee S., Smith J. A., Snedden S., Stone R., Stoughton C., Strauss M. A., Stubbs C., SubbaRao M., Szalay A. S., Szapudi I., Szokoly G. P., Thakar A. R., Tremonti C., Tucker D. L., Uomoto A., Vanden Berk D., Vogeley M. S., Waddell P., Wang S.-i., Watanabe M., Weinberg D. H., Yanny B., Yasuda N., SDSS Collaboration, 2000. *AJ*, **120**, 1579.

Zabludoff A. I., Huchra J. P., Geller M. J., 1990. *ApJS*, **74**, 1.

Zhang Y., Miller C., McKay T., Rooney P., Evrard A. E., Romer A. K., Perfecto R., Song J., Desai S., Mohr J., Wilcox H., Bermeo-Hernandez A., Jeltema T., Hollowood D., Bacon D., Capozzi D., Collins C., Das R., Gerdes D., Hennig C., Hilton M., Hoyle B., Kay S., Liddle A., Mann R. G., Mehrtens N., Nichol R. C., Papovich C., Sahlén M., Soares-Santos M., Stott J., Viana P. T., Abbott T., Abdalla F. B., Banerji M., Bauer A. H., Benoit-Lévy A., Bertin E., Brooks D., Buckley-Geer E., Burke D. L., Carnero Rosell A., Castander F. J., Diehl H. T., Doel P., Cunha C. E., Eifler T. F., Fausti Neto A., Fernandez E., Flaugher B., Fosalba P., Frieman J., Gaztanaga E., Gruen D., Gruendl R. A., Honscheid K., James D., Kuehn K., Kuropatkin N., Lahav O., Maia M. A. G., Makler M., Marshall J. L., Martini P., Miquel R., Ogando R., Plazas A. A., Roodman A., Rykoff E. S., Sako M., Sanchez E., Scarpine V., Schubnell M., Sevilla I., Smith R. C., Sobreira F., Suchyta E., Swanson M. E. C., Tarle G., Thaler J., Tucker D., Vikram V., da Costa L. N., 2016. *ApJ*, **816**, 98.

Zhao D., Aragón-Salamanca A., Conselice C. J., 2015a. *MNRAS*, **448**, 2530.

Zhao D., Aragón-Salamanca A., Conselice C. J., 2015b. *MNRAS*, **453**, 4444.